UNIVERSITÀ DEGLI STUDI DI MILANO

DIPARTIMENTO DI FISICA

CORSO DI DOTTORATO DI RICERCA IN

FISICA, ASTROFISICA E FISICA APPLICATA

CICLO XXXI

Optical and electrical properties of supersonic cluster beam implanted metal – polymer nanocomposites

Settore Scientifico disciplinare FIS/03

Tesi di Dottorato di:

Chloé Minnai

Coordinatore: Prof. Francesco Ragusa

Supervisore: Dr. Marco Potenza

Co-Supervisore: Prof. Paolo Milani

A.A. 2018-2019

1 Introduction

1.1 Free Clusters

Clusters are aggregates composed of a countable number of atoms or molecules, starting with the dimer and reaching, with a vaguely defined upper bound of several hundred thousand atoms, into that interesting size range[1].

Clusters have properties that are different from both atoms and bulk materials[1,2]. In these small aggregates the surface-to-volume ratio is very large and hence the surface atoms, play a dominant role compared to the bulk ones. Considering as an example a cluster with 1000 atoms, about a quarter of the atoms lie on the surface, for this reason its properties may be considerably different compared with the bulk.

The substantial contribution of the surface atoms is the origin of unique optical, electronic, and magnetic properties which has been widely investigated so far[3,4]. The technological potentialities of metal clusters have been proposed since the 70′s when several pioneering investigations started and gave birth in the 90′s to the very rich field of cluster physics.[1] The aim of these studies was to enlighten the peculiar physical properties of isolated clusters, to understand their dependence upon their properties such as the material, their size, the number of atoms which compose them, with the ultimate goal of controlling these properties.

In figure 1.1, the dependence of a generic cluster property G as a function of the number of atoms N and on the reverse of the cluster dimension is shown. We can see that the smaller is the cluster the more it differs from the bulk, due to the quantum size and surface size effects which become predominant at this scale.

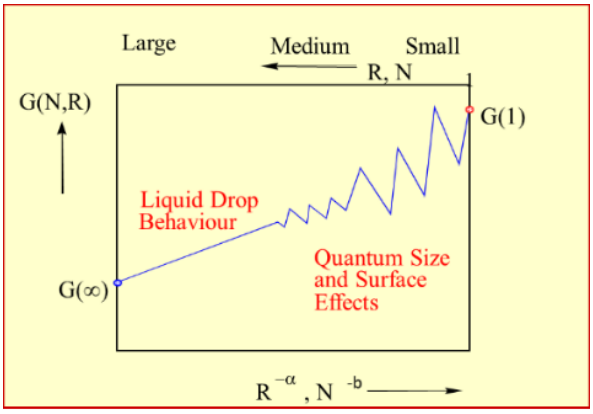

Figure 1.1: Dependence of a generic cluster properties on its dimension and number of atoms[5].

This peculiar trend is common to many physical properties of clusters and motivated the scientific community to investigate its origin, in order to control specific cluster properties for applications[4,6,7]. As an example, the interest in the electrical properties of metal clusters significantly grown in the age of miniaturization of electronic devices [1]. Surprisingly, the interest in their optical properties dates back to the IV century, when the bright and fascinating colours of noble metal nanoparticles were used as decorative pigments in stained glasses and artworks [8,9] (see figure 1.2a as an example).

The fundamental knowledge on the optical properties of metal nanoparticles and how to prepare them looks back at a long history connected with the names of many illustrious chemists and physicists.[10] It seems that the art of preparing silver and gold nanoparticles solutions was well known since the 16th century, when these where commonly called *luna potabile* and *aurum potabile* [10].

It was by studying gold colloidal solution prepared by himself (see figure 2b) that Michel Faraday understood that the colours of stained glasses were due to the presence of metal nanoparticles, and that the different colors corresponded to a different size of the particles embedded. This idea came from the observation that blue gold dispersions could be prepared from red ones but not vice versa and that blue solids precipitated much faster than red ones, leading him to conclude that the blue particles were larger in size than the red ones[11,12].

Faraday's work was followed by Rayleigh[13], who extensively studied how the intensity of the effect and the resonant wavelength depended on the size and shape of the nanoparticles. This was confirmed at the beginning of 20th century when with the invention of the ultramicroscope by Siedentopf and Zsigmondy, it become possible to characterize nanoparticles size by measuring their Rayleigh scattering, hence going below the resolution of optical microscopes.

Interestingly, glass-gold nanocomposites were the object of the first report on an ultramicroscope. About at the same time (1904), Kirchner and Zsigmondy suggested the influence of the particle reciprocal distance on the phenomenon. This idea was mainly based on the observation that a nanocomposite made of colloidal gold and gelatine, reversibly changed the color from blue to red upon swelling with water).

These observations were fundamental for the theoretical studies of Mie and Maxwell Garnett who starting from the Drude model, provided models explaining the plasmonic resonance of insulated spherical nanoparticles (the Mie's theory) and what happens when the nanoparticles are embedded in a polymer matrix: the effect of interaction of nanoparticle with themselves and with a surrounding medium (the Maxwell-Garnett theory).

Nowadays we know the bright colors of water suspensions of noble metal nanoparticles are due to a resonance phenomenon occurring when metal particles are irradiated by the light. This resonance, generally called "Surface Plasmon Resonance" (SPR) [2] consists in a large amplitude electromagnetic field. For particles much smaller than the wavelength such as metal nanoparticles plasmon oscillates locally around the particle and it is hence called "Localized Surface Plasmon Resonance" (LSPR). Moreover, with the rapid advances in nanoparticle synthesis [14] experimentally confirmed how the color of the suspension depends on the metal, the size and shape of the particle in use[15–18]. An example is shown in figure 1.2c, where nanoparticles with different shapes are suspended which originate in different colours.

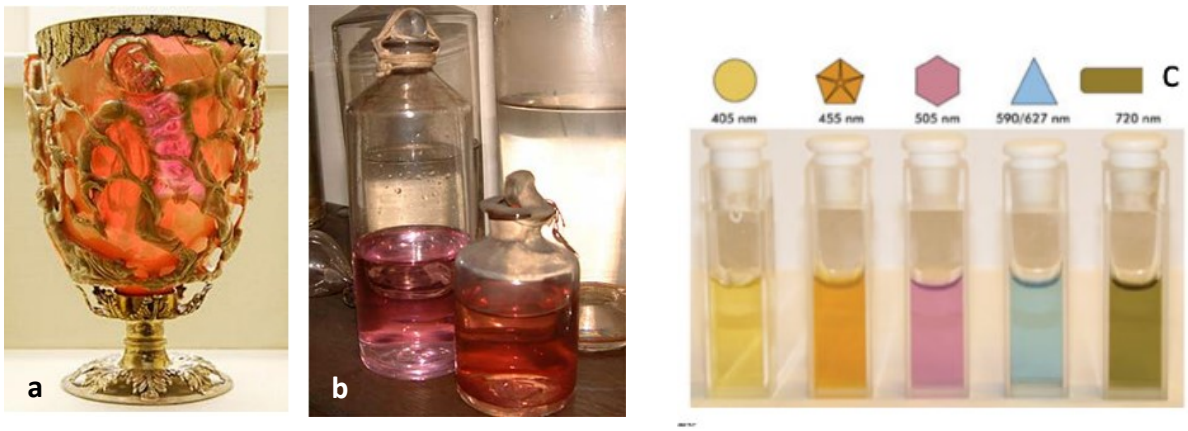

Figure 1.2 (a) The Lycurgus cup (IV century) is the most ancient example of using nanoparticles to change the optical properties of a dielectric. The red colour is due to the plasmonic resonance of the gold nanoparticles embedded in the glass matrix. (b) Suspensions of gold nanoparticles prepared by Michel Faraday (c) Suspensions containing silver nanoparticles with different shapes. The shapes strongly affect the optical absorption of the material.

This enlightens a key point of the cluster potentialities which is the possibility to control and tune the physical properties of an ensemble of clusters (the optical absorption in this case) by controlling the properties of each component of the ensemble (the cluster size and shape for instance)[15,19].

An important factor to consider when dealing with nanoparticles dispersed in a solution is that the optical response is well defined (qualitatively, the color of the solution is as bright as in the solutions shown in figure 1.2c) if the nanoparticles are almost monodispersed in both their size and shape. For this reason, it is of fundamental importance when new recipes are developed to avoid the formation of uncontrolled aggregates, i.e. to preserve the nanoparticles individuality.

Their excellent properties, their facile surface conjugation to a variety of chemical and biomolecular ligands [20], their biocompatibility, and high chemical and photostability have brought nanoparticles to the forefront of nanotechnology research directed toward a wide range of applications ranging from photonics [21–23], biomedicine [23–25], sensing and cathalisys[8].

1.2 From free clusters to nanostructured materials

By assembling preformed clusters, one can build **nanostructured materials**. These can be divided in two main categories: **cluster assembled films** and **nanocomposites**. In the former case nanoparticles are deposited on a substrate in the latter they are incorporated in a matrix.

Nanostructured materials are different from the corresponding bulk materials in a number of respects.[6,26–28] This offers an exciting pathway for the construction of macroscopic materials with designer-specified optical, electrical, and catalytic properties [9,19,29,30] which reflect the ones of their building blocks.

An important point that needs to be considered when the clusters are no longer single non-interacting units but part of an ensemble is how to preserve the cluster individuality and what is the effect of dealing with clusters with a distribution of sizes. [31,32]

Of course, the importance of having a system formed of monodispersed clusters depends on the context where the system is employed. Many applications do not require having a mass selection on the nanoparticles: an example comes from the reinforced rubbers, which consists in nanocomposite made incorporating nanoparticles in a rubber in order to reinforce its mechanical properties. For this kind of applications, the priority is to have a system which can be produced at the mass scale and introducing a production step which select the particles size could significantly reduce the scalability of the whole system.

Having a nanostructured material with monodispersed cluster can be an advantage for the optical properties of the system, as the narrower is the size distribution the sharper will be its absorption spectrum. However, many experiments demonstrate this requirement is not fundamental both for biological[33] and catalytic applications for instance but lead to numerous complications in matter of fabrication.

The possibility to fabricate clusters that have a narrow size distribution, with well-defined boundaries and not aggregated with the neighbour ones, strongly depend on the fabrication technique

Some approaches to ensure a production of particle with a narrow size selection is the chemical reduction of a metal salt and the growing of clusters produced in the gas phase and subsequently selecting them with specific mass selectors. However, in this latter case, it should be noted that the sharper the selection the lower will be the production rate.

A fundamental question that needs to be addressed when dealing with cluster-assembled systems is to what extent the properties of the isolated clusters are retained despite the cluster − cluster interaction.

In this regard, how closely particles are packed together is a key physical parameter to consider [34–36]. In fact, if the typical interparticle distance is large there will be few interactions between the nanoparticles, conversely the coupling will be stronger as this is reduced, and the material properties will change till the extreme scenario in which the particles are so densely packed that interactions become strong enough to make the material similar to bulk.

For instance, upon an increasing of the cluster packing density, a change in the optical and electrical properties of the system occurs: the sample can switch from being optically transparent and insulating to highly absorbent and conductive, with a resistance change up to several orders of magnitude.

In other words, the optical and electrical properties of a nanostructured material can be varied in a wide range of values by changing the interparticle distance. The possibility of creating materials whose macroscopic physical properties can be tuned by controlling the nanoscopic one, is probably the key driving force of cluster assemblies.

However, the direct control of the interparticle distance may not be easy; considering for instance a nanocomposite, this will be characterized by a distribution of distances, which can be calculated for low covered systems, after their fabrication by imaging it, but cannot be easily set before it.

For this reason, this parameter is mainly used in the theoretical models describing the sample properties for a low amount of deposited particles. For highly interacting systems, i.e. for large amount of particles, this distance-parameter is often replaced by the cluster concentration, which indicates the amount of particle per area or volume composing the system. Clearly, the cluster concentration and interparticle distances are correlated: for high cluster concentration the distances decrease.

This means that the cluster concentration can be estimated in real time during the sample fabrication by controlling the amount of particles. Moreover, some systems allow for tuning the interparticle distances even after fabrication. This is possible for instance if particles are incorporated in a soft matrix (rubber for example): in this case, it is possible to act on the interparticle distances by a mechanical deformation, causing in turn a reorganization of the clusters embedded.

1.3 Polymer nanocomposites

Composite materials are heterogenous materials consisting of two or more phases having different physical properties. These materials benefit from the combination of favorable matrix and filler properties which once integrated provide a material with properties which are better than the one of each of the components.

Polymers as matrices are particularly attractive because they are versatile, generally low-cost and can be easily processed into many shapes, including thin films.[37,38]

In figure 1.3 we show some examples of polymer often used as matrix for composite materials. In frame a, we can see a thermo-responsive polymer reversibly changing its shape (from open to close) upon a variation of the temperature. An origami made with paper is shown in frame b. A polymer often used to make nanocomposites is elastomeric rubber (frame c). Its popularity comes from the possibility to reversibly elongate it up to a certain percentage conserving its volume, and once the strain is removed the elastomer comes back in its original configuration. Hydrogel spheres are shown in box d; their peculiarity is the ease they have in adsorbing liquids such as water, and remarkably changing their volume as consequence. Finally, in frame e we see the Bakelite polymer, the first synthetic plastic, widely used since the 50's for many domestic electrical devices.

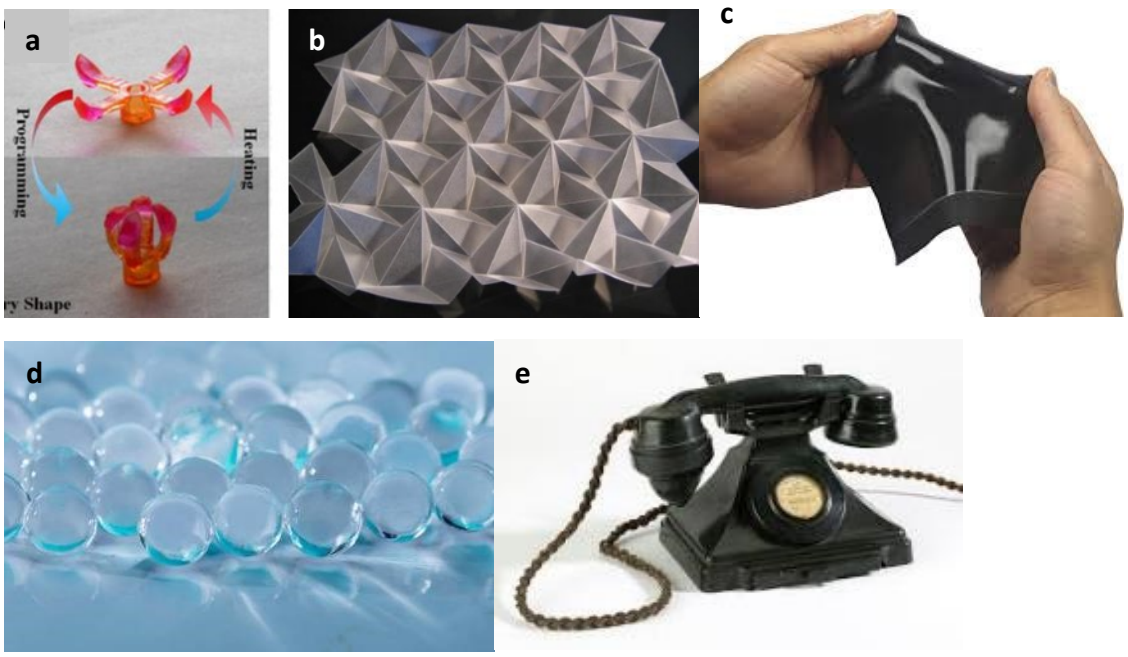

Figure 1.3: Examples of a wide variety of polymer-based objects. (a) thermo-responsive polymer, (b) paper origami, (c) stretched elastomeric rubber, (d) hydrogel spheres, (e) Bakelite: the first synthetic plastic.

The structural properties of these polymers are interesting; however, their functional properties principally consist in being electrically insulating and optically transparent if no additives are used. The idea of including a filler to synergistically integrate new exciting functional properties to the structural ones is the rational of making polymer composite materials.

Among many possibilities, nanosized fillers are particularly appealing: by including them in a polymer matrix one obtains what is known as a polymer nanocomposite (PN).[10,39]

By examining the literature concerning the polymer nanocomposites, one finds two well-studied systems: metal − polymer nanocomposites (MPNs) and carbon− polymer nanocomposites (CPNs).[40] The former filler consists in metal nanoparticles, the advantage of using them is the possibility to reflect their exciting properties at the macroscopic scale of a mechanically deformable sample. Metal nanoparticles can be fabricated with a large variety of shapes and sizes; this in turn reflects in having a high tunability of the MPN properties[41].

The main drawback consists in their high cost and high interaction; this implies that it is necessary to address specific fabrication techniques which guarantee a precise control on the filler organisation in the polymer in order to produce MPNs in a cost-efficient way.

On the contrary, carbon nanofiller is significantly cheaper, it can be fabricated with many shapes and structures as well: carbon-black or carbon nanotubes, fibres for instance. The rational for making carbon-polymer nanocomposites essentially consists in reaching the highest conductance for the lowest amount of particles embedded[40]. These systems are generally not particularly requiring in terms of distribution of the filler in the matrix, and to fabricate them it is often sufficient to mix together the filler and polymer matrix and then let the mixture polymerize.

This approach leads to the formation of an **isotropic PN**: the filler is distributed isotropically within the whole volume of matrix, as schematized in figure 1.4. This result is very successful when the filler of choice has a high aspect ratio (such as for carbon structures) because it optimizes the physical contacts between the filler increasing the whole conductance.

However, this method is not often used to produce MPNs because to fully exploit the optical properties of metal nanoparticles a high control on the particle shape and size is needed. This technique offers a poor control on the reorganization of the particles once they are incorporated in the matrix leading to the formation of aggregates. Moreover, in view of fabricating a nanocomposite with a high conductance, a large amount of nanoparticles needs to be used, as these are spread in the whole sample volume and their isotropic shape is not in favour of maximising the number of contacts as for the carbon-based nanocomposites.

For these reasons, other approaches are generally used to fabricate metal − polymer nanocomposites. These may consist for instance in the chemical reduction of metal salt directly in the polymer, the co-sputtering of the metal and polymer phases, the production of nanoparticles in the gas phase and subsequent implantation in the polymer substrate.

These techniques guarantee a high control on the particle properties. They can lead to the formation of PNs which are not necessarily isotropic. For instance, it can be also assembled (figure 1.4 ii) and/or interfacial (figure 1.4 iii).

In **assembled PN**, the filler is organized into clusters or regions of anisotropic density within the polymer matrix. The directed assembly or self-assembly of particles is typically desired for the formation of nanojunctions, where strong interaction with the electrical field is present.

Interfacial PN involve nanoparticles that straddle a metal−dielectric or dielectric−dielectric interface. These composites are often two-dimensional (2D) and engineered for integration within planar device architectures. These are particularly interesting for their plasmonic properties as it possesses optical or electronic properties that are distinct both from bulk materials and assembled PN.

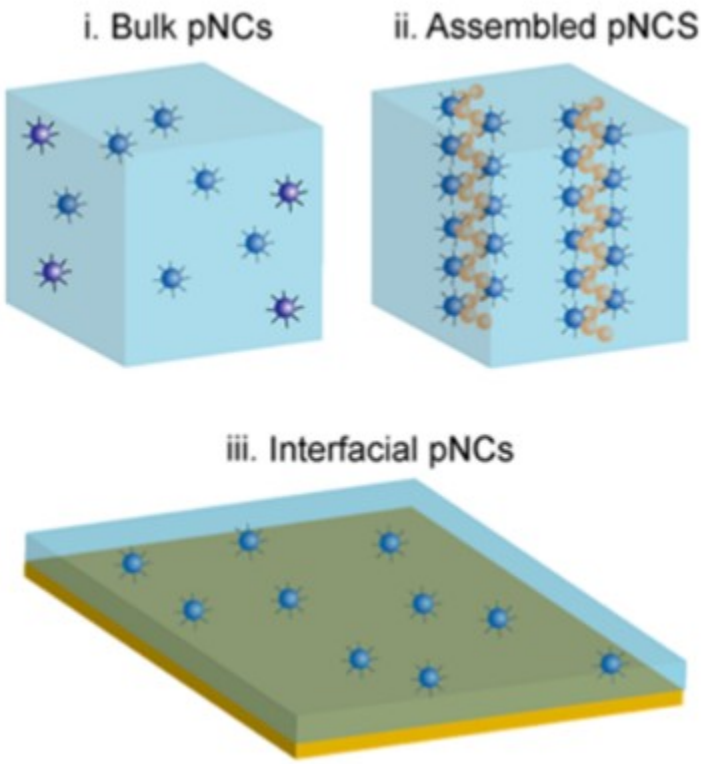

Figure 1.4: Possible structural architectures for polymer nanocomposites. Isotropic or bulk architecture (i); assembled (ii) and interfacial (iii). From reference [42]

1.4 Metal – polymer nanocomposites

The systems studied in this thesis are metal- polymer nanocomposites. MPNs have been the object of several studies and used for many applications. This is mainly due to their interesting functional properties[43] which include electric conductivity ranging from single-electron hopping and tunnelling to percolation,[2] particle surface plasmon resonances giving rise to characteristic optical features[44] explored in the new field of plasmonics, magnetic properties governed by ferromagnetic single domain behavior or superparamagnetism, granular giant magnetoresistance, and enhancement of catalytic activity owing to the large effective surface area of the nanoparticles and the marked contribution of the surface energy to the chemical potential.

These properties can also be found in cluster-assembled films (CAF) but become extremely interesting if thought in combination with the structural properties of a polymer. This because, as mentioned, such properties strongly depend on the interparticle distances. As for the thin films, these can be set during the sample fabrication by varying the filler concentration: by increasing the amount of clusters embedded, it is possible to continuously vary the optical and electrical properties of the MPN from the one of pure polymers, to those of the filler. Interestingly, in MPNs the distances are not fixed at the sample fabrication, but can be modulated afterwards acting with an external stimulus (such as a mechanical deformation) able to make the filler reorganize into the matrix

Clearly, this becomes even more appealing if the reorganization can be done reversibly, in a controlled and reproduceable way. Polymer nanocomposites which fit these requirements are generally called **responsive PN** and are subject of increasing interest because of the possibility of

controlling their physical properties after fabrication, acting with a macroscopic stimulus on the sample.

There are many possible stimuli which can induce a filler reorganization. It can be electrical or simply a mechanical deformation. Responsive PNs can be bent or stretched, for instance. This latter in turn can be done uniaxially, biaxially or radially as it will be shown more in detail in chapter. All these deformations, force the nanoparticles to rearrange into the matrix, thus changing their interparticle distances and therefore, the nanocomposite physical properties.

The possibility to tune the physical properties of MPN after their fabrication, according to the specific situation where the system is employed made MPNs appealing for a wide range of applications: from the realization of strain sensors with an electrical response to the strain applied [45] to plasmonic devices with a response which depends on the degree of bending response [46] (figure 1.5a). Recently, stretchable MPNs were also used to create multiplexed metasurface holograms wherein the hologram switches from one image to another with increasing strain. This was achieved by depositing a pattern of Au nanorods into a stretchable elastomer film that yielded more than one hologram at different image planes. By optimizing the nanorod pattern, the authors were able to achieve up to three holograms appearing at the same image plane at three different values of strain.

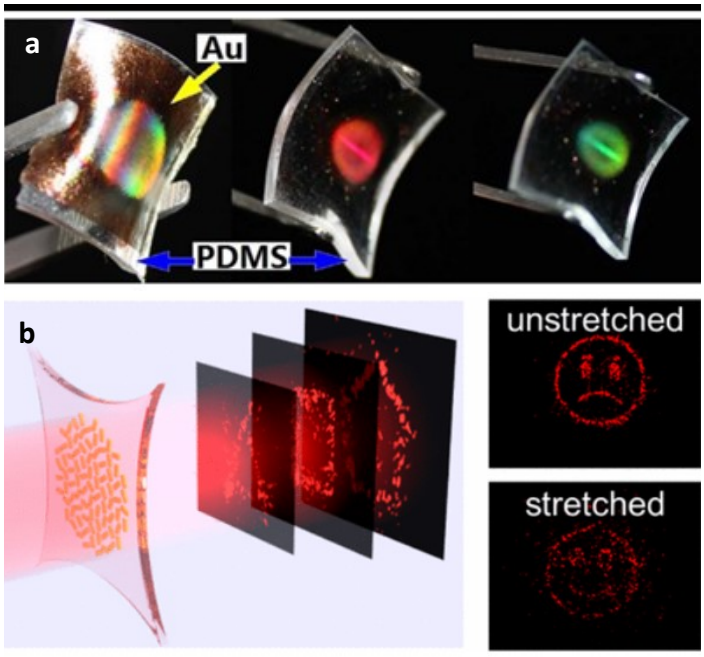

Figure 1.5 (a) Effect of a mechanical bending on the plasmonic resonance of a gold-PDMS nanocomposite [45] (b) hologram switches with strain in metal polymer nanocomposites [47]

1.5 Metal- polymer nanocomposite for adaptive optical elements

Adaptive optics[48] is a technology based on optical systems that can dynamically change their shape to compensate for aberrations or tune their optical properties whenever necessary, mimicking the human eye[49]. Strong interest is focused on fabrication of optical elements such as lenses[50], gratings[51], mirrors[52], able to change their geometrical shapes thus improving the image quality in applications for which structural rigidity represents a limitation rather than an advantage. These include in vivo medical imaging, microscopy and spectroscopy[50], optical telecommunications[52].

Adaptive elements might be electrostatically actuated or piezoelectric-driven, tunable gratings, and they have been proposed for replacing rigid optical elements such as glass or metal gratings and mirrors. However, they are to date complex and expensive, which is limiting the spread of such adaptive optics solutions.

Since the 70s Whitesides proposed elastomeric substrates as a simple and low-cost alternative for the fabrication of optical elements that can be easily stretched and deformed. Transparent stretchable optical components made of silicone have been used for the fabrication of lenses, light valves [53], transmission diffraction gratings and wave-front engineering devices[54]. While such devices are operating in transmission mode, much effort has been focused in the realisation of reflective adaptive optical elements as well.

Covering an elastomeric substrate with a reflecting metal film leads to some intrinsic complications. For example, metallization of elastomeric substrates by thin-film coating techniques such as thermal evaporation or electrodeposition results in a poorly adherent reflecting layer which easily undergoes cracking and delamination. Besides, even in static conditions the mismatch between the metal and the supporting elastomer mechanical properties causes the formation of buckling instabilities and wrinkles on the surface.

The stretchable reflective diffraction grating has emerged as a powerful adaptive optical element. The use of tunable gratings based on stretchable reflective substrates could revolutionize the design of optical spectrometers or hyperspectral cameras, and significantly widen their field of applications.

Commonly, high-resolution curved diffraction gratings are fabricated with different methods such as ruling engines: this is a slow and delicate process requiring a careful control on the mechanics of the engine and on external vibrations. This process being technically demanding, most of the gratings adopted in instrumental applications are more affordable replicas of a ruled master grating. Alternative fabrication methods are based on the interference fringe field in a photoresist to create a holographic grating or subtractive technologies such as electron beam lithography, ion beam etching, and laser ablation. Such methods require complex hardware and are very effective, although expensive.

In this respect, the use of metal–polymer nanocomposites has been demonstrated to be a successful strategy, as the direct incorporation of metal clusters as reflecting elements in the stretchable matrix solves the problem of the mismatching between the elastic properties of the two phases.

1.6 Thesis overview

The goal of this work was to study the optical and electrical properties of systems assembled by clusters: MPNs and cluster assembled thin films (CAF).

Regarding the MPN, the interest was to create optical devices which could be controlled and tuned with mechanical deformation. To do it, it was necessary to first understand how mechanical deformation (in particular uniaxial stretching), affects the plasmonic response and the electrical resistance of Au-PDMS systems.

The reflectance properties of MPNs was also studied to develop reflective and bendable diffracting gratings which could be adapted to concave surfaces in order to add focusing power to the diffracting one.

A further study on MPNs and CAF, was focused on understanding the interplay between their structural and functional properties. To this goal, the evolution of the electrical resistance was studied during the growing of the nanostructured materials on different substrates. Then, the electrical properties of the systems in response to a voltage applied were explored, to find if peculiar phenomena such as resistance switching, could occur.

Recipes to fabricate robust and reproducible devices which exhibit resistance switching were developed, both for cluster-assembled thin films and MPNs; in this latter case the possibility of controlling the switching activity with mechanical bending was studied as well.

This thesis is organized as follows:

Chapter 2: here I discuss the structural and functional properties of metal – polymer nanocomposites. In particular:

- I discuss how the properties of the filler (its concentration, size and shape distribution, its organization in the polymer) and the matrix ones, influences the structural properties of the nanocomposite.
- I show how a MPN can be mechanically deformed and how this affect the overall organisation of the filler embedded in the matrix.

Then we move to the functional properties of MPN, focusing on the electrical and optical ones.

- The fundamental results of the main theoretical models (Mie's and Maxwell-Garnett's theory for the optical properties, the percolation theory for the electrical ones) are reported;
- I discuss how these functional properties depend on the structural ones.

The fundamental point of the chapter is to show that the optical and electrical properties depend on the interparticle distance between the clusters embedded in the matrix, and that these distances can be controlled acting on the nanocomposite with a mechanical deformation.

Chapter 3: in this chapter I report the common approaches to fabricate MPN and the working principle of the technique used to fabricate the MPN and cluster-assembled films.

Chapter 4: in this section I describe how the samples fabricated were characterized.

Chapter 5:in the first part of this section I report the results regarding the optical and electrical properties of the Au-PDMS nanocomposites. In the second one an introduction of the resistance switching phenomena is provided and the results obtained on cluster-assembled films are shown.

In summary, the results discussed are the following:

- The evolution of the optical and electrical properties of the metal-polymer nanocomposites are shown: a redshift up to 300 nm occur in response to the stretching applied; this is accompanied by an increase of the resistance. Finite different time domain simulations are used to understand the physical origin of the observations and to elaborate a model.

- The focusing power of elastomeric reflecting gratings, bent to adhere to a concave ellipsoidal surface is shown as well. In particular, we demonstrate the possibility of reconstructing a punctual light source and a slit one with a spatial resolution of about 70 um and a spatial one of about 2 nm, without the use of any further optical element.

- The resistive switching activity of cluster-assembled films is studied on system made depositing gold clusters on diverse hard substrates such as glass, plexiglass and silicon. Under the bias of voltage sweeps, peculiar resistance switching occurred. These results motivated us to the transposition of the study of the same concept on a soft substrate (cellulose paper).

- The switching activity of gold/paper nanocomposite was confirmed and the possibility to exploit the flexibility of the substrate to control resistance switching up to four orders of magnitude was demonstrated.

Chapter 6: the conclusions and perspectives of this work are reported here.

2 Metal polymer nanocomposites properties

The high versatility of MPN can be considered the origin of their success. These materials have **functional properties** which cover different fields, from optics, to the magnetic, electric and catalytic one. The preparation of a sample with specific physical properties requires a specific design of the nanocomposite which allows to best fit the desired applications. In other words, the structural properties of the nanocomposite need to be carefully designed to match the functional properties needed.

The main **structural properties** of a polymer nanocomposite are schematized in figure 2.1. These regard the properties of the filler (such as its chemistry, shape and size) and the one of the matrix, which can be transparent or opaque, stretchable or flexible. Different degrees of elasticity determine different possibilities of mechanical deformation.

The nano & microstructure of the nanocomposite is a further parameter to control: how close the particles are packed together, their concentration and arrangement into the matrix. Finally, at the macroscopic scale of the sample, the nanocomposites can have different architectures: bulk, assembled or interfacial for instance.

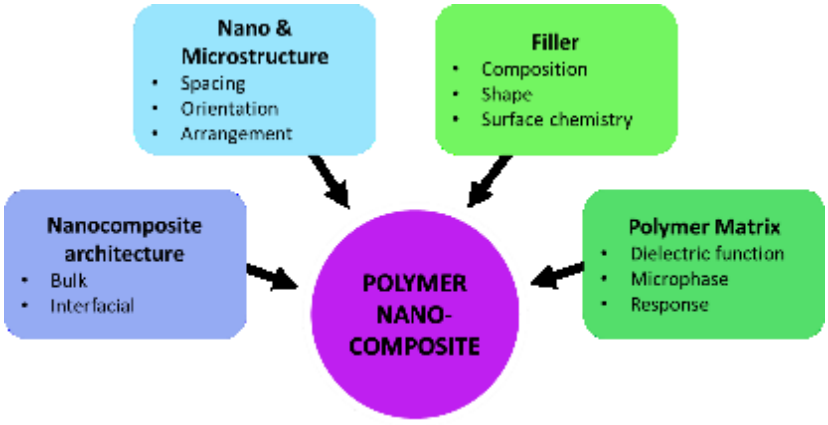

Figure 2.1: Principal factors which influence the structural and functional properties of a polymer nanocomposite and a metal–polymer nanocomposite: the nanocomposite architecture, its

nano- and microstructure, the chemical and physical properties of the filler, and the ones of the polymer matrix. Adapted from reference [42].

2.1 Structural properties

Examples of nanocomposites with different structural properties are shown in Figure 2.2. In the top figures we see silver nanoparticles embedded in a Bakelite matrix. The main difference between the two pictures is clearly the **filler concentration**. In figure 2.2a few particles are embedded: the nanocomposite here consists mainly in a polymer matrix with some metal inclusions. On the contrary, in figure 2.2b the particles are densely packed, the gaps are significantly smaller since the filler concentration is higher.

In both cases the nanoparticles are almost spherical and with a wide **size distribution**. A much narrower one is shown in figure 2.2c where spherical particles are homogenously dispersed in the whole volume of the polymer.

Finally, the system considered in figure 2.2d has a different **filler shape**, no more spherical but nanotubes. These fill the matrix homogeneously at the frame scale. The nanotubes have various **orientations** but tend to assume the same one in the regions where they touch each other. Moreover, some tiny pieces of nanotubes are present in the matrix indicating there is not a homogeneity in the length of the tubes.

Below we describe more in detail how these structural properties can be quantified.

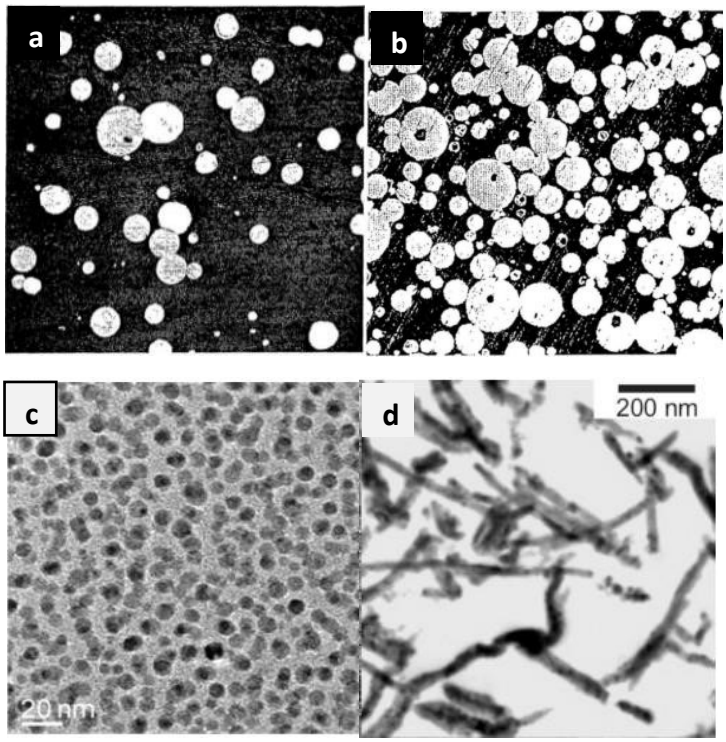

Figure 2.2 Four examples of polymer nanocomposites with different structures. The top cases (a) and (b) consist in silver nanoparticles embedded in a Bakelite matrix. A lower amount of particles

is embedded in (a). Regarding the scale, the real length of the micrograph side is ~ 1.45 mm; from reference [55]*. (c) TEM micrograph of Nylon/Ag nanocomposites; from reference* [43] *(d) carbon nanotubes embedded in a polymer matrix; from reference* [56]

2.1.1 Filler concentration or filling fraction

How close the particles are packed together is one of the most relevant parameters upon which the physical properties of a MPN depends on. To quantitatively refer to it, the concept of **filler volume concentration** or **filling factor** is commonly used. This is defined as the ratio between the total volume of the filler and the volume of the nanocomposite

$$f = V_f / V_{nc}$$

Ideally it ranges from 0 (pristine polymer) to ~1 when the polymer is saturated with nanoparticles.

This parameter is important since it provides an indication of the interparticle distances. Comparing for instance figure 2.2a and 2.2b, particles are more closely packed in the second case where they are closer to each other, which gives a higher filling factor.

The advantage of having a quantity closely related to the distribution of interparticle distances is twofold. On one hand, as we will see in sections 2.1 and 2.2, the interparticle distances control the optical and electrical properties, hence many applications require a good control them. On the other hand, despite its importance it is very challenging to determine the interparticle distances and to control it in real time during the sample fabrication. A parameter which provides an indirect estimation of the gaps therefore gives the possibility to control not only the structural but also the functional properties of the nanocomposite.

According to the fabrication technique, there can be different possibilities of controlling and vary the filling factor. Controlling it in its whole range of values and in real time, is a big advantage as it gives access to a wider range of functional properties which can be tuned during the sample fabrication. This guarantees a high reproducibility and reliability of the approach.

Another point to consider is that not all the fabrication techniques can guarantee a disentanglement of the filling factor from the other structural properties of the composite. It can indeed happen that varying the filling factor affects particle dimension or shape, due to aggregation or coalescence phenomena. However, as the functional properties of a composite depend on the cluster dimension as well, their control become particularly critical.

2.1.2 Filler shape & size distribution

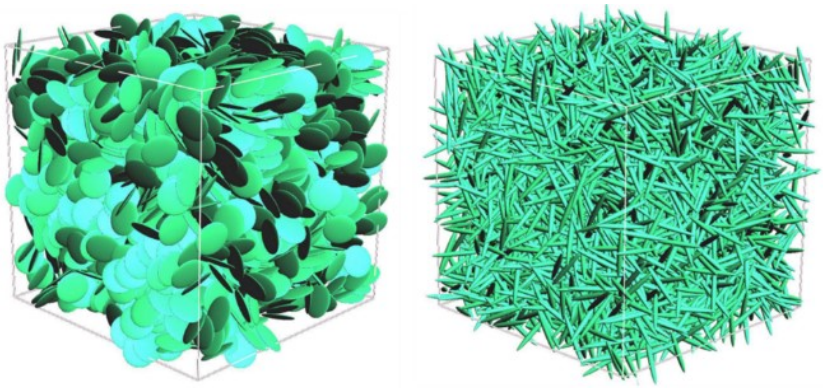

Figure 2.3: (left) A cubic portion of a material filled with a distribution of hard core non-intersecting nanoflakes. (right) A similar distribution of hard core non-intersecting nanorods. From reference [40]

Besides the filler concentration, another parameter which significantly influences the properties of a composite is the particle shape.

The filler embedded in the polymer can be spherical, like the one shown in figure 2.2a-conductance for example. This is obviously the most symmetric and isotropic filler which can be chosen. However, one can also choose an anisotropic filler, like the nanotubes shown in figure 2.2d, or other geometries, such as flakes, ellipsoids and nanowires as in figure 2.3.

To quantify the deviation of the particle shape from that of a sphere, the concept of **shape-anisotropy** is generally used. This is the ratio between the major particle dimension to its minor dimension. The more the particles deviate from the spherical shape, the larger will be its shape-anisotropy value.

Studying the effect of shape-anisotropy on the functional properties of nanocomposites, it was soon realized this parameter had significant consequences. As another example, incorporating carbon black in a polymer matrix, it was observed that the more complex was the particles structure, the higher was the composite conductivities at a given volume fraction. This is not surprising if we consider that more structured fillers have larger geometrically connected networks and, therefore, will more easily originate better connected networks.[57]

Composite materials with shape-anisotropy fillers are interesting for a wide range of applications. One of the most important advantage they offer is their high surface-area-to-footprint ratio, which made nanotubes widely used in diverse technological fields as they effectively increase the available sensing area[58] for instance. Another reason which made these elements popular is economical[40] as due to their high connectivity: the higher is the filler shape-anisotropy, the lower is the amount of material necessary to reach a certain conductance.

The main criticality of composite with shape-anisotropic filler is the fabrication. This is often done by mixing together pre-formed particles and the polymer matrix when this is still in a liquid phase, and then let the mixture polymerize. This strategy is conceptually very simple but has some limitations in the control of the distribution of the particle in the composite volume, its aggregation and mutual orientation, which in turn influences the functional properties of the sample. For more details about this point references [40,59,60] can be addressed.

Fixing now the particle shape, a further parameter to consider is its size. In figure 2.2b and 2.2c, we compared two MPNs with spherical filler but different size distributions. The fabrication technique determines how narrow the distribution is. As it will be discussed more in detail in Chapter 3, there are three main approaches to fabricate nanocomposites:

i. Inorganic particles can be synthetized in situ, for instance in solution, where the solvent can also be a monomer and the nanocomposites are then formed by in situ polymerization[10];

ii. filler and polymer can be co-sputtered or co-evaporated on a substrate;

iii. nanoparticles can be produced in the gas phase and then incorporated in the matrix (this is the approach followed in this work).

The obvious question which rises is the following: to what extent it is necessary to have a narrow distribution of nanoparticles size. It is also worth to understand how the size distribution affects the functional properties of a nanocomposite, which applications require to have monodispersed filler, and which do not need such a constraint.

These questions will be addressed in section 2.2 when the functional properties of nanocomposite are described.

2.1.3 Nanocomposite architecture

The "nanocomposite architecture" indicates the overall organization of the filler in the matrix at the macroscopic scale of the sample.

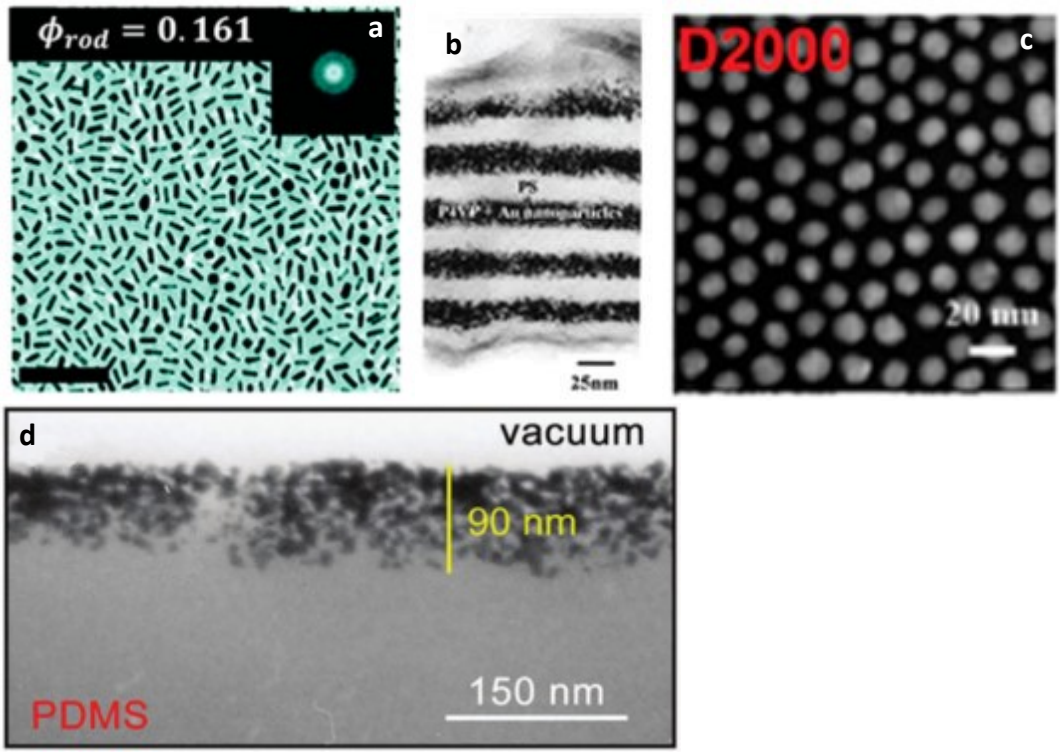

Figure 2.4: (a) bulk/isotropic PN: the filler is homogeneously dispersed in the polymer matrix, (b) assembled PN consisting in a multilayer structure, (c) assembled PN consisting in an almost regular array of nanoparticles, (d) assembled and interfacial PN: the particles are embedded at the surface of the polymer matrix. From references [42,61]

The examples discussed so far, from an architectural point of view, are all **isotropic / bulk nanocomposite**: the filler is isotropically distributed in the whole polymer matrix (see figure. 2.11a for a further example). However, this is not the only possible architecture which can be realized. As shown in figure 2.4, particles can also be organized into cluster or regions of anisotropic density within the dielectric matrix. These are generally called **assembled nanocomposites**; some examples are shown in frame b and c. A further category is the one of the **interfacial nanocomposites.** Nanoparticles straddle a metal – dielectric or dielectric-dielectric interface. An example is the 2D nanocomposites, which consists in a thin layer of nanocomposite at the surface of the polymer one, as shown in frame d.

A further category is often introduced to indicate how the nanocomposite reacts to an external stimulus such as for instance a mechanical deformation. If the nanocomposite reorganizes in a reversible way, it can be labelled as a **responsive nanocomposite**. These systems are extremely appealing as they are capable of modulating their properties upon being triggered by an external stimulus.

In recent years, intense focus has been directed towards assembled and responsive nanocomposites[42]. These materials exhibit advanced functions by rationally engineering how nanostructures self-assemble and perform within complex nanocomposite materials.

2.1.4 Nanocomposite evolution

The fundamental interest in the investigation of diffusion and interface formation at metal-polymer interfaces lies in the combination of so extremely dissimilar materials as metals and polymers. While metals are densely packed crystalline materials with a high cohesive energy, polymers are made up of large macromolecules of some 10^2 to some 10^5 covalently bonded monomeric units that are held together by very weak van der Waals interactions in an open structure[62].

This is the origin of interesting phenomena which regard the diffusion of particles into a polymer matrix and the evolution of the particle nanostructure once they are embedded in it.

Spreading inorganic nanoparticles (such as metal clusters) on a polymer surface and heating the system, the particles will be entirely buried under the polymer surface. This means that there is a driving force embedding metal clusters in the polymer and that the Gibbs free energy of a metal particle inside the polymer is lower than that of the particle at the surface. In other words, the surface tension of the metal particles exceeds the sum of the interfacial tension and the polymer surface tension[62].

In the systems considered in this thesis, the particles are implanted in the polymer rather than let spontaneously penetrate it. The mechanism which describes how this happens is simulated in reference [63].

Cardia and co-workers simulated the penetration mechanism of gold clusters with a size distribution which ranges from 3 nm to 10 nm and an implantation kinetic energy in the range 0.5 - 2 eV/atom. The simulation demonstrated that even if the kinetic energy is comparatively lower than the one implied in the ion implantation technique (which is keV/ion), the neutral clusters are able to penetrate up to tens of nm into the polymeric target forming a buried conducting layer and avoiding charging and carbonization [63].

The mechanism driving the supersonic cluster beam implantation is the so-called “clearing-the-way” effect, namely the front atoms in the cluster collide with target atoms conveying them sufficient

momentum to clear the way for the following cluster atoms. As a consequence, the low-energy cluster penetration depth is increased with respect to the high-energy single ion penetration.

More specifically, it was found that the penetration depth linearly depends on the cluster energy and on the microstructure of the polymer: a penetration depth of 7 nm/eV and of 6 nm/eV is found in melt and cross-linked PDMS respectively[63].

Once the particles are embedded in the polymer, regardless the technique used to make it happen, they generally undergo structural changes which regards both the size and shape distribution.[64] The possibility of nanostructural changes is mainly determined by the degree of crystallinity of the polymer as this strongly influences the way in which particles are organized in the matrix. For instance, amorphous polymers have an extremely large free volume, which typically exceeds ten percent[62]. This volume generally plays a very important role, helping the diffusion of particles in amorphous polymers. Conversely, in a polymer crystal diffusion has been observed to be very small compared to its values in the amorphous phase, and the diffusivities of small penetrants in this kind of polymers is lower than in amorphous ones. An intermediate situation consists in the semicrystalline polymers. The crystallites are usually considered as impermeable islands embedded in a continuum of permeable amorphous substance[62].

Considering a closed system consisting of particles embedded in an amorphous polymer, where no material is being lost or supplied, various types of material transport can happen. These can be caused by atomic diffusion through the matrix (Ostwald ripening) atomic diffusion along the particle surface (recrystallization and coalescence) and particle migration[64].

The schematic in figure 2.5 shows the effect of these nanostructural changes.

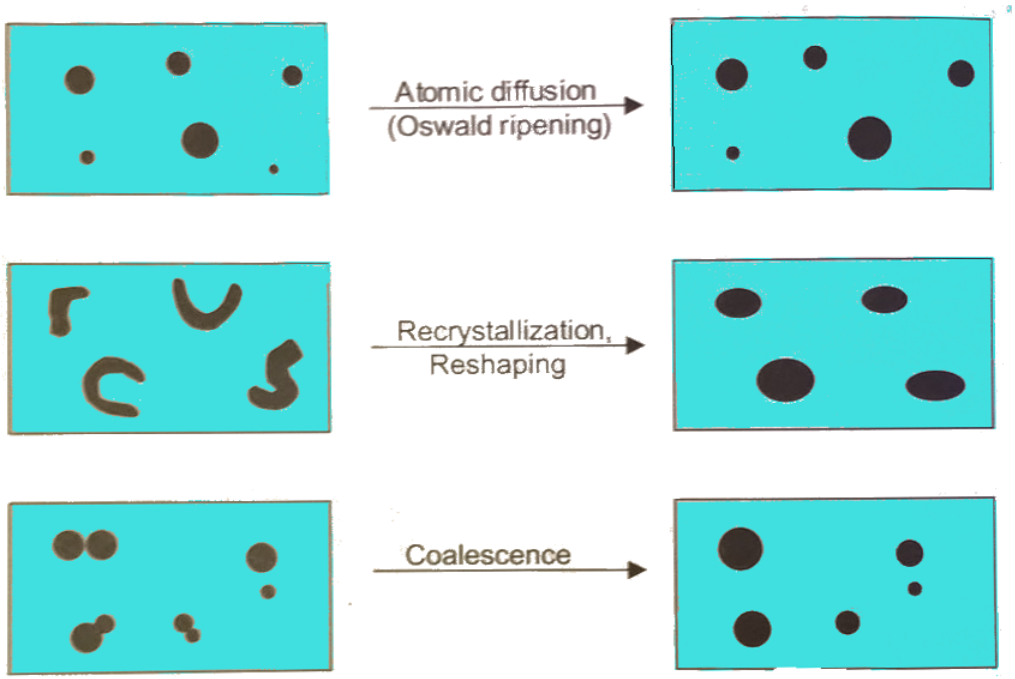

Figure 2.5: Schematic representation of possible nanostructural changes a nanocomposite can undergo. (a) atomic diffusion or Ostwald ripening, (b) Recrystallization and reshaping, (c) coalescence. Adapted from reference [64].

The driving force of these nanostructural changes is the fact that the proportion of surface energy is much higher in small particles compared to the total binging energy, due to the high proportion of surface atoms. For this reason, in response to a thermal activation or simply because of aging of the sample, the nanostructures tend to reorganize in the polymer in order to reduce the number of surface atoms: atomic diffusion from smaller to larger particles occurs through the matrix. This process for size and shape changes in embedded particles is called Ostwald ripening or atomic diffusion (see frame a).

Recrystallization and coalescence also are processes based on the minimization of the surface energy. The former regards non-spherical particles (see frame b), whereas the latter regards pairs of contacting particles (see frame c). Both lead to the formation of more spherical particles by diffusion of metal atoms along grain boundaries and along the particle surface.

More specifically, in metal-polymer nanocomposites obtained by implanting metal clusters in PDMS matrix by means of supersonic cluster beam implantation, the particles can undergo both atomic diffusion and coalescence once they are embedded into the polymer. These phenomena can happen spontaneously or catalysed by mechanical deformation as it will be discussed in the result section.

2.1.5 Nanocomposite elasticity and Young modulus

Before describing the mechanical properties of a metal-polymer nanocomposites, it is convenient to first briefly describe polymers.

The meaning of the parameters which quantitatively describe the mechanical properties of a material can be easily understood considering a stress-strain graph (also called tensile graph), like the one shown in figure 2.6. From this graph we can define:

The **Young's modulus (***E***)** as the slope of the curve representing stress σ vs. strain ϵ in the small strain regime ($\epsilon \rightarrow 0$).[65] In other words, E is the physical parameter that characterizes the reversible response of a material under small stress, the lower it is, the easiest the material can be deformed.

The **strength** is the force needed to break a sample (the height of the curve when the sample breaks), while the **toughness** measures the energy a sample can absorb before it breaks: graphically it is the area under the curve.

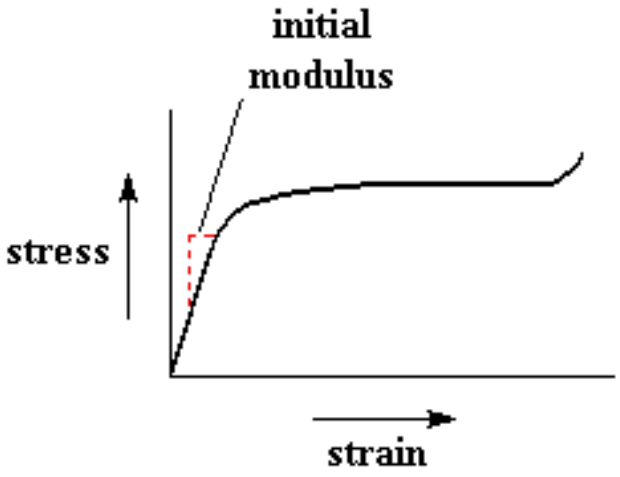

Figure 2.6: Stress -strain graph for a generic flexible plastic. From reference [66,67]

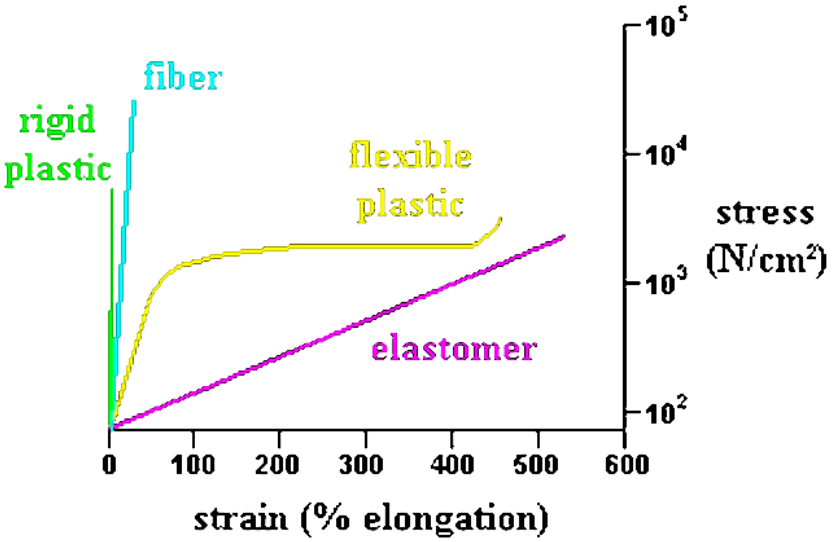

Figure 2.7: Stress -strain graph for a generic rigid plastic (green curve), fiber (blue curve), flexible plastic (yellow) elastomer (violet). From reference [66,67]

Polymer	E^* GPa	σ_b (s_y)† MPa	ε_b (e_y)‡ %
Cellulose acetate	2	30 (60)	30 (6)
Nylon-6	1.9	75 (50)	300 (30)
Nylon-6,6	2.0	80 (57)	200 (25)
Polycarbonate	2.5	60 (65)	125 (30)
Polyethylene (all grades)	0.2–1	10–30 (8–30)	600–800 (9–20)
Poly(ethylene terephthalate)	3.0	54	275 (6)
Poly(methyl methacrylate)	3.2	65	10
Polyoxymethylene	2.7	65	40
Polypropylene	1.4	33 (32)	400 (12)
Polysulfone	3.4	50	2.5
Polystyrene	2.5	65	75
Polytetrafluoroethylene	0.5	25 (13)	200 (63)
Poly(vinyl acetate)	0.6	29–49	10–20
Poly(vinyl chloride)	2.6	50 (48)	30 (3)
Silicone rubber	—	4.8–7.0	100–400

Table 1: Mechanical properties of different polymers. Polydimethylsiloxane belongs to the class of silicone rubber. From reference [68]

For sake of clarity, let us consider now the tensile graphs of some polymers (figure 2.7).

Rigid plastics such as polystyrene, polymethyl methacrylate or polycarbonate are strong but not tough. Compared to other polymers, considerable force is needed to break these materials, but not much energy is required. In other words, they cannot stretch very far before breaking: a material like this is called *brittle,* and its tensile curve resembles the green one in the graph above.

Fibers as nylon fiber tend to have stress-strain curves similar to the one represented in blue: like the rigid plastics, they are stronger than they are tough, and do not deform very much under tensile stress.

Flexible Plastics as polyethylene and polypropylene have a tensile curve like the yellow one. Their initial Young modulus is high, indicating how much stress they can withstand before deforming. These materials are both strong and tough. They can absorb more energy than the rigid plastics and fibres before breaking because they can dissipate it via deformation.

Elastomers like polydimethylsiloxane, polyisoprene, polybutadiene and polyisobutylene have completely different mechanical behavior from the other types of materials. Elastomers have very low Young moduli, which means they can be easily stretched without breaking. However, this is not of much use unless the material can bounce back to its original size and shape once the stress is released. *Reversible elongation* is exactly the feature which made elastomers very popular in applications.

In figure 2.8, we report the Young Moduli of some common polymers and materials. Elastomeric rubbers (such as the typical polydimethylsiloxane (PDMS)) have E ~ 1 MPa, which is lower than other rubbery materials which ranges from 10 to 100 MPa. Gels Young modulus are some orders of magnitude lower (~10 Pa). All these highly elastic materials are easily stretched by mechanical forces, while their volume stays constant.[69]

Let us consider some solids as well, to complete the spectrum of materials commonly used to make a composite. Usually, Young's modulus of a solid is high, hence it cannot be reversibly stretched by much before it undergoes deformation or damage. Some relevant examples include Gold (70 GPa), Silicon (150 GPa), diamond-like Carbon (DLC, 500 GPa), and graphene (1000 GPa along its plane), by far one of the strongest materials.

As we can see in graph in figure 2.8 top, which report the Young modulus of families of material and their density, the metals and polymer occupies two well distinct regions of the graph, indicating the high discrepancy in their elasticity. This implies that the combination of elastic substrates with metal filler sets up tremendous mechanical contrasts.[69] This is one of the key forces in making composites materials: engineering their mechanical properties by matching the best properties of two or more categories.

Finally, table 1 indicates for some commercial polymers their Young modulus, the tension at the breaking point and the elongation at the breaking point.

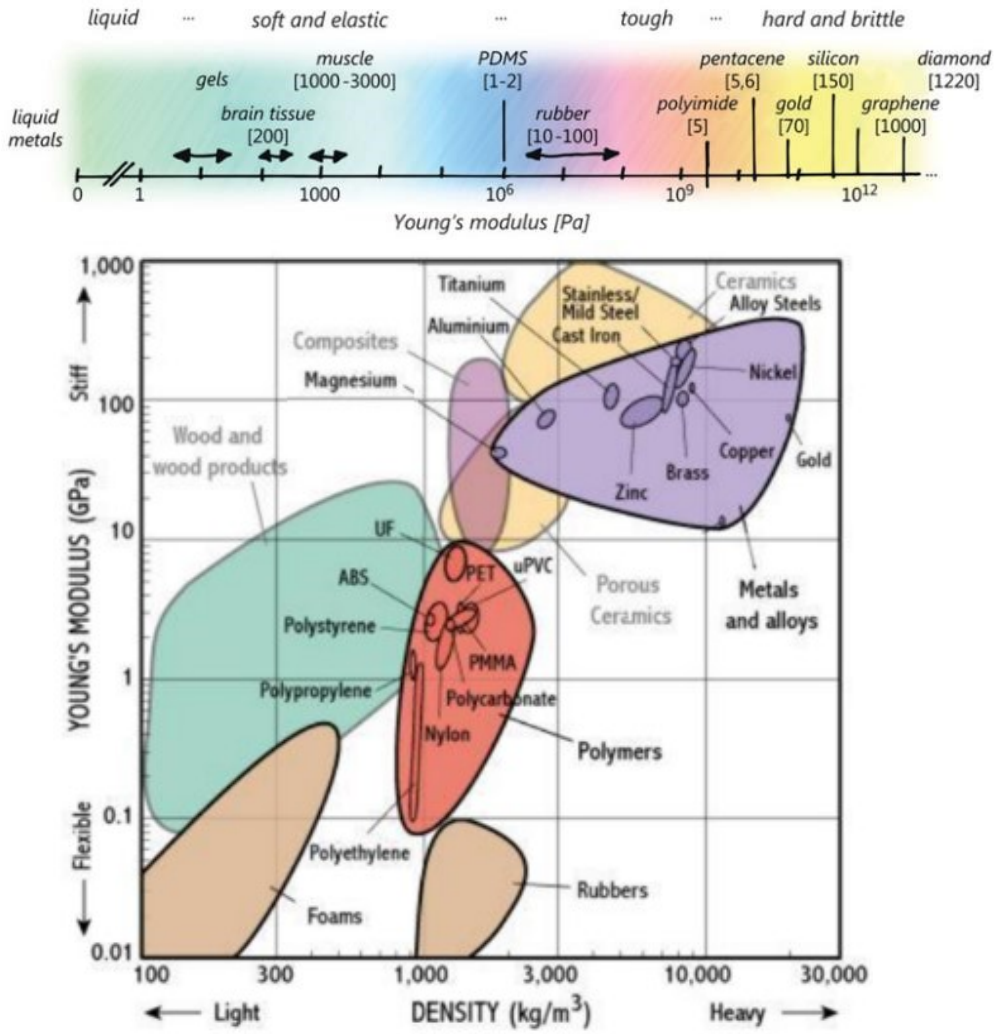

Figure 2.8: (Top) Log-Log chart of the Young modulus as a function of the density of several materials, including wood products, polymers, nanocomposites, metals and ceramics. Metals and polymers are highlighted in violet and red respectively. Labels indicate some specific substances by headless arrows. The polymer family is treated in detail in the lower graph (bottom): representation of the Young modulus of various polymers. The materials are divided in four main categories: liquids, soft and elastic, tough, hard/brittle materials. The numbers in brackets are in Pa for soft, MPa for tough, and GPa for hard materials, respectively. Polydimethylsiloxane (PDMS) falls at the centre of the scale. From reference [69,70]

Many studies were focused on understanding how the filler structural properties influences the elasticity of the composite material.

The dependence of the Young modulus on the filler amount has been widely characterized for many different combinations of filler and polymers. The Guth's law[71] is the main theoretical result: it predicts a quadratic dependence between the two quantities and follows the formula written below.

$$E = E_m[1 + 0.67\alpha\Phi + 14.1(\alpha\Phi)^2]$$

Where E is Young's modulus of filled elastomer, E_m is matrix Young's modulus and Φ is the filling factor while α is a shape factor (length/breadth) which takes into account the evolving structure

of the spherical filler when the filler concentration is higher than 10%. This has been confirmed by a number of experimental results; an example of how the filler shape influences the trend of the law is shown in figure 2.9.

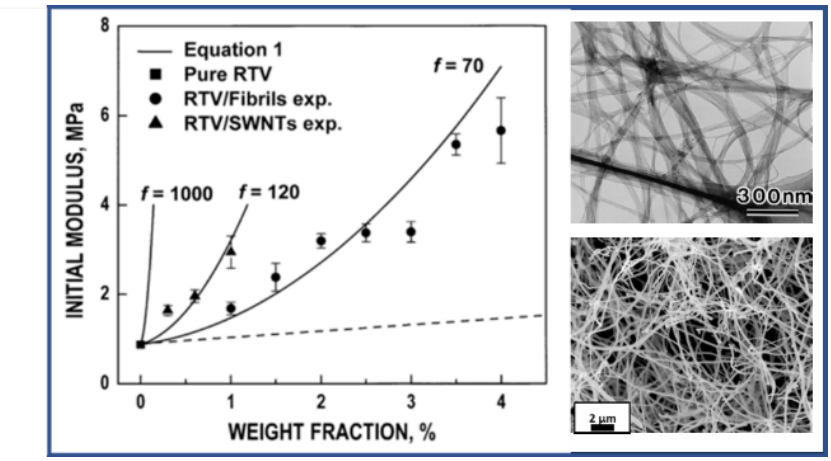

Figure 2.9: Young modulus dependence of a nanocomposite consisting in carbon fibrils (bottom inset) and carbon single wall nanotubes (top inset) embedded in an elastomeric matrix of RTV. Adapted from references [60,72,73]

Here isotropic nanocomposites are obtained embedding in an elastomer (RTV silicone rubber) two different fillers: either vapor-grown carbon nanofibrils or single-wall carbon nanotubes (SWNTs). The structure of these fillers is shown in figures 2.9b and 2.9c respectively. We can see in the graph that the Young modulus in the two cases follow a different trend, and that they both agree with what predicted by the Guth law. More importantly, this experiment confirms that the filler structure has relevant effects on the composite elasticity.

A further important parameter to consider is the composite architecture. Comparing for instance an assembled nanocomposite having an interfacial architecture like the one in 2.4d, with an isotropic one having the same thickness and filler properties; the Young moduli of the two systems will be different.

This because, this value is given by the sum of the contribution of each layer weighted by its thickness. Thus, if the composite is isotropic, its overall E will be higher than the interfacial one, where the presence of a thick layer of pristine polymer under the nanocomposite one, strongly increases the elasticity of the whole sample.

Other references can be addressed to understand the effect of the filler orientation, size and shape distribution [40,59,60,69,74,75]

2.1.6 Dynamic properties: effect of mechanical deformation on composite material.

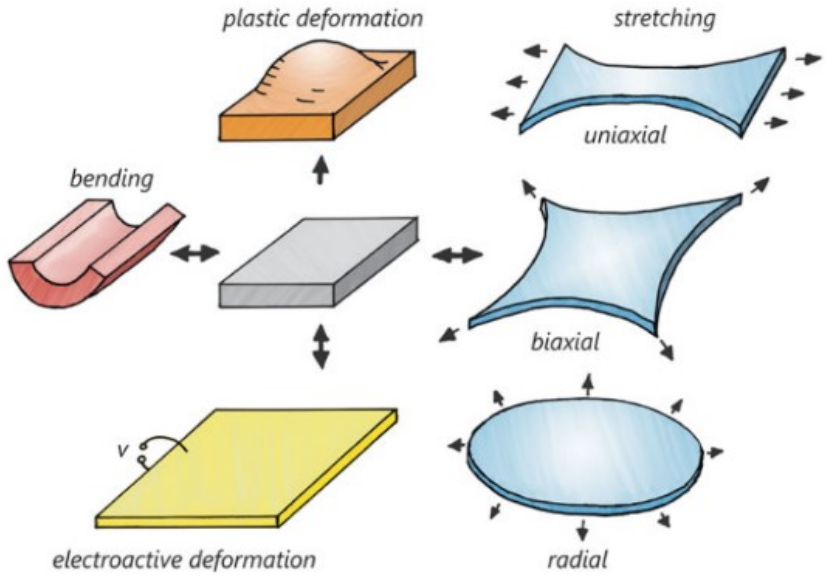

Figure 2.10: Main kinds of deformations a polymer, depicted in grey in the unperturbed configuration: bending (red), plastic deformation (orange), electroactive deformation via electrical stimuli (yellow), uniaxial, biaxial and radial stretching (light blue). From reference [69]

The possibility of changing the functional properties of a material in a controlled, reproducible and reversible way, acting with a simple mechanical deformation is probably the key driving force to develop metal – polymer nanocomposites.

There are many ways to deform a polymer and hence a polymer nanocomposite. The principal ones are sketched in figure *2.10*. Starting from a polymer in a relaxed configuration (the grey one in the center of the picture) one can bend it in a concave shape like the one drawn in red or, giving a convex shape. Otherwise one can plastically change its shape (orange) or act with an electrical stimulus to cause an "electroactive deformation" as in reference[76]. Finally, the polymer can also be stretched uniaxially, biaxially or radially.

If we move now to a composite material, we should also consider how the mechanical deformation affects the structural properties of the composite. We can indeed easily imagine that the filler will reorganize changing its mutual distances and reciprocal orientation (in case of a shape-anisotropic filler), in turn modifying its functional properties.

The literature regarding the evolution of structural and functional properties of a nanocomposite in response to a mechanical deformation is wide[42,46,77–79].

Carbon nanocomposites are probably the most studied system on this respect. This may be due to their ease of fabrication and the important applications which could be developed once the reorganization of the filler in response of a mechanical deformation would be fully understood. Few studies can be found also on systems consisting of a monolayer of metal particles, usually gold, embedded in an elastomeric matrix. In this case studies are generally focused on the optical properties of the system because of the unique plasmonic response of these clusters. Moreover, the use of an isotropic filler like gold nanoparticles would significantly increase the fabrication cost of a highly conductive system, compared to what would be obtained choosing a cheaper and intrinsically better-

connected filler like the carbon black for instance. For this reason, most of the studies which are focused on developing nanocomposites with high conductance and a low amount of filler deal with carbon-based nanocomposites; while studies which aim to optimize the optical response of the system generally use gold nanoparticle. These also have the advantage that can be processed in a controlled and reproduceable way in many different shape and sizes.

Finally, some studies regard how nanoparticles reorganize upon bending. This is extremely interesting as it allows flexible but not stretchable polymers to be used for fabrication of responsive nanocomposites as well.

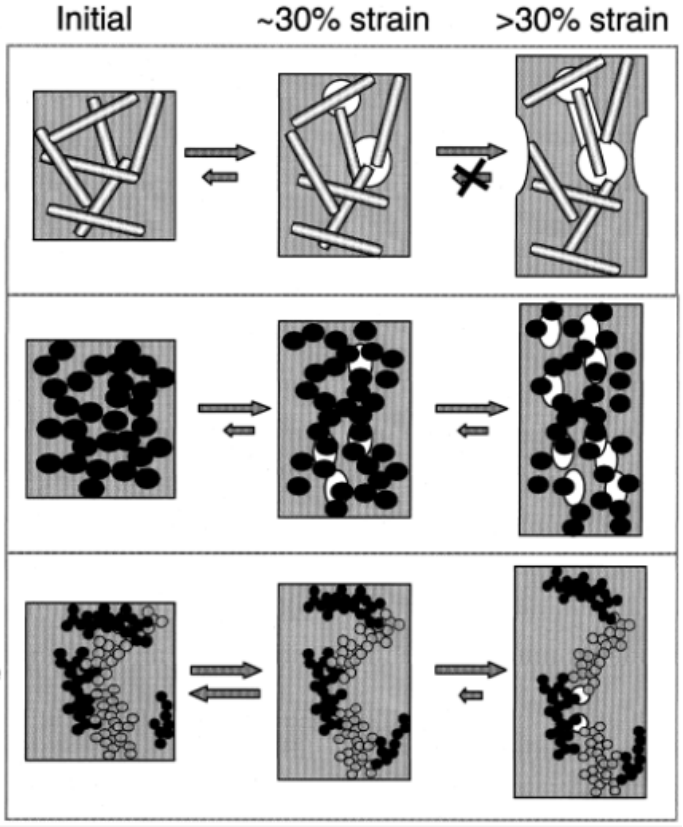

Figure 2.11: effect of uniaxial stretching on carbon-elastomer nanocomposites. Three nanocomposites are considered: elastomeric matrix where either carbon fibers (CF), low structure carbon black (LSCB) or high structured one (HSCB) are embedded. From reference [75]

The possibility of using a mechanical deformation to change the functional properties of a nanocomposite is extremely requiring as a deep understanding of how the filler reorganize upon the particular kind of deformation is necessary. Moreover, not all MPNs are suitable to undergo a mechanical deformation able to change the interparticle distance in a reversible and repetitive way.

This possibility depends on the structure of the nanocomposite, on its resilience to the deformation, on its elasticity, on the amount of filler embedded in, on its shape etc.

The work by Flandin et al. is particularly enlightening in this respect. In reference [75] they show the effect of uniaxial stretching on three kind of nanocomposites consisting in an elastomeric matrix where either carbon fibers (CF), low structure carbon black (LSCB) or high structured one (HSCB) are embedded.

The result obtained is schematized in figure 2.11. A 30% stretching causes mechanical failure both in CF and LSCB while this happened to HSCB in response to a stretching upper to the 30%, and it remains perfectly reversible if smaller deformations are applied.

Probably because of these issues, most of the research done to understand how uniaxial stretching and bending influenced the structural and functional properties of a MPN were performed on systems consisting in a spherical filler embedded in an elastomeric matrix, generally polydimethylsiloxane (PDMS).

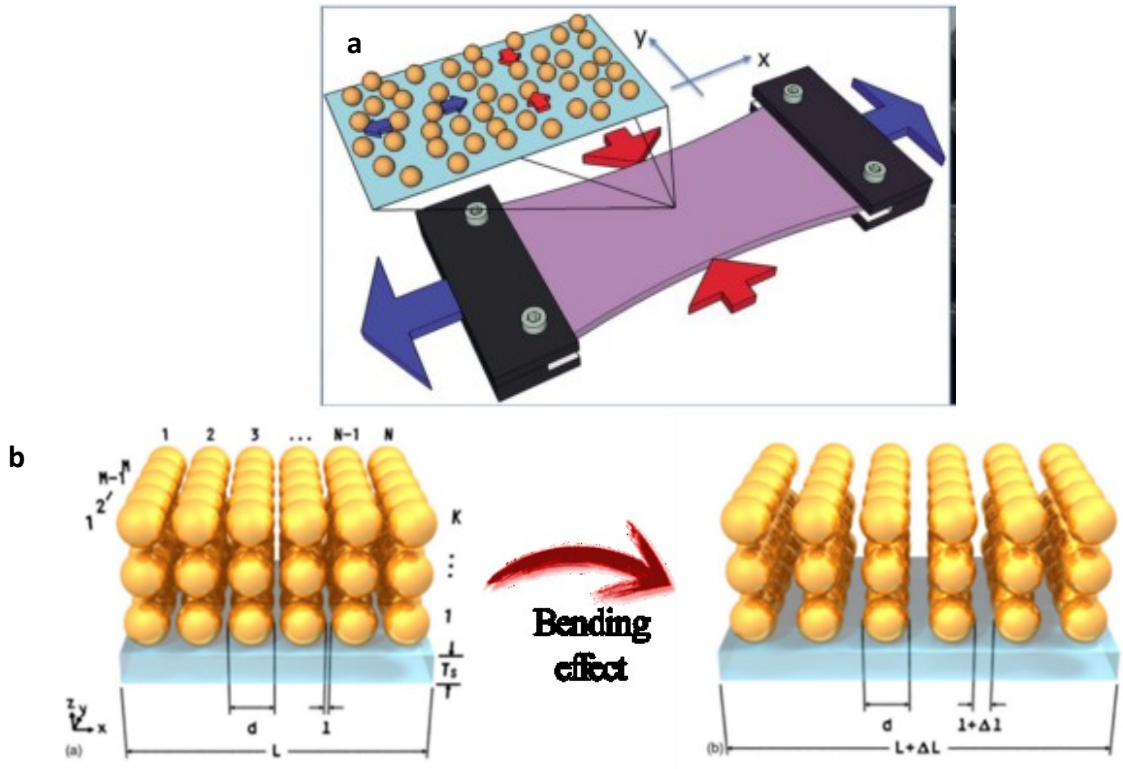

Figure 2.12: effect of uniaxial stretching and bending on the interparticle distance of MPN consisting in spherical filler integrated in elastomeric matrix (a) or adherent to a flexible substrate (b). From references [79] *and* [80]

A simple model for how **uniaxial stretching** reorganizes a monolayer of spherical nanoparticles embedded in PDMS is shown in figure 2.12a. First, we notice the effect is twofold: the nanocomposite elongates in the stretching direction and compresses in the transverse one. Such compression is proportional to the Poisson modulus of the polymer, which is 0.5 for PDMS, meaning that upon a stretching up to the N% in one direction, the polymer will undergo a compression up to the N/2% in the opposite one. The nanoparticles embedded in the matrix move consequently: as indicated by the colored arrows, they move away in the stretching direction and move closer in the transversal one. In other words, by stretching an elastomeric substrate containing immobilized metal nanoparticles one can increase the distance between nanoparticles in roughly the same proportion as the applied strain[42].

Mechanical bending is another simple way of deforming a metal – polymer nanocomposite. A model explaining its effect on a spherical nanofiller embedded in a dielectric matrix is shown in

figure 2.12b. When the nanocomposite is bent with a convex shape the interparticle distance (namely, l_0 in the schematic considered here) increases to a value $l_0 + \Delta l_0$. If the nanocomposite is bent with a concave shape, l_0 will decrease. Knowing the degree of bending it is possible to have and estimation of Δl_0, this is however challenging, since in most cases one has to deal with a non-trivial distribution of the filler shape, size and interparticle gaps, rather than having an ideal, ordered structure like the one pictured.

Both these models show that mechanical deformation is a simple yet effective strategy for altering the separation distance between nanoparticles, and they have been used to explain the evolution of the optical response and electrical conductance of the MPN undergoing the mechanical deformation. This will be the topic of the next chapter and of most of the experiments done during this work.

2.2 Functional properties

The goal of this section is to show how the optical and electrical properties of a MPN depend on its structure. In particular we will see that the interparticle distances play a dominant role. As mentioned previously, these can be set during the sample fabrication, controlling the amount of particles embedded and tuned afterwards by deforming the material. How this can be done is detailed in these sections.

2.2.1 Electrical properties

In general, polymers are excellent insulators: their conductivities lie in the $10^{-13} \div 10^{-18}$ S/cm range [81]. Nonetheless, additives can impact this parameter up to the point of causing it to become close to that of metals.

How this happens has been the object of several studies. Josef Gurland in the 60's, started studying a system consisting in a Bakelite polymer where spherical silver particles were embedded [55], with the of understanding the dependence of the composite conductance on the amount of silver particles embedded.

The main result of his research is shown in figure 2.13 where we see the resistivity as a function of the filler fraction.

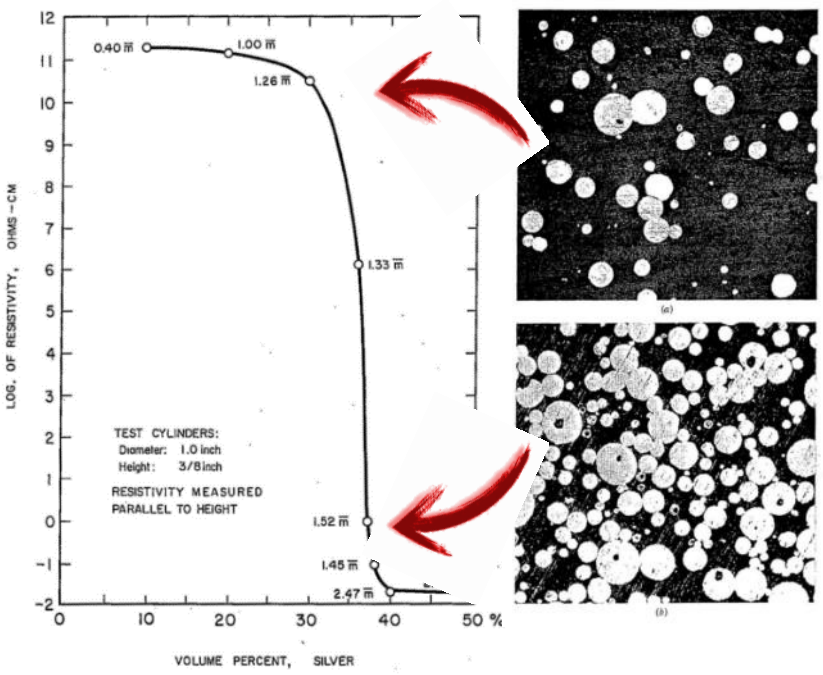

Figure 2.13: percolation curve acquired for a Bakelite system with embedded silver nanoparticles [55]*. Two structures are portrayed in the insets: (top-left) dielectric regime with low concentrated particles, (bottom-left) conductive regime with densely packed particles. Adapted from reference* [55]

This graph enlightens a behaviour which is common to most random insulator-conductor mixtures: once a certain filling fraction ϕ of the conductive phase is reached, a sharp decrease of the resistivity is recorded. This transition is associated with the formation of a network of electrically connected filler particles spanning the whole sample.

Here, the critical ϕ is about 0.3. For lower silver concentrations, when the composite structure is probably similar to the one shown in the top inset, the resistivity is roughly that of pristine Bakelite, while between $\phi = 0.3$ and $\phi = 0.4$ the resistivity drops abruptly by more than twelve orders of magnitude to settle at around 0.2 $\Omega \cdot$cm. This sigmoidal-shaped curve is the fingerprint of conductive polymer composites[55,82].

Gurland's research showed that the filler concentration modulates a MPN electrical conductance. However, it is important to remind that the conductance is strictly connected to the interparticle distance which determines the degree of connectivity of the filler. Besides depending on the filler concentration, the particle gaps (hence the nanocomposite conductance) also depend on the filler shape, size and distribution. We mentioned for instance, that given a certain filling factor the nanocomposite conductance is generally much lower for shape-anisotropy filler compared to an isotropic one (see section 2.1.3).

2.2.1.1 Percolation theory

Percolation is a phenomenon which can be found in many different systems. Percolation theory can describe the physical properties of glass transitions and porous media, but also serves as a model for processes not directly related to material science, such as the spread of fires and the propagation of diseases[83,84].

This theory was demonstrated to be suitable for describing the problem of clustering of conductive particles in an insulating matrix[85], both in the case in which particles are deposited on a rigid substrate and in the case they are incorporated in a polymeric one. In the former case the vacuum plays the role of the insulating matrix, in the latter this is carried out by the polymer[4]. In particular, it is useful to describe the evolution of the electrical conductance of the system while the particle concentration increased.

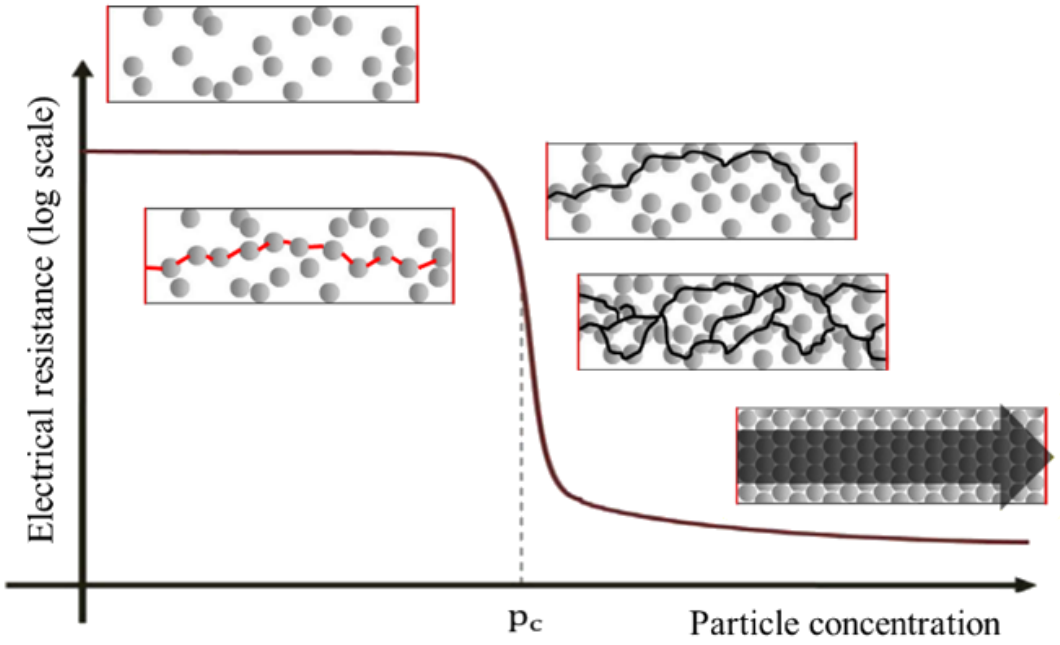

Figure 2.14: Electrical resistance as a function of the volume fraction, the latter parameter ranging between 0 and 1, ϕc is the percolation threshold. The inserts depict schematically the composite structure at the different stages. The curve shows a typical percolative behaviour of a metal-polymer composite system. At low volume fractions (ϕ < ϕc) the resistivity of the composite system approaches that of the polymer matrix. At ϕ ~ ϕc the observable undergoes an abrupt change. If ϕ>ϕc resistivity is drastically reduced, and it exponentially approaches the resistivity of the metal filler.

The typical curve showing how the resistance of a metal / insulating system evolves by increasing the metal filler concentration is shown in figure 2.14. At low ϕ the nanocomposite resistivity is almost the same as the polymer matrix, as the amount of particles increases, the resistivity of the system slowly decreases, until a critical volume fraction ϕ_c is reached: the amount of particles is just enough to form a continuous conductive path through the matrix. This is called the percolation threshold ϕ_c, at which the resistivity of the nanocomposite falls by several orders of magnitude. Once this threshold is exceeded, the resistivity of the system is again little sensitive to changes in the filler fraction, and slowly reaches the limiting resistivity of the implanted metal.

The following power-law relation describes the resistivity of nanocomposite materials when $\phi > \phi_c$:

$$\rho \propto \rho_0 \cdot (\phi - \phi_c)^{-q} \qquad (2.4)$$

where ρ is the resistivity of the nanocomposite, ρ_0 is the conductivity of the filler metal[82].

While the critical volume fraction ϕ_c depends on microscopic details such as the microstructure and the mean interparticle conductance, the exponent q is a universal parameter which is fundamentally related only to the dimensionality of the system [86,87]. Numerical simulations and experiments predict $-q = 1.3$ for two-dimensional systems, and $-q = 2.0$ for three-dimensional systems [88,89]. Nevertheless, experiments can depart significantly from these values.

However, it is fundamental to underline that the percolation mechanism implied by Eq. 2.4, where a sharp threshold is predicted which set the conductance of a metal/insulating system, is no more valid when the metal filler has a submicron dimension. In this case, the tunnelling between the particles cause the absence of any "critical" concentration.

In other words, at nanometric scales, the definition of two objects being in contact with each other is somewhat broader. This means that particles do not need to be in touch with each other to let the electrons drift along the path (figure 2.15), so that the sharp cut-off in the resistivity at the percolation threshold ϕ_c is smoother. Furthermore, below ϕ_c the conductivity is not zero, because the matrix itself has the potential of conducting electrons, even when there are no particles embedded in it.

In general, the tunnelling conductivity σ is proportional to $\exp(-2\delta/\xi)$, where δ is the mean particle separation and ξ is the tunnelling decay length.

Considering a system in the limit of dilute particles of size D the mean particle separation δ scales as $\delta \propto D/\phi^{1/d}$, where d is the system dimensionality; so, for sufficiently large temperatures is thus expected to follow $\sigma \propto \exp\left(-a_d D / \xi\phi^{1/d}\right)$ where ad is a dimensionless constant, which for point particles dispersed in a three-dimensional (two-dimensional) volume takes up the value $a_3 \sim 1.41$ ($a_2 \sim 2.12$) ξ is related to the electronic wavefunction decay in the polymer, typically ranging between some Ångstroms and some nanometers depending on the material properties. At room temperature, tunnelling contribution to the conductance becomes non-negligible when ξ is less than a few tens of nanometers, if the particles are neutral.

Among the many studies describing how the structural properties of the filler influence the percolation curve, it is worth mentioning the research done by Brown et al [84,90,91]and Balberg and co-workers (see references [57,82,83,92–95] for instance).

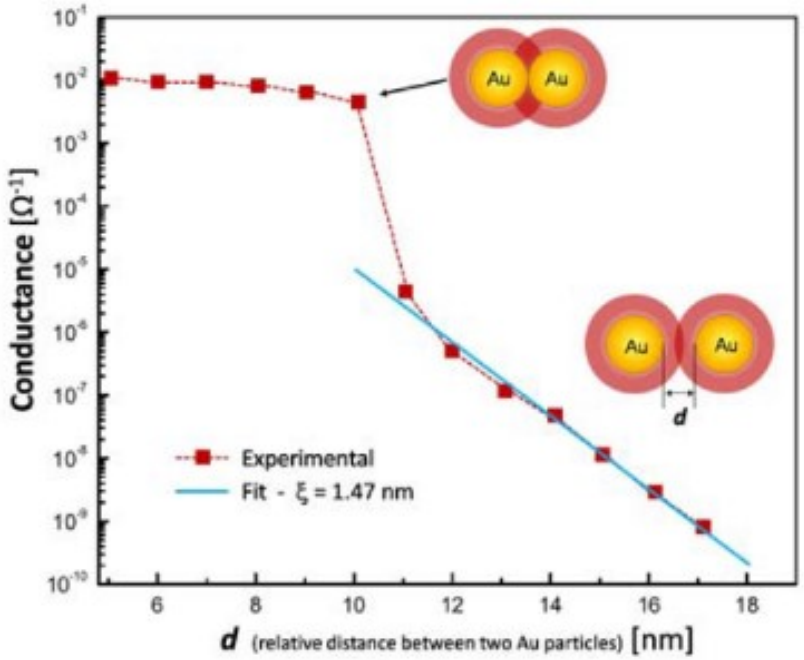

Figure 2.15: Electrical conductance between two gold particles about 10μm in diameter as a function of the centre-to-centre distance. The surrounding medium is air, and the large jump in conductance at about 10 nm is compatible to the particles establishing physical contact [96].

Both the groups realized that given some assumptions the percolative like behaviour of the conductivity and electrical transport of several composite systems in dielectric regime is indeed better described by a tunnelling-like mechanism [57], where the conducting particles are still not touching. In a nanocomposite system with spherical nanoparticles, if ϕ is not too large, the following approximation for the global conductivity σ holds [83,97]:

$$\sigma \simeq \sigma_0 \cdot e^{-1.41\frac{D}{\xi}\phi^{1/3}} \qquad (2.6)$$

when $D/\xi \rightarrow 0$, a change in the particle density does not affect the connectivity between the particles [57]. On the other hand, if ϕ is sufficiently high so that particles are effectively in contact with each other, equation (2.4) holds, as expected.

In eq. 2.6 we have also assumed that the metallic particles are spherical and of fixed diameter. Although as discussed in reference [83] we do not expect that small deviations from sphericity would have any important effect, metallic inclusions with high aspect ratios can change appreciably the location of ϕ_c and the low-density tunnelling regime. For example, the tunnelling conductivity of dispersions of rod particles of diameter D and length $L>>D$ scales approximately as $\sigma \propto \exp(-D^2/\xi\phi L)$ for isotropic orientation of rods [83].

Concerning the assumption of fixed particle size, we note that some composite films show a more or less pronounced reduction of the mean particle size D as ϕ decreases. This effect can be included in equation 2.6 by considering an explicit ϕ dependence of D which simulates the observed one. In principle, it is possible to consider the effect of particle size polydispersity, although this would require detailed knowledge of the size distribution and its possible dependence on ϕ. In the absence of this information, the theoretical estimates can be tentatively interpreted in terms of effective sizes D_{eff} of polydisperse particles

For large values of ϕ, as the amount of deposited material increases, initially isolated particles start to coalesce, resulting in a significant drop of the average interparticle distance. This also results in the formation of larger nanoclusters at a nanometric and micrometric scale. Since the interparticle spacing is lower, the electron tunnelling probability grows, and fragmented metallic paths with higher Ohmic conduction exist within nanoclusters [98]. More metallic well-connected percolation paths are formed, until a complete metallic network of inclusions is formed. Tunnelling is then replaced by the more effective Ohmic conduction, which is well described by the following Ohm's formulas:

$$R = \frac{V}{I} \qquad (2.9)$$

$$R = \rho \frac{l}{h \cdot w} \qquad (2.10)$$

where l is the length of the nanocomposite, w its width and h its height.

This latter quantity plays a key role in this regime: if the maximum volume fraction is reached it can be considered equal to the maximum penetration depth d_{nc} only. Once the nanocomposite is saturated with metal particles, a thin film of metal particles begins to grow on the surface which significantly affects the conductance of the nanocomposite.

In the ohmic regime, when the volume fraction is well above the critical threshold, the resistivity can be considered constant while h is roughly proportional to the equivalent thickness t_{eq}. This leads to:

$$R \propto 1/t_{eq} \quad \Rightarrow \quad G \propto t_{eq} \qquad (2.11)$$

which implies that the conductance G of the systems grows linearly with the equivalent thickness of the deposited metal.

2.2.1.2 Effect of the filler properties on the electrical properties

Besides its concentration, the filler structure as well plays an important role in determining the electrical properties of a MPN.

A meaningful example regarding the influence of the filler shape on the percolation curve is shown in figure 2.16. These data come from an elaboration of the data acquired by Flandin and co-workers to study the effect of uniaxial stretching on the electrical resistance of carbon-elastomer nanocomposites (see figure 2.9). The curves show the conductance evolution for increasing filling factors; the blue one refers to the low structured carbon black (LSCB) and the red one to the high structured one (HSCB). We notice that the critical threshold which sets the beginning of a tunnelling conductivity is significantly higher for the LSCB.

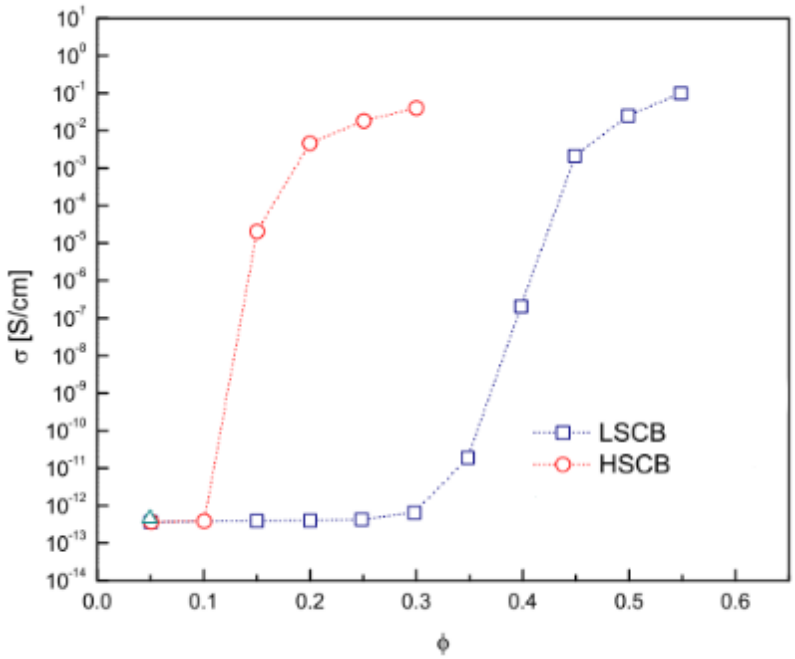

Figure 2.16: Percolative curves of carbon-based nanocomposites (i.e. the conductance as a function of the filling factor). The red plot refers to high structured carbon black (HSCB), whereas the blue plot refers to low structured carbon black (LSCB). In the latter case, the critical threshold at which tunnelling effects arise is significantly higher. [40]

Fixing the particle shape, one should consider their size distribution, as most of the particle fabrication techniques lead to the formation of nanoparticles with a non-uniform particle size.

The size distribution is extremely relevant determining the conductance of composite system since polydisperse systems can be packed more densely (this can be easily imagined if we think that the smaller particles can occupy the interstices left by the larger ones) at a given volume fraction a higher conductivity is reached.

Modelling the dependence of the composite conductance one should also consider the aspect-ratio distribution, as well as the non-uniform geometry. We have then a series of effects which come from the interaction of the filler particles with themselves and the polymer matrix. This may happen during the processing phase: if the composite is fabricated with the mixing approach described before, we should consider that the mixing can favour a certain *particle orientation*, leading to local anisotropy which reduces the conductivities with respect to a same volume fraction isotropic system. Similarly, particle agglomeration and segregation originate in inhomogeneous nanocomposites. Moreover, filler breaking can have relevant consequences on the composite conductivity as well.

Finally, an important point regard the procedure of measuring the samples: as it can be seen from graphs shown in figure 2.16 these curves where acquired pointwise. This is clearly the only way to do it if the nanocomposites are synthetized following the chemical approach and leads to the problem of the reproducibility which were already discussed by Balberg.

For all these reasons it can be quite challenging to characterize the effect of the structural properties of the filler on the composite conductivity.

A possible route to perform these studies consist in simplifying as much as possible the system in order to disentangle the effect of the different parameters.

- A fabrication technique which allows to fabricate MPN with a wide range of filling factors directly embedding the filler in the matrix may be valuable, as this would dramatically reduce the problem following from the mixing process.

- The possibility to measure real time the amount of clusters embedded in the polymer matrix would increase the reproducibility.
- A simple geometry like the spherical one would eliminate the problems linked to the use of a shape-anisotropic filler.

2.2.1.3 Effect of a mechanical deformation in responsive polymer

The possibility to have a deformable MPN with controlled electrical properties, can be interesting for many reasons.

In terms of applications, flexible and stretchable conductive materials can be used to realize devices for flexible and wearable electronics, smart sensors[45,75,99–103]. All these applications require a conductive layer perfectly adherent to the polymer and that can be stretched and bent without undergoing mechanical failures. To this purposes MPN offer the noticeable advantage that the conductive filler is integrated in the polymer one and hence intrinsically adherent to it.

Another motivation comes from the possibility to use the electrical conductance of the nanocomposite as a probe to study the reorganisation of the filler embedded in the polymer in response to a mechanical deformation, this being the starting point to develop reliable and reproduceable applications.

Much research has been done to understand how this happens[45,75] but much is still do be done: the challenge consists in the fact that it is hard to access the nano and microstructure of the nanocomposite while the sample undergoes a deformation, hence it is necessary to rely on indirect probes to understand its effect.

Electrical properties are a valuable probe to this goal because they directly depend on the nanocomposite structure: on the interparticle distance, on the filler orientation (in case of shape anisotropy) etc. In other terms, measuring the sample resistance while it is undergoing a mechanical deformation gives an idea on how the particles are moving, whether they are separating or getting closer, and how they are changing their mutual orientations in case of a shape-anisotropic filler.

Clearly, the possibility of tuning the electrical properties of a MPN with a mechanical deformation in a reversible way is interesting on its own, not necessarily in relation to a fundamental understanding of the reorganization of the filler in the polymer matrix. This indeed implies to have a device which can be adapted to the peculiar situation where it is used.

In this section we report the state of the art regarding the effect of a mechanical deformation on the electrical conductance of MPN, with some possible applications.

A systematic study on the effect of uniaxial stretching on the electrical conductance of carbon-elastomer nanocomposite was done by Flandin and co-workers. In reference[75] they studied how the electrical resistance changed upon a 30% stretching. Three different fillers where tested (see figure 2.18): carbon fibres, high and low structured carbon black (CB).

The resistance was recorded both in the stretching direction and in the transversal one. According to the filler structure, two trends were found: the resistance increases in both directions (carbon fibres filler, figure 2.19b), or it decreases with the carbon black, figure 2.19a.

Focusing on the CB, it was found that the resistance decreases more slowly in the stretching direction than in the transversal one.

The model Flandin et al. used to explain the behaviour observed in the CB is similar to the one discussed in section 2.1.6 for the spherical filler embedded in elastomeric matrix. Broadly, the stretching causes an elongation of the composite which makes the filler moving apart; but at the same time, in the opposite direction a compression occurs which pushes the particles closer to each other.

More specifically, the rotation and translation of carbon black induced by stretching, preserves the number of contacts and hence the number of conducting pathways. In addition to this effect, elongation along the stretching direction also causes breakage of the existing continuous conducting network by increasing the gap between particles, while the compression in the transversal one is in favour to the resistance decrease.

Interestingly, the carbon fibres have a much lower mobility in the matrix and tend to segregate in response to a mechanical deformation. See ref [75] for further details.

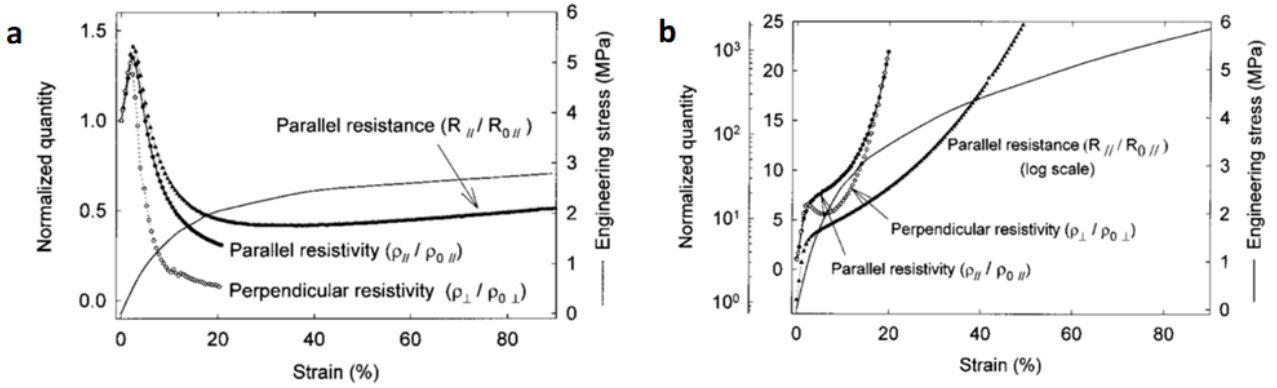

Figure 2.17 Resistance evolution upon stretching of carbon – PDMS nanocomposites.[100]

An example of how the bending affects the resistance of a nanocomposite made depositing gold clusters on a paper substrate is reported in reference[45]. The sample is subsequently bent in a convex shape and then relaxed setting it back in its flat position. This causes a dramatic change in its resistance, as we can see from the graphs in figure 2.17. This example is particularly interesting as it shows how the reorganization of metal nanoparticles can be exploited to convert a mechanical strain into a reliable output signal (electrical current) which depends on inter-particle electron tunnelling. In other terms, the nanoscopic interparticle distance reflects on the macroscopic quantity which is the sample resistance.

These two macroscopic and nanoscopic quantities can be linked with a mathematical relationship. As explained by Herrmann et al. [103] and referring to figure 2.12, the resistance variation upon a bending is described by the following formula:

$$\Delta R/R = e^{\beta \Delta l} - 1 = e^{\beta(d+l)\epsilon} - 1 \equiv e^{g\epsilon} - 1,$$

where

$$g \equiv \beta(d + l)$$

d the nanoparticle diameter, *l* inter-particle distance and β is the parameter describing describes the tunnelling of electrons along the substrate $R \alpha \beta l$. Using realistic values of β 10 nm^{-1} and $d+l$ 10 nm, we estimate a gauge factor 100. This extremely high value is the origin of the interest in the exploitation of strain for the realisation of mechanical sensors.

2.2.2 Optical properties

2.2.2.1 Plasmonic theories

Mie Theory

The fundamentals of light scattering by particles can be well understood and modelled in terms of a homogeneous dielectric sphere. The goal is to write the electric field scattered by an isolated sphere of given radius and material, knowing the incident electric field. In 1908, Gustav Mie[104] was the first to give the general exact solution to this electrodynamics problem.
Briefly, this is obtained by solving Maxwell with appropriate boundary conditions, in spherical coordinates, and using multipole expansions of the external electromagnetic field. Thanks to this model, it is possible to predict the amount of light absorbed and scattered by the particle, i.e. its extinction cross section. The size dependence of the optical spectra of large clusters is governed by the size of the particle with respect to the wavelength of light.
The solution was given for spheres of any dielectric constant and size: those parameters, together with the dielectric function of the surrounding medium ε_m, are set as input parameters in the computations [105]. The solution for the electric and magnetic fields is given in terms of an infinite series of terms, whose convergence might be slow depending on such parameters [104].
In the present work however, it is sufficient to consider a significant simplification to the general model, also known as quasi-static approximation ($\lambda \gg R$). Under this assumption, the electric field of the incoming light can be considered constant, hence the problem is reduced to the simpler electrostatics domain: phase shifts of the incident electrodynamic field over the particle diameter length scale are negligible.

Quasi-static approximation: $\lambda \gg R$
First, we can focus our attention only to the electric field: once derived, it is trivial to obtain the magnetic field. Let us denote the incident electric field by the vector $\vec{E}_0$. This polarizes the particle, so that the electric field $\vec{E}_i$ inside the particle is given by:

$$\vec{E}_i = \vec{E}_0 \frac{3\varepsilon_m}{\varepsilon+2\varepsilon_m} \qquad (2.28)$$

Solving Laplace equation $\nabla^2\varphi = 0$, where φ is the electric potential, gives the field surrounding the particle, provided that both φ and the normal component of the electric displacement $\boldsymbol{D} = \epsilon_m \boldsymbol{E}_0$ are continuous at the sphere surface.
The induced dipole moment in the sphere arising from the polarization of the conduction electron density is $\boldsymbol{P} = \epsilon_m \alpha \boldsymbol{E}_0$, while the static polarizability α of the sphere can be obtained by solving of Laplace equation [105]:

$$\alpha = 4\pi\varepsilon_0 R^3 \frac{\varepsilon-\varepsilon_m}{\varepsilon+2\varepsilon_m} \qquad (2.29)$$

Such polarizability of a small sphere of sub-wavelength diameter in the electrostatic approximation might be complex, depending on the dielectric functions in play. It is worth noting that α reaches its maximum whenever the denominator approaches a minimum:

$$|\varepsilon + 2\varepsilon_m| = |\varepsilon 1(\omega) + 2\varepsilon_m|^2 + [\varepsilon 2(\omega)]^2 \qquad (2.30)$$

which for the case of small or slowly-varying Im[ε] around the resonance simplifies to:

$$\varepsilon_1(\omega) = -2\varepsilon_m \qquad (2.31)$$

The above relationship is called the *Frohlich condition* and it models the dipole surface plasmon of a metal nanoparticle responding to an oscillating field. In terms of the Drude model, this metal particle embedded in a medium with dielectric constant ε_m has a resonant frequency given by:

$$\omega_{lsp} = \frac{\omega_p}{\sqrt{1+2\varepsilon_m}} \qquad (2.32)$$

The polarization effects of the ion background core might be taken into account by writing:

$$\omega_{lsp} = \frac{\omega_p}{\sqrt{\varepsilon_{core}+2\varepsilon_m}} \qquad (2.33)$$

It is worth noting that the resonance frequency strongly depends on the dielectric environment. For example, (2.32) and (2.33) imply that the resonance is red-shifted as ε_m is increased. Locally, the polarization of the dielectric medium acts by reducing the effective surface polarization charge of the metal particle. The reduced surface charge leads to a restoring force on the electrons of lower intensity, which then causes the shift of the resonance frequency towards lower values. This can be exploited to move the resonance plasmon frequency of the noble metals - such as Au or Cu - away from their interband transitions.

Limitations of Mie Theory

The Mie results might be generalized to a collection of particles, if they are considered not to interact with each other, that is, if the electric field around one particle due to the excitation of surface plasmon resonance is not felt by other surrounding particles. When it comes to many particles, Mie theory qualitatively describes the optical properties of the system given the average size of the scatterers.

For example, if the particle diameter $2R$ is much smaller than the wavelength of the incident light, and the particle concentration is very low, the optical extinction spectra can be described well by Mie theory. An absorption peak would result due to the excitation of dipole plasma mode $L = 1$.

Nonetheless, this model falls short in accounting for the effects due polydispersity and interactions with the matrix, even in the simple case of isolated particles [105].

While Mie theory is valid for spheres of any size, its main limitation is that the dielectric constant of a small particle is different from that of the bulk [106], and the Maxwell equations break down at points very close to the border [105].

Maxwell-Garnett Effective Medium Theory

Depending on the volume fraction of clusters in a nanocomposite, the average separation between two embedded particles can approach very small values. The electromagnetic coupling of clusters becomes non- negligible at centre-to-centre distances smaller than about five times their radius [105,107].

Since the interparticle coupling is stronger than the coupling within the surrounding medium, Mie theory fails to describe the optical absorption spectrum.

For gold nanoparticles, the wavelength at which absorption due to dipole-dipole interactions occurs ranges from 520 nm to 750 nm, in the limiting cases of isolated particles and 0.5 nm apart particles respectively. The resulting spectrum is a combination of single particle plasmon resonance and a peak due to particle-particle interactions [2]. Generally, it has been found that, with decreasing interparticle distance the surface plasmon resonance shifts to longer wavelengths, as depicted in figure 2.18.

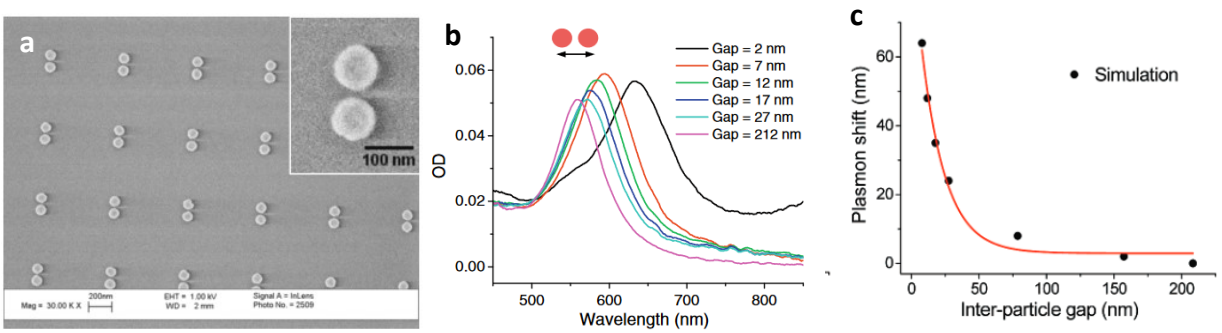

Figure 2.18: (a) Extinction spectra of Lithographically-fabricated array of 88-nm diameter gold nanodisc pairs with controlled inter-particle separation. A red-shift occurs with decreasing gap for polarization along the interparticle axis. From reference [29] (b) Shift in the plasmon wavelength maximum of a pair of Au nanodiscs as a function of the interparticle edge-to-edge separation[30]

A successful model has proven to be the Maxwell Garnett effective medium theory[109]. It strongly simplifies the derivation of the particle interaction contribution, by evaluating an average polarizability of the composite medium, weighted by the concentrations of its components [2,44,109].

The Maxwell Garnett model applies in the quasi-static limit ($2R \ll \lambda$), even in the case of small interparticle distances. Moreover, particles need not to be assumed spherical.

The optical properties of the nanocomposite can be ascribed to two main contributions: the embedded particles as single individuals and the macroscopic, collective properties of the population as a whole. The effect of interparticle coupling is determined by the position distribution of the particles. A convenient approximation is to consider a statistical average over a large number of aggregates which gives the average volume fraction ϕ. In this case, the more the distribution differs from the isotropic, homogeneous case, the less accurate is the approximation for the filling factor.

Two limiting cases are worth considering:

1. if $\phi \ll 1$ the interactions between clusters can be neglected, Mie theory holds, and the optical properties of the nanocomposite is simply the sum of the single cluster properties.
2. if $\phi \to 1$ clusters are no longer separate entities, but the system approaches a continuum. It is well represented by a dendritic structure whose optical properties are governed by the collective electromagnetic interactions and contact between the cluster.

In the latter case, the contribution of the dielectric constant ε_m of the matrix is overwhelmed by the interacting clusters in the neighbourhood of each nanoparticle. This is where the effective medium theory comes into play: the inhomogeneous medium surrounding the particle is modelled as a homogeneous *effective medium*, characterized by a dielectric constant ε_{eff}, which depends on the filling factor ϕ as well as the dielectric functions of both the polymer and the embedded particles.

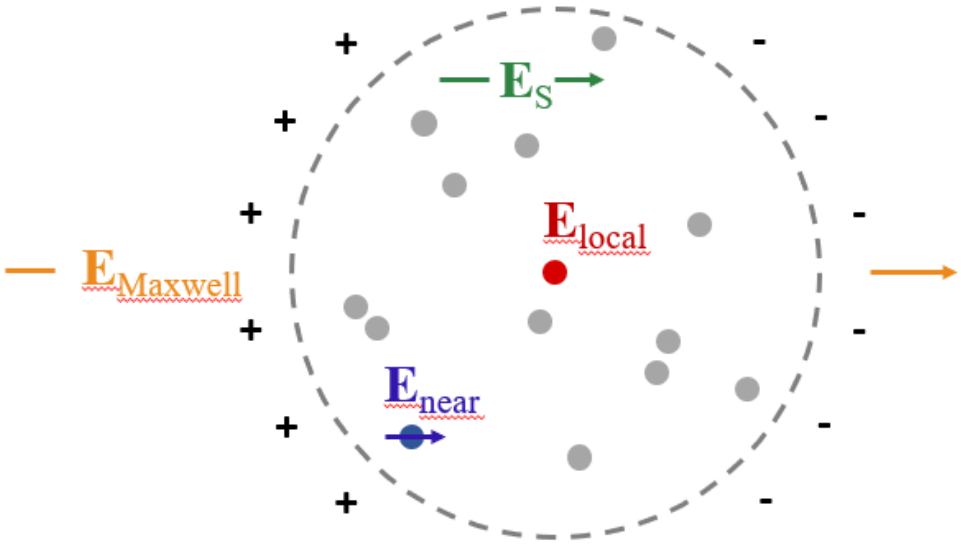

Figure 2.19: Lorentz sphere model applied to cluster matter. The signs outside the dashed circle stand for polarization charges at the boundary of the spherical cavity cantered at the selected particle[2].

We stress that the surroundings can be considered homogeneous on a scale larger than the length scale of spatial correlations, while closer clusters contribute to the effective local field individually depending on their arrangement and position. In fact, the neighbouring clusters are split into two groups: the ones closer than a distance of the order of the correlation length, and the ones outside such sphere, known as the *Lorentz sphere,* centred at the point at which the local field is to be calculated (see figure 2.19). For this latter group the number of components is sufficiently high to allow for an accurate average [2].

Let us consider an external electromagnetic field incident on the system, and a particular particle among the ones embedded in the matrix, whose dielectric function ε_m is assumed real. The local electric field at this point is:

$$\boldsymbol{E}_{local} = \boldsymbol{E}_{Maxwell} + \boldsymbol{E}_S + \boldsymbol{E}_{near} \qquad (2.47)$$

where $E_{Maxwell}$ is the incident external field plus the field arising from polarization charges at the sample surface, E_S is the field due to the polarization charges at the surface of the Lorentz sphere, and E_{near} is the sum of the contributions *Ej near* of polarizable particles inside of the Lorentz sphere.
The quasi-static approximation implies:

$$E_S = \frac{P}{3\varepsilon_0\varepsilon_m} \qquad (2.48)$$

where

$$P = E_{local}\sum_j n_j\alpha_j = \varepsilon_0(\varepsilon_{eff} - \varepsilon_m)E_{Maxwell} \qquad (2.49)$$

where nj is the number density of the j-th particle, whereas its polarizability αj is given by:

$$\alpha j = \frac{\varepsilon-\varepsilon_m}{\varepsilon+2\varepsilon_m}R^3 \qquad (2.50)$$

The assumption which underlies this effective dielectric function ε_{eff} is that the sample responds linearly to the external field in terms of the polarizabilities of the particles and matrix material. The composite sample may be replaced by an effective medium, by considering an effective dielectric function $\varepsilon_{eff}(\omega) = \varepsilon_{1,eff} + i\,\varepsilon_{2,eff}$. Formally, the effective dielectric function can be defined as the dielectric function which the system would have if it was replaced by a homogeneous material. A good approximation given by the present model is

$$\varepsilon_{eff}(\omega) = \varepsilon_m \frac{1 + \frac{2}{3\varepsilon_0\varepsilon_m}\sum_j n_j\alpha_j}{1 - \frac{1}{3\varepsilon_0\varepsilon_m}\sum_j n_j\alpha_j} \qquad (2.51)$$

which leads to the Clausius-Mossotti relation [2]

$$\frac{\varepsilon_{eff} - \varepsilon_m}{\varepsilon_{eff} + 2\varepsilon_m} = \frac{4\pi}{3}\sum_j n_j \frac{\varepsilon - \varepsilon_m}{\varepsilon + 2\varepsilon_m} R^3 \qquad (2.52)$$

alternatively, introducing the filler volume fraction ϕ, we obtain the Lorentz-Lorentz formula:

$$\frac{\varepsilon_{eff} - \varepsilon_m}{\varepsilon_{eff} + 2\varepsilon_m} = \phi \frac{\varepsilon - \varepsilon_m}{\varepsilon + 2\varepsilon_m} \qquad (2.53)$$

Rearranging the expression in (2.53) one can write the Maxwell-Garnett formula as:

$$\varepsilon_{eff} = \varepsilon_m \frac{1+2\phi\Lambda}{1-\phi\Lambda}, \quad \Lambda = \frac{1}{\varepsilon_m}\frac{\varepsilon - \varepsilon_m}{\varepsilon + 2\varepsilon_m} = \frac{\alpha}{3\,\varepsilon_0\varepsilon_m V} \qquad (2.54)$$

The surface-plasmon resonance occurs when

$$\varepsilon(\omega_{spr}^{MG})(1-\phi) + \varepsilon_m(2+\phi) = 0 \qquad (2.55)$$

Using the Drude model for the dielectric function $\epsilon(\omega)$

$$\varepsilon(\omega) = \varepsilon_{core} - \frac{\omega_p^2}{\omega^2 + i\omega\gamma}, \quad \gamma \approx 10^{14} Hz \qquad (2.55b)$$

we obtain the following expression for the frequency of the localized surface plasmon:

$$\omega_{spr}^{MG} = \frac{\omega_p}{\sqrt{\frac{2+\phi}{1-\phi}\varepsilon_m + \varepsilon_{core}}} \qquad (2.56)$$

This reduces to the result predicted by Mie theory if $\phi = 0$.

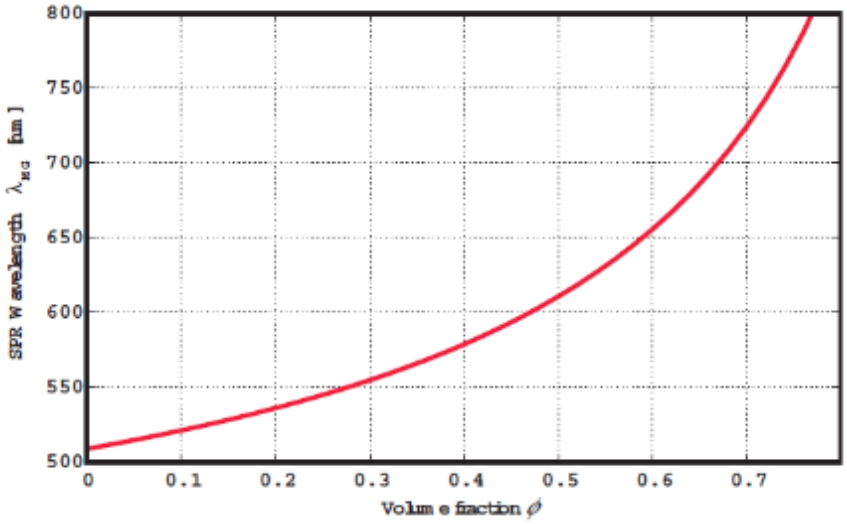

Figure 2.20: $\lambda_{MG}(\phi)$ from equation (2.56) in the case of Au nanoparticles ($\epsilon core$ = 9.84, ~ω_p = 9.1 eV [110]) embedded in a polydimethylsiloxane matrix (ϵm = 2.049). The case of ϕ = 0 agrees with Mie theory prediction λ_{Mie} = 508.72 nm.

In figure 2.20, the surface plasmon resonance (SPR) peak position $\lambda_{MG\,spr}$ as a function of ϕ is shown, in the case of Au nanoparticles embedded in an elastomeric matrix. The SPR peaks shift towards longer wavelengths at increasing values of the volume fraction.

2.2.2.2 Effect of the filler shape and distribution on the optical properties

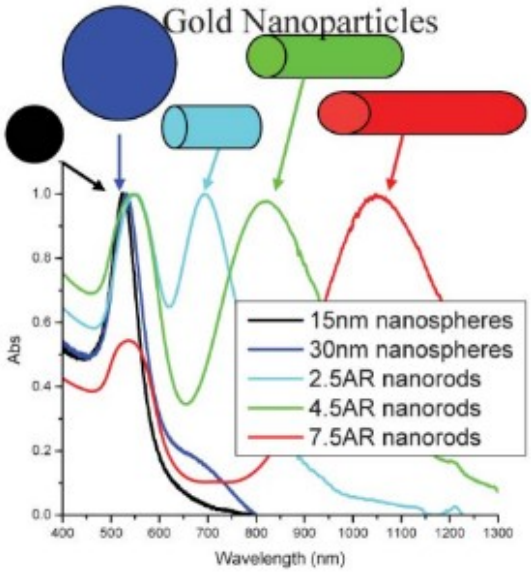

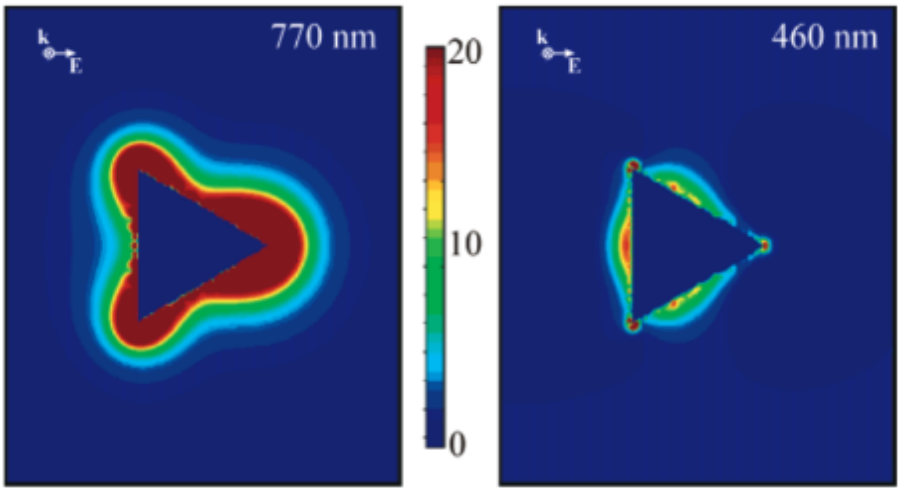

Figure 2.21. Top: effect of the particle shape on its optical absorption spectrum (from reference [111]). Bottom: effect of the particle dimension on its coupling with the electrical field (from reference [17]).

Particle shape has a significant influence on the plasmonic coupling as well. This has been briefly described in the case of free nanoparticles in solutions, where we have seen how different shapes correspond to different resonant wavelengths (see the different colors of the solutions contained in the cuvettes shown in figure 1.2c). In figure 2.21 we see the absorption spectra recorded for gold particles with different shapes (sphere and rods) and with different shape-anisotropy (three kinds of nanotubes). The different absorption spectra are caused by a different coupling of the electrical field with the particle, this indeed is essentially bound to its geometry[17,42,112]. For example, as we can see in the simulation of the electrical field coupled with triangular nanoparticles (see figure 2.21) there it is more localized at corners.

Similarly, given the particle geometry, changing the particle dimension a different coupling of the electrical field is expected[17,18]. This gives rise to a problem: the techniques to fabricate MPN provide a filler with a **distribution of sizes**, which can be particularly broad (like the one used to produce the nanoparticles embedded in the Bakelite matrix shown in figure 2.2a and 2.2b) or remarkably narrow (figure 2.2c), but still remains a non monosized filler.

Due to the fabrication challenges which need to be addressed to have a very narrow size distribution, a fundamental point to discuss is to which extent it is important to have it.

A narrow size distributed filler such as in optical nanocomposites have the advantage to provide a well-defined absorption spectrum, with a narrow peak at the resonant wavelength. On the contrary, the higher the degree of polydispersity the broader will be the spectrum. This very aspect also affects the theoretical modelling of the spectra, since the mathematical description of the size-distribution function may not be trivial. An important consequence is that this leads to a distribution of **interparticle distances**, which strongly affects the optical response of the nanocomposite as well. As shown in figure 2.18, the resonant wavelength can change up to ~ 100 nm upon a variation of the particle gaps of ~200 nm.

As reported previously, in all these techniques the filler has a range of interparticle distance *d* which depends on the particle concentration, size, distribution, shapes, orientation. With these techniques one can control the interparticle distances by controlling the filling factor. Indeed, if the filler is spherical *d* can be estimated knowing the particle and geometry and the volume of polymer in which they are dispersed. This can be easier in the case of a spherical filler with a narrow size distribution homogeneously distributed in the polymer.

A third method consists in controlling the particle distances *a posteriori*, acting with a mechanical deformation of the nanocomposite. This allows to compensate all the intrinsic difficulties mentioned before and it allows to tune real time the optical response of a device depending on the situation where it is employed. Doing in this way one can fabricate MPN with a high filler concentration, hence with a good conductance, with the only requirement that the size distribution is narrow enough to have an absorption spectrum peaked at a certain wavelength.

2.2.2.3 Effect of mechanical deformation on the optical properties of MPN

Studying the evolution of the optical properties of a MPN in response to a mechanical deformation is interesting for many reasons. On one hand, we know the mechanical deformation affects the interparticle distance and hence the resonant wavelength. This implies that being able to predict the effect of a mechanical deformation on the optical absorption of a nanocomposite, one can tune it in order to match the necessity of the particular situation where the sample is employed.

An understanding of how particles reorganize upon mechanical deformation is thus interesting from a fundamental point of view, but also as the starting point for developing applications and has been the object of several studies.

The optical response of the MPN can be effectively modulated by simply stretching the elastomeric substrate in which metal nanoparticles are embedded. Indeed, this alters the separation distance between particles by a factor roughly equal to the applied strain.[42]

One of the first examples of this approach was MPN consisting of ~100 nm Au bowties and rods with sub-50 nm gaps patterned via nano-stencil lithography on a flexible elastomer film. Appreciable shifts in the transmission spectra were observed when applying a mechanical strain ~5% to the nanorod−polymer composite, orthogonally to the longitudinal axes of the rods.

The magnitude of such optical shifts could in principle have been enhanced by shrinking the initial gap between the nanoparticles, yet the limited resolution of top-down patterning methods makes the generation of gaps smaller than 10 nm challenging.

Similar approaches based on stretching have been also applied to composites containing Au semishells, aiming at an application as strain sensors (see reference 57 and 115 in ref. [42]). The stretching of MPN was also recently used to create multiplexed metal surface holograms wherein the hologram switches from one image to another with increasing strain.[47] This was achieved by depositing a pattern of Au nanorods into a stretchable elastomer film that yielded more than one hologram at different image planes. By optimizing the nanorod pattern, the authors were able to achieve up to three holograms appearing at the same image plane at three different values of strain.

Other interesting studies were done on system consisting in a monolayer of nanoparticles in PDMS with the goal of providing a theoretical model able to mathematically explain the experimental results (a nanoparticle monolayer is computationally easier to model compared to a thicker nanocomposite).

Cataldi et al [79] observed a 70 nm shift stretching up to the 20% a MPN consisting in a monolayer of a gold particles in a PDMS matrix. Qualitatively, the samples undergo a reversible color change as shown in the pictures. The model provided to explain this result is schematically shown in figure 2.12. When the nanocomposite undergoes a uniaxial stretching, the nanoparticles drift apart in the stretching direction and get closer in the transversal one, as indicted by the colored arrows.

Indicating with s the interparticle gaps, the following equation was found to describe the plasmonic peak shift.

$$\frac{\Delta\lambda}{\lambda_0} = k \exp\left(-\frac{s}{\tau D}\right) \qquad (1)$$

Where *D* is the particles diameter, while *k* is the maximum plasmonic shift for the particle dimer and *T* is the decay constant that depends on the considered system.

An interesting comparison of the effect of stretching on two nanocomposite consisting either in a ordered monolayer of nanoparticles embedded in PDMS or in a complex 3D structure (see figure 2.22) was done by Chiang and collaborators [78]. For both the samples a redshift of the absorption spectrum occurs in response to the mechanical deformation, with the difference that for the monolayer-nanocomposite the shift is up to 40 nm, while for the disordered one, it reaches 70 nm. The physical origin of this difference is traced back in a major interaction between the particles in the disordered nanocomposite.

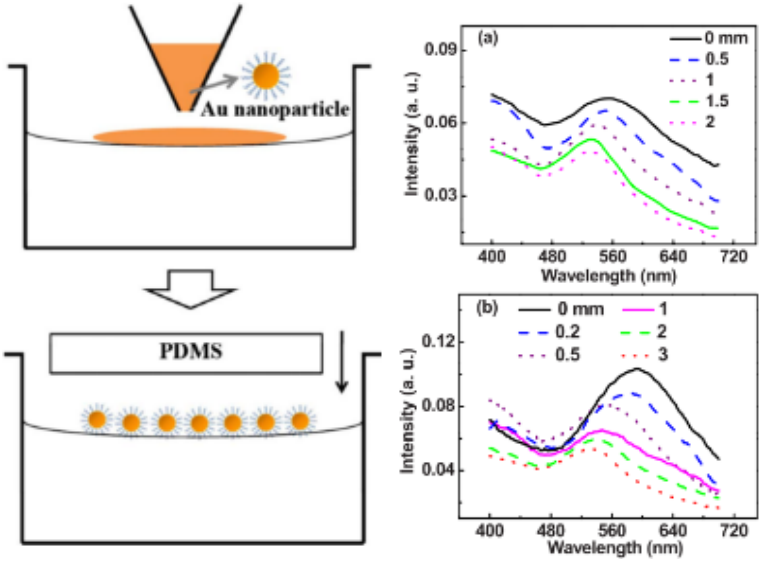

Figure 2.22 Schematic representation of a disordered 3D layer (top) of Au nanoparticles compared to an ordered monolayer (bottom) of the same particles. Both nanocomposites are synthetized with a chemical approach and consist in clusters embedded in PDMS. While undergoing stretching, both the samples show an appreciable redshift, which is larger for the disordered distribution of nanoparticles as compared to the redshift observed in the monolayer nanocomposite. Authors attribute this behaviour to the fewer interactions between particles arranged in an ordered, flat, pattern.[78]

Finally, the effect of mechanical bending on the optical response of the nanocomposite was studied by Zhang et al[46] who developed a straightforward approach to create soft plasmonic photonic crystals consisting of gold nanolines arranged on stretchable substrates with nanoscale periods, centimeter-scale areas, and high reproducibility using annealed gold nanoparticle colloids. The system exhibits excellent bending performance[46].

Before moving on it is worth summarizing the main concept of this section.

One of the main advantages of using MPN is the possibility to tune the functional properties of the whole macroscopic system, by controlling the structural ones. A parameter which plays a fundamental role in this respect, is the interparticle distances, upon which both the optical and electrical properties significantly depend.

The control can be done during the sample fabrication, controlling the amount of particle embedded in the system hence changing how close the particles are packed together. On the other hand, certain MPN allow the control of this parameter even after the sample fabrication, by acting

with an external stimulus and causing the reorganization of the filler. Among the different ways of stimulating a nanocomposite, mechanical deformation is one of the simplest, controllable and studied.

3 Metal – polymer nanocomposite fabrication

Depending on the architecture of the nanocomposite which needs to be fabricated, different techniques can be addresses. For sake of clarity, let us briefly remind the main nanocomposite architectures shown in figure 1.4. Polymer nanocomposite (PN) can be divided in mainly three categories:

i. **Bulk or isotropic PN**: the filler is isotropically distributed in the polymer matrix;
ii. **Assembled PN**: the filler is organized into clusters or regions of anisotropic density within a dielectric matrix;
iii. **Interfacial PN**: nanoparticle straddle a metal – dielectric or dielectric-dielectric interface.

Here we report some fabrication techniques which are commonly used to produce them.

3.1 Bulk polymer nanocomposites

3.1.1 Wet chemical methods

Wet chemical methods[43] are a usual choice to produce bulk metal polymer nanocomposites. These methods can be classified into two broad groups: (1) in situ methods where metal particles are synthesized directly within a polymer matrix and (2) nanoparticle−polymer blends (or ex-situ method) where preformed metal nanoparticles are mixed together to form a binary or multiphasic mixture, which is subsequently let polymerized.

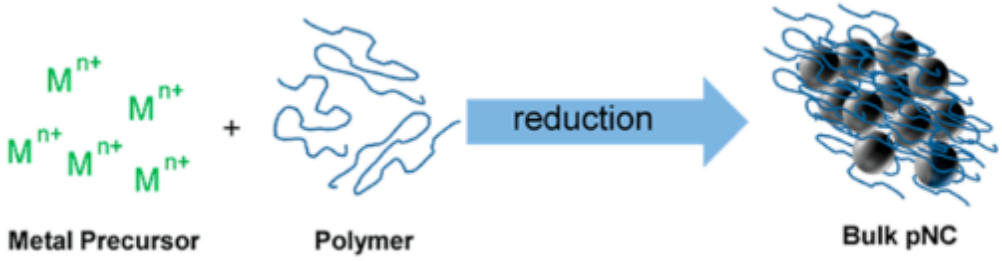

Figure 3.1: Schematic representation of the in situ – wet chemical synthesis approach. The metal precursor is reduced in the polymer to create a Bulk MPN.

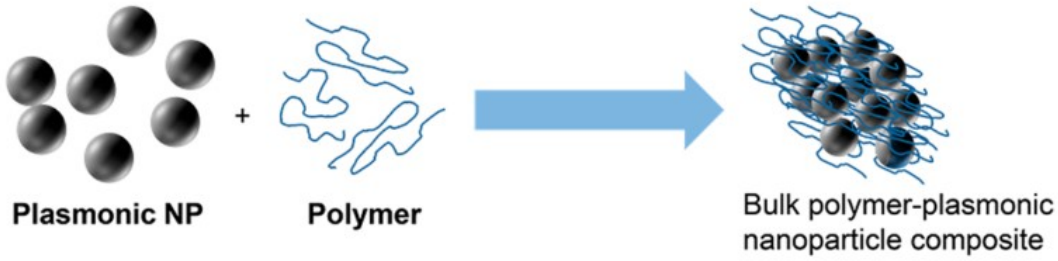

Figure 3.2: Schematic representation of the ex situ – wet chemical synthesis approach (also called nanoparticle-polymer blend approach). The metal nanoparticles are directly incorporated in the polymer matrix to create a Bulk MPN. A functionalisation of the nanoparticles may be necessary to avoid the formation of aggregates.

1. **In situ synthesis** of nanoparticles within the polymer generally occurs by reduction of a metal salt (often Ag or Au salts) that are preloaded into the matrix polymer or decomposition of a metal complex.

   Metal salt reduction can be achieved by thermolysis, irradiation with a high-energy source (e.g., electron beam, ion beam, or X-ray), or chemical reduction using agents.
   The size and shape of metal nanoparticles generated can be controlled by adjusting the reducing power (e.g., temperature or irradiation dose rate).

   A major disadvantage of in situ synthesis methods is that these techniques tend to produce nanoparticles that are largely polydisperse in both morphology and particle size.

2. **Nanoparticle–Polymer Blends**. This technique[42] overcomes the polydispersity challenge by incorporating already synthesized metal nanoparticles into a polymer matrix.

   The nanoparticles can be produced by chemical methods which guarantee a good control of particle size and shape, and then they are dispersed in a monomer solution to be polymerized afterwards. However[10], due to their high specific surface energies (500–2000 mJ/m^2 for inorganic materials and 20–50 mJ/m^2 for polymers), metal particles interact strongly and tend to aggregate fast. To avoid the formation of strongly connected agglomerates, nanoparticles need to be therefore functionalized with organic tails, which also tend to enhance solubility.

   The most important advantage of this procedure is a good control on the dimension, shape and distribution of the particles. Nanoparticles with a very narrow size distribution can

be produced and used to obtain sharper particle plasmon resonances. In addition to spheres, many shapes that can be fabricated including core/shell particles, rods and wires.

On the other hand, some constraints exist on particles concentration, since it might inhibit the polymerization process if its value is high. This is why the resistance of samples fabricated with this approach tends to be high. Moreover, many polymers degrade when interacting with the acids used during the nanocomposite fabrication, which narrows the possible choices of materials suitable to be synthetized with this procedure.

3.1.2 Vapor phase deposition

As described in reference [43,113], many vapor phase deposition techniques have been applied to prepare bulk metal–polymer nanocomposites. They are generally based on co- or tandem deposition of the metallic and organic components and formation of the metallic nanoparticles by self-organization.

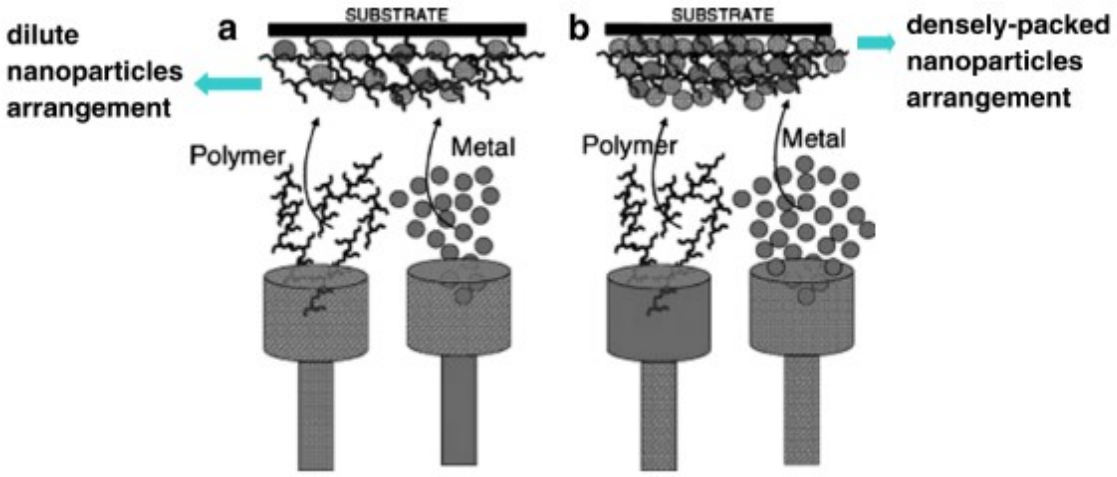

Figure 3.3: schematic representation of the co-evaporation or co-sputtering processes used to fabricate bulk metal – polymer nanocomposites.

More specifically, when energetic metal atoms impinge on the polymer surface they undergo various processes including random walk on the surface, diffusion into the bulk, or desorption. [39,114] Within their diffusion distance, metal atoms may collide or may be captured by a surface defect. This leads to aggregation and formation of stable metal clusters which are embedded into in the polymer matrix during the metal filling factor depends on the condensation coefficient of metal atoms on a given polymer surface as well as on the metal/polymer deposition ratio. The very easy control of the nanoparticle filling factor over the whole range from zero to unity is one big advantage of vapor phase deposition in addition to the good overall process control.

Moreover, controlled variation of the metal and polymer deposition rate ratio further allows preparation of nanocomposites with well-defined filling factor profiles and gradient layers. Vapor phase deposition also makes it easy to prepare nanocomposites with alloy particles. Depending on the specific technique, one can use alloy targets or additional deposition sources, for instance.

3.2 Assembled and interfacial polymer nanocomposites

In recent years, intense focus has been directed toward polymer nanocomposites that exhibit advanced optical functions by rationally engineering the organization of the filler in the matrix[42].

This generally requires a careful nanofabrication which can be achieved by following "top–down" and "bottom–up" methods.

Top–down approach corresponds to using nanofabrication tools that are controlled by external experimental parameters to create nanoscaled structures/ functional devices with the desired characteristics starting from larger dimensions and reducing them to the required values [113].

These are powerful and versatile, allowing to fabricate a wide range of structures with a good resolution. Some examples of top-down techniques are electron beam lithography (EBL) or imprint lithography, soft lithography and optical lithography. This in particular can be used over much larger areas compared to the previous ones, however, this approach is in general limited to simple periodic patterns[115].

In figure 3.4 some examples assembled nanocomposites prepared with this method.

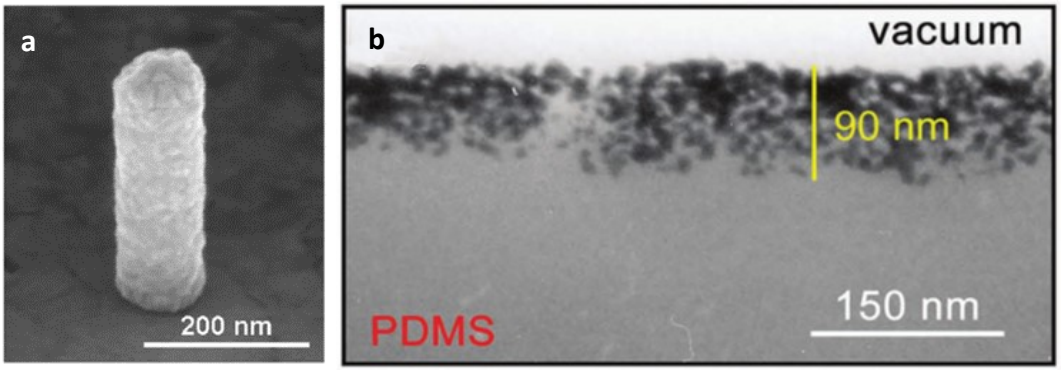

Figure 3.4: (a) Nanopillar prepared with electron beam lithography [from ref. 29 of reference [113]] (b) TEM images of cross-sections of Au/PDMS nanocomposite samples obtained with supersonic cluster beam implantation [61]

Top-down approaches are powerful to explore a wide range of structures with the advantage of excellent control and high resolution, down to ten nanometers, with good reproducibility[113,115]. However, they are expensive, limited in the sample size that can be produced, and slow.

Bottom–up approaches basically use atoms, clusters or small molecules as the building blocks of multi-level structures that perform various operations and are extremely promising since it minimize waste and unused materials[113].

Self-organizing functional systems and devices are the ultimate aim of bottom–up fabrication. Some challenges include the surface preparation and conditioning for the controlled deposition of the atoms, control of impurities and site uniformity, quality of the reactants, etc.

A particular kind of assembled polymer nanocomposite is represented by the so-called "2D nanocomposites". These consist in a thin layer of nanocomposite grown on the top of a polymer

matrix. They can be realized for instance by direct implantation of metal clusters or metal ions at the surface of the polymer matrix.

Supersonic cluster beam implantation is the technique which was used in this thesis to implant neutral cluster in the polymer matrix, fabricating 2D nanocomposites.

3.3 Supersonic cluster beam implantation

Supersonic cluster beam implantation (SCBI), is a technique which allows to produce MPN with excellent mechanical electrical and optical properties.

Metal clusters are produced in a source, and supersonically accelerated to a substrate. The clusters are neutral, and with an energy lower than 1eV/atom. This is enough to let the nanoparticle penetrate the polymer matrix avoiding charging and carbonization, thus, without damaging its mechanical properties. The beam is highly collimated and with a diameter in the centimetre range. This ensure both the possibility to realize patterned nanocomposite with the use of stencil masks, and the possibility so scale up with the fabrication of many devices.

With SCBI it is possible to implant particles without limitation in the filling factor and to control this value real-time during the sample fabrication. Differently from other vapour phase deposition approaches, there are no evidences of damaging of the sample mechanical properties, and the physical properties of the MPN are disentangled from its filling factor.

An example of assembled polymer is shown in figure 3.4b. This consists in a thin layer of nanocomposite at the top of the polymer matrix. These nanocomposites are particularly interesting for many reasons:

- Being the particle embedded at the surface of the polymer matrix, the mechanical properties of the composite are very close to the one of the polymer itself.
  This has a fundamental consequence: if an elastomeric matrix is chosen, its stretchability will be preserved despite the incorporation of the filler. Such assembled material may behave like responsive composites as the filler can be reorganized in a reversible way with a mechanical deformation.

- As the nanocomposite is concentrate in a small volume, if a proper fabrication technique is employed, a low amount of filler is necessary to reach a high volume fraction. This has the immediate advantage that the functional properties of the composite can be tuned in a wide range of values.

- 2D nanocomposites are generally fabricated by implanting the filler in the preformed polymer matrix; as a consequence, patterned structures can be easily fabricated simply using proper masks to preserve the polymer area which do not need to be functionalized with the particles.

3.3.1 Supersonic molecular beams

A focused beam of neutral molecules,[116] at a low enough pressure so that collisions between them can be neglected, is called a molecular beam. A typical apparatus which allows to obtain such beam is outlined in figure 3.5 It consists of two main chambers, kept at a different pressure, the only connection between which is a small hole called nozzle. The basic working principle is to let the

pressure gradient cause the gas in the high-pressure chamber to expand through the nozzle into the low-pressure chamber. Actually, the hole is commonly a more complex device, engineered to ensure the gas flow follows a desired path. There are two main conditions under which the expansion takes place: effusive expansion takes place if the nozzle diameter is smaller than the mean free path of the gas particles, otherwise the expansion is called supersonic.

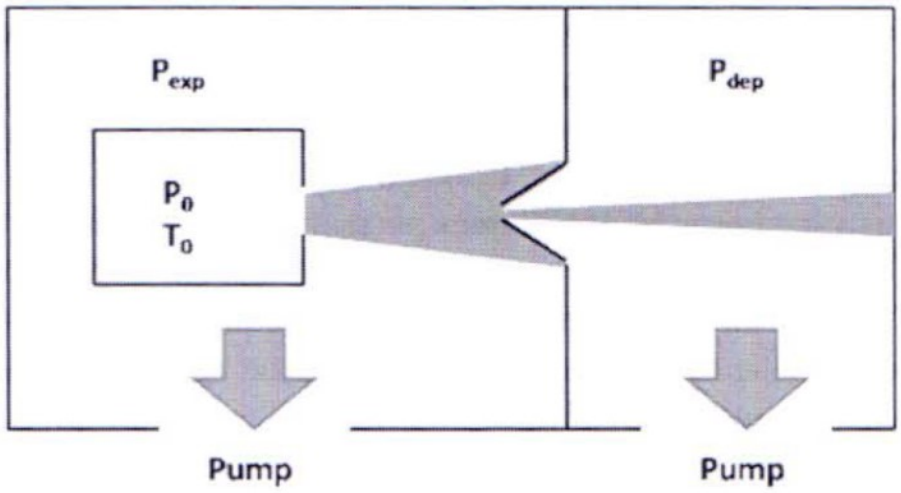

Fig. 3.5 Molecular beam source. The gas kept in a chamber at a pressure P_0 and temperature T_0 expands through the hole in the first chamber at a pressure P_{exp}, A conical collimator named 'skimmer' selects the central part of the beam which can enter a second chamber where the deposition occurs.

The parameter to be tuned in order to obtain one or the other kind of process is the mean free path of the particles, which in turn can be controlled by varying the pressure difference between the two chambers.

In particular, there is a critical value of the pressure of the second chamber, below which the supersonic regime is ensured:

$$P_c = P_0 \left(\frac{2}{\gamma + 1}\right)^{\frac{\gamma}{\gamma - 1}}$$

where P_0 is the pressure in the first chamber, and γ is the heat capacity ratio of the gas.

During the supersonic expansion, the chaotic thermal motion of the particles is converted in a one directional flux. The translational temperature, which determines the width of the speed distribution, decreases, while the average speed of the molecules rises.

The process being adiabatic, by imposing the conservation of energy it follows that the enthalpy per unit mass before the expansion is

$$h_0 = h(x) + \frac{v(x)^2}{2}$$

where h is the enthalpy after the expansion and v is the translational speed of the particles. This relation shows that during the expansion the enthalpy decreases so that the speed must rise. Furthermore, the translational temperature of an ideal gas obeys the following relation:

$$\frac{T}{T_0} = \left(1 + \frac{\gamma - 1}{2} M^2\right)^{-1}$$

being M the Mach number, i.e. the ratio between the local beam speed and the speed of sound, and T_0 the temperature of the source.

It can be noticed that departing from the nozzle, the speed, hence the Mach number, increases while the density, the temperature and the collision rate decrease.

When the beam properties cease to evolve, the transition from collisional regime to molecular regime is complete. The Mach number at the transition M_T can be evaluated by means of the following empiric relation:

$$M_T = A \left(\frac{P_0 d}{T_0}\right)^{0.4}$$

The constant A equals 47 for Helium and 90 for Argon, P_0 stands for the pressure in the source in Torricelli units, whereas d is the diameter of the nozzle in centimetres. the previous equations give rise to a new relation for the temperature at the transition point:

$$\frac{T_T}{T_0} = 3T_0/M_T^2$$

During the expansion the beam is isolated from the environment in which it evolves, so that it keeps its own thermodynamic properties until they match the ones of the surroundings forming a shock wave. This is orthogonal to the propagation axis and in known as the Mach disk. The distance from the nozzle at which this occurs depends on the nozzle diameter as well as the pressure P_{source} of the source and P_{exp} of the expansion chamber. The following empirical law applies:

$$\frac{x}{d} = 0.67 \cdot \sqrt{P_{source}/P_{exp}}$$

Finally, a conical skimmer is commonly used to select the central part of the beam, whose geometry is engineered to minimize perturbations of the beam dynamics.

3.3.2 Experimental apparatus and setup

The aim of this chapter is to outline in detail the apparatus used for the preparation of metal-polymer nanocomposites. The implantation process and the Pulsed Microplasma Cluster Source (PMCS) used to produce the metal clusters to be implanted in the polymer substrate will be discussed.

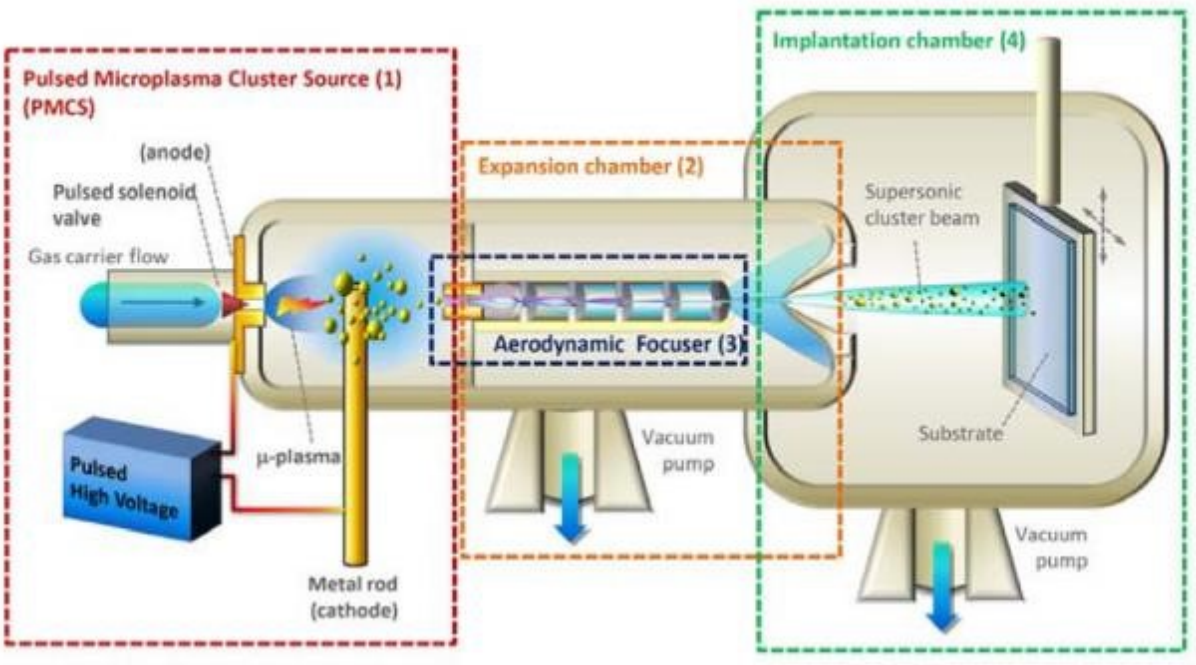

Figure 3.6: Schematic of the Multiline Apparatus for Nanocomposites.

In the present work, the synthesis of the metal-polymer nanocomposite materials has been achieved by means of Supersonic Cluster Beam Implantation (SCBI).
The apparatus for the SCBI synthesis features a remotely controlled manipulator allows for both rotating and translating the sample holder along any direction.

The main components of the apparatus are (figure 3.6):
1. PMCS cluster source
2. expansion chamber
3. aerodynamic focuser
4. implantation chamber

The synthesis process can be summarized in the following steps[117]: high-voltage electrical discharges form a noble gas plasma (He or Ar), which in turn sputters atoms from a gold rod. Atoms aggregate into clusters in the PMCS source. The mixture of nanoparticles suspended in the noble gas passes through an aerodynamic focuser and expands into the expansion chamber, kept at a pressure of about $7 \cdot 10^{-7}$ Torr by a turbo-molecular pump (the injection of gas rises the pressure in such chamber up to 10^{-3} Torr during the implantation).

The collimated beam coming out of the focuser expands at supersonic speed in the expansion chamber, where the supersonic cluster beam is intercepted by a *skimmer*, a cone with a hole in the summit, before entering the implantation chamber. Here, a turbomolecular pump with 0.5 m^3/s flow rate keeps the pressure at about $5 \cdot 10^{-5}$ Torr and removes the gas molecules from the beam while the metal clusters keep their trajectory. Note that the low-conductance skimmer allows to maintain a differential vacuum between the expansion and the implantation chamber, even if they are in principle connected to each other.

A pre-vacuum of about $7 \cdot 10^{-2}$ Torr is obtained via a *roots* pump both in the expansion and implantation chambers, while a *scroll* pump keeps the cluster source at a pressure of 7×10^{-2} Torr.

In the implantation chamber, the polymer used as substrate is placed on a sample holder, which intercepts the cluster beam. The metal nanoparticles, thanks to their kinetic energy, are hence implanted in the polymer matrix.

3.3.2.1 Pulsed Microplasma Cluster Source (PMCS)

Like most cluster sources, the working principle of PMCS consists of three stages[118]. First, the target material is vaporised, then the clusters mix with the gas with which they thermalize, and finally the mixture is expelled from the source.

During the synthesis, the metal rod changes its shape due to erosion, the dynamics of the gas change accordingly, and fluctuations in the intensity of the beam might cause a variability of the cluster size [118]. Despite the change in the target geometry PMCS exhibits a high stability, as well as a high beam intensity.

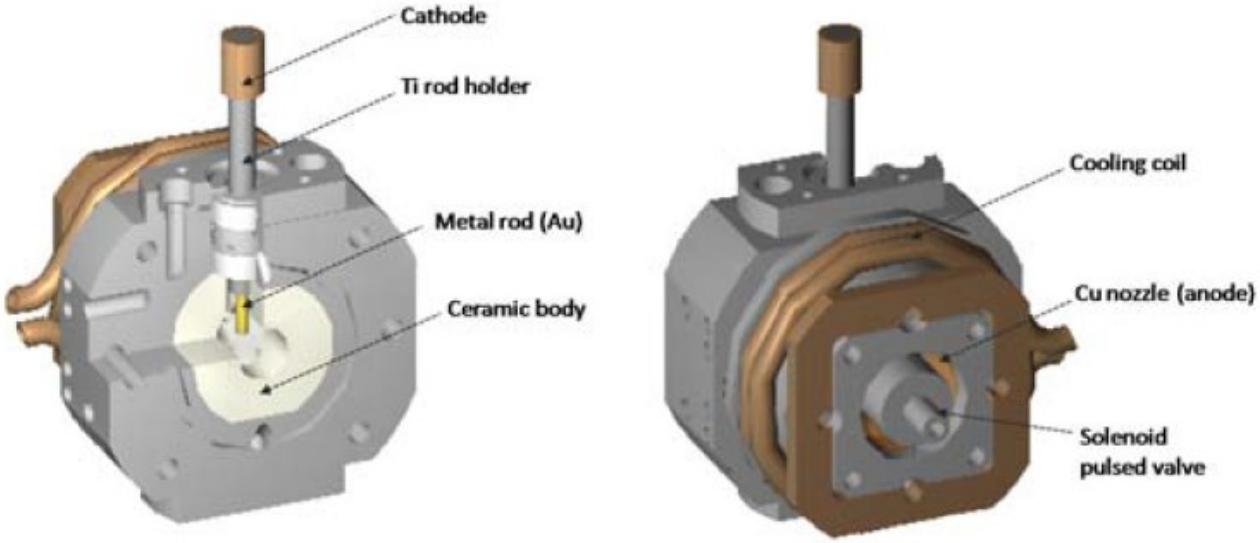

Figure 3.7: Front and back view of the PMCS cluster source. The section on the left shows the inside of the source ceramic body, where ablation and the formation of metal clusters take place. The discharge is applied between the metal rod, which acts as a cathode, and the copper plate. The gas enters the source though a nozzle. As shown on the right, the copper plate is placed between the solenoid valve and the ceramic body of the source.

The PMCS source consists of a hollow ceramic cylindrical shape, open on two sides. The metal rod to be sputtered is placed at the centre of the cylinder, orthogonal to its axis (figure 3.7).

An inert gas at high pressure (50 bar) is injected in the source through a pulsed valve at the entrance, whereas a low-conductance nozzle at the exit serves as a gateway to the expansion chamber. The cluster synthesis principle is as follows (figure 3.8 a): initially, the cavity is in vacuum ($\sim 10^{-4}$ mbar), and the inlet valve is open during 300 μs. The high-pressure noble gas enters the source and a small region, where both pressure and density are high is created [29] close to the metal rod

Subsequently, after about 700 μs, a 700-1000 V voltage is applied (figure 3.8 b) between the metal rod (cathode) and the copper nozzle (anode) during 100 μs. This electric potential difference ionizes the noble gas, so that and ions (He+ or Ar+) accelerated towards the cathode erode the rod by ion sputtering. The metal rod is kept in rotation by a stepper motor, which ensures homogeneous erosion around the central axis of the target.

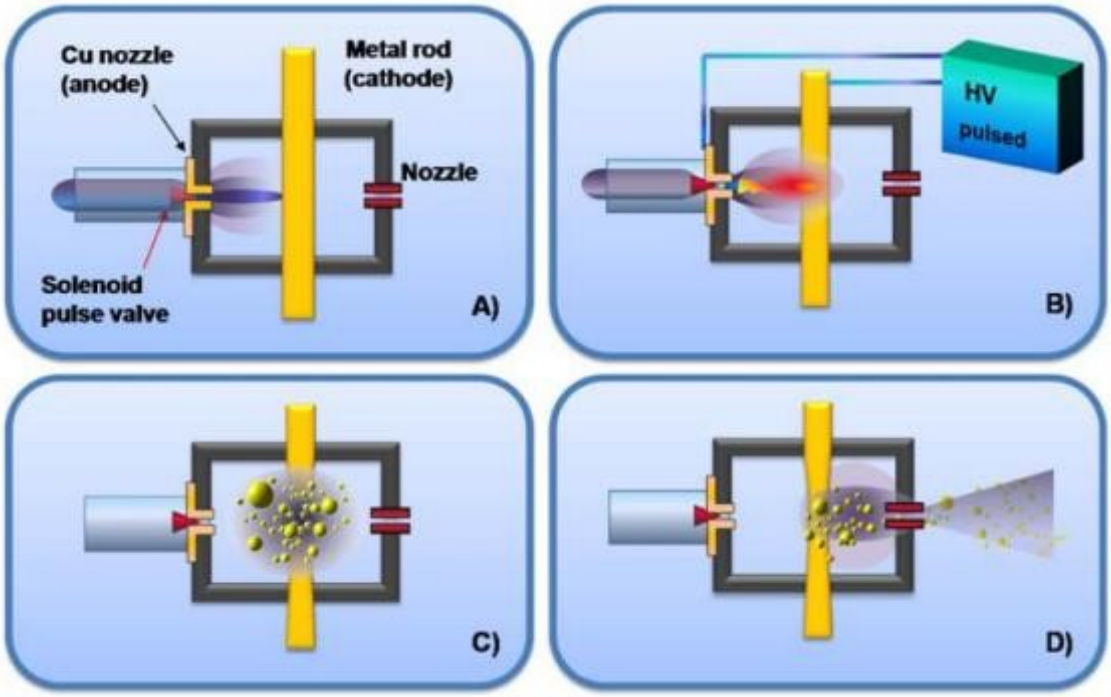

Figure 3.8: Pulsed Microplasma Cluster Source working principle. (a) The solenoid valve opens for about 300 µs and Ar gas enters the source at 40 bar. (b) A voltage ~750V is applied at the cathode, ionizing the gas. A plasma plume sputters the metal atoms of the rod. (c) The thermalized ablated metal atoms aggregate and form clusters. (d) Finally, the cluster-gas mixture exits the source via a supersonic expansion due to the pressure difference with the expansion chamber.

The erosion of the rod leads to the formation of an oversaturated gas of metal atoms (Figure 3.8 c). These condense into metal clusters suspended in the inert gas inside the ceramic cavity; their size generally ranges between 2 and 15 nm and is about 4 nm for Au.

3.3.2.2 Aerodynamic focuser

The aerodynamic focuser (see figure 3.9) consists of a series of metal disks with a central 2 mm diameter hole known as *aerodynamic lenses*, separated by small cylinders. The last lens has a smaller hole 1 mm in diameter. The mixture of gas and clusters is forced into the focuser by the pressure gradient: this procedure widens and narrows the gas flow lines (see figure 3.9 b) so the focuser also acts like a filter on the clusters mass [118,119].

The clusters and gas mixture escapes from the source through the nozzle (Figure 3.8 d), pushed by the pressure gradient between the source and the expansion chamber, and is accelerated up to a supersonic speed of about 500-1000 m/s [29]. The particles velocities are almost parallel to each other, so that collisions are drastically reduced. This stops the aggregation in the beam, so that clusters are able to reach the substrate without interacting after leaving the source.

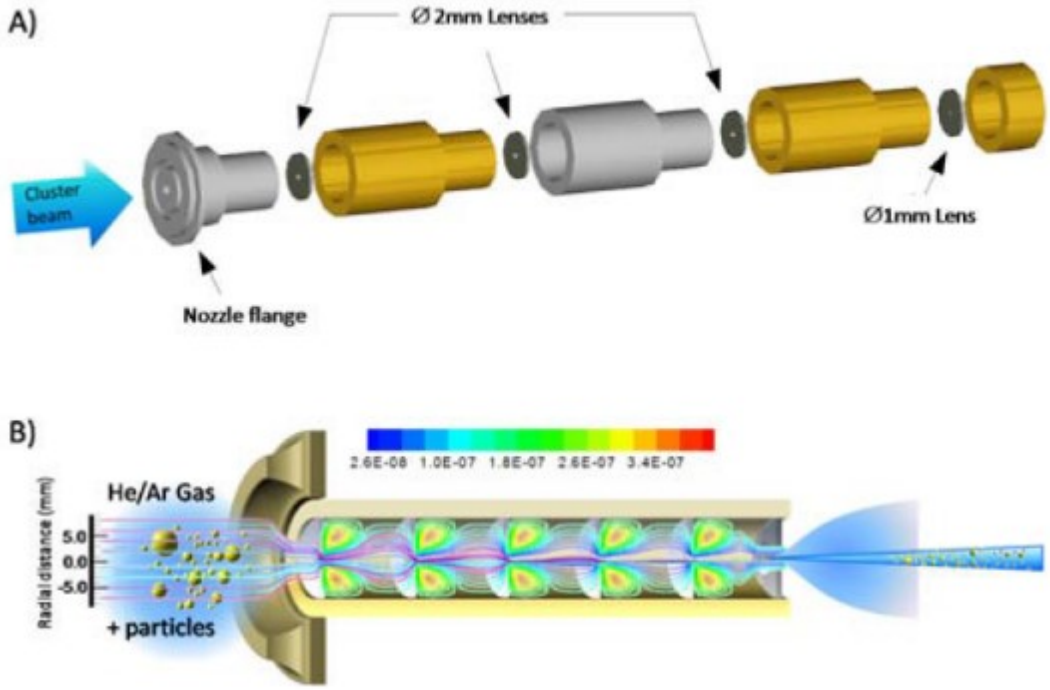

Figure 3.9: (a) Expanded view of the aerodynamic focuser. The diameters displayed refer to the hole diameters of the aerodynamic lenses. The cylinders that form the focuser are made of steel and brass and mounted alternately, in order to avoid the seizing of the threads. (b) Schematic representation of the aerodynamic focuser and its working principle.

3.3.2.3 Deposition apparatus

In the third chamber the beam is intercepted by a sample holder on which the substrates are placed.

The sample holder can be moved during the implantation by four automated manipulators: three of them allow to translate the sample holder along three orthogonal directions, x, y, z, while the fourth one can rotate the sample. This has two main advantages: on one hand, moving the manipulator during the sample fabrication (performing a ***rastering***) allows to homogeneously cover an area which is much wider than the cluster beam (see figure 3.10).

The sample holder has 6 faces, different substrate can be placed on each of them. Once the samples on one face are fabricated, the sample holder can be rotated by 60° in order to intercept the next face and the substrates placed on it. This allows to deposit a large number of samples keeping the apparatus under vacuum, hence saving a considerable amount of time.

In the centre of the holder, a quartz crystal **microbalance** is placed. This is fixed to the deposition chamber, so that when the sample rotates the microbalance remain in place. Its role is to monitor the amount of material deposited or implanted in the substrate. The values acquired by the microbalance are recorded by a LabVIEW program. The typical output is shown in figure 3.10, where we report the **deposition rate** and thickness of material deposited in time. The peak-shaped graph indicates the deposition was made rastering the sample holder so that the microbalance is intercepted at regular intervals, when the maximum deposition rates are recorded. At the same time, the amount of material deposited on the substrate (and on the microbalance) increases. The trend is roughly linear as the deposition rate is almost constant.

Supersonic cluster beams have the advantage to have a deposition rate which can be varied in a wide range of values. To tune this value, one can act on the position of the rod in the cavity, or on other parameters such as the pressure of the source chamber.

This is interesting for two main reasons: the possibility to tune the rate reaching high values, is extremely convenient when high amounts of particles need to be deposited without a specific cluster structure, for instance to make samples with a low resistance.

On the other hand, the deposition rate is a parameter which affects the growing of a nanostructured material. The possibility of controlling it over a wide range of values, allows to study how the growing mechanism changes and study also the interplay of the structural and functional properties of the nanostructured material.

With a SCB apparatus there are several ways to change the deposition rate. For instance, to increase it one can rise the pressure and amount of the gas injected in the source or the duration of the charge applied to sputter the rod. One can also act on the position of the rod in the cavity, the distance between its extremity and the inlet of the valve is able to cause a variation of the cluster deposited over two orders of magnitude. Another way of increasing the amount of deposited clusters consists in removing one or more focusing cavities or increasing the diameter of the focusing lenses. In doing so, one reduces the mass selection thus obtaining a more intense but less collimated beam.

However, if the goal is to compare the growing process of a nanostructured material varying the deposition rate, it is important to disentangle it from the structure of the cluster produced. For this reason, it is better to change the rate by changing the position of the metal rod in the cavity rather than the other parameters.

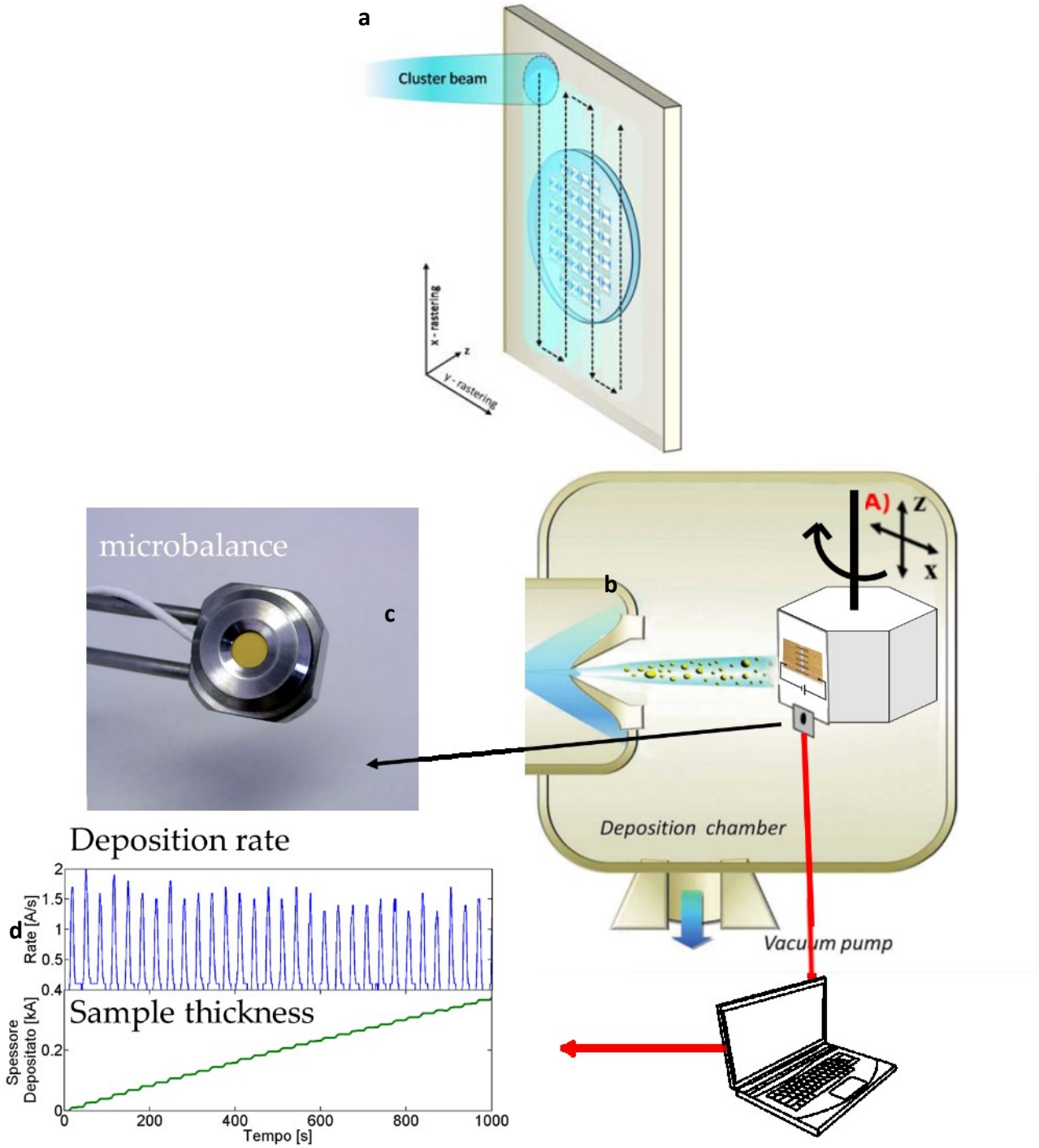

Figure 3.10: (a) Schematic representation of the rastering process: the cluster beam is intercepted by the sample holder, which can move along the reference axes x and y. The arrows indicate the path covered by the spot as the sample holder moves. The sample motion allows multiple overlap of metallic paths: the final result is the metallization of a large area of uniform thickness, the surrounding edges having a smooth thickness gradient. (b) Schematic representation of the deposition chamber equipment. (c) A microbalance intercepts the cluster beam while the sample holder is rastering allowing the measuring of the amount of material deposited. (d) A program records in real time the amount of particles deposited and the deposition rate and plots this values in a graph like the one shown.

3.3.3 Deposition and implantation

Supersonic cluster beam approach is particularly versatile for the fabrication of nanostructured material. This approach is suitable both for the production of cluster – assembled thin films and nanocomposite materials. To obtain one or the other, it is sufficient to change the mechanical properties of the substrate.

If clusters impact on a hard substrate, they will deposit on it forming a cluster-assembled thin film. If the particles reach a soft substrate, like a soft polymer, they penetrate it, forming a nanocomposite at the top of the polymeric matrix (figure 3.11 top).

Scanning the cluster assembled film with AFM we can observe the clusters forming a porous material. This is due to the fact that the clusters have a low energy per atom (less than 1 eV). In this regime (also called ballistic regime, the particles reach the substrate with a "**soft landing**", this avoids their destruction when they impact on the substrate.

A nanocomposite can be characterized with TEM, in order to view its cross section. In such a way it is possible to measure the penetration depth, the clusters mean size and have an idea of their reciprocal distances. For instance, in the case shown in figure 3.11a, we can see this is an assembled interfacial nanocomposite, it is possible to estimate its thickness is about 90 nm; the nanoparticles have a spherical shape.

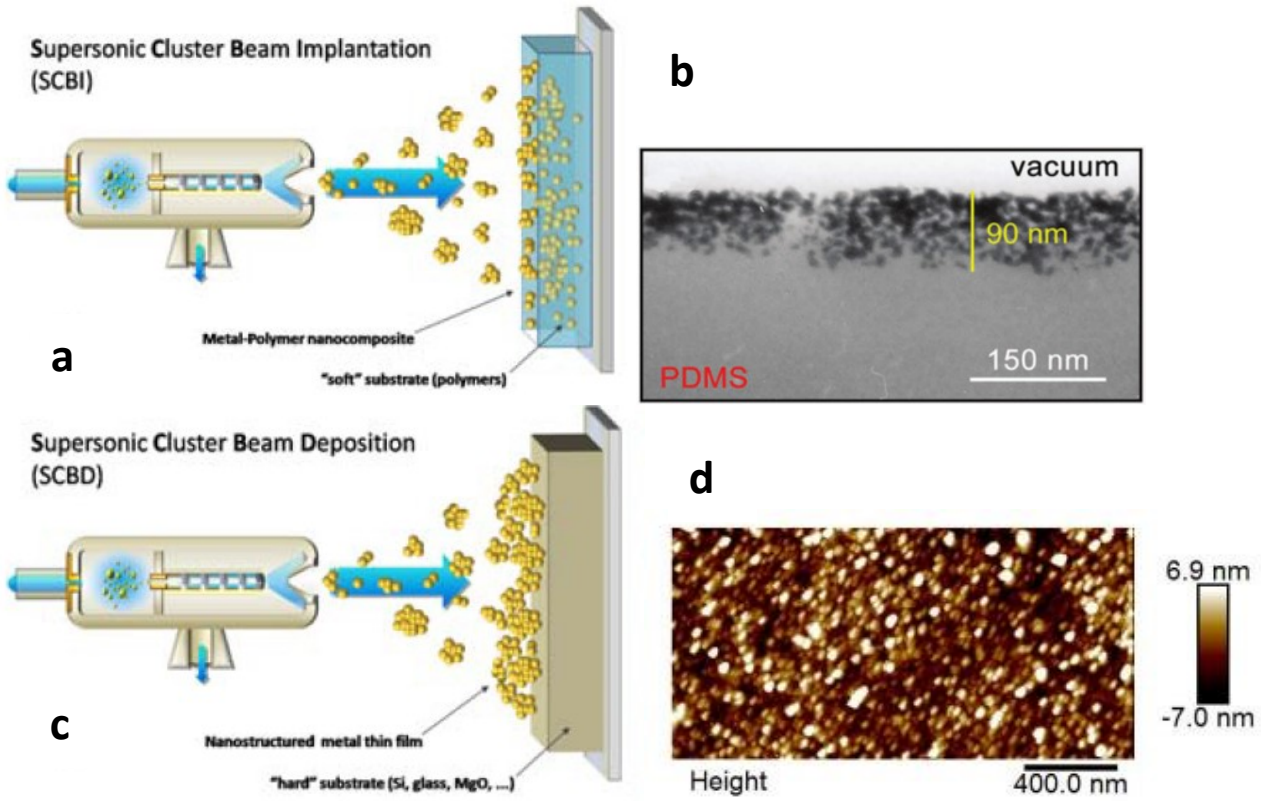

Figure 3.11. (a,b) Supersonic Cluster Beam Implantation on a soft polymeric substrate. Particles are able to penetrate the substrate up to about 200 nm and a metal-polymer nanocomposite is formed at the surface of the polymer matrix. (c,d) Supersonic Cluster Beam Deposition on a hard, impenetrable substrate such as glass or silicon. In this case, clusters pile up on the surface giving rise to a porous nanostructured film.

3.3.3.1 Cluster beam main properties

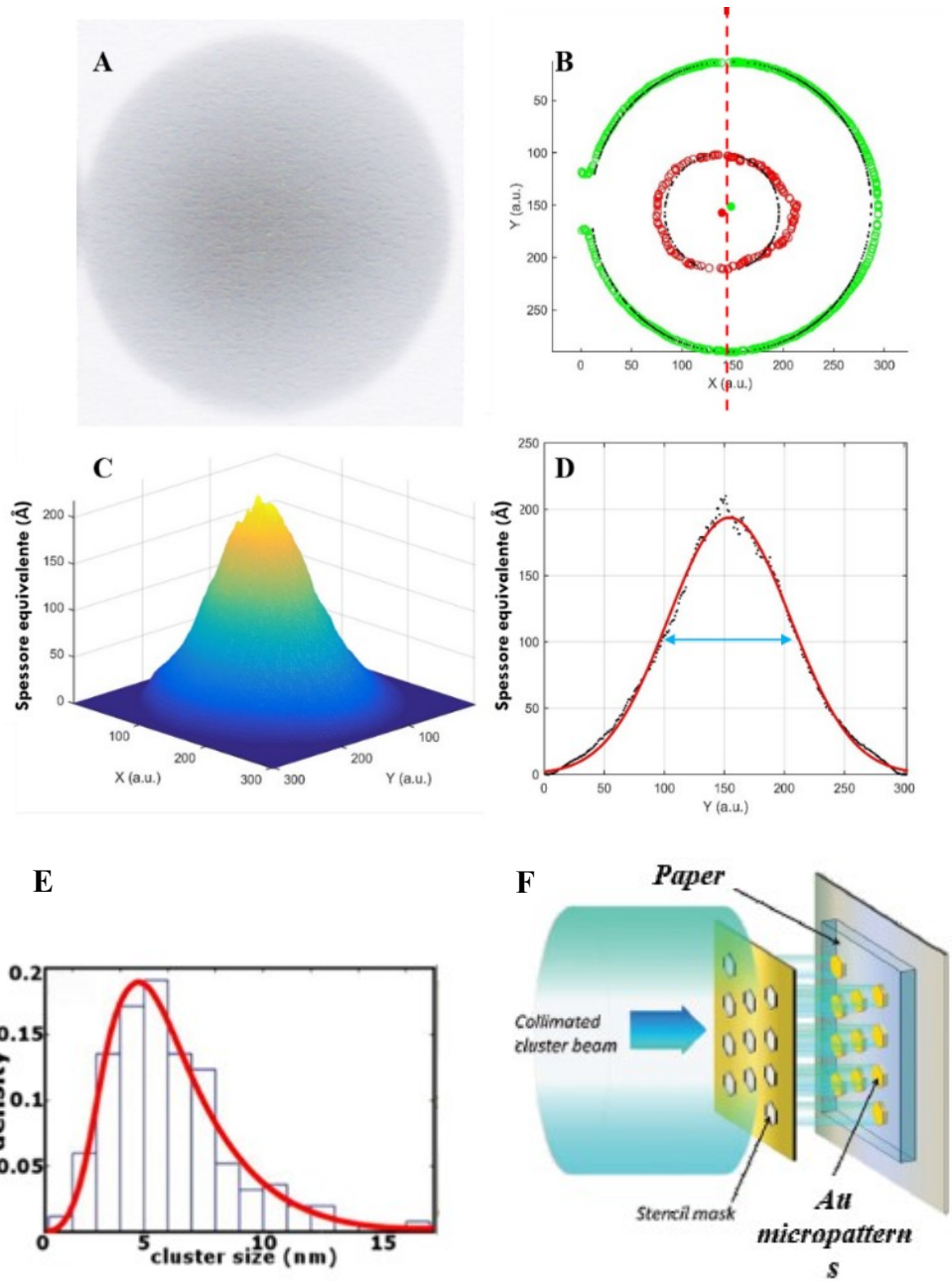

Figure 3.12: (a) cluster beam profile (b) 2D reconstruction of the spot profile; (c) 3D reconstruction of the spot profile (d) reconstruction with a profilometer of the spot thickness profile. (e) Cluster size distribution measured with AFM on a sub-monolayer gold system. (f) use of a stencil mask to produce patterned samples. [61]

Cluster beam profile. The area of the cluster beam is a circular spot having a diameter of 3÷4 cm. the beam profile is gaussian; its profile can be characterized, with an AFM or profilometer by depositing a certain amount of material on a silicon wafer partially masked and measuring the thickness obtained at different distances from the centre. The typical output is shown in figure 3.12.

During the focalization procedure, which consists in the alignment of the focuser with the skimmer, an analysis real time of the spot produced is particularly useful. To this goal, a camera is placed in front of the sample holder; the face used to align the beam is covered with blank paper.

Once the beam intercepts the paper, a well-visible spot is formed (figure 3.12a). The image acquired by the camera can be captured and analysed with a Matlab routine which allows to see the 3D reconstruction of the spot (figure 3.12c), and the 2D one (figure 3.12b), where an outer circle indicates the spot boundary, and an inner one indicates the darker region of the spot, corresponding to a larger amount of particle deposited. This is the peak of the gaussian beam (figure 3.12d) which exit from the focuser, while the whole spot corresponds to the portion of this gaussian intercepted by the skimmer.

The two circles are concentric if the focuser and skimmer are well aligned, if this is not the case, one or both of them should be moved with the micrometric screws, in order to make the circles concentric.

A further property of the supersonic cluster beam is its high collimation. Being its divergence is lower than 1°, stencil masks can be used to make **patterned samples** (see figure 3.12f). This is very convenient as this approach is much simpler than using photolithographic techniques which are often required to avoid the typical shadowing effect which occurs with highly divergent beams.

This chamber is also equipped with two cameras which allows to watch the samples during their fabrication under two different points of view; this is particularly useful for determining the area to raster, and as we will see in next section, during the focalization and alignment of the cluster beam.

A parameter which strongly affects the functional properties of the nanostructured material is its amount of particles.

To calculate it in the case of a cluster - assembled film, one can simply scratch it, or make a step by covering a part of the sample before its deposition and then measure its high after deposition.

If particles are embedded to form a nanocomposite, another rout should be followed to have an estimation of this quantity. A possible one consists in placing a silicon substrate, half covered, close to the polymeric one, which intercepts the same amount of material intercepted by the polymer.

Once the sample fabrication is completed the mask can be removed, and the thickness of the film grown on the hard substrate can be measured with AFM. This measure provides the nanocomposite **equivalent thickness** t_{eq}.

A further parameter which is important to describe the properties of a nanocomposite is its **volume fraction** (VF). This is defined as the ratio between the total volume of the metal clusters (the filler) and the volume of polymer, in which the clusters are implanted[61]. Considering a nanocomposite homogeneously filled, this corresponds to the ratio between the equivalent thickness of the implanted nanoparticles and the thickness of the nanocomposite layer (the nanoparticle implantation depth).

This latter is obtained by characterising the cross section of the nanocomposite with a transmission electron microscopy (TEM), while the equivalent thickness is obtained as jus described. For example, in the case shown in figure 3.11, the equivalent thickness and the nanocomposite one are 29 and 150±12 nm respectively; from these values a volume fraction of $2.5 \cdot 10^{-3}$ is obtained.

3.3.3.2 Substrates

Different substrates can be used for supersonic cluster beam deposition or implantation. The one mainly used in this work are Glass, Silicon, PDMS and paper.

Glass/Silicon

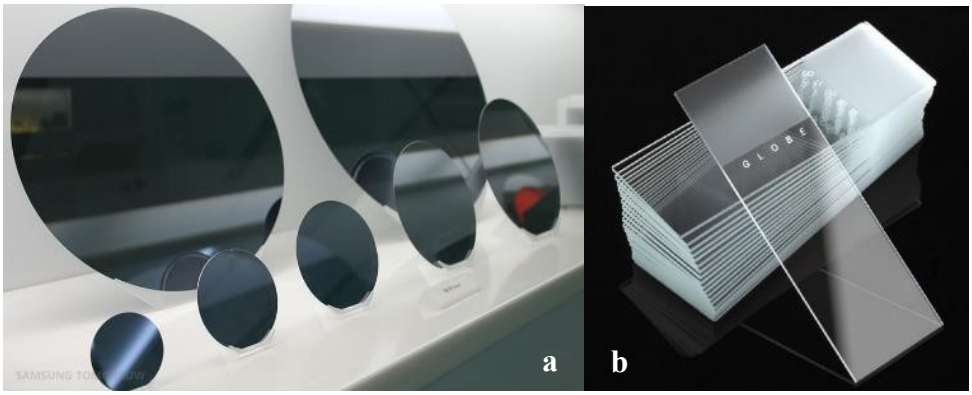

Figure 3.13: (a) silicon wafers with different dimensions [120] *(b) example of glass microscope slides* [121]

Glass and Silicon are hard substrate. The glass used in this work is in the form of microscope slide: a thin flat piece of glass, typically 75 by 26 mm and about 1 mm thick, used to hold objects for examination under a microscope. Microscope slides are usually made of optical quality glass, such as soda lime glass or borosilicate glass. The surface roughness (the standard height deviation of a surface) of the glass substrates used in this thesis was measured by AFM to be 0.35 nm.

Pieces of silicon wafers were also used as a substrate for cluster deposition. Silicon wafer are formed by highly pure, nearly defect-free single crystalline material. This results in a very low roughness which is typically < 1 nm which corresponds to a smoothness on atomic scale[122].

Polydimethylsiloxane (PDMS)

Polydimethylsiloxane (PDMS) is a very common silicon elastomer, which has found applications in biomedical and microfluidic devices, prostheses and stretchable electronics.

The general formula of its chain is $CH_3((CH_3)_2\ SiO)_nCH_3$; it is a silicone based polymer characterized by a backbone of many Si-O bonds (figure 3.13), to which the organic functional groups are linked. Every silicon atom is linked with two oxygen atoms and two methyl groups CH_3 .

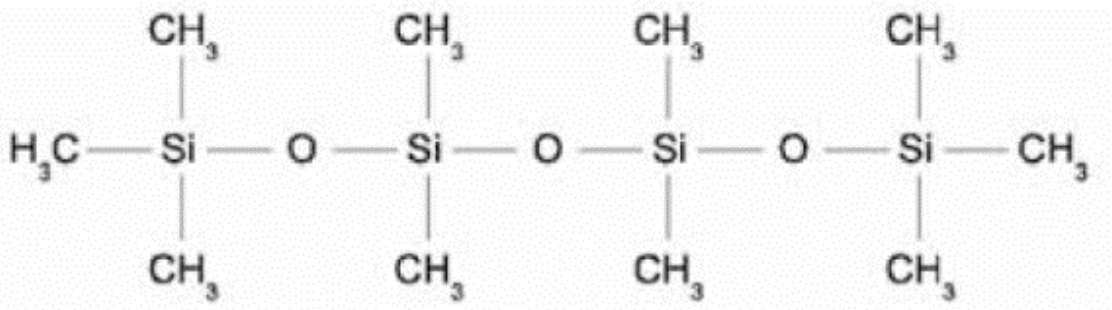

Figure 3.14: Two-dimensional representation of a dimethylsiloxane (PDMS) short chain.

PDMS is an interesting polymer for applications thanks to its biocompatibility and chemical safety. Being transparent in the visible range, it is suitable for application in optics. It is cheap relative to other equivalent polymers, and it can be easily fabricated using standard molding protocols. Some other properties include:

- Biocompatibility: PDMS is not harmful for the human organism and it is commonly used as biocompatible material in the production of implants and biomedical devices.
- Solvent compatible: the PDMS does not degrade with most chemical solvents [123]. Interaction of PDMS with many chemical solvents usually leads to the absorption of the latter and to the swelling of the PDMS. On the other hand, PDMS tends to degrade completely when attacked by KOH, HNO3, HF, H2SO4.
- Hydrophobicity: PDMS exhibits high hydrophobicity [123], its wettability contact angles are more than 100 with water drops or organic solvents. If needed, the surface of PDMS can be temporarily made hydrophilic by an oxygen plasma treatment [123].
- Good dielectric behaviour: as reported in the Sylgard datasheet, PDMS used in this work is a good insulator, which can stand up to 14 kV/mm, and its dielectric constant is loosely dependent on frequency (2.72 at 100 Hz and 2.68 at 100 kHz).

Depending on the degree of crosslinking obtained from the mixing of the base and curing agents, it is possible to tune its stiffness, adhesion and hydrophobicity. PDMS can thus be a fluid, gel or elastomer while still retaining its chemical composition.

It is a fluid if the crosslinking is very short and very short linear chains are formed which are not bonded between each other. Increasing the chain length also the viscosity of the fluid increases. This is usually used as silicone lubricants. Alternatively, very little cross-linked polymers produce a gel when mixed with PDMS fluids. Finally, increased degree of cross-linking makes PDMS an elastomer, in which chains are entangled. The product is a very flexible and stretchable solid, having generally a Young's modulus of about 7.5×10^5 Pa. Further increasing the degree of crosslinking produces a more rigid elastic silicone, with a higher Young's modulus.

Like many other polymers, PDMS can have its chains arranged in two limiting cases: in a crystalline form, if the chains follow a lattice pattern, or in an amorphous form, if the chains or networks are arranged in a disordered manner. The stiffness of the elastomer is higher if the crystalline order prevails on the amorphous one. A higher degree of crosslinking leads to the formation of wider lattices and therefore to a much more ordered arrangement of the chains. Similarly, since PDMS can also exist in a fluid form, crystallinity increases the fluid viscosity, the polymer chains being longer. The crystallinity degree of the polymer is strongly dependent on the temperature at which the polymer is formed: high temperatures cause a higher disorder of the chains.

There are two main parameters which determine this behaviour: the melting temperature *Tm* and the glass transition temperature *Tg*, usually lower than *Tm*. The melting temperature is the temperature above which the polymer chains in the crystalline state break and form a disordered liquid. On the other hand, below the glass transition temperature, the polymer chains in the amorphous state are unable to move, while above this temperature, the polymer chains gain a greater mobility and can slide past each other. This means that if a force is applied to a polymer below *Tg*, it will tend to break due to its stiffness instead of being deformed.

The glass transition temperature of PDMS is about -120°C [124], which is much lower than other standard polymers, so that a deformable elastomer is obtained at room temperature.

Paper

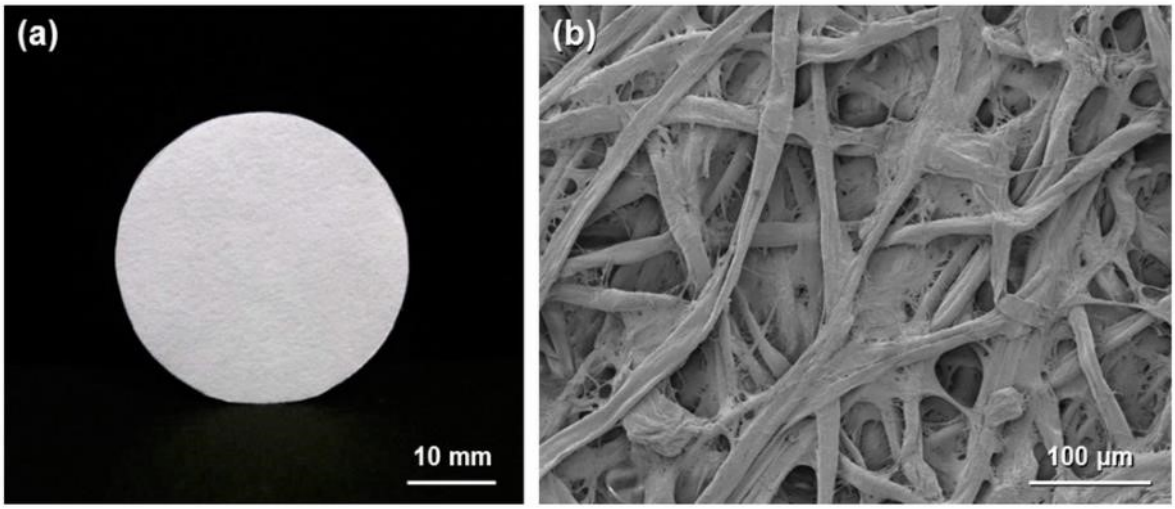

Figure 3.15: Image of paper at low magnification (a) and high magnification (b). From reference [125]

Paper is a fibrous material based on cellulose, an organic compound which in turn is composed of D-glucose linear chains, hence a polysaccharide.

Its uses range from personal stationery to industrial and architectural applications. It is commonly obtained from pressed vegetal fibers, which make a poorly conductive and hygroscopic material, whose density is around 0.9 g/cm3. It is often found as thin sheets 80 to 150 grams per square meter. The paper used in this work is commercial plain white paper for ink-jet and laser printer (Xerox Digital, 75 g/m2, roughness: 170 ml/min). It is composed of interwoven fibers with different lengths and with diameters in the range ~ 1- 20 µm.

3.3.4 Sample fabrication

3.3.4.1 Plasmonic nanocomposites (PNC)

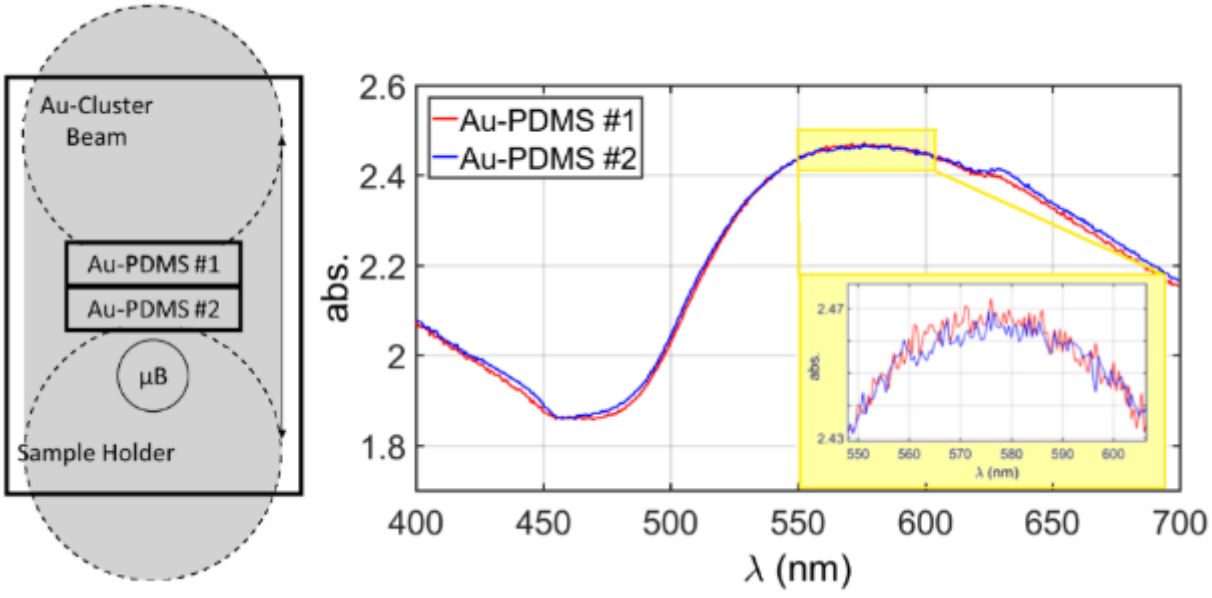

Figure 3.16: left: schematic representation of the fabrication of MPN. During the cluster implantation the sample holder moves up and down to cover homogeneously the substrates to be implanted. Right: to check the degree of homogeneity of the samples produced their absorption spectra are compared. From reference [126]

The metal – polymer nanocomposites fabricated to study the evolution of the optical and electrical properties in response to uniaxial stretching were prepared as follows.

PDMS membranes with a thickness of about 60 μm are fabricated by spin coating the polymer on a substrate for 60 s at 800 rpm; the polymerization is performed with a 60 min annealing at 100 °C.

Gold nanoparticles were implanted in the polymer with SCBI. During cluster implantation, the holder displaces the substrate in the two directions orthogonal to the cluster beam axis, allowing the parallel fabrication of multiple samples with an area of 2 cm^2.

The choice of gold for the clusters was primarily motivated by the fact that its plasmonic absorption follows in the visible range, and because of its higher stability to oxidation compared to silver for example.

The evolution of the optical properties in response to uniaxial stretching was first studied for different nanocomposite volume fraction. To this goal, samples were fabricated with an equivalent thickness in the range 120-320 nm.

An image of the PDMS substrate before and after the implantation are shown in figure.

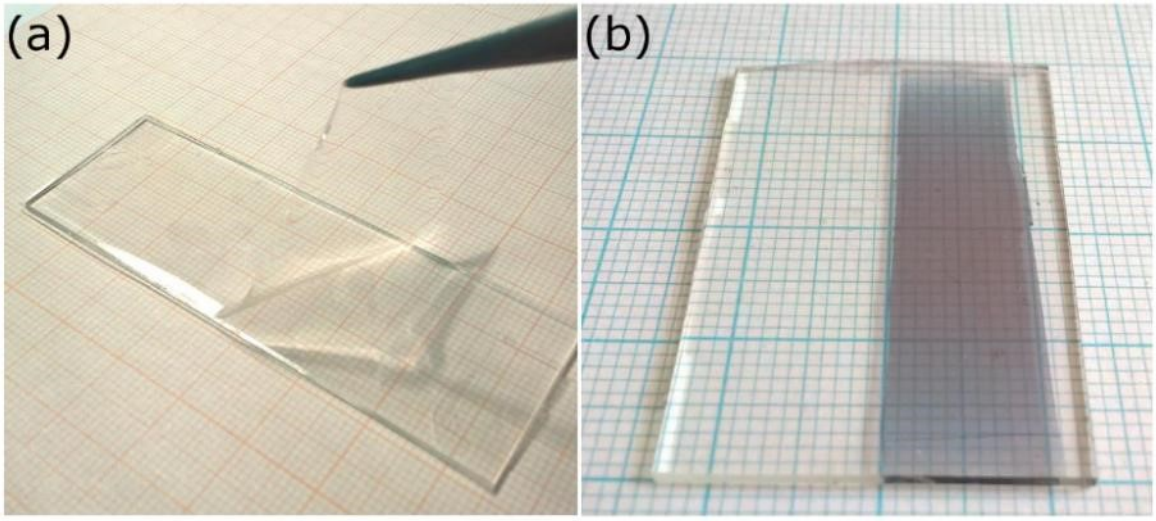

Figure 3.17: PDMS substrates before (a) and after (b) the implantation of gold nanoparticles.

A further study regards how the optical and electrical properties of the nanocomposite are coupled and change in response to the uniaxial stretching. For this experiment, the sample volume fraction is fixed to a value of ~30%.

A technical point which need to be addressed is how to record the resistance of the sample while this is undergoing a mechanical deformation, avoiding a damaging of the nanocomposite. This requires using specific soft interconnections to make an electrical contact with the nanocomposite, without damaging it.

This was done in two different ways for the measurements in the stretching direction and in the transversal one. In the first case, some conductive rubber was prepared mixing together PDMS and

silver micrometric powder. This conductive rubber is let polymerize with a copper wire in it and then clamped to the sample.

In the opposite direction, a two steps approach is followed. First two contacts are electroless plated directly at the sample extremities. This allowed to create a thick conductive layer which overlap the nanocomposite, then the resistance is measured directly on the plated contacts.

Thanks to these connections, it was possible to study simultaneously both the optical absorption and the electrical resistance of the PNC undergoing uniaxial deformation.

3.3.4.2 Soft Gratings (SG)

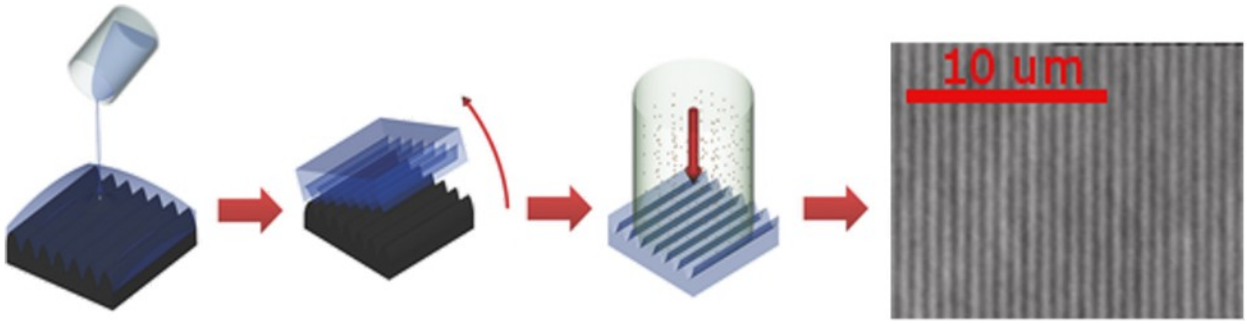

Figure 3.18: schematic representation of the step to produce a reflective elastomeric grating. Adapted from reference [48,127].

Soft gratings for adaptive optical applications are fabricated as schematized in the figure 3.18. PDMS is prepared as described in section and poured on a master grating (step 1). Once the PDMS polymerizes, it can be detached by the master (step 2). To make the sample reflecting, metal nanoparticles are embedded in the transparent grating with SCBI (step 3). With an optical microscope it is possible to check how good is the transfer of the master to the PDMS and eventually choose the best region obtained. The typical result is shown in step 4.

To provide a focusing power to the diffracting grating, this is stuck to a concave surface carefully prepared to optimize its adhesion to the grating.

The experimental methods developed to do this study regard:

i. The choice of a proper master and the development of a recipe to obtain a PDMS grating from it.
ii. The fabrication of a proper concave surface able to optimize the light focusing;
iii. The choice of the metal to make the grating reflective and amount of particle to embedded to have a good reflectivity.

Grating master: as a master, plastic gratings in the format of a roll were chosen; the groove density is 1000 grooves/mm. These gratings are very cheap and easy to use. Moreover, the bonding of PDMS with plastic is much lower than with a common silicon, favouring the detachment after polymerization. To prevent a damaging of the master due to exposure to high temperature, the PDMS was let polymerize at room temperature for 48h rather than in an oven for a shorter time.

Grating metallization: The transparent PDMS gratings were then made reflective by implanting gold nanoparticles using a SCBI apparatus. We chose gold because the interest was to optimize the

system for the infrared light and gold has a good reflectivity in this region compared to other noble metals. Moreover, this material has a good stability in terms of oxidation compared to silver for example whose reflectivity is dramatically affected.

We metallized PDMS gratings with an equivalent thickness of approximately 40 nm, at a deposition rate of about 0.08 Å × s^{-1}. This value chosen in order to maximize the sample reflection and is the result of a characterization of the dependence of the absorption and reflectivity on the nanocomposite filling factor. Broadly, if the amount of particles embedded is low, the sample is almost transparent, thus poorly reflecting; by increasing the amount of particles, the sample reflectivity increases but at the same time its absorbance. Above a certain threshold ($T_{threshold}$), the sample absorption dominates, and the sample turns back to have a poor reflectivity.

To find the best amount of particle to implant, several mirrors were produced by implanting different amount of particles in PDMS flat substrates, and rastering only in the vertical direction. Then, the intensity of each sample is measured with a laser He-Ne and a camera with no lenses.

To have a more precise information, the sample are scanned in the direction perpendicular to the one of the rastering (red arrow in figure 1) acquiring 5 images every 0.5 mm, the overall scanned area is ~ 14 mm large. This is done because, the cluster beam has a gaussian profile (see figures 3.12) hence, rastering only on the vertical direction, the cluster amount will be higher in the central area and lower at the boundaries.

Two different trends of the reflectivity versus x were found according to the amount of particles embedded. Figure 3.19 shows the results obtained for two sample with a significantly different amount of particles:

As expected from what said before, if the cluster amount is lower than $T_{threshold}$, the mirror is more reflecting at the centre (red curve); while above the threshold the trend is the opposite and the sample become more reflecting at the periphery (blue curve).

Comparing the overall reflectivity of the samples higher values were found for the samples with an equivalent thickness of ~40 nm.

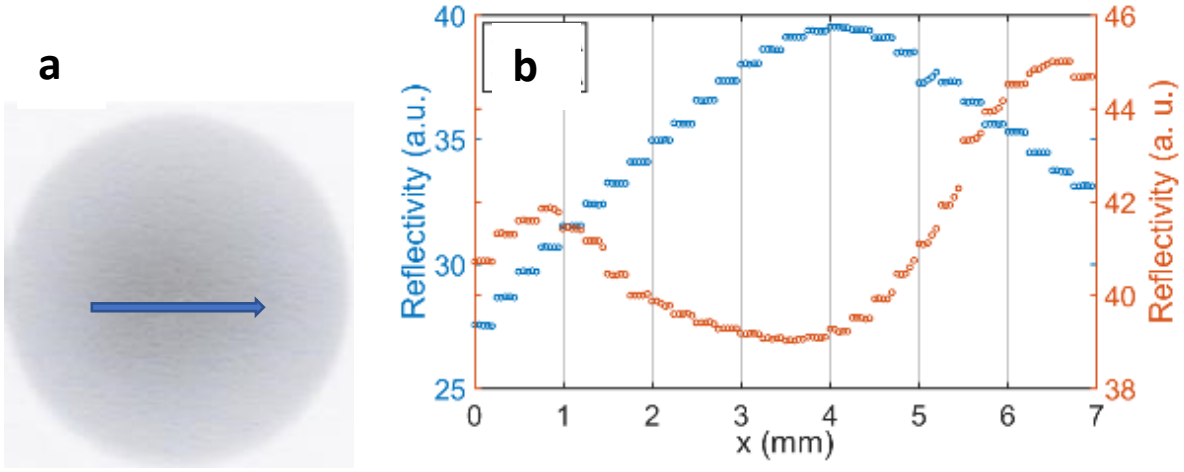

Figure 3.19: (a) schematic representation of the scanning direction (blue arrow) (b) scan of the reflectivity for two samples with different amount of particles embedded in the polymer matrix. The starting point is slightly different from sample to sample.

Focusing surface: Several geometries were tested to optimize the focusing power of the diffracting grating. the first choice was a spherical one. This was fabricated by turning a brass rod on a lathe. Surfaces differently polished were tested to maximise the adhesion of the grating to the focusing surface. High polishing ensured the best results.

This spherical surface provided good results both for the spatial and spectral resolution, in order to increase the special resolution an ellipsoid of revolution was adopted. The two-foci of the ellipsoid allow to directly conjugate the plane in which the object lies with the sensor with tunable magnification. This allows to use no other optical element besides the grating and the surface, and reduces the aberration of the system

3.3.4.3 Samples for electrical characterizations

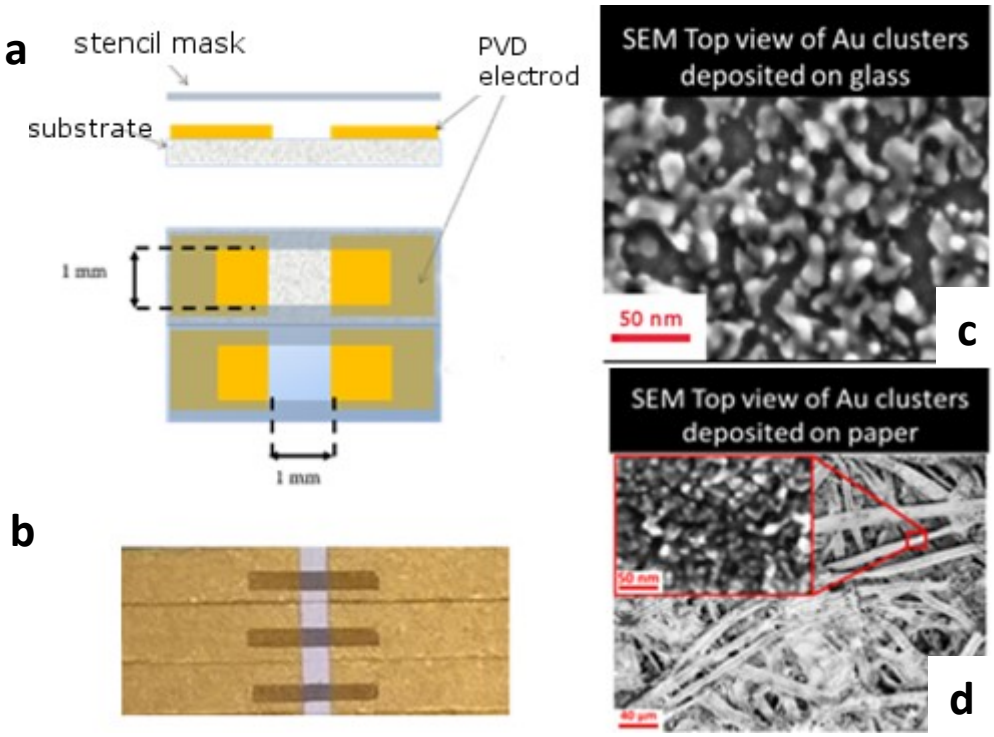

Figure 3.20: (a) schematic representation of the sample used to acquire a percolation curve. First contacts are deposited on the substrate with PVD, at a distance of 1mm. Then a stencil mask is placed in contact to it partially overlapping the contacts. Some contacting wires are placed between the sample and the stencil mask, well adherent to the sample, in order to require the current flowing through the sample during its fabrication. (b) The typical sample produced in the case of gold clusters deposited on paper. (c) Top view of gold clusters deposited on a hard substrate. (d) Top view of gold clusters deposited on paper substrate. At high magnification we can see the clusters, at low magnification, we see the fibrous structure of the paper. Both (c) and (d) are acquired with Scanning Electron Microscope (SEM)

The goal of the exploration of the electrical properties of nanostructured material fabricated with SCB is mainly to verify if resistance switching phenomena could be observed in these systems, characterize the mechanism and understand how to control it. However, to do this, it is first necessary to understand under which fabrication and characterization conditions the samples could exhibit these phenomena.

This possibility was explored in systems grown in different conditions. The main parameters which were varied to study their effect on the growing mechanism and switching activity are the

substrate, the **deposition rate** and the **amount of particle** deposited. All the characterizations were done using gold clusters

For a potential matching of the switching properties of the cluster network with its optical one the interest was mainly in the noble metals. Among them silver is well known for its fast switching activity and also for its tendency to oxidize quickly, which could be an interesting process to examine. However, we decided to use gold to reduce this oxidation which would have been difficult to characterize and control.

To determine which parameters optimized the switching activity several samples were fabricated in different conditions. Their percolation curve is used as a probe to understand how these parameters affect the system.

To this goal samples were fabricated as schematized in figure 3.20 a. Gold PVD contacts are first deposited on the substrate at a distance of 1 mm; the sample is then covered with a stencil mask which covers all its surface but a strip 1 mm high and 10 mm long, partially overlapping the contacts.

A pair of contacts are fixed to the PVD electrodes. These electrodes are made by paper evaporated with gold till a resistance <5 Ohm is reached (as described before). The contacted sample is placed into the deposition/implantation chamber; once the cluster beam is activated, the sample holder can raster in the vertical direction in order to cover more than one sample per face.

Substrates: different substrates were tested, as different growing mechanism are expected according to the substrate of choice and because of the specific advantage they offer. PDMS as an elastomer is appealing in view of using mechanical deformation (uniaxial stretching for instance) to change the interparticle gaps. However, once the sample is fabricated in response to voltage applications the resistance started drifting to values which were some orders of magnitude lower and the sample exhibit only very few switching events. PMMA and glass were both tested and showed a similar switching activity. Finally, because of its smoothness, silicon substrates were used to make a comparison.

Deposition rate: to test this parameter many samples were realized either fixing its thickness or its final resistance and varying the deposition rate. The switching activity of this samples was characterized, and a favourable deposition rate found.

Amount of cluster: for determining the right amount of cluster to deposit a range of sample fabricated with the same rate and different thicknesses were prepared and their switching activity characterized.

4 Metal-polymer nanocomposite characterization

4.1 Morphological characterisation

4.1.1 TEM characterization

To characterize the cross section of the gold-PDMS nanocomposites, I used a Transmission Electron Microscope (TEM). To this purpose first the nanocomposite needs to be cut in thin lamellae. The lamellae must be very thin because the 50 to 125 kV electrons of the standard electron microscope cannot pass through biological material much thicker than 150 nm. To do this I used crio-ultramicrotomy method.

Ultramicrotomy is a method for cutting specimens into extremely thin slices, with a thickness between 30-100 nm, that can be studied in a transmission electron microscope (TEM) figure 4.1a. This method is used mostly for biological specimens, but sections of polymers and soft metal-polymer nanocomposite can also be prepared. The ultramicrotome (figure 4.1b) is fitted with either a diamond knife, or a glass knife, often used for initial cuts. The thin lamellae obtained with the ultramicrotome, are left floating on water that is held in a boat of the knife (see figure 4.1 c). The sections are then retrieved from the water surface (figure 4.1e) with a handmade tool consisting of a hair stuck at the extremity of a wood stick and mounted on a copper grid covered with a Formard, to be imaged with TEM.

Due to the mechanical properties of the nanocomposite, before cutting it, it is necessary to freeze the sample. To do that, a ultramicrotome equipped with a cryogen chamber was used. This allows to freeze the soft nanocomposite (at -60°C) making it hard enough to be cut. The typical results obtained with SCBI nanocomposite are shown in figure 3.11.

These images were quantitatively analysed with ImageJ to quantify the nanocomposite thickness, cluster dimension and estimate the interparticle gaps.

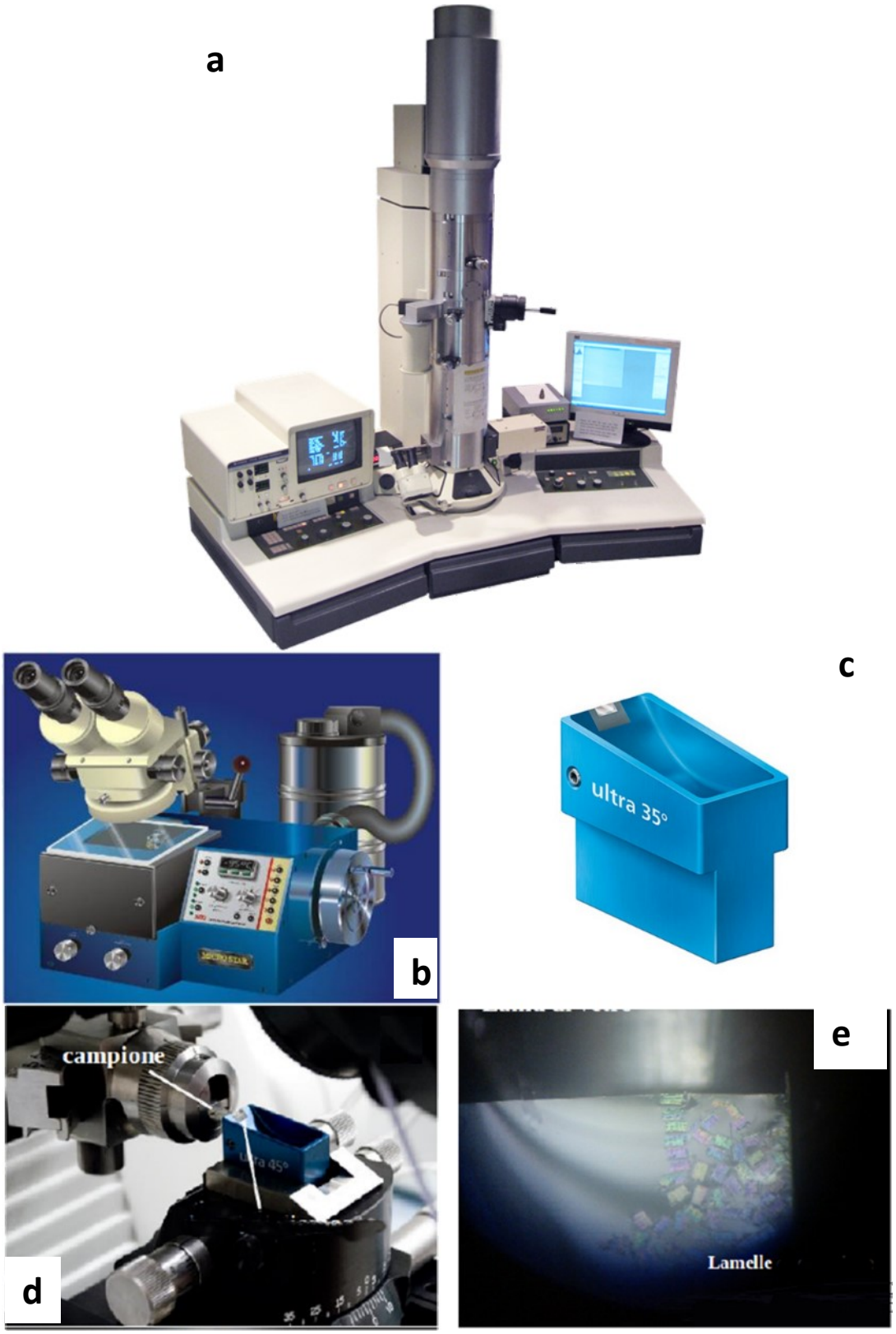

Figure 4.1: a) Picture of a typical TEM setup. (b) schematic of an ultramicrotome equipped with a cryogen chamber. (c) diamond knife used to cut the sample in thin lamellae, equipped with the boat for water to collect the cut lamellae. (d) picture of the ultramicrotome letting the sample fall on the diamond knife to be cut into slices. (e) picture of the lamellae cut and falling on the water of a glass knife.

4.2 Optical characterisation

4.2.1 Plasmonic nanocomposites

The absorption spectra of MPNs were acquired with a UV-Vis spectrophotometer Jasco 7850. To study the evolution of the sample optical absorption in response to uniaxial stretching the spectrophotometer sample holder is equipped with a custom-built, computer controlled motorized uniaxial stretcher.

The optical spectra are generally acquired from 400-800 nm. During the measurements, the sample is kept fixed for several minutes at the desired percentage of stretching. Subsequent measurements are performed varying this elongation between 0 and 50% at regular steps consisting of a 5% increase each. After the spectra acquisition, the sample undergoes continuous stretching cycles, each of which takes some seconds to perform.

A stretching cycle consists in a mechanically controlled elongation of the sample up to a pre-set percentage, and a subsequent relaxation of the sample back to its rest position. In particular, each sample was stretched up to 50% for 5000 cycles. Absorbance spectra were acquired in the visible range at regular elongation steps, after 1, 500, 1000, and 5000 stretching cycles.

Some preliminary analysis had the goal of understanding the stretching routine to follow. To do it, I fabricated Au-PDMS nanocomposites with the same amount of particle embedded and tested different stretching speeds. Surprisingly, this value didn't seem to have a strong influence on the results obtained so I decided to fix it at 1 mm/s, as it was less time consuming but still allowed a good stability of the stretching tool.

4.2.2 Soft grating

To measure the optical response of diffracting grating, I used a simple setup as schematized in figure 4.2.

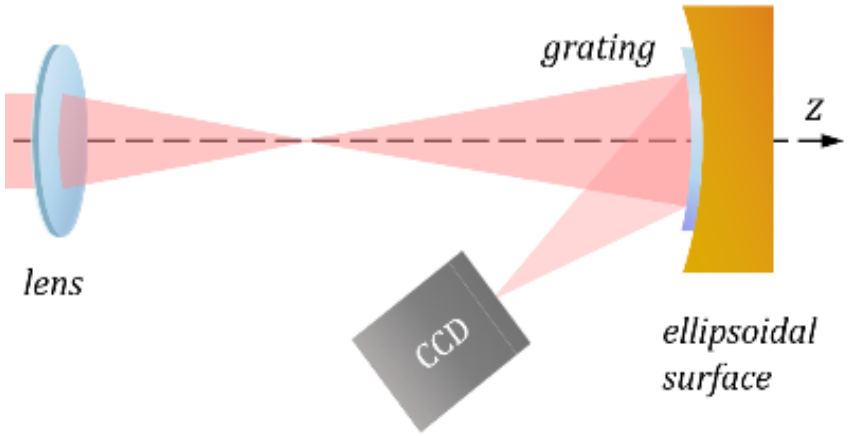

Figure 4.2: Sketch of the optical set up used for measuring the optical response of a diffracting grating bent on an ellipsoidal surface. A lens is used to focus a visible laser beam 633 nm in wavelength. The focal plane of the lens is conjugated with the CCD sensor plane by means of a

reflective grating, adhering on an ellipsoidal surface. The sensor is placed in order to intercept the first diffraction order, tilted about 20° with respect to the optical axis.

A semiconductor laser (633 nm) illuminates either an achromatic doublet or a cylindrical lens to create a point or vertically extended light source.

The reflecting elastomeric grating is stuck onto an ellipsoidal brass surface, while an opaque mask is used to prevent reflection from the exposed metal surface not covered by the grating. The grooves follow the surface curvature, which results in a slight distortion of the grooves. However, comparing the angles of the beams diffracted by the flat grating and the curved one, we assessed this effect was negligible.

The ellipsoidal axis of symmetry is aligned with the laser beam. The diffraction grating is placed at 170 mm from the focus of the lens, the first order of diffraction is collected by a CCD camera placed at 90 mm far from the grating. As a result, the focus of the lens is conjugated with the sensor plane.

The two-foci of the ellipsoid allow to directly conjugate the plane in which the object lies with the sensor. This allows to use no other optical element besides the grating and the surface and reduces the aberration of the system.

The CCD camera is a black and white MCV-50 8-bit camera 768 x 576 square pixel with a side of 8.6 µm. A two-dimensional (2D) picture is recorded, containing the space-wavelength information of the object.

4.3 Electrical characterisation

4.3.1 Percolation measurements

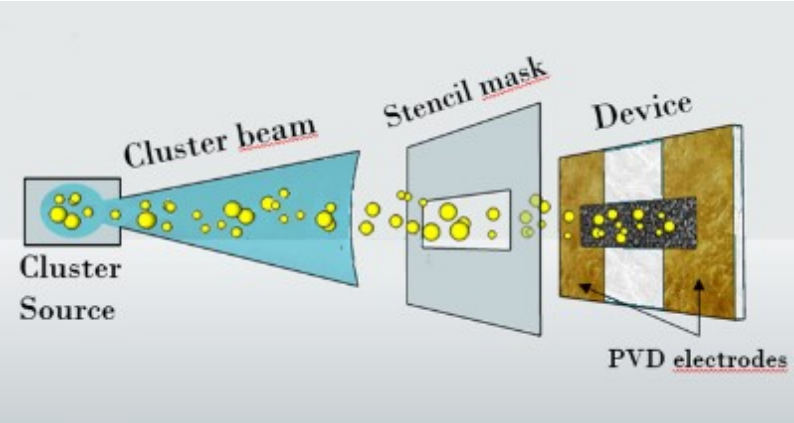

Figure 4.3: Schematic representation of the fabrication of a cluster assembled thin film used to perform resistivity measurements. The cluster beam has a very low divergence, lower than 1°, which allows to reproducibly obtain several geometries simply by means of a stencil mask instead of using photolithography processes. The electrodes have been evaporated on the two ends of the pristine substrate in order to be able to measure the sample resistance directly during its fabrication.

To measure the resistance of a sample during its fabrication a pair of contacts are deposited on the substrate at a distance of 1 mm as sketched in figure 4.3. Then, a pair of paper contacts designed

as described before are fixed to the sample ones. A stencil mask insulates from the whole sample the region where clusters needs to be implanted, including the pre-deposited contacts; this allows a high degree of reproducibility.

During the cluster deposition a very small voltage is applied (~ 1 mV) with a Keithley power supply and the current flowing through the contacts is recorded over time with an Agilent E5270A multimeter.

The output of this measure is a graph showing the resistance evolution in time. The latter can be easily rescaled in the thickness of the film grown by multiplying it by the deposition rate. This requires having a rate which is almost constant; for this reason and more generally to have samples with a high degree of homogeneity it is fundamental to carefully stabilize the source before depositing the samples.

In this work, the percolation curves where studied to have an idea of the growing mechanism of the sample; the parameters which were explores are the substrate and the deposition rate. The deposition rate is varied by changing the position of the metal rod in the cavity, as this is supposed to be the parameters which less affects the cluster formation.

The study of the effect of the substrate morphology on the percolation curve was carried out as follows. Two samples with the same geometry were placed close to each other in order that the beam covered both the samples at the same time (figure 4.4). To do it repeatedly and in a reproducible way we designed and produced with 3D printer specific sample holders which allowed to accommodate the samples and the contacts in a simple and repetitive way.

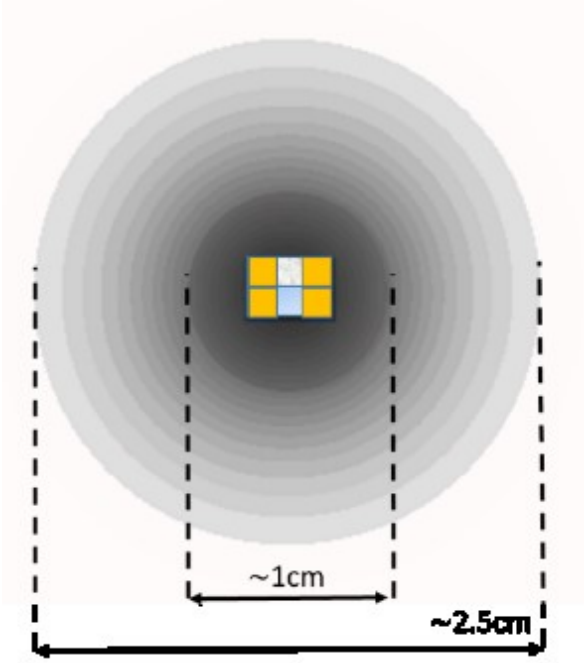

Figure 4.4: Schematic representation of the positioning of the substrates for electrical characterizations.

4.3.2 Resistance switching characterization

The devices have been electrically characterized under ambient atmosphere by applying voltage ramps and recording the resultant current, hence providing the resistance variation in time. A

triangular voltage ramp from 0 V to a maximum voltage, Vmax, is applied, and Vmax is gradually increased until switching is observed.

4.4 Optical & electrical characterization

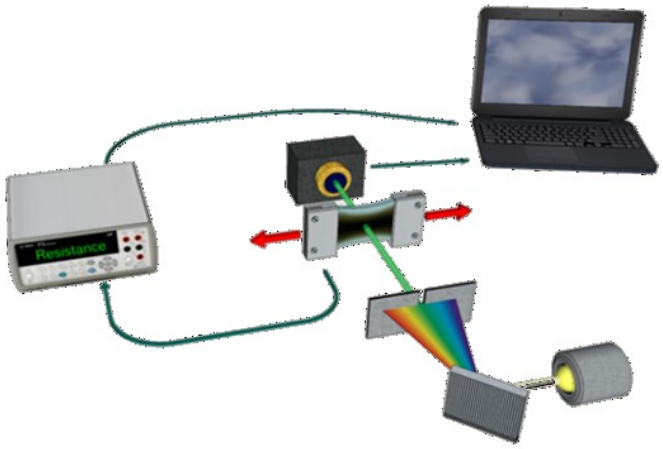

Figure 4.5: Schematic of the experimental setup used to simultaneously measure the optical absorption and electrical resistance of a MPN under the bias of uniaxial stretching. The sample is mounted on a uniaxial stretcher which is placed in a UV-vis spectrophotometer. Electrical contacts allow to measure the sample resistance over time.

To simultaneously investigate the plasmon and the resistance evolution upon stretching of the nanocomposites, the experimental set-up sketched in figure 4.5 was used. The sample is mounted on a custom-built, computer controlled motorized uniaxial stretcher, which is placed into a spectrophotometer for the acquisition of absorption spectra. At the same time the sample resistance in the stretching direction is measured with a standard multimeter: a small voltage is applied with a voltage supplier and the current flowing is recorded; the resistance is calculated with the Ohm law.

4.5 Stretching and Bending setup

To bend the MPN in a reproducible way two different approaches were followed.

Figure 4.6. (a) schematic of a deformable cluster assembled film mechanically bent in a curved shape, concave or convex. (b) A brass ellipsoidal surface on which a deformable PDMS grating adheres. The reflective nanocomposite acquires the shape of the metal surface underneath, gaining optical power.

To bend into a convex/concave shape as sketched in figure 4.6a the sample was stuck to a flat and flexible substrate which was flexed in a reproducible way.

When more complex bending is required, for example when the nanocomposite is to be bended in a spherical or ellipsoidal shape, first a mould is fabricated by turning a brass rod on a lathe then the MPN is stickered to its surface.

5 Results

5.1 Optical and electrical properties of gold-PDMS nanocomposites

One of the core interests of this work was to develop gold – PDMS nanocomposites which could be used both for a fundamental study of the reorganization of particle in response of uniaxial stretching and how this depend on the fabrication parameters, and for developing optical devices suitable for applications in the field of the adaptive optics.

To this goal MPNs are fabricated as described in section with a SCBI apparatus. This lead to the fabrication of an assembled interfacial nanocomposite consisting in a thin layer overlapping the PDMS matrix. The nanocomposite forms a thin layer at the top of the polymer matrix. Its thickness generally varies between 90 and 200 nm depending on the fabrication parameters, but once these are set, the nanocomposite thickness does not depend on the amount of particle embedded in the matrix.

It is worth noting that this implies that if the amount of particle embedded in the polymer is increased these will tend to occupy more densely the same volume of matrix, hence reducing the interparticle gaps.

From the TEM images (such as the one shown in figure 4.8), we also note the nanoparticles have a spherical shape and a size distribution peaked at about 10 nm. This value is higher than what is obtained for the characterization made in the sub-monolayer regime of cluster deposited on hard substrate, where the cluster distribution is peaked at 4.7 nm. This indicates that once the clusters are embedded into the matrix they may undergo a process of Ostwald ripening which leads to increase their size still preserving their spherical geometrical shape.

Finally, we note that the nanoparticles have a relatively broad cluster size distribution; this is supposed to affect the absorption spectrum increasing its broadness. Nevertheless, the absorption spectra all exhibited a well-defined peak and not the typical trend which can be find in highly diffusive systems.

Once the nanocomposite undergoes a uniaxial stretching, both its optical and electrical properties changes, indicating that the mechanical deformation force the filler to reorganize in the matrix. In particular, the stretching causes a redshift of the absorption spectra which can reach 200 nm (see figure 2 from reference [128] here attached).

The samples were stretched up to the 150% of their length (50% more than their rest length). This was possible because the nanocomposite as mentioned has a interfacial architecture and being the nanocomposite about 100 nm thick and the whole PDMS matrix about 60 μm thick, the Young modulus of the whole composite is the one of the elastomer. Moreover, the implantation process occurs at a very low energy, the clusters penetrate the polymer surface with an energy lower than 1eV

per atom, preventing the carbonizing of the matrix which would negatively affect the stretchability of the sample.

This shift is particularly interesting as it covers a wide range of the visible light, from 550 to 750 nm, indicating that these samples could be suitable for optical sensor applications.

In this respect, it is very important to have a device with a stable behaviour in time: to check this point the samples undergo several thousands of cycles and absorption spectra are periodically recorded. Interestingly, we found that the stability of the nanocomposite strongly depends on the amount of particles embedded in the polymer: the higher its filling factor the higher its stability (see figure 4 from reference [128]).

From a fundamental point of view, this also indicates the microstructure of the sample is different in these cases and that the evolution of the absorption spectra in response to uniaxial stretching can be used to check how this happens. Our hypothesis is that by implanting larger amount of particles, favour coalescence phenomena which stabilize the nanocomposite to a certain configuration hence reducing the effects induced by the mechanical deformation.

To understand the origin of this marked shift, we performed Finite Different Time Domain Simulation. This was done placing two gold nanoparticles inside a PDMS layer and studied the coupling between the electrical field and the clusters and how this affect the absorption spectra for different interparticle distances. This was done both considering the electrical field polarized parallel to the cluster axis, and in the transversal direction (see figures 5 and 6 from reference [129] here attached).

The simulations showed that in the former case, the electric field is strongly enhanced compared to the latter and causes a remarkable redshift of the absorption spectrum when the interparticle distance is reduced.

This allowed to elaborate the following model: uniaxial stretching forces the particles to move apart in the stretching direction and to move closer in the transversal one. As a consequence, the cause of the spectra redshift is attributed to a reduction of the nanoparticles distance induced by the compression of the nanocomposite in the direction perpendicular to the stretching, and not to the moving away of the particles in the stretching direction.

The evolution of the electrical properties is used as a second probe to better understand the particles reorganization in the matrix, see figure 2a from reference [129]. According to our model (schematized in figure 1b from reference [129]) we expected an increase of the resistance in the stretching direction and a resistance decrease in the transversal one as particles are also getting closer, which was confirmed by experimental results we recorded.

In summary, the evolution of the optical and electrical properties, indicates that stretching induces a reorganization of the system. The almost linear dependence of the resonant wavelength and resistance value on the percentage of strain applied, shows how easy it is to control the functional properties of SCBI MPN with a simple uniaxial deformation. The reversibility and stability of the process make these responsive nanocomposites particularly promising in view of developing optical and electrical devices which can be mechanically tuned.

We note that the study of the dependence of the optical properties of the sample on the amount of particles, the remarkable plasmonic shift we observed, and the possibility to have a sample which has a high absorption and also a high conductance, is thanks to the possibility we have with SCBI to implant large amount of particles without damaging the polymer matrix. Moreover, as comparing the peak wavelength of the nanocomposites produced, we noticed that there is not a strong correlation between the peak position and the nanocomposite filling factor (figure 3 from reference [128]). This let us think that the structure of the filler is almost disentangled from the amount of filler embedded in the matrix.

In the next pages I report more in detail the results obtained. The paper titled "Metal – polymer nanocomposite with stable plasmonic tuning under cyclic strain conditions" focus on the evolution of the plasmonic response of the nanocomposites upon stretching and the stability of the process.

The paper "Mechanical-optical-electro modulation by stretching a metal – polymer nanocomposites" regard the coupling of the optical and electrical response to stretching. In this case the filling factor is fixed to a value of about 30%. Here the model is corroborated with finite different time domain simulation, to find the theoretical origin of the remarkable plasmonic shift observed.

Metal-polymer nanocomposite with stable plasmonic tuning under cyclic strain conditions

Chloé Minnai, and Paolo Milani

Citation: Appl. Phys. Lett. **107**, 073106 (2015); doi: 10.1063/1.4928725
View online: https://doi.org/10.1063/1.4928725
View Table of Contents: http://aip.scitation.org/toc/apl/107/7
Published by the American Institute of Physics

Metal-polymer nanocomposite with stable plasmonic tuning under cyclic strain conditions

Chloé Minnai and Paolo Milani[a)]
CIMAINA and Dipartimento di Fisica, Università degli Studi di Milano, via Celoria 16, 20133 Milano, Italy

(Received 26 June 2015; accepted 6 August 2015; published online 17 August 2015)

We report the fabrication and characterization of stretchable nanocomposite films with mechanically tunable surface plasmon resonance. The films have been produced by implantation in a Polydimethylsiloxane substrate of neutral gold nanoparticles aerodynamically accelerated in a supersonic expansion. Optical absorption spectroscopy shows that uniaxial stretching of the nanocomposite induce a reversible redshift of the plasmon peak up to 180 nm from the peak wavelength of the non-stretched sample. The range of the plasmon peak shift depends upon the density of implanted nanoparticles. The optical behavior of the nanocomposite evolves upon cyclical stretching due to the rearrangement of the nanoparticles in the elastomeric matrix. We have identified the fabrication and post-deposition treatment conditions to stabilize the plasmonic shift upon cyclical stretching in order to obtain robust and large area nanocomposites with tunable and reproducible optical properties over a wide visible wavelength range. © *2015 AIP Publishing LLC*.
[http://dx.doi.org/10.1063/1.4928725]

Metal nanoparticles show localized surface plasmon resonances (LSPRs) consisting in a collective oscillation of conduction electrons excited by an electromagnetic field;[1] the localization of the field in structures of nanometric dimensions has profound consequences on light amplification and manipulation due to the fact that changes in nanoparticle volume and/or shape can affect dramatically the optical properties.[1,2] LSPRs in Au and Ag nanoparticles are of particular interest, in view of applications, since their frequency spans a wide spectral range from the visible to the near infrared.[3,4]

Plasmonic nanocomposites consisting of Au or Ag nanoparticles embedded in a dielectric matrix are increasingly used for selective light absorption and/or transmission in optoelectronics, biosensing, and solar energy harvesting.[5–10] The tuning of their optical properties can be obtained by selecting nanoparticle dimensions and geometries, particle density, and hence inter-particle distance.[3,4] This passive tuning requires the preparation of the ingredients of the nanocomposite with predetermined characteristics prior to the fabrication. Active tuning has been recently demonstrated where the plasmonic properties of a nanocomposite are continuously modified by mechanic deformation of the nanoparticle-matrix system in order to change the inter-particle distance and hence select different spectral absorption regions.[11–13] Deformable nanocomposites have been reported to show plasmonic shifts up to around 70 nm for uniaxial deformations of about 20%.[11]

Elastomeric matrices represent simple, low-cost, and effective media for the fabrication of mechanically tunable plasmonic nanocomposites by *in situ* doping with precursors from chemical reduction or physical vapor deposition.[14–16] An alternative approach is based on the mixing of preformed nanoparticles in a solvent subsequently used to prepare the polymer.[17,18] These methods present several weaknesses such as the poor control of spatial distribution and aggregation of the dispersed nanoparticles, not to mention the limited amount of nanoparticles that can be dispersed without negatively affecting the polymerization process of the matrix.[15] The functionalization of elastomeric surfaces with noble metal nanoparticles has been proposed as an alternative to obtain stretchable plasmonic nanocomposites: this approach allows a very precise control of nanoparticle size and reciprocal distance; however, surface-functionalized elastomers are quite fragile and their stability has not yet been characterized.[11–13]

In view of applications, a fundamental issue is the stability of the nanocomposite optical properties upon cyclic strain conditions; to date, no characterization of this aspect is reported in the literature, although there are clear evidences that nanoparticles in an elastomeric matrix are a dynamic system undergoing rearrangement and reorganization upon stretching.[19]

Recently, we showed that neutral metal clusters produced in the gas phase and aerodynamically accelerated by a supersonic expansion can be implanted in a Polydimethylsiloxane (PDMS) substrate to obtain a nanocomposite with superior resilience and interesting optical properties for the fabrication of stretchable and conformable reflective gratings;[20,21] this approach is called Supersonic Cluster Beam Implantation (SCBI).

Here, we report the fabrication by SCBI of stretchable Au-PDMS nanocomposites showing a stable plasmon peak shift up to 180 nm induced by mechanical deformation. We characterized the influence of cluster density on the plasmon frequency shift upon stretching, with particular attention to the evolution of the optical properties with increasing number of deformation cycles and on the conditions to obtain stable and reproducible performances upon a large number of stretching cycles.

We fabricated Au-PDMS nanocomposites by implanting different quantities of neutral Au clusters with a size distribution as reported in Figs. 1(a) and 1(b) in PDMS substrates.[22]

[a)]Author to whom correspondence should be addressed. Electronic mail: pmilani@mi.infn.it

Neutral gold clusters were produced by a Pulsed Microplasma Cluster Source (PMCS) and accelerated for implantation in a supersonic expansion, as described in detail in Ref. 23. A PMCS schematically consists of a ceramic body with a cavity where a target gold rod, acting as a cathode, is sputtered by a localized electrical discharge ignited during the pulsed injection of an inert carrier gas (He or Ar) at high pressure (40 bars). The sputtered metal atoms from the target thermalize with the carrier gas and aggregate in the cavity forming metal clusters; the carrier gas-cluster mixture expands out of the PMCS through a nozzle into a low-pressure (10^{-4} mbar) expansion chamber, thus producing a highly collimated supersonic beam with a divergence lower than 1°.[23] The central part of the beam enters a second vacuum chamber (deposition chamber, at a pressure of about 10^{-5} mbar) through a skimmer and it impinges on a PDMS substrate supported by a motorized substrate holder. PDMS films were produced with a Sylgard 184 Elastomer Kit by mixing the base and the curing agent in a 10:1 ratio for about 15 min and by subsequently spin-coating the mixture on a rigid substrate for 60 s at 800 rpm, polymerization is performed with a 60 min annealing at 100 °C. This procedure produces PDMS membranes with a thickness of about 60 μm.

During cluster implantation, the holder displaces the substrate in the two directions orthogonal to the cluster beam axis, allowing the parallel fabrication of multiple samples with an area of 2 cm^2.[24] Supersonic expansion accelerates the clusters to a mean velocity of approximately 1000 $m \cdot s^{-1}$, meaning that the metal clusters are accelerated towards the polymeric substrate with a kinetic energy E_k of roughly 0.5 $eV \cdot atom^{-1}$.

The implanted Au clusters volume fraction (VF) (Au volume concentration) is defined as the ratio between the total volume of the metal clusters (the filler) and the volume of polymer, in which the clusters are implanted. Considering a homogeneously filled nanocomposite, this corresponds to the ratio between the equivalent thickness of the implanted nanoparticles and the thickness of the nanocomposite layer. This latter (nanoparticle implantation depth) is obtained by transmission electron microscopy (TEM) characterization (Fig. 1(c)). The equivalent thickness T_{eq} of nanoparticles implanted into the PDMS is obtained as follows: a half-masked hard substrate (e.g., silicon or glass) is placed close to the polymeric substrate during implantation so that the same amounts of nanoparticles are intercepted both by the substrate and the polymer. Nanoparticles intercepted by the hard substrate result in a nanostructured layer whose thickness can be measured, once the mask is removed, by AFM.[24] Samples with a volume fraction in the range of 22%–48% were produced.

LSPRs evolution upon stretching has been characterized for each sample by recording the absorbance spectra in the visible range, with a spectrophotometer (Jasco 7850). The samples were mounted on a custom-built, computer controlled motorized uniaxial stretcher. Each sample was stretched up to 50% for 5000 cycles. Spectra were acquired at regular elongation state after 1, 500, 1500, and 5000 cycles.

The typical behavior of the plasmon peak upon stretching is reported in Fig. 2(a) where we show the optical absorption spectra at different elongations for a nanocomposite filled with a 31% volume fraction: the applied strain causes a broadening of the spectrum accompanied by an absorbance reduction and by a marked LSPR shift toward larger wavelength. These effects are quantitatively reported in detail in Fig. 2(b), where LSPR wavelength and absorbance are plotted versus stretching: the LSPR peak

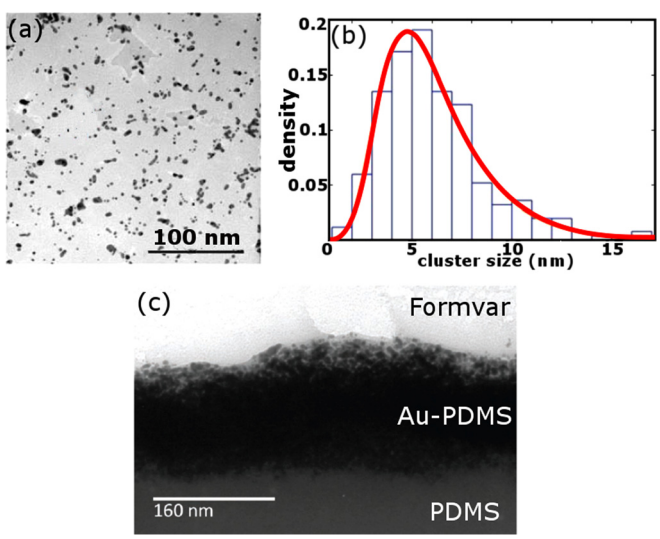

FIG. 1. (a) Transmission electron microscopy (TEM) micrograph of Au clusters deposited on a Formvar grid for the measurement of size distribution. (b) Au cluster size distribution obtained from TEM analysis and log-normal fit (red curve): the distribution is peaked at a value of 4.72 nm. (c) TEM image of a 300 nm-thick section of an Au-PDMS nanocomposite.

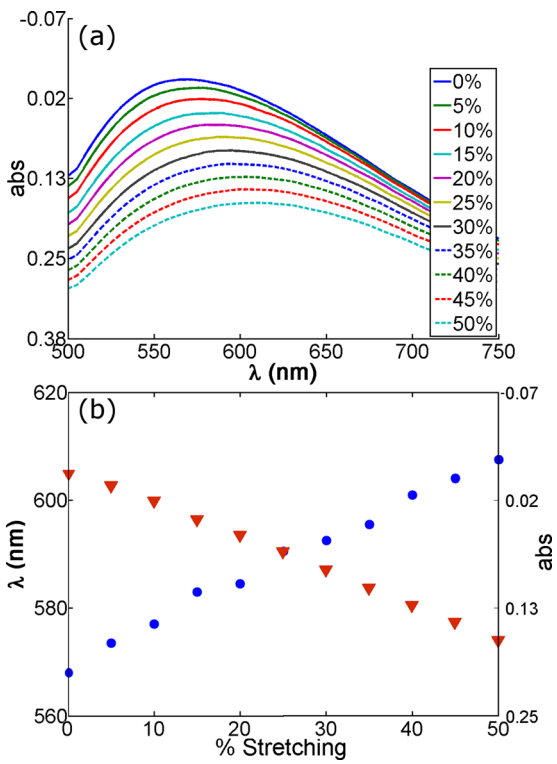

FIG. 2. (a) Absorbance spectra acquired at different applied strains. Absorbances have been normalized as $-\log(I/I_{0\%})$, where I is the measured absorbance and $I_{0\%}$ is the absorbance of the peak recorded in the non-stretched sample. (b) Plasmon peak wavelength (blue dots) and its corresponding absorbance (red triangles) versus strain. The nanocomposite VF is 31%.

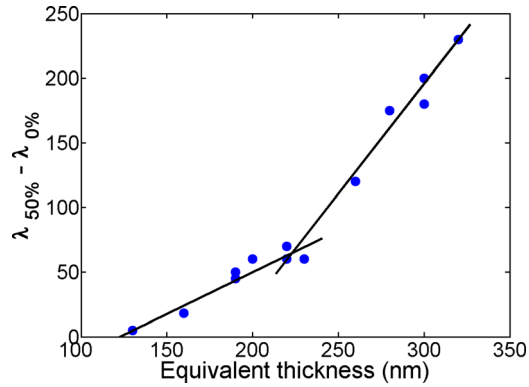

FIG. 3. Shifts of the surface plasmon resonance as a function of the nanocomposite volume fraction for a uniaxial deformation of 50% of the original dimension.

wavelength increases of about 40 nm, while its absorbance reduces of about 0.3 a.u. during a stretching cycle.

Most of the works reported in the literature analyze nanocomposites made from nanoparticle monolayer embedded in a polymeric substrate:[11–13] Cataldi *et al.* found that a stain of 20% causes a 70 nm absorbance peak redshift[11] and Zhu *et al.* found a redshift of 47 nm caused by 37% applied strain.[13]

According to the Maxwell-Garnett theory,[25] the LSPR redshift can be due to both an increase in cluster dimensions and an increase in nanocomposite filling factor.[4] When an elastomer is stretched in one direction, it is simultaneously compressed in the one perpendicular to that of the applied strain.[11,12] The compression degree depends on elastomer Poisson ratio: PDMS has a Poisson ratio of 0.5, so a 50% uniaxial stretching causes a 25% compression inducing a nanoparticle rearrangement and aggregation.[11]

The reduction of absorbance that we observe may be mainly due the reduction of the nanocomposite thickness upon stretching, while the nanoparticle volume fraction does not change. The quantification of the thickness change is difficult to obtain, since the nanocomposite Young's modulus is significantly different from that of the pristine elastomer, as discussed in detail in Ref. 26.

In our system, there is another aspect contributing to the redshift upon stretching: recently, it has been shown that SCBI produces a degradation to chains of low molar mass in the polymeric matrix and the formation of empty volumes.[27] Mechanical deformations can induce the reduction of the empty volumes and, as a consequence, the increase the nanocomposite filling factor.

SCBI has an interesting advantage compared to other nanocomposite production techniques: it allows the direct fabrication of systems with a well-controlled cluster VF over a wide range of values, reaching volume fractions that cannot be obtained with traditional approaches. This provides the possibility to study the influence of VF on the plasmonic behavior in regimes not yet explored. Figure 3 reports the peak wavelength shift for different samples with increasing volume fractions after a 50% stretching cycle.

The strain causes, for all the samples, an increase in peak redshift, as the VF increases, up to roughly 220 nm with a uniaxial deformation of 50%; these values are significantly larger than those reported in the literature for stretchable nanocomposites.[11–13] We observe two different linear trends, with the slope change occurring in correspondence of a volume fraction of about 33%. Several observations suggest that at this VF the cluster-assembled layer buried in the elastomer starts to emerge at the surface, causing a different packing of the nanoparticle upon further deposition.[22] This may reflect in a change of nanoparticle packing and rearrangement and hence optical response upon stretching.

The arrangement of nanoparticles embedded in an elastomeric matrix is affected by mechanical deformations: nanoparticles reorganize upon stretching thus influencing the electrical and optical properties of the nanocomposite.[20,28]

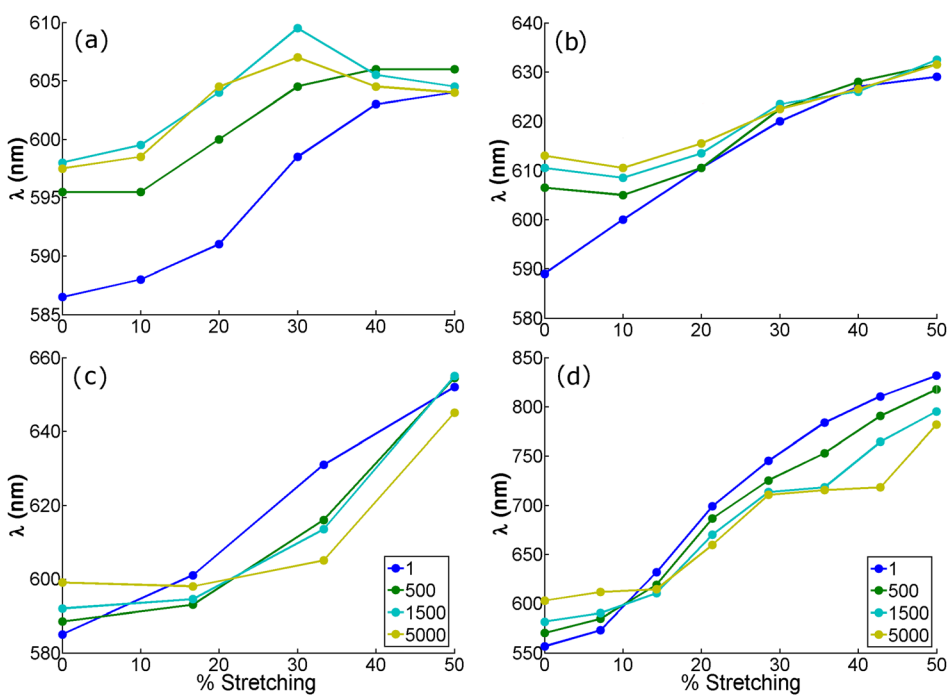

FIG. 4. Evolution of the wavelength of the plasmon peak for an increasing number of stretching cycles for samples with different cluster volume fractions: (a) 24%; (b) 28%; (c) 35%; (d) 45%.

For this reason, it is necessary to characterize the behavior of the plasmonic nanocomposite upon cyclical stretching to check for its stability. Figure 4 reports the optical response evolution at an increasing number of cycles up to 5000 for samples with different volume fractions.

In all the nanocomposites, the plasmonic shift behavior evolves with the number of stretching cycles: it is instable below 500 cycles, then the plasmon shift stabilizes and the curves acquired after 1500 and 5000 cycles tend to overlap within few nanometers. Again we observe a significant influence of the cluster volume fraction with two different regimes below and above a VF of roughly 30%.

More specifically, the 24% VF sample (Fig. 4(a)) shows an initial shift of about 17 nm upon 50% deformation decreasing substantially as the number of cycles increases: after 5000 cycles, it is reduced to about 6 nm. Moreover, the dependence of the plasmonic shift upon deformation is non-monotonic. A similar behavior, although less irregular, is observed for the 28% VF sample (Fig. 4(b)).

A significantly different trend is observed in nanocomposites with a volume fraction superior to 33%. In both the examples reported (Figs. 4(c) and 4(d)), even after 5000 cycles, a substantial plasmon peak position dependence on strain is preserved, the shift is stable, and it amounts at 46 and 179 nm for the 35% and 45% VF samples, respectively. These two shift values are about 32% lower than the ones acquired at the first cycle.

SPR peak shift induced by stretching can be explained by considering that clusters embedded in the matrix rearrange due to polymer deformation, causing their reciprocal distances to change. Aggregation and coagulation are favored if clusters have high mobility in the matrix.[19] For large VF, the mobility is reduced, especially for those nanoparticles above the matrix surface, thus increasing the nanocomposite behavior stability.

In summary, we demonstrated the fabrication of Au-PDMS plasmonic nanocomposites by implanting neutral gold clusters in a PDMS matrix by supersonic cluster beam implantation. The nanocomposites show a plasmon peak shift upon deformation depending on the implanted clusters volume fraction with a stable red shift up to 180 nm with a deformation of 50%. Cyclic stretching induces a rearrangement and reorganization of the embedded clusters affecting the plasmonic behavior. This results in an almost complete disappearance of the plasmon shift for samples with volume fractions below 30% after few hundreds of stretching cycles. For larger volume fractions, a substantial plasmon shift remains and stabilizes after a suitable mechanical post deposition treatment, providing the evidence that nanocomposites produced by SCBI can be used as mechanically tunable optical filters or as components for stretchable optical devices.

We acknowledge Cristian Ghisleri for insightful discussions.

[1]U. Kreibig and M. Vollmer, *Optical Properties of Metal Clusters* (Springer-Verlag, 1995).
[2]N. I. Grigorchuk, J. Phys. Chem. C **116**, 23704 (2012).
[3]M. K. Kinnan and G. Chumanov, J. Phys. Chem. C **114**, 7496 (2010).
[4]S. K. Ghosh and T. Pal, Chem. Rev. **107**, 4797 (2007).
[5]J. Homola, Anal. Bioanal. Chem. **377**, 528 (2003).
[6]T.-H. Meen, J. Tsai, S. Chao, Y. Lin, T. Wu, T. Chang, L. Ji, W. Water, W. Chen, I. Tang, and C. Huang, Nanoscale Res. Lett. **8**, 450 (2013).
[7]S. Pillai, K. R. Catchpole, T. Trupke, and M. A. Green, J. Appl. Phys. **101**, 093105 (2007).
[8]V. J. Sorger, R. F. Oulton, R. M. Ma, and X. Zhang, MRS Bull. **37**, 728 (2012).
[9]M. Millyard, F. M. Huang, R. White, E. Spigone, J. Kivioja, and J. J. Baumberg, Appl. Phys. Lett. **100**, 073101 (2012).
[10]M. K. Hedayati, A. U. Zillohu, T. Strunskus, F. Faupel, and M. Elbahri, Appl. Phys. Lett. **104**, 041103 (2014).
[11]U. Cataldi, R. Caputo, Y. Kurylyak, G. Klein, M. Chekini, C. Umeton, and T. Bürgi, J. Mater. Chem. C **2**, 7927 (2014).
[12]Y. F. Chiang, C. W. Chen, C. H. Wang, C. Y. Hsieh, Y. T. Chen, H. Y. Shih, and Y. F. Chen, Appl. Phys. Lett. **96**, 041904 (2010).
[13]X. Zhu, L. Shi, X. Liu, J. Zi, and Z. Wang, Nano Res. **3**, 807 (2010).
[14]W. Caseri, Macromol. Rapid Commun. **21**, 705 (2000).
[15]F. Faupel, V. Zaporojtchenko, H. Greve, U. Schurmann, V. S. K. Chakravadhanula, C. Hanisch, A. Kulkarni, A. Gerber, E. Quandt, and R. Podschun, Contrib. Plasma Phys. **47**, 537 (2007).
[16]H. Takele, A. Kulkarni, S. Jebril, V. S. K. Chakravadhanula, C. Hanisch, T. Strunskus, V. Zaporojtchenko, and F. Faupel, J. Phys. D: Appl. Phys. **41**, 125409 (2008).
[17]K. Vanherck, T. Verbiest, and I. Vankelecom, J. Phys. Chem. C **116**, 115 (2012).
[18]I. Pastoriza-Santos, J. Pérez-Juste, G. Kickelbick, and L. Liz-Marzán, J. Nanosci. Nanotechnol. **6**, 453 (2006).
[19]Y. Kim, J. Zhu, B. Yeom, M. Di Prima, X. Su, J. G. Kim, S. J. Yoo, C. Uher, and N. A. Kotov, Nature **500**, 59 (2013).
[20]C. Ghisleri, M. Siano, M. A. C. Potenza, L. Ravagnan, and P. Milani, Laser Photonics Rev. **7**, 1020 (2013).
[21]C. Ghisleri, M. A. C. Potenza, L. Ravagnan, A. Bellacicca, and P. Milani, Appl. Phys. Lett. **104**, 061910 (2014).
[22]G. Corbelli, Ph.D. thesis, Università degli Studi di Milano, 2011.
[23]P. Piseri, H. V. Tafreshi, and P. Milani, Curr. Opinion Solid State Mater. Sci. **8**, 195 (2004).
[24]C. Ghisleri, F. Borghi, L. Ravagnan, A. Podestà, C. Melis, L. Colombo, and P. Milani, J. Phys. D: Appl. Phys. **47**, 015301 (2014).
[25]J. C. Maxwell Garnett, Philos. Trans. R. Soc. London, Ser. A **205**, 237 (1904).
[26]F. Borghi, C. Melis, C. Ghisleri, A. Podestà, L. Ravagnan, L. Colombo, and P. Milani, Appl. Phys. Lett. **106**, 121902 (2015).
[27]R. Cardia, C. Melis, and L. Colombo, J. Appl. Phys. **113**, 224307 (2013).
[28]G. Corbelli, C. Ghisleri, M. Marelli, P. Milani, and L. Ravagnan, Adv. Mater. **23**, 4504 (2011).

Mechanical-optical-electro modulation by stretching a polymer-metal nanocomposite

IOP Publishing Nanotechnology
Nanotechnology 28 (2017) 355702 (8pp) https://doi.org/10.1088/1361-6528/aa7c07

Mechanical-optical-electro modulation by stretching a polymer-metal nanocomposite

Chloé Minnai, Marcel Di Vece and Paolo Milani

CIMAINA and Department of Physics, Università degli Studi di Milano, Via Celoria 16, I-20131, Milano, Italy

E-mail: paolo.milani@mi.infn.it

Received 10 May 2017, revised 22 June 2017
Accepted for publication 27 June 2017
Published 25 July 2017

Abstract

We report the simultaneous investigation of both the plasmonic resonance and electrical conductance evolution in stretchable metal–polymer nanocomposite films. The films are produced by the implantation of neutral gold nanoparticles in a polydimethylsiloxane substrate by aerodynamic acceleration in a supersonic expansion. A redshift of the gold nanoparticle plasmon peak is found upon stretching as well as a strong correlation between the plasmonic peak wavelength and the nanocomposite electrical resistance. Optical simulations attribute the optical response to the compression of the polymer perpendicular to the stretching direction, which brings the gold particles closer to each other, increasing the plasmonic coupling. Mechanical stretching can induce a simultaneous modulation of the optical and electrical properties of the nanocomposite.

Supplementary material for this article is available online

Keywords: nanocomposites, optical properties, plasmon, electrical properties, stretchable

(Some figures may appear in colour only in the online journal)

1. Introduction

Metal–polymer nanocomposites (MPNs) are the object of a rapidly increasing interest in view of the fabrication of devices for stretchable and wearable electronics (Huang *et al* 2015), actuation (Vaia 2005), soft robotics (Lu and Kim 2014) and sensing (Sadabadi *et al* 2013). They also represent very interesting systems to study the effect of the interparticle and particle/matrix interaction on the plasmonic resonances and on electrical percolation phenomena (Bréchet *et al* 2001, Vaia 2005, Sadabadi *et al* 2013, Lu and Kim 2014, Huang *et al* 2015, Li *et al* 2016).

MPNs consist of a polymeric matrix in which the concentration of a filler composed by metallic nanoparticles can be varied during the production process, this allows a static control on the final electrical and optical properties (Wohlleben *et al* 2007, Chiang *et al* 2010, Liu and Choi 2010, Pryce *et al* 2011, Tsutsui *et al* 2011, Millyard *et al* 2012, Cataldi *et al* 2014, Hedayati *et al* 2014, Zhang *et al* 2014). The use of stretchable matrices as in the case of elastomers is of particular interest in view of the dynamic modification of the MPNs properties by mechanical stretching.

Polydimetilsiloxane (PDMS) is by far the most used elastomeric matrix for the fabrication of stretchable nanocomposites: it has an excellent mechanical elasticity, as it easily holds over 100% of tensile strain without any structural failure (Heggers *et al* 1983). Moreover PDMS is widely used for the fabrication of in microfluidic and biomedical devices (Sadabadi *et al* 2013).

Nanoparticles in a polymer matrix upon stretching dynamically rearrange in a reversible or irreversible way depending on the type of the deformation, the number of stretching cycles and particle density (Kim *et al* 2013, Minnai and Milani 2015). The effect of a mechanical deformation on the nanoparticle organisation in the polymer matrix, and how this affects the optical absorption and conductivity properties of these nanocomposites is still not completely characterised and understood.

Recently Cataldi *et al* (2014) reported for a nanocomposite a redshift of 70 nm in the plasmonic absorption peak upon a 20% uniaxial stretching. Calculations demonstrate that the uniaxial stretching induces the nanoparticles to drift apart in the stretching direction, and to get closer in the transversal one. Two different decreasing trends for the

electrical resistance in metal–polymer and nanotube-polymer nanocomposites are reported in the parallel or perpendicular direction to stretching (Flandin *et al* 2000, Kim *et al* 2013).

Recently the implantation of neutral metal clusters, accelerated in a supersonic beam, in different polymers was demonstrated as an effective approach to fabricate MPNs with improved electrical, optical and mechanical properties (Corbelli *et al* 2011, Borghi *et al* 2015, Minnai and Milani 2015, Yan *et al* 2017). This technique, called supersonic cluster beam implantation (SCBI) (Ghisleri *et al* 2014), allows the formation of a thin nanocomposite layer below the surface of a polymer. This results in a film with tuneable electrical and optical properties highly resilient to mechanical deformations (Corbelli *et al* 2011, Borghi *et al* 2015, Minnai and Milani 2015, Yan *et al* 2017). The electrical and optical properties of the nanocomposite can be tuned by varying the nanoparticle concentration in the matrix or by mechanically deforming the polymeric matrix and hence varying the particle–particle distance.

Here we report the simultaneous characterisation of both the optical absorption and electrical conductivity evolution upon stretching of nanocomposites obtained by SCBI of gold nanoparticles in PDMS, showing that mechanical stretching can induce a simultaneous and controllable modulation of the optical and electrical properties of the nanocomposite. To reveal the physical origins for the observed phenomena, we performed finite different time domain (FDTD) simulations with which the optical response of the nanoparticles in PDMS was modelled.

We believe this twofold approach (experimental and computational) can provide a comprehensive insight in the matter of nanoparticle reorganisation in a polymeric matrix upon deformation. Moreover, the systematic characterisation of the influence of different stretching regimes on the optical and electrical properties, and the correlation between them, can be advantageous for practical applications in the field of wearable electronics, deformable optics, pressure sensors etc.

2. Experimental methods

2.1. Nanocomposite fabrication by SCBI

Neutral gold clusters are produced by a pulsed microplasma cluster source (PMCS) and accelerated for implantation in a supersonic expansion as described in detail in Wegner *et al* (2006). A PMCS schematically consists of a ceramic body with a cavity where a target gold rod, acting as a cathode, is sputtered by a localised electrical discharge ignited during the pulsed injection of an inert carrier gas (He or Ar) at high pressure (40 bars). The sputtered metal atoms from the target thermalise with the carrier gas and aggregate in the cavity forming metal clusters; the carrier gas-cluster mixture expands out of the PMCS through a nozzle into a low pressure (10^{-4} mbar) expansion chamber, thus producing a highly collimated supersonic beam with a divergence lower than 1° (Wegner *et al* 2006). The central part of the beam enters a deposition chamber, at a pressure of about 10^{-5} mbar, through a skimmer and it impinges on a PDMS substrate, supported by a motorised substrate holder. Supersonic expansion accelerates the clusters to a mean velocity of approximately 1000 m s^{-1}, this implies that the metal clusters have a mean kinetic energy of roughly 0.5 eV/atom (Ghisleri *et al* 2014).

During the cluster implantation, the holder displaces the substrate in the two directions orthogonal to the cluster beam axis, allowing the parallel fabrication of multiple samples, a quartz microbalance allows the control in real time of the amount of particle implanted into the substrate. An image of the PDMS substrate before and after the implantation are shown in figure S2 is available online at stacks.iop.org/NANO/28/355702/mmedia of the supplementary information.

2.2. PDMS substrate fabrication

PDMS substrates are produced with a Sylgard 184 Elastomer Kit by mixing the base and the curing agent in a 10:1 ratio for 15 min and by subsequently spin-coating the mixture on a rigid substrate for 60 s at 800 rpm. The polymerisation is performed with a 60 min annealing at 100 °C. With this recipe PDMS substrates with a thickness of 60 ± 5 μm were fabricated. An image of the PDMS substrate is shown in figure S2(a) in the supplementary information.

2.3. Nanocomposite volume fraction (VF)

The nanocomposite VF is defined as the ratio between the total volume of the metal clusters (the filler) and the volume of polymer, in which the clusters are implanted (Corbelli *et al* 2011). Considering a homogeneously filled nanocomposite, this corresponds to the ratio between the equivalent thickness of the implanted nanoparticles and the thickness of the nanocomposite layer (the nanoparticle implantation depth). This latter is obtained by characterising the cross section of the nanocomposite with a transmission electron microscopy (TEM), while the equivalent thickness T_{eq} of nanoparticles implanted into the PDMS is obtained as follows. A half-masked hard substrate (e.g. silicon or glass) is placed close to the polymeric substrate during implantation so that the same amounts of nanoparticles are intercepted both by the substrate and the polymer. Nanoparticles intercepted by the hard substrate result in a nanostructured layer whose thickness can be measured, once the mask is removed, by atomic force microscopy. For this experiment, samples with a VF of ∼30% were studied.

In figure 1(a) a TEM micrograph of the nanocomposite cross section is reported: the nanocomposite consists of a thin layer at the top of the polymer matrix. The nanoparticle diameter and the nanocomposite thickness have been estimated to be 14 ± 5 nm and 150 ± 12 nm respectively.

2.4. Electrical and optical measurement set-up

To simultaneously investigate the plasmon and the resistance evolution upon stretching of the nanocomposites, the experimental set-up sketched in figure 1(b) was used. The sample is mounted on a custom-built, computer controlled motorised

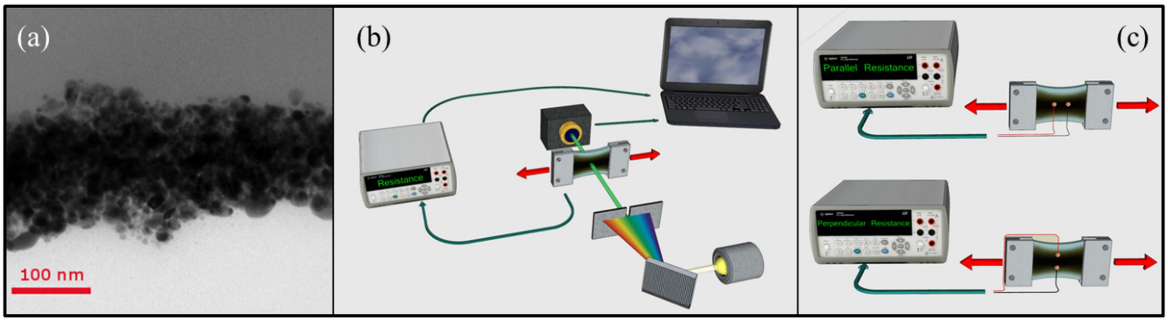

Figure 1. (a) Nanocomposite cross section acquired with TEM. (b) Experimental set-up used for simultaneous optical and electrical investigation. The sample is mounted on a custom-built, computer controlled motorised uniaxial stretcher, which is placed into a spectrophotometer (Jasco 7850) for the acquisition of absorption spectra. At the nanocomposite extremities, soft contacts have been fixed, to record the sample resistance in the stretching direction, with an Agilent multimeter. (c) Set up used for measuring the sample resistance evolution upon stretching in the direction parallel and perpendicular to the stretching direction. (Not to scale.)

uniaxial stretcher, which is placed into a spectrophotometer for the acquisition of absorption spectra. At the same time the sample resistance in the stretching direction is measured with a standard multimeter.

During the measurements, the sample is kept fixed for several minutes at the desired percentage of stretching. Subsequent measurements are performed varying this elongation between 0% and 50% at regular steps consisting of a 5% increase each. After the spectra acquisition, the sample undergoes continuous stretching cycles, each of which takes some seconds to perform.

A stretching cycle consists in a mechanically controlled elongation of the sample up to a pre-set percentage, and a subsequent relaxation of the sample back to its rest position. In particular, each sample was stretched up to 50% for 5000 cycles. Absorbance spectra were acquired in the visible range at regular elongation steps, after 1, 500, 1000 and 5000 stretching cycles.

In order to measure the resistance evolution upon stretching in the directions parallel and perpendicular to the stretching one, pairs of samples were fabricated using the same cluster implantation conditions, as described in the supplementary information. As sketched in figure 1(c), each sample has electrical contacts placed at a distance of 10 mm: one sample has the contacts aligned with the stretching direction (top), the second sample in the perpendicular one (bottom). The contacts were made with electroless plating deposition, which guarantees a negligible change in their resistivity upon stretching.

3. Results and discussion

As already discussed in Minnai and Milani (2015) and reported in figure 2(b), the applied strain causes: (i) a broadening of the optical absorption spectrum, (ii) an optical absorbance reduction (∼50%) and (iii) a marked plasmon resonance peak shift towards longer wavelengths (tens of nm).

According to the Maxwell-Garnett theory, and various other studies on the plasmon interaction between separated nanoparticles (Flandin *et al* 2000, Romero *et al* 2006, Minnai and Milani 2015, Zhu *et al* 2016), the plasmon resonance redshift suggests that the distance between the nanoparticles becomes smaller upon stretching.

However, the study of the resistance evolution in response to the stretching applied suggest an opposite behaviour. This is addressed in figure 2(a) where each curve corresponds with a different cycle.

A gradual decrease of relative resistance upon increased number of cycles and an overall resistance increase during each cycle is found. In particular, the resistance ratio ($R_{50\%}/R_{0\%}$) in the first cycle is 3.23, and it becomes 1.86, 1.75 and 1.73 for the 500th, 1000th and 5000th cycles respectively. This effect is higher from the first to the 500th cycle, after which no significant differences are recorded between the resistance evolutions during the following cycles. It has also to been observed that the resistance of the relaxed sample ($R_{0\%}$) decreases after each cycle.

During the acquisition of each curve, the sample is not stretched as shown by the step-like trend. The change of resistance upon stretching has mostly a constant value. From the inset in figure 2(a) it can be seen that during the time required for the acquisition of a spectrum (each horizontal step) the resistance does not always remain constant. A significant resistance decrease in each step of the first cycle is recorded, this becomes less pronounced after 500 cycles and almost disappeared in the following cycles.

To have further information regarding the particle reorganisation into the polymer, pairs of samples were fabricated using the same cluster implantation conditions (as fully described in the supplementary information). Their resistance both in the parallel and perpendicular direction were measured as function of stretching according to the setup of figure 1(c).

Of the three samples examined, the resistances were measured at 0%, 25% and 50% stretching. The resistance increased a 160% ± 5% and 365% ± 40% in the parallel direction upon a 25% and 50% stretching respectively, while

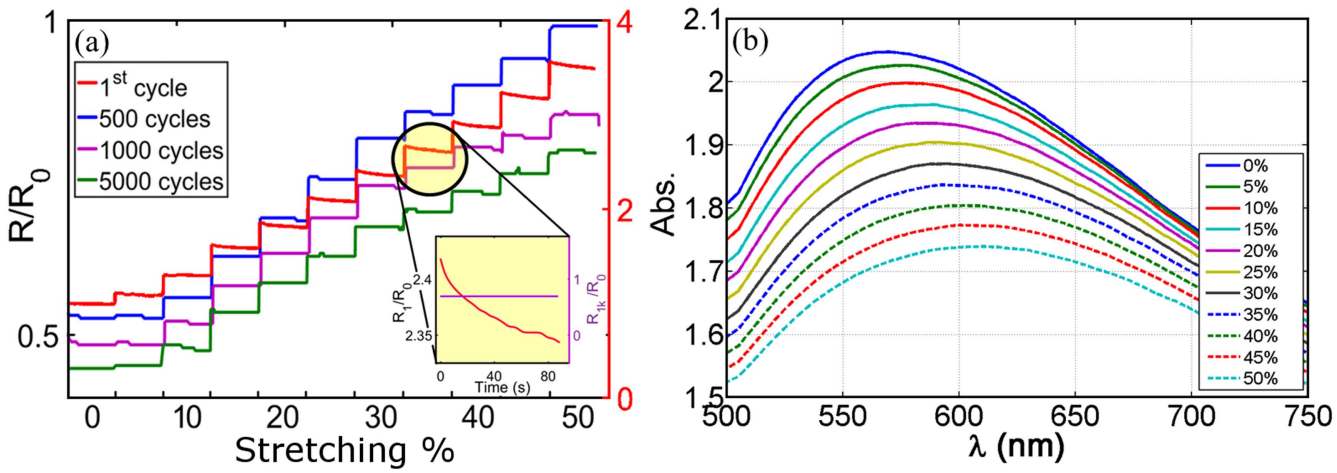

Figure 2. (a) Resistance evolution upon stretching of a sample with the contacts aligned with the stretching direction and a volume fraction of ∼30%. The resistance values are normalised to the resistance of the relaxed sample at the first cycle (R_0). For the first cycle (red curve) the right axis is to be referred, while the left one refers to the 500th, 1000th and 5000th cycles (blue, violet and green curve respectively). (b) Absorption spectra acquired at different stretching steps (reprinted with the permission of AIP Publishing LLC—Applied Physics Letter) Minnai and Milani (2015).

a 35% ± 10% and 53% ± 5% decrease in the transversal direction occurred.

This is particularly interesting because it indicates that a different reorganisation of the nanoparticle is occurring in the two different directions. This anisotropic behaviour is consistent with observations made on nanotube-polymer nanocomposites (Flandin *et al* 2000, Flandin *et al* 2001) but it is particularly interesting in systems where the nanoparticles have a spherical shape because the minimal aspect ratio of the particles cannot create *a priori* an anisotropy in the system (Kim *et al* 2013).

The optical and electrical investigations, provide results which appear paradoxical: the plasmon resonance redshift suggests that the distance between the nanoparticles becomes smaller upon stretching, on the contrary, the increase in the resistance suggest an opposite behaviour.

This apparent contradiction becomes even more apparent when the absorption peak wavelength versus the mean resistance of the sample is plotted in the same graph (see figure 3). The relation between resistance change and plasmon resonance wavelength is linear in the first cycle within the entire stretching range, after which a reflection point is reproducibly observed during subsequent cycles. The relation between the resistance and the plasmon peak remains almost linear within the stretching range 5%–40%, while a deviation from the linear trend is observed at the maximum stretched and relaxed position.

To understand the nanoparticles reorganisation in response to a uniaxial stretching, it is also to be considered that when a material is stretched in one direction, it is simultaneously compressed in the perpendicular one by the applied strain (Kim *et al* 2013, Cataldi *et al* 2014). The compression degree depends on the material Poisson ratio, for example, PDMS has a Poisson ratio of 0.5, so a 50% uniaxial stretching causes a 25% compression.

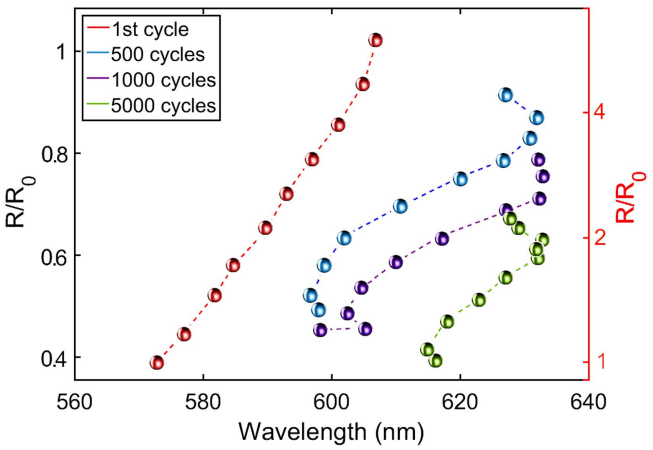

Figure 3. Absorption peak wavelength versus the mean resistance of the sample during the acquisition of the spectrum. The resistance values are normalised to the initial resistance of the relaxed sample at the first cycle (R_0). For the first cycle (red curve) the left axis is to be referred, while the right axis refers to the 500th, 1000th and 5000th cycles (blue, violet and green curve respectively). Each dot corresponds to a 5% stretching step; the error bars are smaller than the dots diameter.

Based on this knowledge and on discussions previously made in Millyard *et al* (2012), Kim *et al* (2013), Cataldi *et al* (2014), Minnai and Milani (2015), we elaborate a model to explain the optical and electrical behaviour of our samples and the coupling between these two quantities.

A schematic is depicted in figure 4, where a Au–PDMS nanocomposite clamped in the stretching tool is shown. On the left the sample is in its rest position, no stretching is applied. Two pairs of particles are highlighted: the particles labelled 1 are aligned in the direction perpendicular to stretching; those labelled 2 are randomly oriented. On the right, a 50% elongation is applied, the particles labelled 1, are now closer, while in the other situation, the particles drift

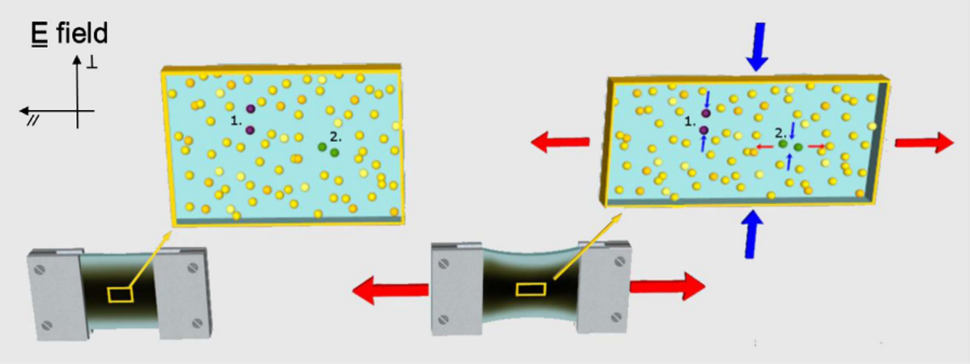

Figure 4. Uniaxial stretching effect on nanoparticles reorganisation. On the left the unstretched sample, on the right the same sample at a 50% stretching. Two pairs of particles have been highlighted: case 1: the two particles are aligned in the direction perpendicular to stretching; case 2: the particles are randomly oriented.

apart in the stretching direction, and closer in the transversal one, as indicated by the red and blue arrows.

In other terms, when a nanocomposite in under the bias of a uniaxial stretching, its structure undergoes a reorganisation: nanoparticles drift apart in the stretching direction, while they get closer in the transversal one because of the Poisson-compression. We believe this model can explain our optical and electrical results; the increase in the resistance in the stretching direction is a clear signature of the nanoparticle drifting apart, while the resistance decrease in the transversal one indicates the particle are getting closer.

According to this model, the redshift in the plasmonic peak position depends on the particles which are getting closer in the perpendicular direction, rather than the particles drifting further apart (a blueshift would be expected in this case). This is consistent with literature (Flandin *et al* 2001) and confirm the model proposed in Cataldi *et al* (2014), Minnai and Milani (2015).

To have a better understanding of the relation between the plasmon resonance and the stretching, FDTD simulations were performed with a commercial software package (Lumerical Solutions Inc.). Two gold particles of each 14 nm diameter were placed at varying distance inside a PDMS layer.

From this simulation, it is clear that the light polarisation has an important influence on the plasmonic resonance. Figure 5 shows that when the light polarisation is along the axis, which connects the two particles, the electric field between the particles is much stronger than when the polarisation is in the perpendicular direction. In the former case, the plasmonic response of the two particles is similar, resulting in a positive charge on one part of the gap and a negative charge on the other side of the gap. These opposite charges result in a strong electric field that creates a strong optical response, as seen in figure 5 (top panel). In contrast, when the polarisation is perpendicular to the axis connecting the particles, the charge on both sides of the gap is always equal because the particle plasmonic response is identical. For this reason, almost no electric field is present between the particles, resulting in the absence of an optical effect, as seen in figure 5 (bottom panel).

Both these behaviours are confirmed by the simulated optical absorption spectra of the two particles. In figure 6 we report the simulated absorption spectra of the two nanoparticles when the electrical field is polarised along the axis connecting the particles (a) and the relative peak wavelength and absorption (b).

The plasmon resonance wavelength is shifted to the red for the small gap sizes due to the strong plasmonic coupling, in agreement with literature (Jain *et al* 2007). When the gap between the particles increases, the coupling decreases and the plasmon resonance shifts back to the blue, as if they were two independent particles. The plasmonic coupling is insufficient to affect the plasmon resonance significantly from a gap distance of about 1.5 nm (figure 6(b)), where the plasmon resonance becomes similar to two independent particles.

The optical absorption strength of the two particles is also dependent on the gap size (figure 6(b), right axis). When a very small gap of 0.3 nm is present (at nominal 0 nm distance), the optical absorption cross section has a much larger value due to a higher optical density of states which increases with a smaller volume.

No significant peak wavelength shift or absorption strength change can be measured when the light polarisation (E-field) is perpendicular to the connecting axis (data not shown) both in the plane perpendicular to the propagation direction (stretching direction) and in the direction of light propagation (neighbouring particles in the vertical direction with respect to the stretching direction). The strength of the optical absorption is about a factor 3 lower than for the parallel polarisation (figure 5), confirming the minimal plasmonic coupling between the particles for perpendicular polarisation.

The shift of the plasmon resonance as observed by the experiments agrees well with the plasmon resonance shift as determined from the simulations assuming that the direction of change is the same. This means that when the nanocomposite is stretched, the particles in the parallel direction become closer to each other, which results in a red shift of the plasmon peak. Because the optical absorption spectra were measured with un-polarised light, the effect of the light polarisation in the direction along the stretching direction

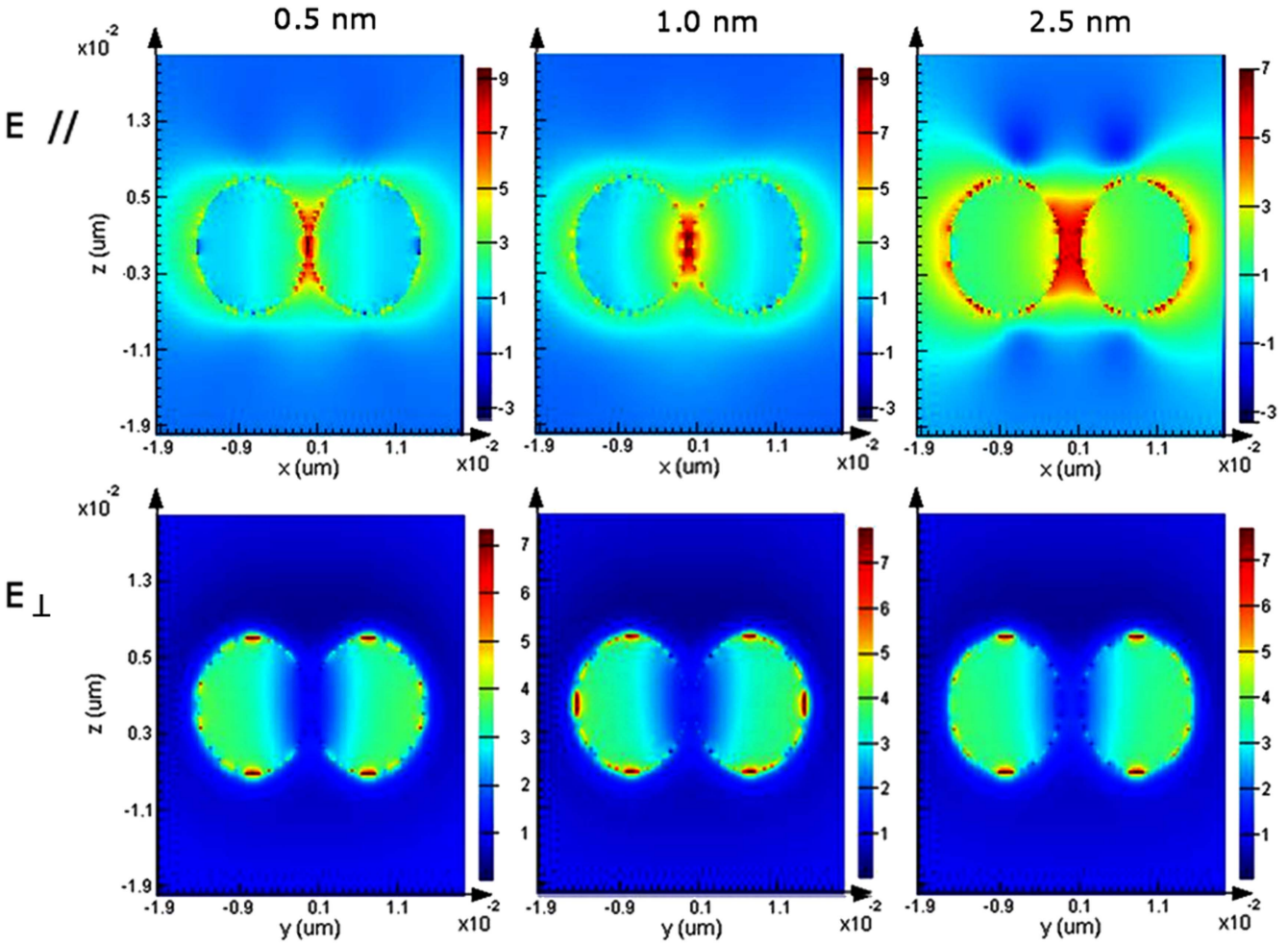

Figure 5. Cross sections of two 14 nm gold nanoparticles in PDMS with the electrical field (**E**). Top: **E** is polarised in the direction parallel to the nanoparticles axis. Bottom: **E** is polarised in the direction perpendicular to the nanoparticles connecting axis. The gap distance increases from 0.5 nm (left column) to 1.5 nm (middle) to 2.5 nm (right).

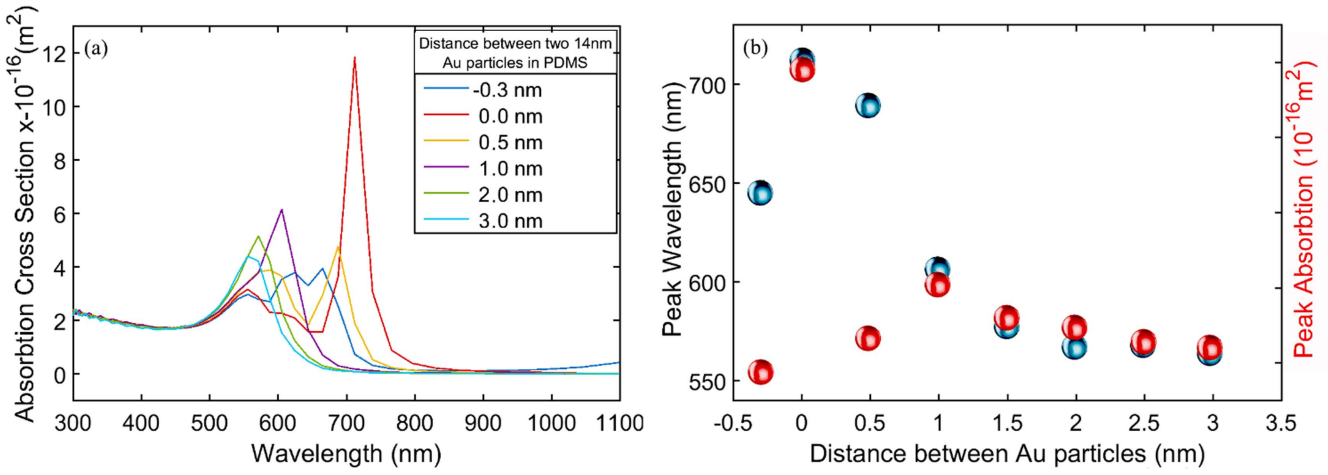

Figure 6. (a) Simulated absorption spectra with electrical field polarised in the direction parallel to the nanoparticle axis. (b) Peak absorption (red dots) and wavelength (blue dots) of the simulated spectra. At a nominal distance of 0 nm the actual gap size is about 0.3 nm while at −0.3 the particles are touching due to simulation software approximations.

should also be considered. Since the distance between the particles increases in the direction of stretching, the shift of the plasmon resonance wavelength is towards the blue (see figure 6(a)). Because the particles are initially far apart, resulting in small coupling, the effect of stretching, and thus increasing the distance between the particles more, on the optical absorption spectrum is very small. Because a blue shift was not measured, according to the simulations the average

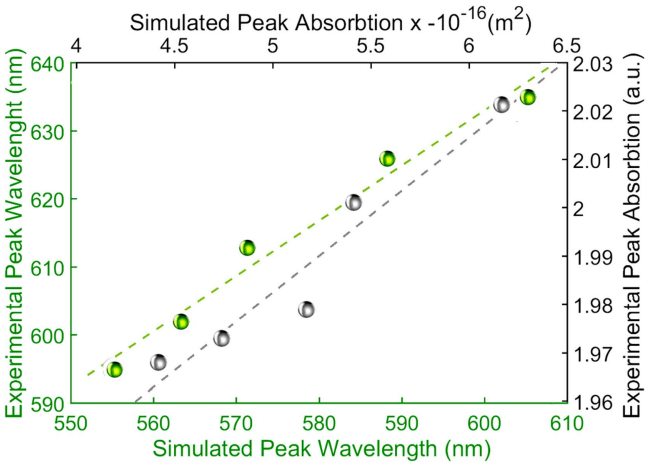

Figure 7. Experimental absorption peak wavelength (green dots) and intensity (grey dots) of the first stretching cycle are plotted versus the simulated values. The error bars are smaller than the dots diameter.

distance between the particles must therefore be around 2 nm, which is the onset of coupling. This distance is confirmed by TEM and the optical absorption from which a gap of 3 nm is estimated to be reduced to 1.3 ± 0.8 nm upon a 40% stretching.

In figure 7 the absorption intensity (grey dots) and the plasmon resonance peak position (green dots) of the experimental absorption spectra have been plotted (y axis) versus the respective simulated values (x axis) in a gap range between 1 and 3 nm. Smaller or larger gaps were not considered because such values were not measured.

The relation between the experimental and simulated plasmon peak position and intensity is remarkably linear, which suggests a strong agreement between the simulation and experiment. This is surprising considering the simple two-particle model of the simulation as compared to the complex particle distribution in the experimental samples. Additionally, the overall peak shift of 40 nm in the simulations is in good agreement with the 45 nm shift found experimentally. Although at very small gap sizes solving the Maxwell equations in FDTD will not suffice because quantum mechanical effects will change the plasmon properties (Zhu *et al* 2016), this is not of concern in this study due to the larger gap sizes in the nanocomposite.

In figure 3 a reflection point is observed in the experiments after 500 cycles, where the plasmon resonance shift turns direction as a function of resistance, going from a blue shift to a red shift or vice versa. A reflection point is also observed in the simulations, corresponding to a gap size of about 0.5 nm. According to the simulations the plasmon resonance wavelength of two particles which are in contact, is blue shifted as compared to the situation when there is a small gap. The more the polymer sample is stretched the more particles get closer in the parallel direction and start to touch. This is in good agreement with the observation that the resistance stops increasing upon extended stretching.

4. Conclusions

We reported a simultaneous characterisation of the electrical conductivity and optical absorption evolution upon stretching of a MPN consisting of gold clusters implanted in PDMS by SCBI. A plasmonic peak redshift and a resistance increase in the stretching direction were observed with a strong correlation. Thanks to the simple structure of the nanocomposites fabricated with SCBI, we could understand the physical origin of the optical response upon stretching with FDTD simulations, providing a simple and reliable model describing the nanoparticles reorganisation induced by stretching. Our results suggest the possibility of using MPNs fabricated by SCBI as optical modulator or mechanical sensor with optical response. Future work could involve polymer composites with different metals, enabling a more complicated and perhaps dedicated optical response to stretching.

Acknowledgments

MDV acknowledges the use of computer facilities of the Physics Department of KULeuven. We thank Llorenç Cremonesi for his assistance in the preparation of the figures.

References

Borghi F, Melis C, Ghisleri C, Podestà A, Ravagnan L, Colombo L and Milani P 2015 Stretchable nanocomposite electrodes with tunable mechanical properties by supersonic cluster beam implantation in elastomers *Appl. Phys. Lett.* **106** 121902

Bréchet Y, Cavaillé J Y Y, Chabert E, Chazeau L, Dendievel R, Flandin L and Gauthier C 2001 Polymer based nanocomposites: effect of filler–filler and filler–matrix interactions *Adv. Eng. Mater.* **3** 571–7

Cataldi U, Caputo R, Kurylyak Y, Klein G, Chekini M, Umeton C and Buergi T 2014 Growing gold nanoparticles on a flexible substrate to enable simple mechanical control of their plasmonic coupling *J. Mater. Chem.* C **2** 7927–33

Chiang Y L, Chen C W, Wang C H, Hsieh C Y, Chen Y T, Shih H Y and Chen Y F 2010 Mechanically tunable surface plasmon resonance based on gold nanoparticles and elastic membrane polydimethylsiloxane composite *Appl. Phys. Lett.* **96** 19–22

Corbelli G, Ghisleri C, Marelli M, Milani P and Ravagnan L 2011 Highly deformable nanostructured elastomeric electrodes with improving conductivity upon cyclical stretching *Adv. Mater.* **23** 4504–8

Flandin L, Brechet Y and Cavaille J Y 2001 Electrically conductive polymer nanocomposites as deformation sensors *Compos. Sci. Technol.* **61** 895–901

Flandin L, Chang A, Nazarenko S, Hiltner A and Baer E 2000 Effect of strain on the properties of an ethylene-octene elastomer with conductive carbon fillers *J. Appl. Polym. Sci.* **76** 894–905

Ghisleri C, Borghi F, Ravagnan L, Podestà A, Melis C, Colombo L and Milani P 2014 Patterning of gold–polydimethylsiloxane (Au–PDMS) nanocomposites by supersonic cluster beam implantation *J. Phys. D: Appl. Phys.* **47** 15301

Hedayati M K, Faupel F and Elbahri M 2014 Review of plasmonic nanocomposite metamaterial absorber *Materials* **7** 1221–48

Heggers J P, Kossovsky N, Parsons R W, Robson M C, Pelley R P and Raine T J 1983 Biocompatibility of silicone implants *Ann. Plast. Surg.* **11** 38–45

Huang G, Xiao H and Fu S 2015 Wearable electronics of silver-nanowire/poly(dimethylsiloxane) nanocomposite for smart clothing *Sci. Rep.* **5** 13971

Jain P K, Huang W and El-sayed M A 2007 On the universal scaling behavior of the distance decay of plasmon coupling in metal nanoparticle pairs: a plasmon ruler equation *Nano Lett.* **7** 2080–8

Kim Y, Zhu J, Yeom B, Di Prima M, Su X, Kim J-G, Yoo S J, Uher C and Kotov N A 2013 Stretchable nanoparticle conductors with self-organized conductive pathways *Nature* **500** 59–63

Li K, Jiang K, Zhang L, Wang Y, Mao L and Zeng J 2016 Raman scattering enhanced within the plasmonic gap between an isolated Ag triangular nanoplate and Ag film *Nanotechnology* **27** 165401

Liu C X and Choi J W 2010 Strain-dependent resistance of PDMS and carbon nanotubes composite microstructures *IEEE Trans. Nanotechnol.* **9** 590–5

Lu N and Kim D-H 2014 Flexible and stretchable electronics paving the way for soft robotics *Soft Robot.* **1** 53–62

Millyard M G, Min Huang F, White R, Spigone E, Kivioja J and Baumberg J J 2012 Stretch-induced plasmonic anisotropy of self-assembled gold nanoparticle mats *Appl. Phys. Lett.* **100** 19–22

Minnai C and Milani P 2015 Metal–polymer nanocomposite with stable plasmonic tuning under cyclic strain conditions *Appl. Phys. Lett.* **107** 73106

Pryce I M, Aydin K, Kelaita Y A, Briggs R M and Atwater H A 2011 Characterization of the tunable response of highly strained compliant optical metamaterials *Phil. Trans. R. Soc.* A **369** 3447–55

Romero I, Aizpurua J, Bryant G W and García De Abajo F J 2006 Plasmons in nearly touching metallic nanoparticles: singular response in the limit of touching dimers *Opt. Express* **14** 9988–99

Sadabadi H, Badilescu S, Packirisamy M and Rolf W 2013 Biosensors and bioelectronics integration of gold nanoparticles in PDMS microfluidics for lab-on-a-chip plasmonic biosensing of growth hormones *Biosens. Bioelectron.* **44** 77–84

Tsutsui Y, Fudouzi H, Hayakawa T and Nogami M 2011 Reversible control in surface plasmon resonance wavelength of gold nanoparticles by using polydimethylsiloxane (PDMS) *IOP Conf. Ser.: Mater. Sci. Eng.* **18** 82008

Vaia R 2005 Nanocomposites: remote-controlled actuators *Nat. Mater.* **4** 429–30

Wegner K, Piseri P, Tafreshi H V and Milani P 2006 Cluster beam deposition: a tool for nanoscale science and technology *J. Phys. D: Appl. Phys.* **39** R439–59

Wohlleben W, Bartels F W, Altmann S and Leyrer R J 2007 Mechano-optical octave-tunable elastic colloidal crystals made from core–shell polymer beads with self-assembly techniques *Langmuir* **23** 2961–9

Yan Y, Santaniello T, Bettini L G, Minnai C, Bellacicca A, Porotti R, Denti I, Faraone G, Lenardi C and Milani P 2017 Electroactive ionic soft actuators with monolithically integrated gold nanocomposite electrodes *Adv. Mater.* **29** 1606109

Zhang X, Zhang J, Liu H, Su X and Wang L 2014 Soft plasmons with stretchable spectroscopic response based on thermally patterned gold nanoparticles. *Sci. Rep.* **4** 4182

Zhu W, Esteban R, Borisov A G, Baumberg J J, Nordlander P, Lezec H J, Aizpurua J and Crozier K B 2016 Quantum mechanical effects in plasmonic structures with subnanometre gaps *Nat. Commun.* **7** 11495

5.2 Diffracting and focusing power of gold-PDMS nanocomposites.

Here I show how SCBI MPN can be used to develop a device suitable for applications in the field of adaptive optics.

The developed optical element is a reflective diffracting grating which gains focusing power by adhering to an ellipsoidal surface.

The samples are fabricated as described in the method section of the draft paper here attached. Transparent gratings are fabricated by a PDMS replica of a master, then they are made reflecting by implanting gold clusters in it. The advantage of using this approach is that the grating can be stretched and bent without damaging its reflectivity or optical power. The use of an ellipsoidal surface allows to conjugate directly the plane of the object to image with the one of the camera. This reduced significantly the aberration problems and allowed to achieve a spatial resolution of ~80 μm and a spectral resolution of about 3 nm, see figure 2.

These results are compared to ray tracing calculations, see figure 6.

The potentialities of this simple device are interesting as no other optical element but the grating and the focusing surface are necessary to reach the resolution obtained. This grating can be used for instance, for the fabrication of a simple and inexpensive device based on diffractive optics for spectrally resolved imaging.

A very simple scheme for spectrally resolved imaging by means of curved polymeric gratings

Chloé Minnai[1,2*], Llorenç Cremonesi[1,2], Paolo Milani[1,2], Marco A. C. Potenza[1,2]

[1] Department of Physics, Università degli Studi di Milano and INFN-Milan, via Celoria, 16 – I-20133 Milan, Italy
[2] CIMAINA, Università degli Studi di Milano, via Celoria, 16 – I-20133 Milan, Italy

E-mail: xxx

Received
Accepted for publication
Published

Abstract

We report the fabrication of a simple and inexpensive device based on diffractive optics for spectrally resolved imaging. A brass surface manufactured on a metal lathe and a deformable, reflecting diffraction grating guarantee spatially and spectrally resolved images without the need for other optical elements. The grating is a metal-polymer nanocomposite replica of a plastic grating: reflectivity of the transparent dielectric substrate is obtained by the implantation of gold clusters, hence preserving deformability. The brass surface is a portion of a rotation ellipsoid, on which the deformable grating adheres to gain optical power. According to the optical tests performed on the system, the achieved spatial resolution of the system is ~80 μm, whereas limiting spectral resolution of about 3 nm is observed. Reflectivity of the zero-order reflection and the first order diffraction approaches 45% and 5% respectively. We detail the results for the reconstruction of an on-axis and off-axis point source, and a vertically extended slit-like source with a 110 μm obstruction.

Keywords: Metal polymer nanocomposite; Adaptive imaging; Multispectral and hyperspectral imaging; Diffraction gratings; Diffractive optics.

Introduction

In the latest decades growing interest is been given towards the fabrication of adaptive optical elements (lenses, mirrors, and gratings) suitable for the realization of compact, inexpensive, and portable devices [1,2,3]. The use of tunable gratings based on stretchable reflective substrates could have a significant impact on the design of optical mini spectrometers and significantly widen their field of applications [4,5,6]. However, the production of reflective and deformable optical elements is not trivial: flexible materials (polymers and especially elastomers) are generally poorly reflective, while highly reflective materials such as metals are not easily deformable [7,8]. An outstanding approach consists in integrating these two materials in the same platform thus to combine the properties of metals and polymers in a metal-polymer nanocomposite [9].

This requires a proper fabrication technique able to both overcome the issues due to the several orders of magnitude of mismatch between the Young moduli of the two materials, and guarantee the possibility of deforming the nanocomposite in a stable and reproduceable way, to maximize the overall resolution of the system. Supersonic Cluster Beam Implantation (SCBI) in polydimethyl-siloxane (PDMS) has been proved to be a suitable approach to this purpose [9,10].

We recently reported the fabrication of reflective diffraction gratings which were successfully used for the realisation of a simple, cheap spectrophotometer and of a hyperspectral camera [11]. In this latter case, we used SCBI gratings with curved grooves which were stuck to a cylindrical substrate to focalize the light both in the vertical and horizontal direction, i.e. in a point. This approach allows to work with undeformed gratings, even if it introduces several constraints that limit the applicability of the method.

The goal of this work is to characterize the diffractive properties of a system consisting only in a diffracting grating with an ellipsoidal concave surface.

To this purpose optical gratings with straight grooves were adhered on a concave ellipsoidal brass surface. The main advantage of using this geometry is the possibility to directly focus the diffracted light in a point without using further optical elements. Moreover, the possibility to exploit the frontal and back focuses to conjugate the slit with the sensor plane, further reduces aberration problems and optimizes the spatial resolution of the system [12].

The optical properties of the system such as spatial and spectra resolution and reflectivity were carefully characterized collecting images via a CCD sensor.

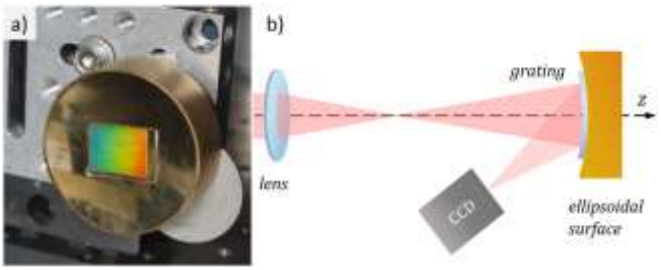

Figure 1. (a) SCBI diffraction grating adhering to the ellipsoidal surface. (b) schematic of the optical setup. The lens is used here to create a pointlike source for performing optical testing as described in the text.

Methods

Transparent deformable gratings were fabricated by making a polydimethylsiloxane (PDMS) replica from a master consisting of a plastic grating with 1000 and 500 grooves/mm.

The master was sliced in rectangles of 20×20 mm. Each rectangle was stuck on a smooth plastic box 100×100 mm. The PDMS liquid precursor (Sylgard 184 Silicone Elastomer Kit from Dow Corning, mixed in a 10:1 ratio) was cast on the master slices reaching the thickness of 1 mm and finally crosslinked at room temperature for 48 h. After cross-linking, the mold was carefully detached from the master, from which a 10×10 mm grating was obtained.

The transparent PDMS gratings were then made reflective by implanting gold nanoparticles using a Supersonic Cluster Beam Implantation (SCBI) apparatus equipped with a pulsed microplasma cluster source (PMCS), following the procedure described in detail in [5].

Briefly, a PMCS consists of a ceramic body with a cavity in which a solid gold target (purity 99.9%) is vaporized by a localized electrical discharge supported by a pulsed injection of an inert gas (Ar) at 40 bar pressure [13].

Metal atoms sputtered from the target aggregate in the source cavity to form metal clusters; the mixture of clusters and inert gas expands through a nozzle forming a supersonic beam into an expansion chamber kept at a pressure of about 10^{-6} mbar [14,15]. Electrically neutral nanoparticles exiting the PMCS are aerodynamically accelerated in a collimated beam with divergence lower than 1° and with a kinetic energy ~0.5 eV/atom [15]. The central part of the cluster beam enters the deposition chamber through a skimmer, and the beam is finally intercepted by the polymeric substrate [14].

The quantity of material implanted into the PDMS can be tuned simply during the implantation process and it is controlled in real time with a microbalance. Close to the sample, a half-masked silicon substrate is placed to intercept the same amount of nanoparticles implanted in the soft polymer.

After the deposition the thickness of the cluster-assembled film deposited on the silicon is measured with an AFM and it corresponds to the equivalent thickness t_{eq} of the metal-polymer nanocomposite.

We metallized PDMS gratings with an equivalent thickness of approximately 50 nm, at a deposition rate of about 0.08 Å·s^{-1}. This value was chosen in order to maximize the sample reflection: if the amount of embedded particles is much lower, the sample is still transparent, so it has a poor reflectivity. On the other hand, larger amounts result in a poor reflectivity due to increased absorbtion. This was checked by implanting a different amount of particles in several flat substrates and comparing the intensity of the beam diffracted at the first order.

In contrast to what reported in [11], to give optical power to the diffraction grating we used an ellipsoidal concave surface with the front and back foci at 170 and 90 mm from the surface respectively. This was fabricated by turning a brass rod on a lathe. Brass proved to minimize roughness with respect to aluminium, for example, and ensured good adhesion of the polymer. The reflecting elastomeric grating is gently adhered onto the ellipsoidal surface (Fig. 1a), whose axis of symmetry is aligned with the laser beam (Fig. 1b).

Due to the surface curvature grooves are slightly deformed, as well as the spacing will depend on the position. Nevertheless, by comparing the measurements of the diffraction angle with those obtained directing the laser beam on the grating adhering on a flat surface the difference was found to be negligible.

Hower, as it can be noted in Fig. 1a, defects on the surface of the grating cause a slight warping of the spectrum. An opaque mask was used to select a 5×5 mm area of the grating, in order to reduce local distortions.

We report in figure 1b a schematic of the setup. The output of a Fiber Pigtailed Laser Diodes (Newport 700P, 633 nm) is sent through a single mode fiber and collimated with a 40 mm focal length collimator. The emerging beam illuminates either an achromatic doublet or a cylindrical lens

in order to create a pointlike or a vertically extended light source respectively, with which optical testing is performed as described below.

The diffraction grating is placed at 170 mm from the pointlike source. The first order of diffraction is collected by a CCD sensor placed 90 mm far from the grating. As a result, the source plane is conjugated to the sensor plane.

Therefore, the recorded two-dimensional (2D) picture contains the space-wavelength information of the object.

The efficiency of the grating was measured by placing the sensor close to the grating so as to obtain a homogeneous illumination.The intensity of the reflected light (zero-order) was 45% of the incident light, while the first diffraction order settled around 5% of the incoming radiation.

The optical properties of the system were characterized in three steps. In each step te spatial and spectral resolution were measured.

First, the impulsive response of a pointlike source on the optical axis was studied. The focal plane of the achromatic doublet (f = 120 mm), was conjugated with the sensor one. The beam waist is about 20 µm wide and the diverging beam illuminates an area of the grating of approximately 5 mm × 5 mm. The point source was translated along the vertical y axis 2 mm upwards and 2 mm downwards from the on-axis position; images were recorded at each 0.15 mm step.

Second, the point-like source was replaced by a vertically-extended one by swapping the achromatic doublet with a cylindrical lens (f = 50 mm). In the focal plane of the lens, the light formed a thin, focal line about 20 µm wide. This was to obtain a light source similar to what a vertical slit would yield, avoiding the drawback of a significant power loss. This test is aimed to assess whether the device is able to work as a line scan camera.

Third, a calibrated copper wire 110 µm in diameter was placed across the vertical line, as a transversal obstruction. This causes the diffraction of the light in the vertical direction as well. The transversal obstruction was moved in the vertical direction, and images for four different positions were recorded including the optical axis, to study how the off-axis sources affect the response of the system.

Results

An example of the images recorded with this setup is shown in figure 2. The images are spatially resolved along the y axis, while the spectral information is recorded in the x axis.

In particular, in this figure we show the reconstruction of the on-axis pointlike source. A peak is visible at the centre of the image, surrounded by other patterns attributable to small distortions of the grating surface. The intensity of the patterns around the peak is about 20% of the maximum. The red curve shows a vertical cross section of the image, centred in the main peak. From the cross section curve we calculate the vertical full width at half-maximum (FWHM) of about 80 µm and gives the limiting spatial resolution. Other measurements gave similar results, the FWHM ranging between 70 and 90 µm.

The limiting spectral resolution was calculated from the horizontal cross section, as follows:

$$\frac{\Delta\lambda}{\lambda} \simeq \frac{d \cdot a}{\lambda \cdot l} \qquad (1)$$

Where d is the grating spacing (1 µm), a ~ 100 µm is the spot FWHM and l = 90 mm the distance between the grating and the camera. This provides the result of ~ 2 nm, which does not change upon scanning other portions of the gratings. Illuminating a larger portion of the gratings (10×10mm) resulted in a width of up to 700 µm, hence a spectral resolution of 12 nm. This indicates that the resolution may be affected by large scale inhomogeneities of the surface of the grating.

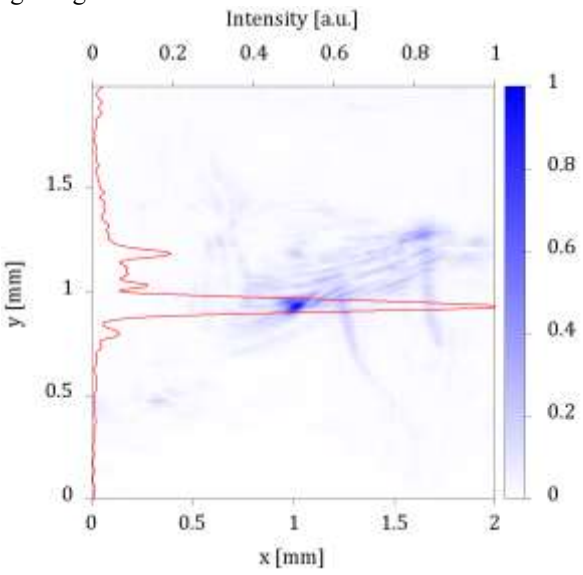

Figure 2. Reconstruction of the on-axis point source. The intensity is normalized on its maximum, displayed as a color gradient from white (minimum) to blue (maximum). On the axes, the position in mm on the screen is reported. Spectral information is recorded along the x axis, while the y axis corresponds to spatial information of the image. The red curve refers to a section at x= 1.1 (λ = 632 nm) of the 2D histogram across its peak. Patterns close to the central peak are related to irregularities of the grating surface and are up to the 30% of the main peak intensity.

The effect of paraxial illumination was studied by translating the laser in the vertical direction with a micrometer drive. Images were recorded at regular 0.15 mm steps up to an extension of 4 mm. This results in a displacement of the image of the spot of about 2 mm. This procedure was first monitored by placing the camera in the

focus of the lens, then repeated placing the sensor in the focal plane of the grating.

From this measure we could estimate the magnification factor of the system given by the inverse ratio of the distance covered by source and the image peak reconstructed by the system, respectively. This gave m = 0.51 which is in good agreement with what expected from the thin lens formula $m = q/p$ = 90/170 = 0.53. Indeed, repeating the procedure placing the source 90 mm and the sensor 170 mm from the grating gave $m \simeq 2$ as expected.

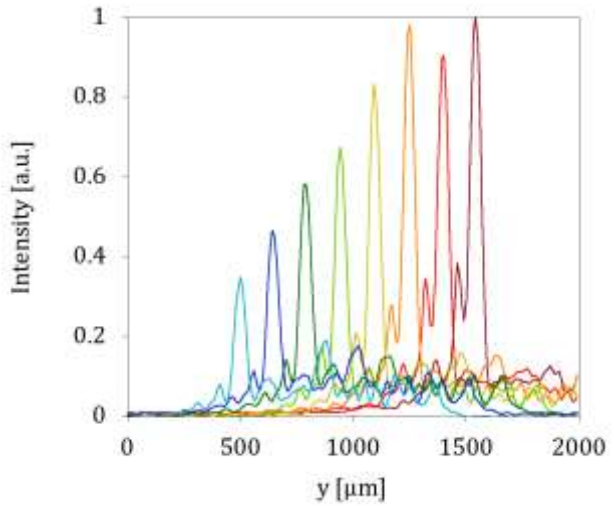

Figure 3. Sections of the Intensity recorded by the sensor when translating the point source. The rightmost plot corresponds to the laser aligned with the optical axis. Each peak corresponds to a 0.15 mm step, in sequence right to left.

As shown in figure 3, the intensity of the peaks reduces when the source is placed further from the central axis, while the vertical FWHM remains ~80 µm for all of them, indicating that the spacial resolution of the system does not change with a paraxial illumination. The same holds for spectral resolutioin.

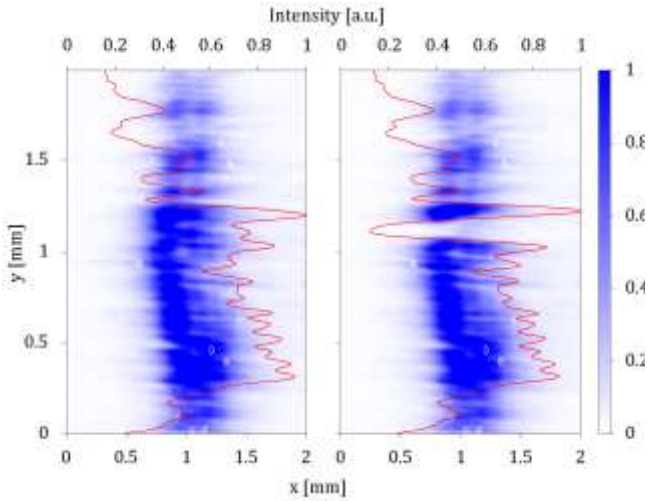

Figure 3. Reconstruction of the vertically extended source (left) and with a 110 µm wire as an obstruction (right). The intensity is normalized on its maximum. Spectral information is recorded along the *x* axis, while the *y* axis corresponds to spatial information of the image. The red curves refer to the average of the intensity profile computed at fixed y.

In figure 4 we report the intensity plot of the vertically-extended source. The image on le right shows the slit with the wire placed in the central position. We can see the light focused in a vertical line with an abrupt separation in the central region, where the wire is placed. The overall extension of the light and dark regions are both demagnified by a factor ~0.5.

The abrupt step corresponding to the starting of the dark region allows to estimate the spatial resolution of the system, here calculated as the number of pixels necessary to record an 90% change in the intensity. This calculation provides a spatial resolution of ~80 µm, which agrees with previous results. We checked if the resolution changed when the obstruction is moved along the slit. While the wire was placed in three equally distant positions, variations of the spatial resolution of the system varied within 10%.

The spectral resolution is evaluated from the FWHM along the x axis, which results in a resolution of 8 nm.

We compared the experimental results to calculations of ray paths via a generalized diffraction grating equation. The surface of the grating is described by the following equation:

$$F(x,y,z) = \frac{x^2+y^2}{{x_0}^2} + \frac{(z-z_0)^2}{{z_0}^2} - 1 = 0 \qquad (2)$$

where x_0 and z_0 are set so that the foci of the ellipsoid are located at f_1 = 90 mm and f_2 = 170 mm on the z axis.

Each ray originates from the source located in **p** and intercects the surface of the grating in a point which we call **p'**, as shown in figure 5. In this point, for each ray the normal **n**= -∇F and tangent vectors **u**=**v**×**n**, **v**=($-xy$, ${x_0}^2-y^2$, yz_0-yz) are calculated, where **v** is parallel to the grooves of the grating so that **u**, **v**, **n** form a Cartesian coordinate system when normalized. With respect to those vectors the angles of incidence ϑ_i and ψ_i are defined (fig. 5), and the first order diffraction angles ϑ_d, ψ_d are given by the following equations:

$$\begin{cases} \sin\theta_i \cdot \cos\psi_i = \frac{\lambda}{d} - \sin\theta_d \cdot \cos\psi_d \\ \sin\theta_i \cdot \sin\psi_i = -\sin\theta_d \cdot \sin\psi_d \end{cases} \qquad (3)$$

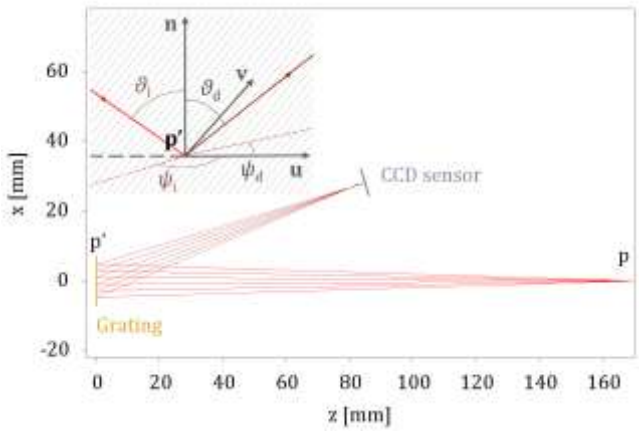

Figure 5. A pencil of light from an on-axis point source is diffracted by the grating, as calculated by the ray tracing method adopted here. The point source in p is located 170 mm from the grating, in its front focal point. Conversely, the sensor is 90 mm far from the grating, in its back focal plane. The ellipsoid is located at the origin of the reference frame.

We note that if the term λ/d is omitted, equations (3) correclty reduce to the case of simple reflecxion from a given surface, so they could be applied to a mirror as well.

In the present case λ/d = 0.316 (Fig. 5), the rays are diffracted by the grating at an angle of 18,4°, which agrees with the angle at which the first diffraction maximum is expected to occur according to basic diffraction theory [16] and with experiment. Orthogonal to the rays lies a plane on which they are projected, representing the CCD sensor.

In Fig. 6 we show the results for a point source located 170 mm from the grating, at varying wavelengths. Rays were generated according to a radial gaussian distribution, its FWHM being 4 mm. Vertical displacement of the point source results in a displacement of the spot demagnified by a factor ~0.5 as expected. The limiting resolution in the calculation is evaluated from the FWHM of the spot on the sensor plane, which ranges from 20-30 µm depending on the wavelength when a 5×5 mm mask is applied on the grating.

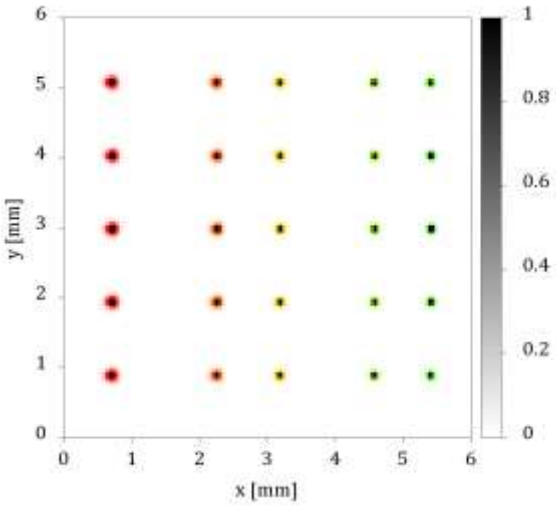

Figure 6. Reconstruction of the point source on the CCD plane, at different vertical positions and different values of the wavelength. False colour scale indicates normalized intensity, from white to black. Intermediate tones have been coloured to distinguish different wavelengths of the source (left to right): 632, 600, 580, 550 and 532 nm.Vertical position depends on vertical displacement of the point source from the axis (top to bottom): -4, -2, 0, 2, 4 mm.

Conclusions

We demonstrated the fabrication of a simple diffractive imaging system with a stretchable metal-polymer nanocomposite grating and a turned metal surface, whose geometry can be customized on a lathe.

The optical elements are hence reduced to just two components, which goes a step in the direction of a simplification and miniaturization of spectrometers and hyperspectral imaging devices.

Results are in good agreement with calculations of ray paths, the system ensures 80 µm spatial and 3 nm spectral resolution. Aberrations introduced by the elliptic geometry of the system proved to be negligible compared to the distortion of the diffracted wavefronts due to irregularities of the grating surface. Reducing this irregularities in the polymer surface curvature is key in order to further improve the resolution of the system.

Acknowledgements

We thank Daniele Viganò, Francesco Cavaliere and the staff from the Mechanical Workshop of the Physics Department of the University of Milan for their precious support and advice.

References

[1] Wilbur J L, Jackman R J, Whitesides G M, Cheung E L, Lee L K and Prentiss M G 1996 *Chemistry of materials* **8** 1380

[2] Son S I, Pugal D, Hwang T, Choi H R, Koo J C, Lee Y and Nam J D 2012 *Applied optics* **51** 2987

[3] Ghisleri C Potenza M A C Ravagnan L Bellacicca A and Milani P 2014 *Applied Physics Letters* **104** 061910

[4] Hosokawa K, Hanada K, and Maeda R 2001 *Journal of micromechanics and microengineering* **12** 1

[5] Ghisleri C, M Siano M, Ravagnan L, Potenza M A C and Milani P 2013 *Laser and Photonics Reviews* **7** 1020

[6] Potenza MAC, Minnai C and Milani P 2016 *International Symposium on Clusters and Nanomaterials* **10174** 101740G

[7] Guerrero RA, Barretto J T, Uy J L, Culaba I B and Chan B O 2007 *Optics communications* **270** 1

[8] Li T, Huang Z, Suo Z, Lacour S P and Wagner S 2004 *Applied physics letters* **85** 3435

[9] Corbelli G, Ghisleri C, Marelli M, Milani P, and Ravagnan L 2011 *Advanced Materials* **23** 4504

[10] Minnai C and Milani P 2015 *Applied Physics Letters* **107** 073106

[11] Potenza MAC, Nazzari D, Cremonesi L, Denti I and Milani P 2017 *Review of Scientific Instruments* **88** 113105

[12] Pottier P and Packirisamy M 2012 *Applied optics* **51** 4073

[13] Wegner K, Piseri P, Tafreshi H V and Milani P 2006 *Journal of Physics D: Applied Physics* **39** R439

[14] Piseri P, Podesta A, Barborini E and Milani P 2001 *Review of Scientific Instruments* **72** 2261

[15] Tafreshi HV, Benedek G, Piseri P, S Vinati, Barborini E and Milani P 2002 *Aerosol Science and Technology* **36** 593

[16] Born M and Wolf E 1999 *Principles of Optics* (Cambridge: Cambridge University Press)

5.3 Electrical properties and resistance switching

5.3.1 Electrical characterization

The characterization of the percolation curves, acquired on nanostructured materials fabricated with supersonic cluster beam deposition, was used to compare the structure of the clusters grown on a hard substrate (glass) with the one grown on paper.

To perform this characterization, two samples with the same geometry are placed close to each other on the sample holder (see figure in section 4.3.1). Then, the centre of the cluster beam is directed towards them in such a way that both the samples are in the high homogeneous part of the beam at the same time. This is possible because the homogenous part of the cluster beam has a diameter about 10 mm, while the area of the sample between the two contacts is 1 mm^2 wide.

A pair of representative percolation curves acquired are shown in figure 5.1.

In both the cases, we clearly distinguish, the dielectric, tunnelling and percolating regimes; what changes is primarily the critical thickness at which the sample stops following the dielectric regime.

More specifically, for all the pair of samples fabricated, the onset of the conductivity in the glass samples occurred at half as much as gold was necessary to set the conductivity on paper.

We suppose this is due to a different cluster structure which is grown in the two cases: probably on the paper substrate a quasi 3D structure is grown.

Moreover, the trend with which the resistance decreases in the percolation regime is slightly different in the two cases (see figure 5.2). The percolative part of the graph was fitted with a power law, according to what expected from the percolation theory; the best q-value found for the glass curve is systematically lower than the one found for paper. Both of them remain more appropriate for a 2D system rather than a 3D one.

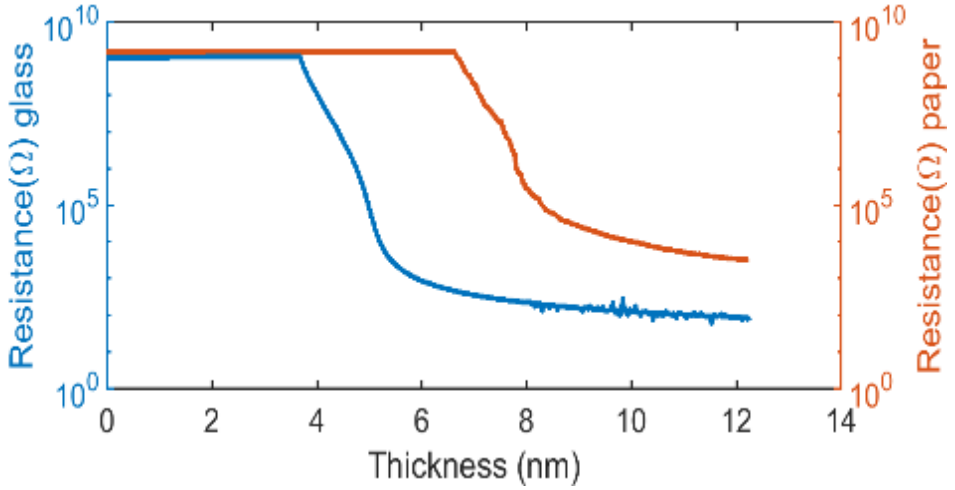

Figure 5.1: Percolative curves of an Au/paper sample (red curve) and Au/glass sample (blue curve) as a function of the equivalent deposited thickness, which in turn is related to the amount of particles on the substrate. In both cases the dielectric, tunnelling and percolating regimes are well visible. The paper sample has a larger critical equivalent thickness and a slower decrease, probably due to the more complex structure of the fibres compared to the smoother surface of the glass.

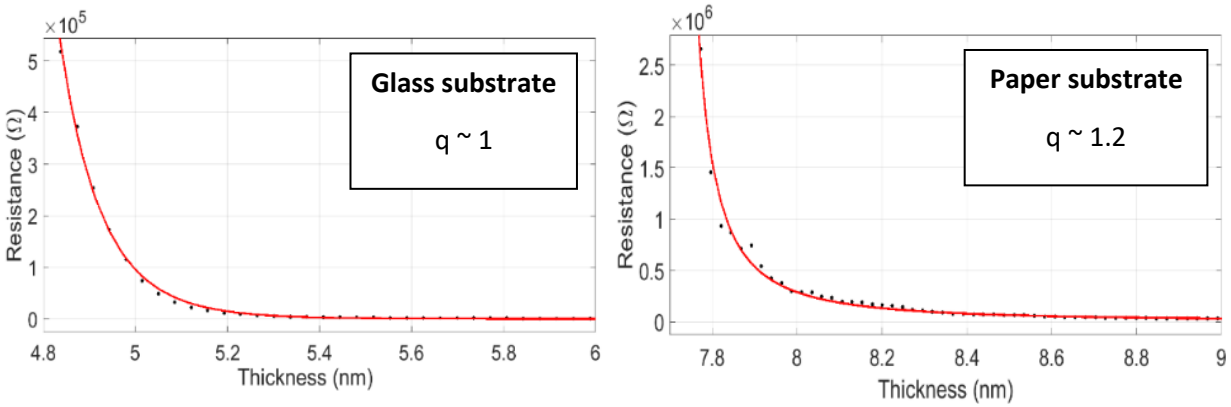

Figure 5.2: Fitting of the percolative part of the curves. The fit was done with power law, according to what expected from the percolation theory; the best q-value found for the glass curve is systematically lower than the one found for paper.

These tests were repeated varying the deposition rate. In all the cases considered the conduction onset on paper substrates occurred with twice as much as gold than the one deposited on the glass substrate. Moreover, it was found a quasi-linear dependence of the q value which best fits the percolation regime, with the deposition rate: larger q-values are found at higher deposition rates.

We observed that the rate strongly affected the percolation curve, indicating that different nanoscopic structures grows changing this parameter. In figure 5.3 we show as an example the effect of three different rate on the percolation curve. We observe for instance that the final resistance of about 10 kOhm is reached at different film thicknesses.

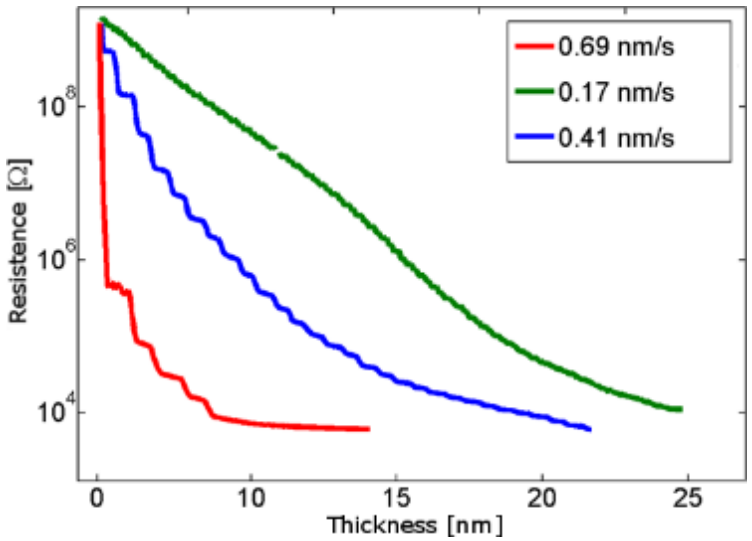

Figure 5.3: Plots of sample electrical resistance versus the equivalent thickness of deposited particles. The three percolation curves approach a resistance of about 10^4 Ω, still they clearly show a critical dependence on the deposition rate, since a much lower amount of clusters is enough to reach this resistance if the deposition is fast (red curve). For sake of graphical clarity, the onset points of the curves have been set to zero nanometres.

5.3.2 Resistive switching

The approaching end of Moore's law as the compass for the technology roadmap of the semiconductor industry[130] has prompted a change of strategy towards the integration of different capabilities such as sensing, actuation, power management, data storage, and remote connectivity on the same device.[131] This requires the fabrication of platforms where the integration of different materials and functionalities is the enabling factor while miniaturization is not the major issue. Among different strategies for the fabrication of this novel class of hybrid devices, the combination of top-down fabrication with bottom-up synthetic methods appears very promising.[132] In particular, devices obtained by the bottom-up assembly of atomic clusters on microfabricated platforms leads to functional properties that are promising for a wide spectrum of applications.[133]

The same considerations are also affecting the way in which computing architectures and data storage systems are integrated on complex platforms. A new approach for computer architectures aims to achieve low-power consumption by using brain-like neuromorphic systems that are characterized by high parallelism and network structures that are able to process information very efficiently.[134–141] One of the most promising architectures[134,140] is based on an assembly of interconnected nanoscale switching elements that exhibit synapse-like behaviour.[140,142,143] The elemental building blocks of these kinds of networks are memristors[143–145] which are nonlinear circuit elements that change their resistance depending on the history of bias applied to them.[146] Memristive behaviour is associated with electrical and structural changes caused by the displacement and rearrangement of mobile ions or oxygen vacancies, the formation and rupture of conductive paths or phase transitions.[145,147–149]

There has been significant progress in the emulation of neurons and synapses using CMOS circuitry[137,138] but the prospect that the same functionality could be achieved from networks of neuron-like and synapse-like elements that are randomly assembled from nanoscale components is very appealing since such biomimetic architectures could potentially by-pass fundamental bottlenecks and cost constraints.[138,140] Bottom-up random assembly of nanoscale building blocks has been proposed as a cheaper and simpler alternative route to fabrication of neuromorphic networks of memristive devices.[140] To create operable networks two basic issues must be addressed: which materials to use and how to pattern them into complex configurations without negatively affecting their functional characteristics.

Metal nanowires and nanoparticles are considered very interesting candidates to solve these issues - for example networks of sulphidised silver nanowires can be used to achieve simple pattern recognition.[134,140] In a similar, yet alternative approach cluster-assembled percolating networks exhibit interesting switching behaviour[150] and numerical simulations[84] show that they may exhibit potentiation in response to applied voltage inputs. Potentiation is a characteristic of biological systems like the brain that comprise neurons and synapses, and results from activation of a number of synapses to produce a connected pathway across the system.[151] In a simplified form such a connection represents learning by the system from its inputs (a memory). These ideas can be seen as aligning with a wider interest in neuromorphic behaviour.[144,152,153]

The assembly of atomic clusters produced in the gas phase has reached a high degree of maturity and it can be considered an enabling technology for the large-scale fabrication of devices for sensor and biomedical applications.[33,97,133] Cluster-assembled materials possess a nanostructure that derives from the individual clusters and which follow universal scaling laws.[91,154] The electrical properties at the percolation threshold of assemblies of metallic nanoparticles and nanoislands have long been subjects of intense investigation as a particular class of inhomogeneous conductors.[86,150,155] Percolation phenomena play a major role in the metal-insulator transitions observed in many such disordered and composite systems,[27,156] and in the anomalous conductivities of ultrathin metallic films.[157–159]

In the next pages I report the main results obtained studying the switching properties of nanostructured materials fabricated with SCBD. The networks are prepared by depositing gold clusters on standard glass substrates or standard printing paper at room temperature of nanoparticles with a density above the electrical percolation threshold. Detailed electrical characterisation reveals complex sequences of switching events with individual events that can be characterised according to three main archetypes. The films exhibit a remarkably reproducible switching behaviour based on the formation and destruction of atomic-scale conductive paths. These points are mainly discussed in paper titled "Facile fabrication of complex networks of memristive devices"[160]. In the paper titled "The nanocoherer : an electrically and mechanically resettable resistive switching device based on gold clusters assembled on paper" [161] the resistance switching activity is studied on a paper substrate. Here, thanks to its flexibility it was possible to study the effect of a mechanical deformation (bending) on the switching activity, demonstrating that this could be controlled through it and that switching event with a resistance ratio up to four orders of magnitude can be induced with the mechanical deformation at fixed voltage applied.

5.3.2.1 Resistance switching in nanostructured materials

The study of resistance switching in pure cluster assembled materials is relatively new and few systems has been explored so far[97,134,162–164]. To the best of our knowledge, no examples of studies regarding pure gold clusters were reported. This made necessary to start this research from the development of a recipe which guarantees the production of nanostructured material which could exhibit resistance switching in a controlled and reproduceable way.

The starting hypothesis was that the switching activity of the sample mainly depended in its nano- and microstructure and hence that its structural properties needed to be well controlled and studied to reproducibly obtain switching devices.

The study of the evolution of the electrical conductance of the sample during its fabrication is a good probe to this purpose. The percolation curve of a nanostructured material represents its fingerprint as it describes how particles are interconnected and how their interconnections evolve in time. This also has the advantage of being recordable in real time during the sample fabrication. The simplicity of this measurement is a guarantee for its reproducibility and reliability. Finally, its acquisition is immediate and shows the whole history of the sample.

As a starting point, we choose to vary the substrate, the deposition rate and the amount of particles deposited. These probably being the parameters which more relevantly affects the grown of a nanostructured material. The fabrication parameters were optimized for growing cluster-assembled films on glass and on paper.

The choice of paper was motivated by the possibility to have a substrate which could be flexed, and which could give to the film an overall 3D structure without requiring an implantation process which would need to take in consideration how the layer of polymer among the clusters affect the switching activity.

The use of SCBD was particularly helpful for these analysis because of the possibility to fabricate many samples per time (exploiting the multiple faces of the sample holder and the rastering technique).

The main results obtained are the following: with this work it was possible to depict an idea of the interplay between the structural and functional properties of the cluster assembled film, and the fabrication parameters able to make the samples switch reproducibly and in a controlled way were found.

The devices are fabricated as described in section 3.3.4.3 and electrically characterized under ambient atmosphere and temperature by applying triangular voltage ramps and recording the resultant current, hence providing the resistance variation in time (see section 4.3.2).

In the beginning of the characterisation, voltage ramps cause small switching events near the maximum of the voltage applied. After some voltage sweeps, dramatic resistance switching occurs meaning that the device is activated. After the activation each device exhibits a complex sequence of switching events. With a change of resistance up to ~ 400%, and the switching activity stabilizes to values which remain stable over days (see figure 1 from reference [160], here attached).

Detailed electrical characterisation reveals complex sequences of switching events with individual switching events that can be characterised according to few main archetypes consisting mainly in a resistance increase at high voltages or in a resistance increase at low voltage. Both these phenomena can be traced back in the formation and destruction of atomic-scale conductive paths (the schematic of the model is shown in figure 3b).

A resistance increase at high voltages can be explained as the application of a voltage tends to increase the resistance of the network by breaking pre-existing connections between particles in the film via electromigration. The resistance decrease at high voltage can be due to an electric field induced diffusion of atoms at the cluster surface and Van der Waals attraction which leads to a gap reduction when the electric field become stronger, causing the formation of the atomic scale wire.

Regarding the cluster assembled on paper (reference [161] here joint), the main result is the observation in the same device two switching distinct behaviours typical of a network of nanoscale switching elements and high resistance ratio switching up to four orders of magnitude (figure 4 from reference [161]). The two observed regimes are both stable, the transition between different switching regimes is reversible, once an electrical state is set, it remains stable over a period of several months.

The mechanical deformation, the bending of the sample in a concave or convex shape is able itself to control the switching activity occurring at a fixed low voltage. By bending the sample it is possible to force the sample to switch between two distinct resistance levels with a resistance ratio of four orders of magnitude, as shown in figure 5 from reference [161].

The device retains a state of internal resistance following the history of the applied voltage similarly to that reported for memristors. Their behaviour is particularly interesting as they exhibited two distinct features. Through the application of suitable voltage ramps, it is indeed possible to obtain, in the same device, either a complex pattern of resistive switching similar to the one observed on glass substrates, or sequences of reproducible and stable switching with an amplitude up to five orders of magnitude. The two different switching regimes in the same device are both stable, the transition between them is reversible, and it can be controlled by applying voltage ramps or by mechanical deformation of the substrate.

The coexistence in the same device of complex switching patterns in a small and high resistance range was never been reported before, to the best of our knowledge, in the literature: complex switching patterns are generally associated with a switching activity spread over a *network of junctions*, while the high resistance ratio switching is found in the breaking and reconnection of a *single junction.*

Mechanical deformation of the sample can also be used to force the sample to switch reversibly from a high resistance (HR) state to a low one (LR), with a resistance ratio up to four orders of magnitude: a macroscopic bending of the device into a concave shape causes a switching from HR to LR, whereas bending to a convex shape induces a switching in the opposite direction. This behavior is reproducible and stable over a very large number of bending cycles. The possibility of changing the resistance state via mechanical deformation is due to the strong adhesion of the cluster-assembled film to the paper substrate, and in both cases the behavior can be related to the breaking and reconnection of connections among the clusters.

The results obtained in both Au/glass and Au/paper systems, shows that the clusters forming the samples behave like switching elements and once assembled in a macroscopic sample, the nanoscopic building blocks partially retain their individuality and are connected by grain boundaries and atomic-scale junctions. The whole system behaves like a complex network which exhibit complex but reproducible switching behaviour over periods of days, even in ambient conditions and using a very simple measurement methodology.

Some analogies with neuromorphic networks were found, making these devices convenient test-bed for exploration of the basic mechanism of the switching processes and also the possibility of convenient fabrication of devices[134,140–142]comprising large numbers of switching elements.

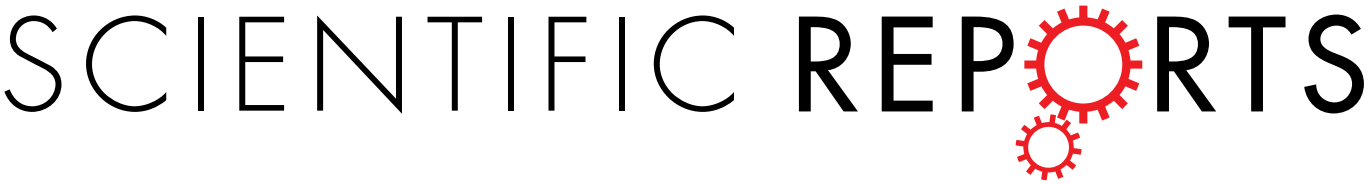

OPEN

Facile fabrication of complex networks of memristive devices

Chloé Minnai[1], Andrea Bellacicca[1], Simon A. Brown[2] & Paolo Milani[1]

Received: 5 April 2017
Accepted: 10 July 2017
Published online: 11 August 2017

We describe the memristive properties of cluster-assembled gold films. We show that resistive switching is observed in pure metallic nanostructured films at room temperature and atmospheric pressure, in response to applied voltage inputs. In particular, we observe resistance changes up to 400% and archetypal switching events that have remarkable symmetry with the applied voltage. We associated this symmetry with 'potentiation' and 'anti-potentiation' processes involving the activation of synapses and of pathways comprising multiple synapses. The stability and reproducibility of the resistance switching, which lasted over many hours, make these devices ideal test-beds for exploration of the basic mechanisms of the switching processes, and allow convenient fabrication of devices that may have neuromorphic properties.

The approaching end of Moore's law as the compass for the technology roadmap of the semiconductor industry[1] has prompted a change of strategy towards the integration of different capabilities such as sensing, actuation, power management, data storage, and remote connectivity on the same device[2]. This requires the fabrication of platforms where the integration of different materials and functionalities is the enabling factor, and miniaturization is not the major issue. Among different strategies for the fabrication of this novel class of hybrid devices, the combination of top-down fabrication with bottom-up synthetic methods appears very promising[3]. In particular, devices obtained by the bottom-up assembly of atomic clusters on microfabricated platforms leads to functional properties that are promising for a wide spectrum of applications[4].

The same considerations are also affecting the way in which computing architectures and data storage systems are integrated on complex platforms. A new approach for computer architectures aims to achieve low-power consumption by using brain-like neuromorphic systems that are characterized by high parallelism and network structures that are able to process information very efficiently[5–12]. One of the most promising architectures[5,11] is based on an assembly of interconnected nanoscale switching elements that exhibit synapse-like behaviour[11,13,14]. The elemental building blocks of these kinds of networks are memristors[14–16] which are nonlinear circuit elements that change their resistance depending on the history of bias applied to them[17]. Memristive behaviour is associated with electrical and structural changes caused by the displacement and rearrangement of mobile ions or oxygen vacancies, the formation and rupture of conductive paths or phase transitions[16,18–20].

Fabrication using standard lithographic techniques such as those used for CMOS technology or for two-terminal planar memristors[8,21,22] is costly and complicated due to the need to deterministically create robust intra- and inter-device connections. There has been significant progress in the emulation of neurons and synapses using CMOS circuitry[8,9] but the prospect that the same functionality could be achieved from networks of neuron-like and synapse-like elements that are randomly assembled from nanoscale components is very appealing since such biomimetic architectures could potentially by-pass fundamental bottlenecks and cost constraints[9,11]. Bottom-up random assembly of nanoscale building blocks has been proposed as a cheaper and simpler alternative route to fabrication of neuromorphic networks of memristive devices[11]. To create operable networks two basic issues must be addressed: which materials to use and how to pattern them into complex configurations without negatively affecting their functional characteristics.

Metal nanowires and nanoparticles are considered very interesting candidates to solve these issues - for example networks of sulphidised silver nanowires can be used to achieve simple pattern recognition[5,11]. In a similar alternative approach cluster-assembled percolating networks exhibit interesting switching behaviour[23] and numerical simulations[24] show that they may exhibit potentiation in response to applied voltage inputs. Potentiation is a characteristic of biological systems like the brain that comprise neurons and synapses, and results from activation of a number of synapses to produce a connected pathway across the system[25]. In a simplified

[1]CIMAINA and Dipartimento di Fisica, Università degli Studi di Milano, via Celoria 16, 20133, Milano, Italy. [2]The MacDiarmid Institute for Advanced Materials and Nanotechnology, Department of Physics and Astronomy, University of Canterbury, Private Bag 4800, Christchurch, 8140, New Zealand. Correspondence and requests for materials should be addressed to S.A.B. (email: simon.brown@canterbury.ac.nz) or P.M. (email: paolo.milani@mi.infn.it)

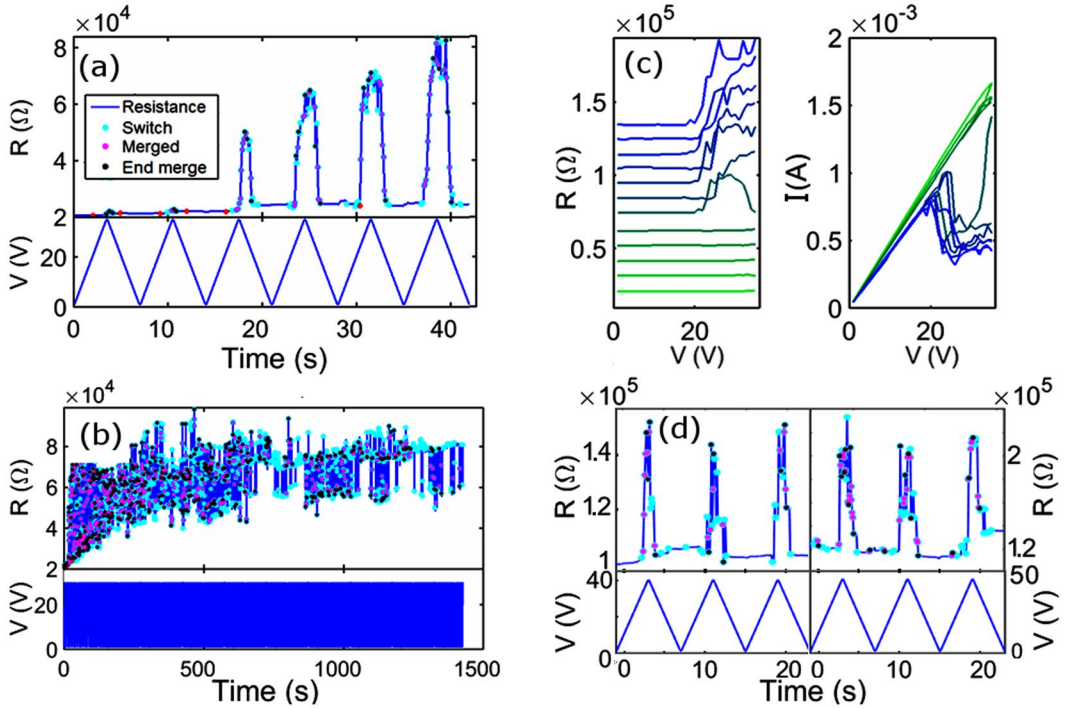

Figure 1. Switching events in SCBD Au-glass thin film. **(a)** Detailed view of initial switching events. Each event is labelled with a coloured symbol. Top: the resistance changes as a function of time (R(t)). Bottom: the voltage ramp (V(t)), in this case between 0 and $V_{max} = 40$ V. **(b)** Much longer switching sequence; the first 40 s corresponds to the data in (**a**). **(c)** R(V) and I(V) curves corresponding to switching events reported in (**a**). R(V) curves are offset for clarity. The first voltage ramps are shown in bright green and the last in deep blue. Alternate curves correspond to increases and decreases in voltage. **(d)** Comparison between the switching behaviour of the devices near the end of the first (left panel) and second (right panel) days of measurements.

form such a connection represents learning by the system from its inputs (a memory). These ideas can be seen as aligning with a wider interest in neuromorphic behaviour[15,26,27].

The assembling of atomic clusters produced in the gas phase has reached a high degree of maturity and it can be considered an enabling technology for the large-scale fabrication of devices for sensor and biomedical applications[4,28,29]. Cluster-assembled materials possess a nanostructure that derives from the individual clusters and which follow universal scaling laws[30,31]. The electrical properties at the percolation threshold of assemblies of metallic nanoparticles and nanoislands have been subjects of intense investigation as a particular class of inhomogeneous conductors[23,32,33]. Percolation phenomena play a major role in the metal-insulator transitions observed in many such disordered and composite systems[34,35], and in the anomalous conductivities of ultrathin metallic films[36–38].

Here we present the facile fabrication of cluster-assembled gold nanostructured films that exhibit memristive switching properties. The networks are prepared by supersonic cluster beam deposition (SCBD)[39] on standard glass substrates at room temperature of nanoparticles with a density close to the electrical percolation threshold. Detailed electrical characterisation reveals complex sequences of switching events and we show that the individual switching events can be characterised according to 3 main archetypes. The films exhibit remarkably reproducible switching behaviour and we show that switching mechanism is based on the formation and destruction of atomic-scale conductive paths.

Results

During the cluster deposition the device resistance is observed to drop approximately exponentially, consistent with a reduction in the size of tunnelling gaps between the particles as the film coverage increases[24,40]. By monitoring the resistance it is possible to terminate the deposition when the cluster density is close to the percolation threshold and the resistance is in the range of interest (1 kΩ to 1 MΩ).

By applying voltage ramps (to a maximum voltage, V_{max}) to the cluster-assembled films we observe the onset of complex switching behaviour, with individual switching events resulting in discrete changes in the measured resistance (see Fig. 1 and the Supplementary Information). Initially, at low $V_{max} \sim 10$ V, no switching is observed for any of the films. As V_{max} is increased beyond 10 V, we observed two different types of behaviour. If the device's initial resistance is lower than about 10 kΩ, the voltage ramping causes a continuous gradual increase in the resistance. No switching events occur even for V ~60 V. On the other hand, samples with a resistance higher than 10 kΩ exhibit a well-defined voltage threshold beyond which a complex cascade of switching events occurs. $V_{threshold}$ increases with the initial resistance of the sample: 30–40 V is enough to activate samples with an initial resistance in the range 10–20 kΩ, whilst 90–100 V is necessary to activate samples with a resistance in the range

60–70 kΩ. We focus here on the most common, archetypal switching events that were recorded thousands of times in all devices fabricated with a resistance higher than 10 kΩ. Samples with different densities of nanoparticles and hence with lower and higher resistances have been also produced and characterized as reported in the Supplementay Informations (Fig. S1).

Figure 1 shows a typical switching history of a cluster-assembled film with an initial resistance of ~20 kΩ in the first few voltage ramps (Fig. 1(a)) small switching events, hardly visible on this scale, are observed near V_{max}, then (3rd voltage cycle) much more dramatic switching is observed. In each cycle a cascade of events is observed during the increase in voltage, as discussed later, this behaviour is similar to the potentiation process discussed in ref. 28. The remarkable feature is that when the voltage decreases there is an almost exact reversal of the sequence: the resistance decreases so that the final resistance at the end of each voltage ramp (when the voltage returns to ~0 V) is very similar to the initial resistance. In the 6th cycle the cascade of switching events results in a change of resistance of ~80 kΩ, an increase of ~400%.

For each device, we continued ramping the voltage to the same V_{max} until it was established that the switching was reproducible over many cycles, or until the number of events diminished. In the latter case, it was almost always found that the switching was reactivated when V_{max} was increased by a few volts. We observe that right after the activation, and when V_{max} is increased, the switching rate and amplitude increase. Subsequently the sample resistance stabilizes at a slightly higher value, and the switching effect (amplitude and rate) returns to values which are then consistent for days - see Fig. 1(d). This stabilization process is particularly evident right after the activation (see Fig. 1(b)), another example is shown in Fig. S1. This behaviour is typically observed for many hours up to several days. Note that the device resistance remains in a well-defined range over many hours of continuous measurements (Fig. 1(b)). In Fig. 1(d) we show that the devices exhibit a similar switching behaviour over periods of days: typical data towards the end of the first and second days of measurements are shown in the left and right panels respectively.

For the sake of completeness, we report in Fig. 1(c) the I(V) and R(V) curves corresponding to the data shown in Fig. 1(a). Obviously, the increase in resistance in each cycle corresponds to the decrease in current at higher voltages in each I(V) curve. I(V) and R(V) curves are typically used to demonstrate memristive behaviour [18,19] but in the present case we believe R(t) curves are a more effective way of showing the observed switching behaviour, and all the data presented below is shown in this form.

Each device exhibits a complex sequence of switching events (as in Fig. 1), but when $V_{max} \sim V_{threshold}$ the switching is less complex and archetypal events can be identified, as shown in Fig. 2.

In Fig. 2(a), the pink region highlights a typical event in which a stepwise increase in resistance is observed while increasing the voltage (Type A event), and the green region highlights a stepwise decrease in resistance that occurs while decreasing the voltage (Type B event). In both cases, the resistance change is reversed by a single stepwise jump at a comparable voltage (typically ~ 10 V) on the subsequent voltage ramp. In both cases the device changes state from a low voltage, low resistance 'ON' state to a high voltage, high resistance 'OFF' state.

One of the remarkable features of these transitions is their symmetry i.e. the transitions occur at almost exactly the same voltage during the increasing and decreasing voltage ramps and the measured resistance returns to its original value. This means that a connection breaks when the voltage is at its high level and *the same* connection is restored when the voltage is at a low level. Spikes in resistance near V_{max} are also commonly observed (e.g. at the left edge of the green region in Fig. 2(a)); we believe that these are examples of Type A events that last for a shorter time.

A further type of switching event is shown in the blue panel of Fig. 2(a). In these Type C events there is a symmetrical increase in resistance at *low* voltage. Note that these events are different from those of the Type B where the increase in R occurs at high voltages. Type C events clearly have a different physical origin to Type A and B events and are due to destruction of connections as the voltage is reduced, or, completely equivalently, the formation of connections as the voltage is increased[23].

The data presented so far were obtained with unipolar voltage ramps. Further information is obtained from *bipolar* voltage ramps i.e. voltage ramps in which consecutive cycles have opposite polarities i.e. $+V_{max}$ and $-V_{max}$. Figure 2(b) shows R(t), R(V) and I(V) curves for bipolar switching to a low voltage, low resistance state similar to the Type B events. Note however that in these cases the symmetric switching events happen at the same voltage (i.e. |V|) but with *opposite* sign. Hence the switching mechanism is polarity *independent*.

Figure 2(c) shows a typical dataset in which multiple switching events are observed on each voltage cycle. Events are observed only above a threshold voltage and the device resistance returns to a value close to the original one when the voltage drops below the threshold. In each cycle there is a cascade of switching events which generally increase the resistance, although the resistance commonly switches back and forth a few times between the new level and the previous level. When the voltage is decreased the pattern of switching is reversed until, below the threshold, the resistance returns to a value close to its original value.

The inset of Fig. 2(c) (shaded yellow) shows that the resistance values measured while increasing the voltage are similar to those measured during the decreasing voltage. This "Mayan pyramid" profile results from a series of consecutive Type A events and suggests strongly that the same states of the switches are accessed on both increasing and decreasing voltage ramps. Similar cascades are observed on many consecutive voltage ramps with the resistance always returning to a value close to its original value.

It can also be noticed in Figs 1(a) and 2(c) (inset), that more events occur when the voltage is close to V_{max}. This is even more evident in Fig. 2(d) where during each ramp, the voltage is kept constant for some time at the V_{max} value. A cascade of events is observed when the voltage is maximum, suggesting that the connections are continuously broken and re-formed.

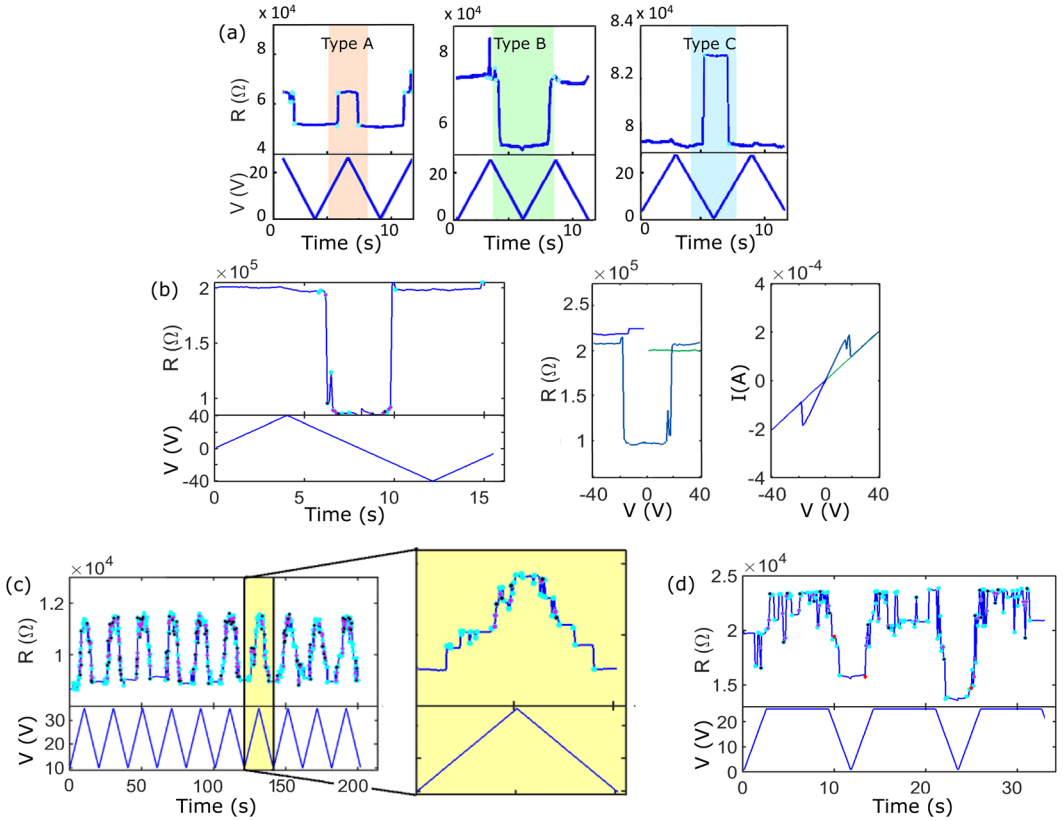

Figure 2. Examples of characteristic switching events. **(a)** The three simplest types of events are reported: resistance increase at high voltage (pink region); resistance decrease at low voltages (green region); and resistance increase at low voltage (blue region). These archetypes are referred to as Type A, B and C respectively. **(b)** Example of bipolar switching occurring while the voltage is ramped between positive and negative V_{max} values. The R(t), R(V) and I(V) curves are shown. **(c)** Examples of highly reproducible sequences of multiple overlapping switching events on consecutive cycles resulting in 'anti-potentiation'; in the inset: multiple well-resolved events resulting in a 'Mayan pyramid' R(t) profile. **(d)** Switching events recorded at high voltage.

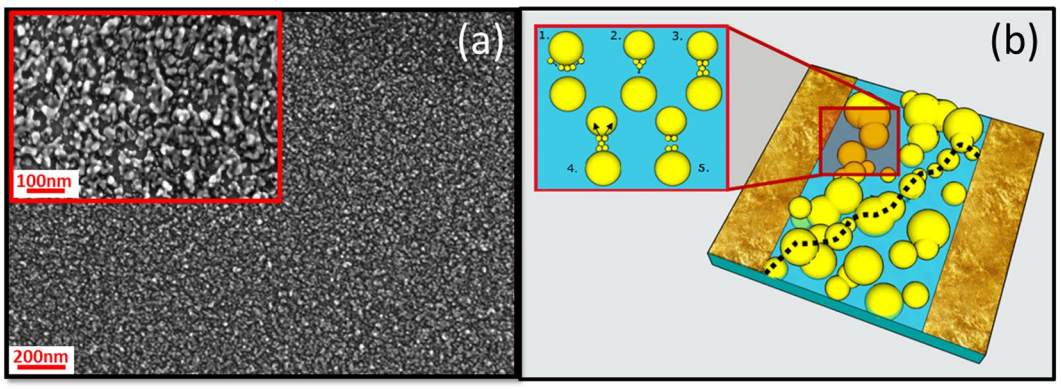

Figure 3. SCBD Au-Glass thin film. **(a)** Au clusters deposited on glass substrate with SCBD acquired with a Field Emission Scanning Electron Microscopy (FEG-SEM). **(b)** Schematic illustration of a percolating-tunneling system. A tunneling path is marked with a dashed line. In the inset the main phenomena which can lead to the formation of an atomic scale wire in a tunnel gap are depicted: 1. EFISD or van der Waals forces; 2. EFIE process; 3. Connected atomic wire. 4. Electromigration affecting the atomic wire: 5. Breaking of the atomic wire due to electromigration.

Discussion

SEM images of the nanostructured films (Fig. 3(a)) clearly show a complex structure resulting from the random assembling of clusters to form a non-continuous film: both connected particles and tunnel gaps can be distinctly

observed, as shown schematically in Fig. 3(b) where, for sake of simplicity, complex aggregated structures have been replaced with large spherical particles. We believe that the mechanism underlying the observed complex switching phenomena can be related to the formation, growth and breaking of junctions between the particles forming the films. A similar model was used to explain the formation of atomic scale wires in percolating films of Sn nanoparticles[23].

In the inset of Fig. 3(b) a sequence of cartoons shows the mechanism leading to atomic wire formation (inset, sequence 1–3) and destruction (inset, sequence 3–5). The mechanism of formation or growth of connections between adjacent grains may be similar to that which is responsible, in the macroscopic case, for the Branly effect[34, 41, 42]. There, the effect is usually explained by diffusion of atoms at an already existing junction or gap and by Joule heating, but we believe that Joule heating alone cannot be responsible for switching since in our experience it causes local destruction of the films that cannot be reversed.

We believe that the strong electric field within the tunnel gaps in the film leads to Electric Field Induced Surface Diffusion (EFISD) or Electrical Field Evaporation (EFIE) (inset, 2) and that attractive van der Waals forces (which are independent of applied electric field) can also drive formation of atomic scale connections. In the case of non-connected grains, as the gap reduces, the electric field become stronger, causing the formation of an atomic scale wire (inset, 3). EFISD, EFIE and van der Waals forces can all create new pathways between the particles. On the other hand, the high electrical currents within the reorganized junctions and the newly formed connections, cause electromigration[22] (inset, 4) and, as a consequence, the breakdown and the disconnection of the path. We believe these processes are at the origin of the switching events reported so far. In particular, for both Type A and B events, the application of a voltage tends to increase the resistance of the network by breaking pre-existing connections between particles in the film via electromigration (inset, sequence 3–5).

Physically, Type A and Type B events have the same origin: a high resistance at high voltage is due to broken connections and at low resistance at low voltage is due to the formation of connections in the film. However, events that result in a high resistance at high voltage (Type A events) are caused when an established connection is broken by the high current that is flowing, resulting in a higher resistance. In Type B events the decrease in resistance during the decreasing voltage ramp is due to formation of a new atomic scale wire, which is broken at a comparable voltage on the next increasing voltage ramp.

The subsequent decreases in resistance occur due to reconnection across those gaps, which are most likely due to van der Waals forces[23, 43]: the wire appears to be formed at voltages below some threshold (typically 10–30 V) because the current that is flowing is no longer sufficient to break the wire. At higher voltages, the wire cannot reform because electromigration instantly breaks it. This argument is also supported by the data shown in Fig. 2(d). Here, when the voltage is kept constant at the maximum value of 25 V, the connections are continuously being broken (causing increases in resistance) and then re-forming (causing the resistance returning to its original value). In this model the state of the network is dynamic, and the observed resistance is determined by the complex interplay of events that break and re-form individual atomic scale wires.

The remarkable symmetry of the Type A and B events indicates that the apparent threshold voltage for switching is the voltage at which the interplay between van der Waals forces and electromigration are equally balanced. Below this voltage van der Waals forces dominate and connections are formed, while at higher voltages electromigration prevails and the connection is broken.

Type C events can be explained with a similar mechanism in which the opposite effects dominate: an increase in voltage causes EFIE or EFISD, forming a connection across the gap between two particles and reducing the device resistance, then, while the voltage is being decreased, the electric current breaks the wire and opens the connection. Hence there is a distinction between electric field driven Type C events and Type A and B events where decreases in resistance are driven by van der Waals forces.

We emphasize again that after a switching event, the resistance returns to approximately its initial value at the end of each voltage cycle. The fact that the same events are repeated on multiple voltage cycles (see for example, Fig. 2(a) and (c)) implies that the *same* connections that are broken while increasing the voltage are re-formed as the voltage is reduced.

The observed features could in principle be explained by other models used to describe similar switching in related systems, but careful examination of the data allows us to eliminate such models. For example, Coulomb blockade (i.e. charging of nanoparticles in the network) can be ruled out by the data from bipolar voltage ramps in Fig. 2(b) since it is demonstrated that the switching behaviour is *insensitive* to the polarity of the applied voltage. In a model of Coulomb blockade, it is inconceivable that charging could consistently occur at a positive voltage and then discharging occurs at an equal and opposite negative voltage. The presence of offset charges in real devices[44, 45] also means that practically speaking Coulomb charging is an asymmetrical process. A Coulomb charging picture can also be ruled out on more general grounds: refs 44, 46 show that for similar size particles charging effects are expected only at low temperatures and require voltages smaller than ~10 V.

Further alternative switching models that could be considered are those responsible for memristive behaviour in oxide devices, which is typically due to either the motion of defects (typically oxygen vacancies[16, 18]), or to the formation of nanoscale chains of particles due to diffusion of ions in an oxide matrix[21, 47]. Both of these models can be ruled out because in those cases resetting the device state *requires* a change in polarity of the applied voltage (either the oxygen vacancies or the ions must be driven back to their original positions). In contrast, in our devices, the switching behaviour is insensitive to the polarity of the applied voltage. For similar reasons it is possible to rule out electrochemical processes[12] as being responsible for the switching behaviour since they also require a reversal of polarity to achieve reproducible switching between states.

It is also interesting to notice that the cascade of switching events that lead to resistance *decreases* (e.g. Fig. 2(c)) is very similar to a potentiation process (i.e. the formation of a pathway comprising groups of particles connected synapses) predicted by simulation in refs 23, 28 and the neuromorphic behaviour observed in ref. 5. A remarkable feature of the present data however is that in many cases (for example Fig. 1(a)) the applied voltage

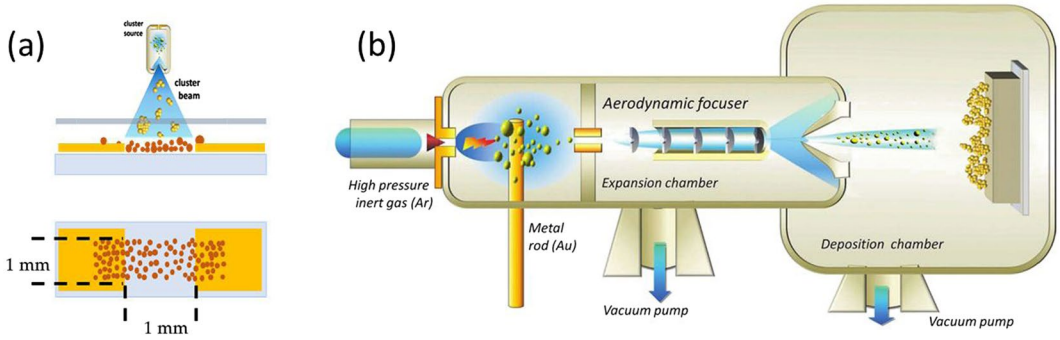

Figure 4. Device fabrication with Supersonic Cluster Beam Deposition. (**a**) Schematic of the cluster-assembled film fabrication. (**b**) Schematic representation of the SCBD apparatus (not to scale).

first *increases* the resistance of the device. This suggests that each cycle begins with a kind of 'anti-potentiation' (breaking of a chain of synaptic connections).

Conclusions

We have shown that complex networks of memristive switching elements can be fabricated by assembling Au clusters on glass substrates by SCBD. Au clusters are deposited in a ballistic regime producing nanostructured films where the nanoscopic building blocks partially retain their individuality and are connected by grain boundaries and atomic-scale junctions. The observed switching behaviour occurs due to the formation (destruction) of nanoscale connections between particles which occurs in response to high electric fields and van der Waals forces (electromigration).

It is remarkable that this atomic scale switching process yields reproducible switching behaviour over periods of days, even in ambient conditions and using a very simple measurement methodology. These devices therefore provide a convenient test-bed for exploration of the basic mechanism of the switching processes and also the possibility of convenient fabrication of neuromorphic devices[5,11–13] comprising large numbers of switching elements.

An important factor that requires further investigation is the role of the network in determining the switching characteristics of the individual elements: both the activity of other switching elements[5] and the series resistance of the network[22] can be expected to influence the switching activity. The first steps in evaluating device performance for real-world applications will be to further explore potentiation in these devices as a route towards both processing and storage[24], and to determine whether these dynamical networks can be used for simple pattern recognition problems[48].

We remark finally that several architectures for neuromorphic computing have been under development for a number of years, and in some cases (e.g. cross-bar architectures[10,49]) relatively well-defined specifications have been developed for the required device parameters. A recent review[10] makes it clear that despite intensive efforts, significant progress is still required for all kinds of neuromorphic devices in order to achieve useful computational performance, and therefore that there is still a need for novel approaches that circumvent the known problems. Target device performance depends significantly on architecture[10], and is surprisingly varied: for example, high resistances and relatively small percentage changes in resistance are required for computation using some crossbar architectures[49]. Our experiments are consistent with the modelling of percolating networks[28], in which the individual junctions exhibit high on / off ratios, but our self-assembled devices will need to meet a set of performance criteria whose development will require further detailed modelling and investigations of possible computational algorithms[10,49].

Methods

Device fabrication. A schematic representation of the film fabrication steps is reported in Fig. 4(a). Neutral gold clusters are deposited on glass slides in the gap between two gold electrodes previously fabricated by thermal evaporation. The cluster-assembled layer forms a 1×10 mm strip partially covering the electrodes. The surface roughness of the glass substrates was measured by AFM to be 1.5 ± 0.3 nm. The gap between the electrodes is 1 mm and the overall device dimension including contact pads is 10×10 mm.

Clusters are deposited by means of a SCBD apparatus equipped with a pulsed microplasma cluster source (PMCS)[39]. In Fig. 4(b) a schematic of the apparatus is reported. The PMCS consists of a ceramic body with a cavity in which a gold target is vaporized by a localized electrical discharge supported by a pulsed injection of an inert gas at high pressure. The metal atoms, sputtered from the target, aggregate in the source cavity to form metal clusters; the mixture of clusters and inert gas expands through a nozzle forming a supersonic beam into an expansion chamber kept at a pressure of about 10^{-6} mbar. Electrically neutral nanoparticles exiting the PMCS are aerodynamically accelerated in a highly-collimated beam with divergence lower than 1° and with a kinetic energy of roughly 0.5 eV/atom[29,39]. The central part of the cluster beam enters, through a skimmer, a second vacuum chamber (deposition chamber) where the beam is intercepted by the substrate. During the cluster deposition, a fixed small voltage (in the range 1–100 mV) is applied to the electrodes in order to monitor *in situ* the evolution of the electrical resistance of the cluster-assembled film.

Electrical Characterisation. The devices have been electrically characterized under ambient atmosphere by applying voltage ramps and recording the resultant current, hence providing the resistance variation in time. A triangular voltage ramp from 0 V to a maximum voltage, V_{max}, is applied, and V_{max} is gradually increased until switching is observed.

References

1. Waldrop, M. More than Moore. *Nature* **530**, 144–147 (2016).
2. Zhang, G. Q. & Roosmalen A. V. *More than Moore: Creating High Value Micro/Nanoelectronics Systems*. (Springer Science, LLC, 2009).
3. Curri, M. L., Comparelli, R., Striccoli, M. & Agostiano, A. Emerging methods for fabricating functional structures by patterning and assembling engineered nanocrystals. *Phys. Chem. Chem. Phys.* **12**, 11153–11796 (2010).
4. Milani, P. & Bettini, L. G. Nano- and Micromanufacturing with Nanoparticles Produced in the Gas Phase: An Emerging Tool for Functional and Length-Scale Integration, in *Gas-Phase Synthesis of Nanoparticles* (ed. Huttel Y.) (Wiley, 2017).
5. Avizienis, A. V. *et al*. Neuromorphic Atomic Switch Networks. *PLoS One* **7**, e42772 (2012).
6. Yang, J. J., Strukov, D. B. & Stewart, D. R. Memristive devices for computing. *Nat. Nanotechnol.* **8**, 13–24 (2013).
7. Choi, S., Sheridan, P. & Lu, W. D. Data Clustering using Memristor Networks. *Sci. Rep.* **5**, 10492 (2015).
8. Xia, Q. *et al*. Memristor-CMOS hybrid integrated circuits for reconfigurable logic. *Nano Lett.* **9**, 3640–3645 (2009).
9. Ohno, T. in *Micro-and Nanoelectronics: Emerging Device Challenges and Solutions* (ed. Brozek, T.) **35**, 283 (Taylor & Francis Group, 2014).
10. Burr, G. W. *et al*. Neuromorphic computing using non-volatile memory. *Adv. Phys. X* **2**, 89–124 (2017).
11. Stieg, A. Z. *et al*. Emergent criticality in complex turing B-type atomic switch networks. *Adv. Mater.* **24**, 286–293 (2012).
12. Ohno, T. *et al*. Sensory and short-term memory formations observed in a Ag2S gap-type atomic switch. *Appl. Phys. Lett.* **99**, 14–17 (2011).
13. Ohno, T. *et al*. Short-term plasticity and long-term potentiation mimicked in single inorganic synapses. *Nat. Mater.* **10**, 591–595 (2011).
14. Kim, H., Yang, C. & Chua, L. O. Memristor Bridge Synapses. in. *Proceedings of the IEEE* **100**, 2061–2070 (2012).
15. Le Doux, J. Synaptic self: How our brains become who we are. (Books, Penguin, 2003).
16. Prodromakis, T., Toumazou, C. & Chua, L. Two centuries of memristors. *Nat. Mater.* **11**, 478–481 (2012).
17. Chua, L. O. Memristor—The Missing Circuit Element. *IEEE Trans. Circuit Theory* **18**, 507–519 (1971).
18. Strukov, D. B., Snider, G. S., Stewart, D. R. & Williams, R. S. The missing memristor found. *Nature* **453**, 80–83 (2008).
19. Waser, R. & Aono, M. Nanoionics-based resistive switching memories. *Nat. Mater.* **6**, 833–840 (2007).
20. Gaba, S., Cai, F., Zhou, J. & Lu, W. D. Ultralow Sub-1-nA operating current resistive memory with intrinsic non-linear characteristics. *IEEE Electron Device Lett.* **35**, 1239–1241 (2014).
21. Yang, J. J. *et al*. The mechanism of electroforming of metal oxide memristive switches. *Nanotechnology* **20**, 215201 (2009).
22. Durkan, C. & Welland, M. E. Size effects in the electrical resistivity of polycrystalline nanowires. *Phys. Rev. B* **61**, 14215–14218 (2000).
23. Sattar, A., Fostner, S. & Brown, S. A. Quantized conductance and switching in percolating nanoparticle films. *Phys. Rev. Lett.* **111**, 136808 (2013).
24. Fostner, S., Brown, R., Carr, J. & Brown, S. A. Continuum percolation with tunneling. *Phys. Rev. B - Condens. Matter Mater. Phys.* **89**, 75402 (2014).
25. Chialvo, D. R. Emergent complex neural dynamics. *Nat. Phys.* **6**, 744–750 (2010).
26. Mead, C. Neuromorphic Electronic Systems. *Proc. IEEE* **78**, 1629–1636 (1990).
27. Merolla, P. A. *et al*. A million spiking-neuron integrated circuit with a scalable communication network and interface. *Science* **345**, 668–673 (2014).
28. Fostner, S. & Brown, S. A. Neuromorphic behavior in percolating nanoparticle films. *Phys. Rev. E* **92**, 52134 (2015).
29. Schulte, C., Podesta, A., Lenardi, C., Tedeschi, G. & Milani, P. Quantitative Control of Protein and Cell Interaction with Nanostructured Surfaces by Cluster Assembling. *Acc. Chem. Res.* **50**, 231–239 (2017).
30. Podestà, A. *et al*. Nanomanufacturing of titania interfaces with controlled structural and functional properties by supersonic cluster beam deposition. *J. Appl. Phys.* **118**, 234309 (2015).
31. Dunbar, A. D. F., Partridge, J. G., Schulze, M., Scott, S. & Brown, S. A. Measurement of the Conductivity Exponent in Random Percolating Networks of Nanoscale Bismuth Clusters. in *Proceedings of the IEEE* 0–5 (2003).
32. Kirkpatrick, S. Percolation and Conduction. *Rev. Mod. Phys.* **45**, 574–588 (1973).
33. Jensen, P. Growth of nanostructures by cluster deposition: Experiments and simple models. *Rev. Mod. Phys.* **71**, 1695–1735 (1999).
34. Gefen, Y. & Shih, W.-H. Nonlinear Behavior near the Percolation Metal-Insulator Transition. *Phys. Rev. Lett.* **57**, 3097–3100 (1986).
35. Beloborodov, I. S., Lopatin, A. V. & Vinokur, V. M. Granular electronic systems. *Rev. Mod. Phys.* **79**, 469–518 (2007).
36. Sondheimer, E. H. The mean free path of electrons in metals. *Adv. Phys.* **1**, 1–42 (1952).
37. Arnason, S. B., Herschfield, S. P. & Hebard, A. F. Bad Metals Made with Good-Metal Components. *Phys. Rev. Lett.* **81**, 3036–3939 (1998).
38. Voss, R. F., Laibowitz, R. B. & Allessandrini, E. I. Fractal (Scaling) Clusters in Thin Gold Films near the Percolation Threshold. *Phys. Rev. Lett.* **49**, 1441–1445 (1982).
39. Wegner, K., Piseri, P., Tafreshi, H. V. & Milani, P. Cluster beam deposition: a tool for nanoscale science and technology. *J. Phys. D: Appl. Phys.* **39**, R439–R459 (2006).
40. Lassesson, A., Brown, S. A., Lith, J. & Van & Schulze, M. Electrical characterization of gold island films: A route to control of nanoparticle deposition. *Appl. Phys. Lett.* **93**, 203111 (2008).
41. Creyssels, M. *et al*. Some aspects of electrical conduction in granular systems of various dimensions. *Eur. Phys. J. E Soft Matter* **23**, 255–264 (2007).
42. Duxbury, P. M., Beale, P. D. & Leath, P. L. Size Effects of Electrical Breakdown in Quenched Random Media. *Phys. Rev. Lett.* **57**, 1052–1055 (1986).
43. Olsen, M., Hummelgård, M. & Olin, H. Surface Modifications by Field Induced Diffusion. *PLoS One* **7**, e30106 (2012).
44. Elteto, K., Antonyan, E. G., Nguyen, T. T. & Jaeger, H. M. Model for the onset of transport in systems with distributed thresholds for conduction. *Phys. Rev. B - Condens. Matter Mater. Phys.* **71**, 1–13 (2005).
45. Middleton, A. A. & Wingreen, N. S. Collective transport in arrays of small metallic dots. *Phys. Rev. Lett.* **71**, 3198–3201 (1993).
46. Parthasarathy, R., Lin, X.-M. & Jaeger, H. M. Electronic Transport in Metal Nanocrystal Arrays: The Effect of Structural Disorder on Scaling Behavior. *Phys. Rev. Lett.* **87**, 186807 (2001).
47. Sawa, A. Resistive switching in transition metal oxides. *Nanotechnology* **11**, 28–36 (2008).
48. Kulkarni, A. D. Artificial Neural Networks for Image Understanding. (John Wiley & Sons, 1997).
49. Gokmen, T. Acceleration of Deep Neural Network Training with Resistive Cross-Point Devices: Design Considerations. *Front. Neurosci.* **10**, 1–13 (2016).

Acknowledgements

S.A.B. gratefully acknowledges funding support from the MacDiarmid Institute of Advanced Materials and Nanotechnology, the Marsden Fund and the Ministry of Business Innovation and Employment in New Zealand. The authors are grateful to Saurabh Bose for suggesting some of the analysis procedures, to Luca Puricelli for the AFM characterization on the substrates and to Matteo Mirigliano for assistance in electrical characterization.

Author Contributions

C.M. and A.B. performed the experiments, C.M., S.B. and P.M. wrote the main manuscript text and All authors reviewed the manuscript.

Additional Information

Supplementary information accompanies this paper at doi:10.1038/s41598-017-08244-y

Competing Interests: The authors declare that they have no competing interests.

Publisher's note: Springer Nature remains neutral with regard to jurisdictional claims in published maps and institutional affiliations.

LETTER

The nanocoherer: an electrically and mechanically resettable resistive switching device based on gold clusters assembled on paper

NANO FUTURES

LETTER

The nanocoherer: an electrically and mechanically resettable resistive switching device based on gold clusters assembled on paper

RECEIVED
28 February 2018

ACCEPTED FOR PUBLICATION
1 March 2018

PUBLISHED
23 March 2018

Chloé Minnai[1], **Matteo Mirigliano**[1], **Simon A Brown**[2,3] and **Paolo Milani**[1,3]

[1] CIMAINA and Dipartimento di Fisica, Università degli Studi di Milano, via Celoria 16, I-20133 Milano, Italy
[2] The MacDiarmid Institute for Advanced Materials and Nanotechnology, Department of Physics and Astronomy, University of Canterbury, Private Bag 4800, Christchurch 8140, New Zealand
[3] Authors to whom any correspondence should be addressed.

E-mail: paolo.milani@mi.infn.it **and** simon.brown@canterbury.ac.nz

Keywords: resistive switching, nanostructured films, electrical transport, memristor, cluster-assembling

Abstract

We report the realization of a resettable resistive switching device based on a nanostructured film fabricated by supersonic cluster beam deposition of gold clusters on plain paper substrates. Through the application of suitable voltage ramps, we obtain, in the same device, either a complex pattern of resistive switchings, or reproducible and stable switchings between low resistance and high resistance states, with an amplitude up to five orders of magnitude. Our device retains a state of internal resistance following the history of the applied voltage similar to that reported for memristors. The two different switching regimes in the same device are both stable, the transition between them is reversible, and it can be controlled by applying voltage ramps or by mechanical deformation of the substrate. The device behavior can be related to the formation, growth and breaking of junctions between the loosely aggregated gold clusters forming the nanostructured films. The fact that our cluster-assembled device is mechanically resettable suggests that it can be considered as the analog of the coherer: a switching device based on metallic powders used for the first radio communication system.

Resistive switching phenomena, in which the application of a voltage or current causes a reversible change of the electrical resistance state are observed in a wide variety of solid-state systems [1, 2]. Recently considerable interest has been focused on the use of resistive switching devices (RSDs) based on nanoscale metal–insulator–metal (MIM) junctions for the realization of non-volatile memories and systems enabling bioinspired computing, as alternatives to silicon-based von Neumann architectures [3, 4].

A particular class of RSDs is represented by memristors: in 1971 Chua proposed the existence of a fourth passive circuit element called the memristor, which complements the resistor, capacitor, and inductor [5]. Memristors are characterized by a reversible resistive switching between low resistance (LR) and high resistance (HR) states when subjected to a periodic voltage [5, 6]. In 2008 Williams and co-workers reported the fabrication and characterization of a solid-state memristor [7] based on nanoscale transition metal oxide films in which the memristive behavior was attributed to ionic (dopant) transport [8, 9].

Increasing attention is also being focused on percolating systems of randomly deposited nanoparticles and nanowires exhibiting room temperature resistive switching, both during, and in response to, applied voltages. This easily fabricated random system can yield stable long-lived states that are similar to those typical of single junction systems [10]. Percolating films of nanoparticles exhibit neuromorphic behavior [11] so they can be considered as building blocks for neural networks and physical systems with emergent collective computational abilities [12] obtainable with low-cost and tolerance-driven fabrication techniques.

The scientific community progressively realized that resistive switching fingerprints were serendipitously observed and documented in systems characterized by a wide range of structures and dimensions [13, 14]. The

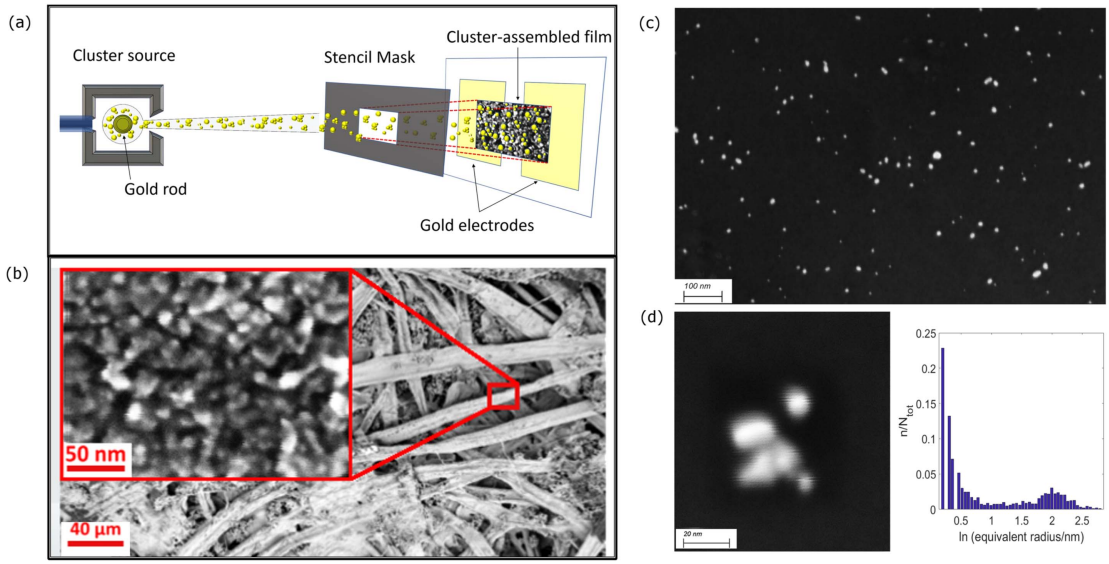

Figure 1. (a) Schematic representation of the experimental set-up (not to scale) and cluster deposition process; (b) SEM micrograph of a typical region of cluster-assembled gold film deposited on paper. The fibrous structure of the substrate is evident. The inset shows a high magnification of the granular structure of the cluster-assembled layer on a single cellulose fiber. (c) SEM imaging of primeval gold clusters deposited on silicon substrate for the characterization of the distribution of their dimensions. (d) Left: a high magnification SEM image of an island formed by gold clusters on silicon. The clusters only partially coalesce and form larger aggregates with loose contacts and junctions. Right: histogram, in logarithmic scale, of the equivalent radius of the primeval clusters.

first report of resistive switching dates back to the beginning of the 20th century, where it was observed in a macroscopic system based on metallic powders: this device was known as the 'coherer' [15, 16]. The coherer consisted of a glass ampoule with two electrodes connected by metallic filings (usually iron or silver) [15]. The initial HR state of loosely connected metallic grains can be switched to an LR state by the interaction with an electromagnetic field (e.g. radio waves) or by the flow of an electric current [16, 17]; the coherer can switch back to its original HR state by mechanical stimulation, for example by tapping or rotating the ampoule [16]. The coherer exhibited a pinched hysteresis in *V*–*I* characteristics [13, 18] and enabled the invention of the radio telegraph system by Marconi [19].

Remarkably, one hundred years later the microscopic mechanism underlying the coherer behavior is still only partially understood. While, in general, it is accepted that percolative behavior of the grains is playing a role [16, 20–23], different models have been suggested such as Joule heating leading to micro-welding of the filings, electrical breakdown, and grain rearrangement due to local electric forces [15].

Here we demonstrate that nanostructured films assembled on plain paper substrates by supersonic cluster beam deposition of gold clusters, show a complex pattern of resistive switching or sequences of reproducible and stable LR to HR switching with an amplitude up to five orders of magnitude. The application of a voltage ramp allows us to select, reversibly, one of the two different behaviors on the same device. The cluster-assembled devices remain in the set resistance state over a period of several months and they can be reset to their initial electrical state by imposing a suitable voltage or by a mechanical deformation of the flexible paper substrate. The possibility of mechanically resetting the device suggests that cluster-assembled nanostructured gold films can be considered as analogous to the coherer.

Resistors on plain paper can be printed by SCBD [24], we used the same experimental approach to fabricate RSDs on paper (figure 1(a)).

Neutral gold clusters are produced with a pulsed microplasma cluster source (PMCS) consisting of a ceramic body with a cavity in which a gold target is vaporized by a localized electrical discharge supported by a pulsed injection of an inert gas at high pressure [25]. The species sputtered from the target aggregate in the cavity to form clusters; the mixture of clusters and inert gas expands through a nozzle forming a supersonic beam into an expansion chamber (figure 1(a)). Clusters exiting the PMCS are aerodynamically accelerated in a highly collimated beam with a divergence lower than 1° and with a kinetic energy of ~0.5 eV/atom [25]. The central part of the cluster beam enters, through a skimmer, a second vacuum chamber kept at a pressure of $\sim 10^{-6}$ mbar, where the beam is intercepted by the substrate [24]. The size distribution of the deposited clusters has a bimodal size distribution peaked at 1 nm and 7 nm (figure 1(d)).

Clusters are deposited in the gap (1 mm) between two gold electrodes previously deposited by thermal evaporation on substrates consisting of commercial plain white paper for ink-jet and laser printer (Xerox Digital, 75 g m^{-2}, roughness: 170 ml min^{-1}). This approach guarantees a high adhesion both of the electrodes to

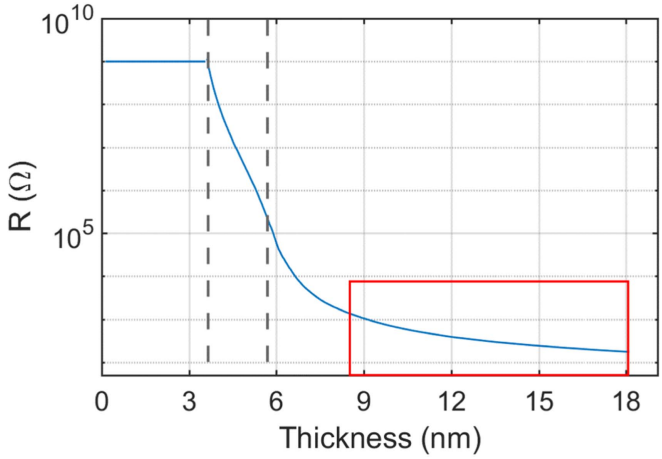

Figure 2. Percolation curve showing the evolution of the resistance with the film thickness. The two vertical lines identify the onset of the tunneling and percolating regimes. Resistive switching behavior was characterized for samples with initial resistance in the region framed with the red line.

the substrate and of the gold clusters to the gold electrodes and the substrate [24]. The overall device dimensions are 5 × 20 mm (figure 1(a)) and the cluster-assembled layer forms a 1 × 10 mm strip partially covering the electrodes.

The microscale and nanoscale structures of a typical cluster-assembled thin film on paper are shown in figure 1(b). The substrate is composed of interwoven fibers with different lengths and with diameters in the range ∼1–20 μm. The gold clusters decorate the surface of the fibers (inset of figure 1(b)) forming a granular film organized over multiple different length scales and closely reminiscent of the structure of the underlying substrate on the microscale. The observed nanoscale morphology is typical of film growth in the ballistic regime [26] and it is characterized by high porosity and roughness, nanoscale grain boundaries, poorly connected and non-compact structures with low density compared to bulk gold [27]. In figure 1(d) we report a high magnification SEM image showing a loosely connected aggregate formed by the juxtaposition of several clusters.

The electrical properties of metallic thin films containing a large number of defects and characterized by disorder at the micro and nanoscale are deeply influenced by the structure of the system [27–29]. In the case of cluster-assembled films, the deposition conditions (deposition rate, mass distribution, stoichiometry, etc) determine the detailed morphology of the granular structure and hence the electrical properties [28, 30].

In figure 2 we show the evolution of the cluster-assembled film resistance with the increase of the film thickness (percolation curve) measured *in situ* during the film deposition. Up to a thickness of roughly 3.5 nm we observe an insulating behavior, then electrical conduction starts and the film resistance decreases exponentially, indicating that the conduction is via tunneling [31]. For a thickness larger than ∼6 nm, the resistance evolution shows a different trend that can be fitted with a power law, indicating the onset of the percolation regime [31].

By monitoring the evolution of the resistance *in situ* and in real time [27], we can fabricate samples with a fixed initial resistance in a wide range of values to study how the initial structural conditions influence the performance of the devices. In this case we selected the initial resistances in the region where the percolating threshold is exceeded, as framed by the red box in figure 2.

Each sample was characterized by applying voltage ramps with an Agilent E5270A equipped with a high-power source monitor unit E5280 that can perform the application of a dc voltage and the measurement of a dc current. Each voltage ramp started from a minimum value up to a peak voltage. For each voltage the current was measured and the resistance was calculated using Ohm's law. We measured the current every 100 ms, since our device is not intended for memory applications, as in the case of MIM devices, we did not characterize the switching time during write and read operations [32, 33].

After the application of at least 200 ramps, the peak voltage was progressively increased until the onset of switching was observed i.e. when discrete changes were observed in the measured resistance, corresponding to individual switching events within the film.

After the onset of switching, the cluster-assembled films show a complex pattern of switching events between different well-defined resistance levels. Figure 3(a) reports a typical example of the switching between two resistance levels, caused by the application of a voltage ramp in an interval between 1 and 5 V. The switching events are very regular and reproducible with resistance changes of ∼130%.

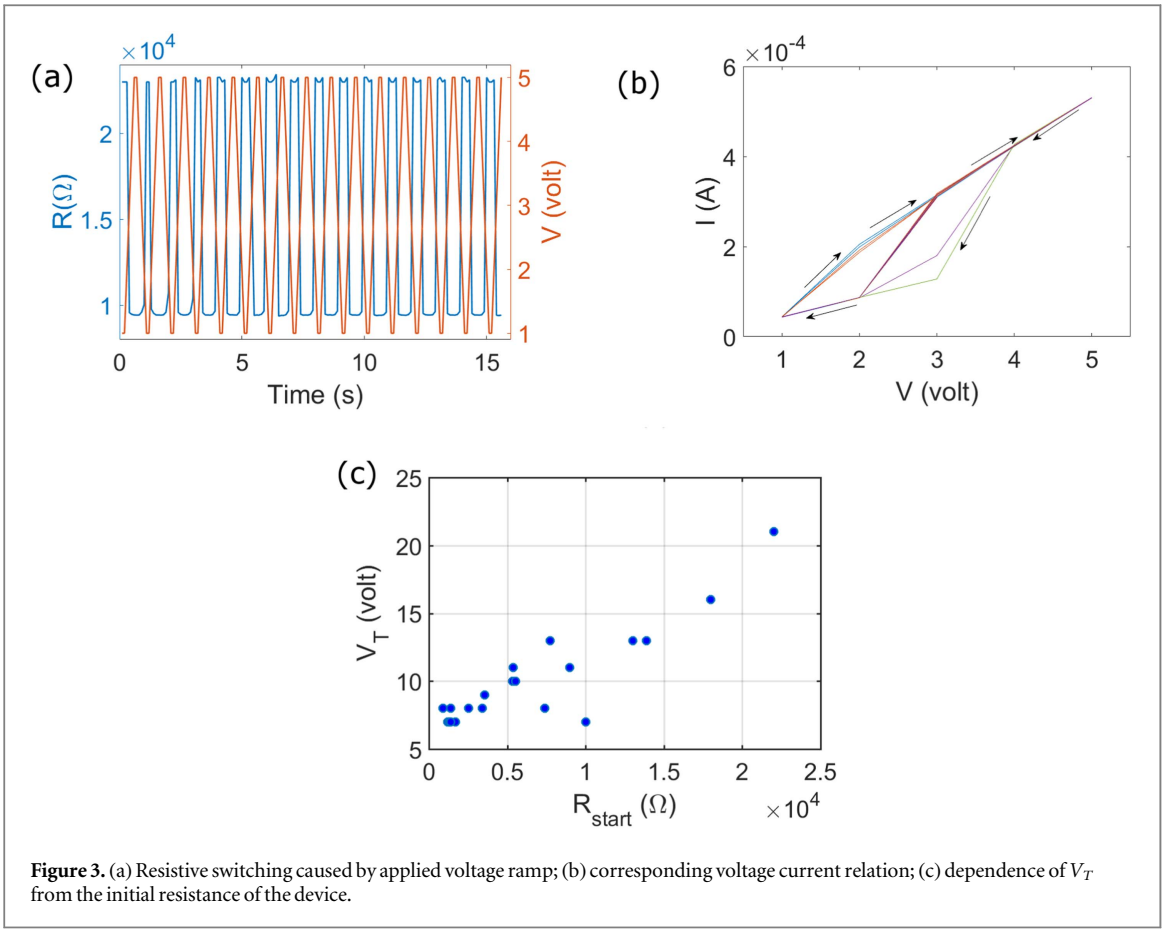

Figure 3. (a) Resistive switching caused by applied voltage ramp; (b) corresponding voltage current relation; (c) dependence of V_T from the initial resistance of the device.

The $I(V)$ plots shown in figure 3(b) exhibit a hysteretic behavior. These plots show that the switching activity is well controlled via the voltage applied: the resistance is switching from the low to the high level in response to the voltage applied. Once the sweep is stopped the device remain in the last electrical state set. We applied a voltage of 0.1 V to read the resistance state finding negligible evolution over a period of months. This behavior is typical of atomic switch networks [10, 34, 35]. We have reported these features for cluster-assembled films deposited on glass substrates [34].

By further increasing the peak voltage, we observe a transition in the sample behavior with the onset of LR to HR switching (see below). The transition occurs at critical peak voltage values V_T in a range between 8–20 V, the LR and HR states are typically separated by 4–5 orders of magnitude.

The threshold voltage V_T for the onset of LR to HR switching depends on the initial resistance of the device (different position of the percolation curve) as shown in figure 3(c) where we show V_T for initial sample resistances in the range 10^2–10^4 Ω. A clear trend to higher V_T values is observed for larger initial resistances, which is consistent with the switching mechanism described below. As a result, depending on the initial resistance of the sample it is possible to choose voltage ramps in order to determine, *a priori*, whether the device will exhibit complex switching patterns in a small resistance range or more dramatic LR to HR switching.

The dependence of V_T from the initial resistance of the cluster-assembled film can be qualitatively understood by considering that electrical properties of the as-deposited films depend upon the degree of organization and packing of the deposited clusters, as it is typical of the ballistic deposition regime governing cluster assembling [27, 36]. A high initial resistance is due to a cluster network with low structural and electrical connectivity requiring a higher critical voltage to activate new electrical junctions and form a large number of effective electrical conducting pathways [10, 37].

Figure 4(a) shows a typical example of switching from the LR to the HR state, with the film resistance changing from ~10^4 to ~10^8 Ω. In response to high-voltage ramps, the resistance increases by about 3 orders of magnitude then, when the voltage applied is significantly reduced or the polarity is inverted (figure 4(b)), it switches back to a value close to the original one.

LR-HR switching can be induced and controlled by applying symmetric bipolar ramps as shown in figure 4(c): the type of switching takes place according to the maximum absolute value of the voltage applied and the resistance switches back when the voltage is reduced. In figure 4(d) the corresponding current–voltage curves are shown.

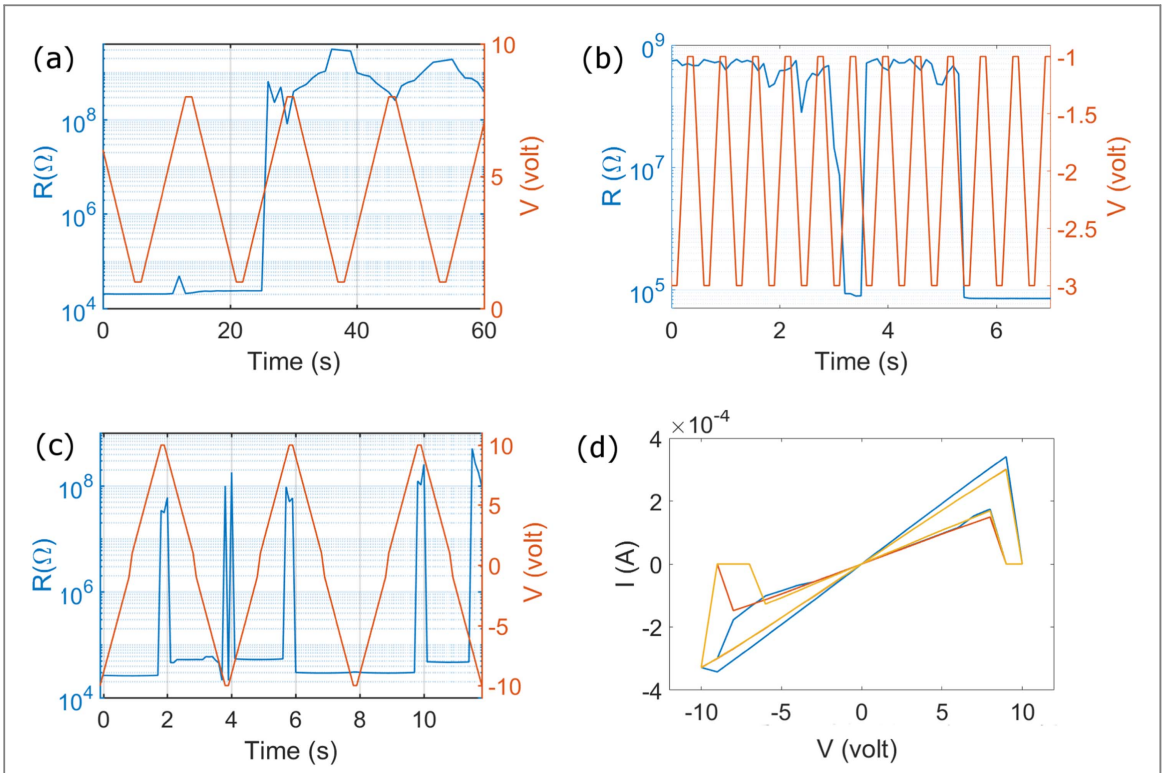

Figure 4. (a) LR to HR switching induced by positive bias ramps; (b) HR to LR switching induced by a ramp with negative voltage; (c) LR to HR switching event induced by bipolar ramps; (d) corresponding voltage–current relation showing the hysteretic loop.

It has to be noted the high degree of consistency of the switching activity shown in figure 4(c): almost all the voltage sweeps have a HR switching occurring at the maximum absolute value of the applied voltage. However, we did not observe long sequences of HR switching occurring with the same regularity reported in figures 3(b) and (c). This might be a consequence of a dramatic change of the cluster network structure that causes the transition between the insulating and conductive regime [37].

The transition between the two switching regimes reported in figures 3 and 4 is reversible: when the voltage of the ramp is significantly reduced or the polarity is inverted, we observe that the resistance of the sample returns back to a value close to the initial one, and exhibits only small switching events (figure 3(a)) as long as the maximum ramp voltage does not reach a critical value that causes another LR to HR switching event. It should be noted that after the first switching event, the threshold voltage beyond which we observe the LR-HR regime is lower.

The mechanism of the switching behavior can be related to the formation, growth and breaking of junctions between the particles forming the films [38, 39]. Atomic scale junctions between grains are formed and dynamically modified by electric field driven migration of atoms, whereas junctions are broken by electromigration [35]. The number and the structure of the junctions (presence of narrow necks and gaps) depend on the initial structure of the cluster-assembled films and hence on the initial cluster size distribution and deposition rate, as suggested by the increase in the observed in the switching voltage V_T with the initial film resistance (figure 3(b)). The influence of the micro and nanostructure on the onset of metallic conductivity regime in granular metal films has been reported also for systems assembled by atomic deposition [40].

A key result of our experiments is that cluster-assembled films on paper exhibit two different switching regimes that are easily controllable and reversible through the applied voltage. The coexistence in the same device of complex switching patterns in a small resistance range and LR to HR bi-stable switching has never been reported, to the best of our knowledge, in the literature: complex switching patterns are generally associated with a switching activity spread over a network of junctions [38], while the HR to LR switching is found in the breaking and reconnection of a single junction [9].

Mechanical deformation of the sample can also be used to force the sample to switch reversibly from the HR state to the LR one: a macroscopic bending of the device into a concave shape (figure 5) causes a switching from HR to LR, whereas bending to a convex shape induces a switching in the opposite direction. This behavior is reproducible and stable over a very large number of bending cycles. The possibility of changing the resistance state via mechanical deformation is due to the strong adhesion of the cluster-assembled film to the paper

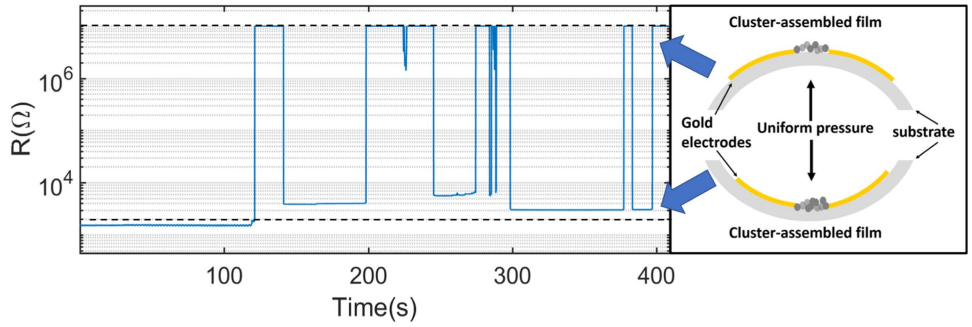

Figure 5. LR to HR switching induced by mechanical stimulation of the substrate, as schematized in the right panel.

substrate, and in both cases the behavior is related to the breaking and reconnection of atomic scale connections among the clusters [39].

In particular, when the paper is bent in a concave shape (figure 5, bottom) the fibrous network is locally compressed, forcing the cluster in a smaller volume and setting new physical (and hence electrical) contacts, causing a decrease in the sample resistance. On the contrary, when the sample is bent in the convex shape (figure 5, top), the fibers are spread in a wider volume, the number of cluster interconnections is reduced and the sample resistance switch to a higher level.

The micro structure of the paper substrate, based on fibrous networks, forces the nanoparticles to organize following preferential directions at the nano and microscale, thus favoring the formation of conducting pathways prone to switching. The pathways have a hierarchical organization resembling that of the substrate. On a single fiber the clusters organize themselves in a way similar to that observed on glass [34], the structures resulting at this scale should be responsible for the switching behavior in a limited resistance range. The preferential organization of the cluster-assembled layer along fibers favors the formation of structures prone to generate switches from LR states to HR states. The role of the paper substrate is mainly structural and the influence of paper hygroscopicity can be ruled out: the devices are operated in air in ambient humidity and the presence of water adsorbed on paper does not affect the overall behavior of the paper devices (the switching behavior reported in figure 3(a) is similar to that reported for clusters-assembled gold films deposited on glass substrates [34]).

In summary, we have shown the possibility of fabricating an RSD by cluster assembling of nanostructured gold films on paper. Our approach allows the deposition of nanostructured films over large areas and with a variety of patterns with an easily scalable two-step fabrication process [24, 41].

We observed in the same device two distinct switching behaviors typical of a network of nanoscale switching elements and LR to HR switching, respectively. The two observed regimes are both stable, the transition between different switching regimes is reversible, once an electrical state is set, it remains stable over a period of several months. The cluster-assembled device can be reset by applying suitable voltage ramps or by the mechanical deformation of the substrate. This latter feature, not yet reported for the 'modern' RSD, suggests that our cluster-assembled devices can be considered as mechanically resettable coherers based on the assembly of nanoscale grains.

ORCID iDs

Simon A Brown https://orcid.org/0000-0002-6041-4331
Paolo Milani https://orcid.org/0000-0001-9325-4963

References

[1] Lee J S, Lee S and Won Noh T 2015 *Appl. Phys. Rev.* **2** 031303
[2] Yang J J, Strukov D B and Stewart D R 2013 *Nat. Nanotechnol.* **8** 13
[3] Burr G W *et al* 2016 *Adv. Phys.* X **2** 89
[4] Borghetti J, Snider G S, Kuekes P J, Yang J J, Stewart D R and Williams R S 2010 *Nature* **464** 873
[5] Chua L O 1971 *IEEE Trans. Circuit Theory* **18** 507
[6] Prodromakis T, Toumazou C and Chua L O 2012 *Nat. Mater.* **11** 478
[7] Strukov D B, Snider G S, Stewart D R and Williams R S 2008 *Nature* **453** 80
[8] Waser R and Aono M 2007 *Nat. Mater.* **6** 833
[9] Sawa A 2008 *Mater. Today* **11** 28
[10] Demis E C, Aguilera R, Sillin H O, Scharnhorst K, Sandouk E J, Aono M, Stieg A Z and Gimzewski J K 2015 *Nanotechnology* **26** 204003

[11] Bose S K, Mallinson J B, Gazoni R M and Brown S A 2017 *IEEE Trans. Electron Device* **64** 5194
[12] Hopfield J J 1982 *Proc. Natl Acad. Sci. USA* **79** 2554
[13] Chua L O 2011 *Appl. Phys.* A **102** 765
[14] Gandhi G, Aggarwal V and Chua L O 2013 *IEEE Circuits Syst. Mag.* **13** 8
[15] Falcon E and Castaing B 2005 *Am. J. Phys.* **73** 302
[16] Dorbolo S, Ausloos M and Vandewalle N 2003 *Phys. Rev.* E **67** 040302
[17] Vandembroucq D, Boccara A C and Roux S 1997 *J. Phys.* III **7** 303
[18] Bose J 1899 *Proc. R. Soc.* **65** 166
[19] Bridgman R 2001 *Phys. World* **14** 29
[20] Dorbolo S, Merlen A, Creyssels M, Vandewalle N, Castaing B and Falcon E 2007 *Europhys. Lett.* **79** 54001
[21] Dorbolo S, Ausloos M and Vandewalle N 2002 *Appl. Phys. Lett.* **81** 936
[22] Falcon E, Castaing B and Creysless M 2003 *Eur. Phys. J.* B **34** 201
[23] Ausloos M, Pękala M, Latuch J, Mucha J, Vanderbemden P, Vertruyen B and Cloots R 2004 *J. Appl. Phys.* **96** 7338
[24] Caruso F, Bellacicca A and Milani P 2016 *Appl. Phys. Lett.* **108** 163501
[25] Wegner K, Piseri P, Vahedi Tafreshi H and Milani P 2006 *J. Phys. D: Appl. Phys.* **39** R439
[26] Borghi F, Sogne E, Lenardi C, Podestà A, Merlini M, Ducati C and Milani P 2016 *J. Appl. Phys.* **120** 055302
[27] Barborini E, Corbelli G, Bertolini G, Repetto P, Leccardi M, Vinati S and Milani P 2010 *New J. Phys.* **12** 073001
[28] Arnason S B, Herschfield S and Hebard A 1998 *Phys. Rev. Lett.* **81** 3936
[29] Gall D 2016 *J. Appl. Phys.* **119** 085101
[30] van Attekun P M, Th M, Woerlee P H, Verkade G C and Hoeben A A M 1984 *Phys. Rev.* B **29** 645
[31] Ambrosetti G, Grimaldi C, Balberg I, Maeder T, Danani A and Ryser P 2010 *Phys. Rev.* B **81** 155434
[32] Hermes C *et al* 2011 *IEEE Electron Device Lett.* **32** 1116
[33] Chen A B, Choi B J, Yang X and Chei I W 2012 *Adv Funct. Mater.* **22** 546
[34] Minnai C, Bellacicca A, Brown S A and Milani P 2017 *Sci. Rep.* **7** 7955
[35] Sattar A, Fostner S and Brown S A 2013 *Phys. Rev. Lett.* **111** 136808
[36] Podestà A, Borghi F, Indrieri M, Bovio S, Piazzoni C and Milani P 2015 *J. Appl. Phys.* **118** 234309
[37] Nirmalraj P N *et al* 2012 *Nano Lett.* **12** 5966
[38] Stieg A Z, Avizienis A V, Sillin H O, Martin-Olmos C, Aono M and Gimzewski J K 2012 *Adv. Mater.* **24** 286
[39] Fostner S and Brown S A 2015 *Phys. Rev.* E **92** 052134
[40] Wei H and Eilers H 2009 *J. Phys. Chem. Solids* **70** 459
[41] Bettini L G, Bellacicca A, Piseri P and Milani P 2017 *Flexible Print. Electron.* **2** 025002

6 Conclusions

In my PhD work I studied the optical and electrical properties of cluster assembled thin films (CAF) and metal – polymer nanocomposites MPNs fabricated with supersonic cluster beam deposition and implantation. I have undertaken and developed a systematic approach for the production and characterization of these systems in order to achieve fundamental information on their structural and functional properties and to assess the possibility of exploiting their properties for the realization of a novel class of devices.

I demonstrated that the use of SCBI for the implantation of noble metal clusters enable the formation of interfacial nanocomposites with stable and reproducible optical properties even upon substantial stretching.

The interest was to create the proof of principle of optical devices which could be controlled and tuned with mechanical deformation. To reach this goal, it was first necessary to understand how mechanical deformation (in particular uniaxial stretching), affects the organization of the nanoparticle in the nanocomposite and understand the interplay between this and the functional properties of the material (its plasmonic response in particular).

The main results obtained are the following: the Au-PDMS nanocomposites show a plasmon peak shift upon deformation depending on the implanted clusters volume fraction with a stable red shift up to 180 nm with a deformation of 50%. Cyclic stretching induces a rearrangement and reorganization of the embedded clusters affecting the plasmonic behavior. This results in an almost complete disappearance of the plasmon shift for samples with volume fractions below 30% after few hundreds of stretching cycles. For larger volume fractions, a substantial plasmon shift remains and stabilizes after a suitable mechanical post deposition treatment, providing the evidence that nanocomposites produced by SCBI can be used as tunable optical filters or as components for stretchable optical devices

Thanks to the simple structure of the nanocomposites fabricated with SCBI, it was possible to correlate the experimental results with FDTD simulations, providing a simple and reliable model describing the nanoparticles reorganization induced by stretching. In particular, I demonstrated that the plasmonic shift is not induced by the stretching itself, rather by the compression induced in the transversal direction. This model was confirmed by the study of the evolution of the resistance also in the direction perpendicular to the stretching one.

The possibility to use MPN for the fabrication of optical devices suitable for applications in the field of the adaptive optics was also demonstrated with the study of the reflectance properties of diffracting grating prepared by replication in PDMS of a master and made reflective by implantation of gold clusters with supersonic cluster beam implantation.

Such gratings are reflective and bendable, so they can be adapted to concave surfaces to add focusing power to the diffracting elements. In particular, I demonstrated the possibility of reconstructing a point source and a vertically extended source with a spatial resolution of about 80

μm and a spatial one of about 3 nm, without the use of any further optical element but the grating stuck to an ellipsoidal surface.

This is of particular interest in view of developing miniaturized and cheap optical setups which still have competitive resolving power.

A consistent part of my work was also devoted to the characterization of the electrical properties of cluster-assembled gold films as a function of the growth conditions. The evolution of the conductivity as a function of film thickness has been systematically characterized and interpreted in the framework of the percolation theory. The percolation curve of a nanostructured material represents its fingerprint as it describes how particles are interconnected and how their interconnections evolve in time.

Cluster-assembled gold films near the percolation threshold showed resistive switching behaviour. Au clusters partially retain their individuality and are connected by grain boundaries and atomic-scale junctions. The electrical properties of the systems in response to a voltage applied were explored and recipes to fabricate robust and reproducible devices which exhibit resistance switching were developed. The resistive switching activity was studied on system made depositing gold clusters on different substrates.

The observed switching behaviour occurs due to the formation (destruction) of nanoscale connections between particles which occurs in response to high electric fields and van der Waals forces (electromigration).

I observed that this switching process yields reproducible switching behaviour over periods of days, even in ambient conditions and using a very simple measurement methodology. These devices therefore provide a convenient test-bed for exploration of the basic mechanism of the switching processes and also the possibility of convenient fabrication of neuromorphic devices comprising large numbers of switching elements.

I also showed the possibility to fabricate resistive switching devices by cluster assembling of nanostructured gold films on paper by depositing nanostructured films over large areas and with a variety of patterns with an easily scalable two-step fabrication process.

The use of paper as a substrate allowed to obtain in the same device two distinct switching behaviours typical of a network of nanoscale switching elements and the low resistance to high resistance switching respectively. The two observed regimes were both stable, the transition between different switching regimes was reversible, once an electrical state is set, it remained stable over a period of several months. The cluster-assembled device can be reset by applying suitable voltage ramps or by mechanical deformation of the substrate.

The mechanical deformation, the bending of the sample in a concave or convex shape was able itself to control the switching activity occurring at a fixed low voltage. By bending the sample, it was possible to force the switching between two distinct resistance levels with a resistance ratio of four orders of magnitude.

7 Bibliography

1. Heer, W. A. De. The physics of simple metal clusters : experimental aspects and simple models. *Rev. Mod. Phys.* **65,** 611 (1993).
2. Kreibig, U. & Vollmer, M. *Optical Properties of Metal Clusters*. *Springer* (1995).
3. Van Wees, B. J. *et al.* Quantized conductance of point contacts in a two-dimensional electron gas. *Phys. Rev. Lett.* **60,** 848–850 (1988).
4. Abeles, B., Sheng, P., Coutts, M. D. & Arie, Y. Advances in Physics Structural and electrical properties of granular metal films. *Adv. Phys.* **3,** 407–461 (1975).
5. Paolo Milani - private comunication.
6. Perez, A. *et al.* Cluster assembled materials : a novel class of nanostructured solids with original structures and properties. *J. Phys. D. Appl. Phys.* **30,** 709 (1997).
7. Barborini, J. E. *et al.* The influence of nanoscale morphology on the resistivity of cluster-assembled nanostructured metallic thin films. *New J. Phys.* **12,** (2010).
8. Jain, P. K., Huang, X. & El-sayed, I. H. Review of Some Interesting Surface Plasmon Resonance-enhanced Properties of Noble Metal Nanoparticles and Their Applications to Biosystems. *Plasmonics* **2,** 107–118 (2007).
9. Daniel, M. & Astruc, D. Gold Nanoparticles : Assembly , Supramolecular Chemistry , Quantum-Size-Related Properties , and Applications toward Biology , Catalysis , and Nanotechnology. (2004).
10. Caseri, W. Nanocomposites of polymers and metals or semiconductors : Historical background and optical properties. *Macromol. Rapid Commun.* **21,** 705–722 (2000).
11. Faraday, M. *Experimental Researches in Chemistry and Physics*. *Taylor and Francis* (1858).
12. Faraday, M. Experimental relations of gold (and other metals) to light. *Philos. Trans. R. Soc. A* 145–181 (1857).
13. Rayleigh, Lord. Philos. Mag. J. Sci., Ser. 5 12, 81 (1881). *Philos. Mag. J. Sci.* **12,** (1881).
14. Burda, C., Chen, X., Narayanan, R. & El-sayed, M. A. *Chemistry and Properties of Nanocrystals of Different Shapes*. (2005).
15. Jain, P. K., Huang, W. & El-sayed, M. A. On the Universal Scaling Behavior of the Distance Decay of Plasmon Coupling in Metal Nanoparticle Pairs : A Plasmon Ruler Equation. *Nano Lett.* **7,** 2080–2088 (2007).
16. El-sayed, M. A. Some Interesting Properties of Metals Confined in Time and Nanometer Space of Different Shapes. *Acc. Chem. Res.* **34,** 257–264 (2001).

17. Kelly, K. L., Coronado, E., Zhao, L. L. & Schatz, G. C. The Optical Properties of Metal Nanoparticles: The Influence of Size, Shape, and Dielectric Environment. *J. Phys. Chem. B* **107,** 668–677 (2003).

18. Link, S. & El-sayed, M. A. Size and Temperature Dependence of the Plasmon Absorption of Colloidal Gold Nanoparticles. **1,** 4212–4217 (1999).

19. Ung, T., Liz-marza, L. M. & Mulvaney, P. Optical Properties of Thin Films of Au@SiO2 Particles. *J. Phys. Chem.* **105,** 3441–3452 (2001).

20. Katz, E. & Willner, I. Integrated nanoparticle–biomolecule hybrid systems: synthesis, properties, and applications. *Angew. Chemie Int. Ed.* **43,** 6042–6108 (2004).

21. Hutter, B. E. & Fendler, J. H. Exploitation of Localized Surface Plasmon Resonance **. 1685–1706 (2004). doi:10.1002/adma.200400271

22. Knebl, D. *et al.* Gap plasmonics of silver nanocube dimers. *Phys. Rev. B* **93,** 081405–081410 (2016).

23. Rosi, N. L. & Mirkin, C. A. Nanostructures in Biodiagnostics. (2005).

24. Alivisatos, P. The use of nanocrystals in biological detection. **22,** 47–52 (2004).

25. Aslan, K., Lakowicz, J. R. & Geddes, C. D. Plasmon light scattering in biology and medicine : new sensing approaches , visions and perspectives. doi:10.1016/j.cbpa.2005.08.021

26. Jensen, P. & Lyon-, C. B. Growth of nanostructures by cluster deposition : Experiments and simple models. **71,** 1695–1735 (1999).

27. Beloborodov, I. S., Lopatin, A. V & Vinokur, V. M. Granular electronic systems. *Rev. Mod. Phys.* **79,** 469–518 (2007).

28. Creyssels, M. *et al.* Some aspects of electrical conduction in granular systems of various dimensions. **264,** 255–264 (2007).

29. Wegner, K., Piseri, P., Tafreshi, H. V. & Milani, P. Cluster beam deposition : a tool for nanoscale science and technology. (2006). doi:10.1088/0022-3727/39/22/R02

30. Nery, E. W. & Kubota, L. T. Sensing approaches on paper-based devices : a review. 7573–7595 (2013). doi:10.1007/s00216-013-6911-4

31. Lei, D. Y., Aubry, A., Luo, Y., Maier, S. A. & Pendry, J. B. Plasmonic interaction between overlapping nanowires. *ACS Nano* **5,** 597–607 (2011).

32. Middleton, A. A. & Wingreen, N. S. Collective transport in arrays of small metallic dots. *Phys. Rev. Lett.* **71,** 3198–3201 (1993).

33. Schulte, C., Podesta, A., Lenardi, C., Tedeschi, G. & Milani, P. Quantitative Control of Protein and Cell Interaction with Nanostructured Surfaces by Cluster Assembling. *Acc. Chem. Res.* **50,** 231–239 (2017).

34. Bréchet, Y. *et al.* Polymer Based Nanocomposites : Effect of Filler-Filler and Filler-Matrix Interactions. *Adv. Eng. Mater.* **3,** 571–577 (2001).

35. Maxwell, D. J., Emory, S. R. & Nie, S. Nanostructured Thin-Film Materials with Surface-Enhanced Optical Properties. *Chem. Mater.* **13,** 1082–1088 (2001).

36. Ung, T. & Liz-marza, L. M. Gold nanoparticle thin films. **202,** 119–126 (2002).

37. Hedayati, M. K. *et al.* Design of a Perfect Black Absorber at Visible Frequencies Using Plasmonic Metamaterials. 5410–5414 (2011). doi:10.1002/adma.201102646

38. Abraham, J. W., Hinz, A., Strunskus, T., Faupel, F. & Bonitz, M. Formation of polymer-based nanoparticles and nanocomposites by plasma-assisted deposition methods. (2018).

39. Faupel, F. *et al.* Deposition of Nanocomposites by Plasmas. **544,** 537–544 (2007).

40. Ambrosetti, G. On the Insulator-Conductor Transition in Polymer Nanocomposites. *PhD the* (ÉCOLE POLYTECHNIQUE FÉDÉRALE DE LAUSANNE, 2010).

41. El-sayed, M. A. Some Interesting Properties of Metals Confined in Time and Nanometer Space of Different Shapes. **34,** 257–264 (2001).

42. Hsu, S., Rodarte, A. L., Som, M., Arya, G. & Tao, A. R. Colloidal Plasmonic Nanocomposites : From Fabrication to Optical Function. *Chem. Rev.* **118,** (2018).

43. Faupel, B. F., Zaporojtchenko, V. & Strunskus, T. Metal-Polymer Nanocomposites for Functional Applications **. *Adv. Eng. Mater.* **12,** 1177–1190 (2010).

44. Maier, A. *Plasmonics: Fundamentals and Applications*. (springer, 2007).

45. Xie, B. *et al.* A tunable palladium nanoparticle film-based strain sensor in a Mott variable-range hopping regime. *Sensors Actuators A. Phys.* **272,** 161–169 (2018).

46. Zhang, X., Zhang, J., Liu, H., Su, X. & Wang, L. Soft plasmons with stretchable spectroscopic response based on thermally patterned gold nanoparticles. *Sci. Rep.* **4,** 4182 (2014).

47. Malek, S. C. ., Ee, H.-S. . & Agarwal, R. S. Multiplexed Metasurface Holograms on a Stretchable Substrate. *Nano Lett.* **17,** (2017).

48. Ghisleri, C. *et al.* Nanocomposite-based stretchable optics. **1026,** 1020–1026 (2013).

49. Porter, J., Queener, H., Lin, J., Thorn, K. & Awwal, A. A. S. *Adaptive optics for vision science: Principles, practices, design, and applications*. **171,** (John Wiley & Sons, 2006).

50. Grewe, B. F., Voigt, F. F., van�t Hoff, M. & Helmchen, F. Fast two-layer two-photon imaging of neuronal cell populations using an electrically tunable lens. *Biomed. Opt. Express* **2,** 2035–2046 (2011).

51. Solgaard, O., Sandejas, F. S. A. & Bloom, D. M. Deformable grating optical modulator. *Opt. Lett.* **17,** 688–690 (1992).

52. Druon, F. *et al.* Wave-front correction of femtosecond terawatt lasers by deformable mirrors. *Opt. Lett.* **23,** 1043–1045 (1998).

53. Grzybowski, B., Qin, D., Haag, R. & Whitesides, G. M. Elastomeric optical elements with deformable surface topographies: applications to force measurements, tunable light transmission and light focusing. *Sensors Actuators A Phys.* **86,** 81–85 (2000).

54. Wilbur, J. L. *et al.* Elastomeric Optics. *Chem. Mater.* **2,** 1380–1385 (1996).

55. Gurland, J. An estimate of contact and contiguity of dispersions in opaque samples. *Trans. Metall. Soc. AIME* **236,** 642–646 (1966).

56. Al-Saleh, M. H. & Sundararaj, U. A review of vapor grown carbon nanofiber/polymer conductive composites. *Carbon N. Y.* **47,** 22 (2009).

57. Ambrosetti, G. *et al.* Solution of the tunneling-percolation problem in the nanocomposite regime. *Phys. Rev. B - Condens. Matter Mater. Phys.* **81,** 1–23 (2010).

58. Verardo, D. *et al.* Nanowires for Biosensing: Lightguiding of Fluorescence as a Function of Diameter and Wavelength. *Nano Lett.* (2018). doi:10.1021/acs.nanolett.8b01360

59. Bréchet, Y. *et al.* Polymer based nanocomposites: Effect of filler-filler and filler-matrix interactions. *Adv. Eng. Mater.* **3,** 571–577 (2001).

60. Frogley, M. D., Ravich, D. & Wagner, H. D. Mechanical properties of carbon nanoparticle-reinforced elastomers. **63,** 1647–1654 (2003).

61. Corbelli, G., Ghisleri, C., Marelli, M., Milani, P. & Ravagnan, L. Highly Deformable Nanostructured Elastomeric Electrodes With Improving Conductivity Upon Cyclical Stretching. *Adv. Mater.* **23,** 4504–4508 (2011).

62. Faupel, F., Willecke, R. & Thran, A. Diffusion of metals in polymers. *Mater. Sci. Eng. R* **22,** 1–55 (1998).

63. Cardia, R. *et al.* Neutral-cluster implantation in polymers by computer experiments Neutral-cluster implantation in polymers by computer experiments. **224307,** (2016).

64. Heilmann, A. *Polymer films with embedded metal nanoparticles*. **52,** (Springer Science & Business Media, 2013).

65. Universitaire, D., Technique, C. & Universitaire, D. Contactless measurement of the elastic Young's modulus of paper by an ultrasonic technique. **37,** 133–139 (1999).

66. Odian, G. *Principles of polymerization*. (1991).

67. https://pslc.ws/italian/mech.htm.

68. https://www.safaribooksonline.com/library/view/polymer-science-and/9780137039975/app02.html.

69. Wagner, S. & Bauer, S. Materials for stretchable electronics. *MRS Bull.* **37,** 207–213 (2012).

70. http://www-materials.eng.cam.ac.uk/mpsite/interactive_charts/stiffness-density/basic.html.

71. Guth, E. Theory of filler reinforcement. *J. Appl. Phys.* **16,** 20–25 (1945).

72. https://en.wikipedia.org/wiki/Carbon_nanofiber.

73. https://sep.yimg.com/ty/cdn/nanolab2000/FH-P-TEM.jpg.

74. Tjong, S. C. Structural and mechanical properties of polymer nanocomposites. **53,** 73–197 (2006).

75. Flandin, L., Chang, A., Nazarenko, S., Hiltner, A. & Baer, E. Effect of strain on the properties of an ethylene-octene elastomer with conductive carbon fillers. *J. Appl. Polym. Sci.* **76,** 894–905 (2000).

76. Yan, Y. *et al.* Electroactive Ionic Soft Actuators with Monolithically Integrated Gold Nanocomposite Electrodes. *Adv. Mater.* **29,** 1606109 (2017).

77. Kim, Y. *et al.* Stretchable nanoparticle conductors with self-organized conductive pathways. *Nature* **500,** 59–63 (2013).

78. Chiang, Y. L. *et al.* Mechanically tunable surface plasmon resonance based on gold nanoparticles and elastic membrane polydimethylsiloxane composite. *Appl. Phys. Lett.* **96,** 19–22 (2010).

79. Cataldi, U. *et al.* Growing gold nanoparticles on a flexible substrate to enable simple mechanical control of their plasmonic coupling. *J. Mater. Chem. C* **2,** 7927–7933 (2014).

80. Herrmann, J. *et al.* Nanoparticle films as sensitive strain gauges. *Appl. Phys. Lett.* **91,** 183105–183107 (2007).

81. Bloor, T. and Blyte, D. *Electrical properties of polymers*. (2005).

82. Ambrosetti, G., Balberg, I. & Grimaldi, C. Percolation-to-hopping crossover in conductor-insulator composites. *Phys. Rev. B - Condens. Matter Mater. Phys.* **82,** 1–8 (2010).

83. Grimaldi, C. Theory of percolation and tunneling regimes in nanogranular metal films. **214201,** 1–11 (2014).

84. Fostner, S., Brown, R., Carr, J. & Brown, S. A. Continuum percolation with tunneling. *Phys. Rev. B - Condens. Matter Mater. Phys.* **89,** 75402 (2014).

85. Sahimi, M. *Heterogeneous Materials I. Linear Transport and Optical Properties*. (2003).

86. Kirkpatrick, S. Percolation and Conduction. *Rev. Mod. Phys.* **45,** 574–588 (1973).

87. Nan, C. Physics of inhomogeneous inorganic materials. *Prog. Mater. Sci.* **37,** 1 (1993).

88. L. Benguigui, P. R. Experimental realization of superelasticity near the percolation threshold. *Phys. Rev. Lett.* **70,** 2423 (1993).

89. M. Sahimi, S. A. Mechanics of disordered solids II. Percolation on elastic networks with bond-bending forces. *Phys. Rev. B* **47,** 703 (1993).

90. Schmelzer, J., Brown, S. A., Wurl, A. & Hyslop, M. Finite-Size Effects in the Conductivity of Cluster Assembled Nanostructures. 3–6 (2002). doi:10.1103/PhysRevLett.88.226802

91. Dunbar, A. D. F., Partridge, J. G., Schulze, M., Scott, S. & Brown, S. A. Measurement of the Conductivity Exponent in Random Percolating Networks of Nanoscale Bismuth Clusters. in *Proceedings of the IEEE* 0–5 (2003).

92. Balberg, I. Tunneling and Nonuniversal Conductivity in Composite Materials. *Lett. Phys. Rev.* **59,** 1305–1308 (1987).

93. Balberg, I. Tunnelling and percolation in lattices and the continuum. *J. Phys. D. Appl. Phys.* **42,** 64003 (2009).

94. Balberg, I., Azulay, D., Toker, D. & Millo, O. Percolation and Tunneling in Composite Materials. *Int. J. Mod. Phys. B* **18,** 2091–2121 (2004).

95. Balberg, I. Tunneling and percolation in lattices and continuum. *J. Phys. D Appl. Phys.* **42,** 64003 (2009).

96. Y. Zweifel, C. J. G. Plummer, H.-H. K. A microscopic investigation of conducting filled polymers. **3,** 1715–1721 (1998).

97. Fostner, S. & Brown, S. A. Neuromorphic behavior in percolating nanoparticle films. *Phys. Rev. E* **92,** 52134 (2015).

98. Wei, H. & Eilers, H. Electrical conductivity of thin- fi lm composites containing silver nanoparticles embedded in a dielectric fl uoropolymer matrix. *Thin Solid Films* **517,** 575–581 (2008).

99. Liu, C. X. & Choi, J. W. Strain-dependent resistance of PDMS and carbon nanotubes composite microstructures. *IEEE Trans. Nanotechnol.* **9,** 590–595 (2010).

100. Flandin, L., Brechet, Y. & Cavaille, J. Y. Electrically conductive polymer nanocomposites as deformation sensors. *Compos. Sci. Technol.* **61,** 895–901 (2001).

101. Bellacicca, A., Prof, C. & Ragusa, F. Smart materials for stretchable electronics , sensors and soft actuation. (2016).

102. Khan, S., Lorenzelli, L., Dahiya, R. S. & Member, S. Technologies for Printing Sensors and Electronics Over Large Flexible Substrates : A Review. **15,** 3164–3185 (2015).

103. Herrmann, J. *et al.* Nanoparticle films as sensitive strain gauges. *Appl. Phys. Lett.* **183105,** 1–4 (2017).

104. Mie, G. Contributions to the optics of turbid media, particularly of colloidal metal solutions. *Ann. Phys.* **25,** 377 (1908).

105. Ghosh, S. K. & Pal, T. Interparticle Coupling Effect on the Surface Plasmon Resonance of Gold Nanoparticles : From Theory to Applications. *Chem. Rev.* **107,** 4797 (2007).

106. Kubo, M. & Nakamura, S. The Dielectric Constant of Dispersion of Spherical Particles By Masaji KUBO and Sankichi NAKAMURA. **229,** (1953).

107. Gérardy, J. M., Ausloos, M. Absorption spectrum of clusters of spheres from the general solution of Maxwell's equations. IV. Proximity, bulk, surface, and shadow effects (in binary clusters). *Phys. Rev. B* **27,** 6446 (1983).

108. Jain, P. K. & El-sayed, M. A. Plasmonic coupling in noble metal nanostructures. *Chem. Phys. Lett.* **487,** 153–164 (2010).

109. Garnett, J. C. M. Colours in Metal Glasses and in Metallic Films. *Philos. Trans. R. Soc.* **203,** 805 (1904).

110. Wang, J. *et al.* Effects of particle size and spacing on the optical properties of gold nanocrystals in alumina Effects of particle size and spacing on the optical properties of gold nanocrystals in alumina. **114303,** (2016).

111. Eustis, S., El-sayed, M. A. & Kasha, M. Why gold nanoparticles are more precious than pretty gold : Noble metal surface plasmon resonance and its enhancement of the radiative and nonradiative properties of nanocrystals of different shapes. 209–217 (2006). doi:10.1039/b514191e

112. Park, H., Joo, J. H., Kim, H. & Lee, J. Shape-Dependent Reversible Assembly Properties of Polyvalent DNA À Silver Nanocube Conjugates. 2278–2284 (2012). doi:10.1021/jp210732u

113. Biswas, A. *et al.* Advances in top – down and bottom – up surface nanofabrication : Techniques , applications & future prospects. *Adv. Colloid Interface Sci.* **170,** 2–27 (2012).

114. Hedayati, M. K., Faupel, F. & Elbahri, M. Review of plasmonic nanocomposite metamaterial absorber. *Materials (Basel).* **7,** 1221–1248 (2014).

115. Murray, B. W. A. & Barnes, W. L. Plasmonic Materials **. 3771–3782 (2007). doi:10.1002/adma.200700678

116. Milani, P. & Iannotta, S. *Cluster beam synthesis of nanostructured materials*. (2012).

117. Corbelli, G. Synthesis and Charachterization of metal-polimer nanocomposites for stretchable electronics applications. (2011).

118. E. Barborini, P. Piseri, P. M. A pulsed microplasma source of high intensity supersonic carbon cluster beams. *J. Phys. D Appl. Phys.* **32,** L105 (1999).

119. Fonzo, F. Di *et al.* Focused nanoparticle-beam deposition of patterned microstructures Focused nanoparticle-beam deposition of patterned microstructures. **910,** 1–4 (2016).

120. https://semiengineering.com/inspecting-unpatterned-wafers/.

121. https://www.universalmedicalinc.com/microscope-slides-diamond-white-glass-90.html.

122. https://www.microchemicals.com/products/wafers/wafer_specification.html.

123. A. Mata, A. Fleischman, S. R. Characterization of Polydimethylsiloxane (PDMS) Properties for Biomedical Micro-Nanosystems. *Biomed. Microdevices* **7,** 281 (2005).

124. D'Angelo, P., Barra, M., Cassinese, A., Guido, S., & Tomaiuolo, G. An electric criterion to evaluate glass transition temperature: dielectric relaxation measurements. *Macromol. Symp.* **247,** 43–49

(2007).

125. Koga, H., Kitaoka, T. & Isogai, A. Chemically-Modified Cellulose Paper as a Microstructured Catalytic Reactor. *Molecules* **20,** 1495–1508 (2015).

126. Minnai, C., Di Vece, M. & Milani, P. Mechano-optical-electro modulation by stretching a polymer-metal nanocomposite. *Nanotechnology* (2017).

127. Potenza, M. A. C. *et al.* Hyperspectral imaging with deformable gratings fabricated with metal-elastomer nanocomposites. *Rev. Sci. Instrum.* **88,** 113105 (2017).

128. Minnai, C. & Milani, P. Metal-polymer nanocomposite with stable plasmonic tuning under cyclic strain conditions. *Appl. Phys. Lett.* **107,** 73106 (2015).

129. Minnai, C., Vece, M. Di & Milani, P. Mechanical-optical-electro modulation by stretching a polymer-metal nanocomposite. *Nanotechnology* **28,** 355702 (2017).

130. Waldrop, M. More than Moore. *Nature* **530,** 144–147 (2016).

131. Zhang, G. Q. & Roosmalen A. V. *More than Moore: Creating High Value Micro/Nanoelectronics Systems*. (Springer Science, LLC, 2009).

132. Curri, M. L., Comparelli, R., Striccoli, M. & Agostiano, A. Emerging methods for fabricating functional structures by patterning and assembling engineered nanocrystals. *Phys. Chem. Chem. Phys.* **12,** 11153–11796 (2010).

133. Paolo Milani & Bettini, L. G. *Nano- and Micromanufacturing with Nanoparticles Produced in the Gas Phase: An Emerging Tool for Functional and Length-Scale Integration, in Gas-Phase Synthesis of Nanoparticles*. (Wiley, 2017).

134. Avizienis, A. V. *et al.* Neuromorphic Atomic Switch Networks. *PLoS One* **7,** e42772 (2012).

135. Yang, J. J., Strukov, D. B. & Stewart, D. R. Memristive devices for computing. *Nat. Nanotechnol.* **8,** 13–24 (2013).

136. Choi, S., Sheridan, P. & Lu, W. D. Data Clustering using Memristor Networks. *Sci. Rep.* **5,** 10492 (2015).

137. Xia, Q. *et al.* Memristor-CMOS hybrid integrated circuits for reconfigurable logic. *Nano Lett.* **9,** 3640–3645 (2009).

138. Ohno, T. in *Micro-and Nanoelectronics: Emerging Device Challenges and Solutions* (ed. Brozek, T.) **35,** 283 (Taylor & Francis Group, 2014).

139. Burr, G. W. *et al.* Neuromorphic computing using non-volatile memory. *Adv. Phys. X* **2,** 89–124 (2017).

140. Stieg, A. Z. *et al.* Emergent criticality in complex turing B-type atomic switch networks. *Adv. Mater.* **24,** 286–293 (2012).

141. Ohno, T. *et al.* Sensory and short-term memory formations observed in a Ag2S gap-type atomic switch. *Appl. Phys. Lett.* **99,** 14–17 (2011).

142. Ohno, T. *et al.* Short-term plasticity and long-term potentiation mimicked in single inorganic synapses. *Nat. Mater.* **10,** 591–595 (2011).

143. Kim, H., Yang, C. & Chua, L. O. Memristor Bridge Synapses. in *Proceedings of the IEEE* **100,** 2061–2070 (2012).

144. Le Doux, J. *Synaptic self: How our brains become who we are*. (Books, Penguin, 2003).

145. Prodromakis, T., Toumazou, C. & Chua, L. Two centuries of memristors. *Nat. Mater.* **11,** 478–481 (2012).

146. Chua, L. O. Memristor—The Missing Circuit Element. *IEEE Trans. Circuit Theory* **18,** 507–519 (1971).

147. Strukov, D. B., Snider, G. S., Stewart, D. R. & Williams, R. S. The missing memristor found. *Nat. Lett.* **453,** 80–83 (2008).

148. Waser, R. & Aono, M. Nanoionics-based resistive switching memories. *Nat. Mater.* **6,** 833–840 (2007).

149. Gaba, S., Cai, F., Zhou, J. & Lu, W. D. Ultralow Sub-1-nA operating current resistive memory with intrinsic non-linear characteristics. *IEEE Electron Device Lett.* **35,** 1239–1241 (2014).

150. Sattar, A., Fostner, S. & Brown, S. A. Quantized conductance and switching in percolating nanoparticle films. *Phys. Rev. Lett.* **111,** 136808 (2013).

151. Chialvo, D. R. Emergent complex neural dynamics. *Nat. Phys.* **6,** 744–750 (2010).

152. Mead, C. Neuromorphic Electronic Systems. *Proc. IEEE* **78,** 1629–1636 (1990).

153. Merolla, P. A. *et al.* A million spiking-neuron integrated circuit with a scalable communication network and interface. *Science* **345,** 668–673 (2014).

154. Podestà, A. *et al.* Nanomanufacturing of titania interfaces with controlled structural and functional properties by supersonic cluster beam deposition. *J. Appl. Phys.* **118,** 234309 (2015).

155. Jensen, P. Growth of nanostructures by cluster deposition: Experiments and simple models. *Rev. Mod. Phys.* **71,** 1695–1735 (1999).

156. Gefen, Y. & Shih, W.-H. Nonlinear Behavior near the Percolation Metal-Insulator Transition. *Phys. Rev. Lett.* **57,** 3097–3100 (1986).

157. Sondheimer, E. H. The mean free path of electrons in metals. *Adv. Phys.* **1,** 1–42 (1952).

158. Arnason, S. B., Herschfield, S. P. & Hebard, A. F. Bad Metals Made with Good-Metal Components. **81,** 3036–3939 (1998).

159. Voss, R. F., Laibowitz, R. B. & Allessandrini, E. I. Fractal (Scaling) Clusters in Thin Gold Films near the Percolation Threshold. *Phys. Rev. Lett.* **49,** 1441–1445 (1982).

160. Minnai, C., Bellacicca, A., Brown, S. A. & Milani, P. Facile fabrication of complex networks of memristive devices. *Sci. Rep.* **7,** 7955 (2017).

161. Minnai, C., Mirigliano, M. & Brown, S. A. The nanocoherer : an electrically and mechanically resettable resistive switching device based on gold clusters assembled on paper. *Nano Futur.* **2,** 11002 (2018).

162. Demis, E. C. *et al.* Atomic switch networks — nanoarchitectonic design of a complex system for natural computing. (2015). doi:10.1088/0957-4484/26/20/204003

163. Bose, S. K., Shirai, S., Mallinson, J. B. & Brown, S. A. Synaptic dynamics in complex self-assembled nanoparticle networks. *R. Soc. Chem.* (2018).

164. Bose, S. K., Mallinson, J. B., Gazoni, R. M. & Brown, S. A. Stable Self-Assembled Atomic-Switch Networks for Neuromorphic Applications. *IEEE Trans. Electron Devices* **64,** 5194–5201 (2017).

8 Appendix

Electroactive Ionic Soft Actuators with Monolithically Integrated Gold Nanocomposite Electrodes

Yunsong Yan, Tommaso Santaniello, Luca Giacomo Bettini, Chloé Minnai, Andrea Bellacicca, Riccardo Porotti, Ilaria Denti, Gabriele Faraone, Marco Merlini, Cristina Lenardi, and Paolo Milani**

Electroactive ionic gel/metal nanocomposites are produced by implanting supersonically accelerated neutral gold nanoparticles into a novel chemically crosslinked ion conductive soft polymer. The ionic gel consists of chemically crosslinked poly(acrylic acid) and polyacrylonitrile networks, blended with halloysite nanoclays and imidazolium-based ionic liquid. The material exhibits mechanical properties similar to that of elastomers (Young's modulus ≈ 0.35 MPa) together with high ionic conductivity. The fabrication of thin (≈100 nm thick) nanostructured compliant electrodes by means of supersonic cluster beam implantation (SCBI) does not significantly alter the mechanical properties of the soft polymer and provides controlled electrical properties and large surface area for ions storage. SCBI is cost effective and suitable for the scaleup manufacturing of electroactive soft actuators. This study reports the high-strain electromechanical actuation performance of the novel ionic gel/metal nanocomposites in a low-voltage regime (from 0.1 to 5 V), with long-term stability up to 76 000 cycles with no electrode delamination or deterioration. The observed behavior is due to both the intrinsic features of the ionic gel (elasticity and ionic transport capability) and the electrical and morphological features of the electrodes, providing low specific resistance (<100 Ω cm^{-2}), high electrochemical capacitance (≈mF g^{-1}), and minimal mechanical stress at the polymer/metal composite interface upon deformation.

The development of soft robots with muscle-like actuation relies on the fabrication of compliant and flexible actuators with the embedded ability to controllably deform and adapt to the external environment.[1–6] One of the most promising actuation mechanisms for soft robotics is based on the use of electroactive polymers (EAPs), capable to reversibly change their size and shape under the application of electrical stimuli.[5] The simplest configuration of an EAP-based actuator consists of a polymeric layer sandwiched between two conformable metal electrodes to obtain a deformable electrostatic capacitor.[2,5,7]

Among different EAPs, ionic-polymer–metal composites (IPMC), consisting of ionic polymers provided with metallic electrodes, are potential interesting candidates for the fabrication of lightweight soft actuators, since they can provide large bending actuation in response to low applied voltages (0.1–5 V).[8] The efficient and rapid electromechanical transduction of IPMC actuators depends on the coupling of highly elastic properties with effective ionic transport, and it is a consequence of the migration and spatial redistribution of mobile ions in the polymeric structure.[7–10] Another key requisite, in view of applications, is the fabrication of compliant and well-adherent electrodes that are physically interpenetrating with the polymer layer. In fact, the intercalation of ions into the electrode layers and the resulting material volumetric change are fundamental for strain generation.[11]

Several routes have been explored in order to improve IPMC-based actuators' performances. To improve the ionic transport capability of the polymers, sacrificial template strategies, predominantly based on block-copolymers synthesis, were implemented in order to generate inner channels or interconnected pores at the nanoscale to favor the ions flux.[12,13] This approach resulted in an increase of the electromechanical performance; however, it is based on very complex and expensive manufacturing processes.[14]

Nafion and Flemion attracted an increasing attention due to their easiness to be metalized, their fast response time, and capability of working exposed to air.[15,16] However, the high cost of the materials, as well as the considerable fatigue effects endured by the electrodes upon cycling, is severely limiting their use in mechatronic and robotic systems.[17,18]

Dr. Y. Yan, Dr. T. Santaniello, Dr. L. G. Bettini, C. Minnai, Dr. A. Bellacicca, R. Porotti, I. Denti, G. Faraone, Prof. C. Lenardi, Prof. P. Milani
Interdisciplinary Centre for Nanostructured Materials and Interfaces (CIMaINa)
Physics Department
University of Milan
Via Celoria 16, 20133 Milan, Italy
E-mail: tommaso.santaniello@unimi.it; paolo.milani@mi.infn.it
Dr. Y. Yan, Prof. P. Milani
SEMM—European School of Molecular Medicine
Campus IFOM-IEO
Via Adamello 16, 20139 Milan, Italy
Prof. M. Merlini
Department of Earth Science "Ardito Desio"
University of Milan
Via Mangiagalli/Botticelli, 32/23, 20133 Milan, Italy

DOI: 10.1002/adma.201606109

Electrodes fabrication manly relies on electroless plating and hot pressing[19] or chemical and physical vapor deposition processes[20] to produce noble metal highly conductive layers. For all these approaches, the flexibility and the adhesion of the electrodes during deformation cycles are a major problem. Carbonaceous materials, such as functionalized carbon nanotubes and doped graphene, were proposed as an alternative to noble metals for the production of chemically modified porous electrodes with higher flexibility.[21,22] In this framework, layer-by-layer fabrication techniques were used for manufacturing a class of composites based on ion-permeable electrolytes, such as poly(vinylidene difluoride) (PVDF) and poly(styrene sulfonate) (PSS), able to generate large strains when electrically stimulated (bucky gels).[23,24]

However, in both cases, the large Young's modulus mismatch between the polymeric material (from fractions to hundreds of MPa) and the material composing the electrodes (from tenths to hundreds of GPa)[25] causes electrode cracking and delamination during actuation, therefore limiting the lifetime and the bending of the systems.[26]

Here we demonstrate the fabrication of an actuator based on a novel ionic gel/metal nanocomposite (IGMN) fabricated with chemically crosslinked poly(acrylic acid) (PAA) and polyacrylonitrile (PAN) networks blended with halloysite nanoclays (HNCs) and imidazolium-based ionic liquid. The polymeric matrix has mechanical properties similar to that of elastomers together with an effective ion transport through a sieve-like structure. The ionic conductivity of the system is enhanced by the interaction between the embedded HNC and the imidazolium cation, which promotes a partial dissociation of the ionic liquid through an oxygen reduction reaction.

We used supersonic cluster beam implantation (SCBI)[27] to implant cluster-assembled electrodes (≈100 nm thick) in the ionic gel without significantly altering the mechanical properties of the soft polymer, providing, at the same time, controlled electrical properties and large surface area for ions storage.

The novelty of the produced soft actuators dwells into the synergistic coupling between the intrinsic properties of the soft ionic gel (elasticity and conductivity) and the thin nanostructured electrodes monolithically integrated with the polymer. This coupling eventually leads to tailored electrochemical and mechanical characteristics of the nanocomposites, which, in turn, determines the specific electromechanical performance of the system and implies the minimization of the mechanical stresses at the polymer/metal interface upon the electrically induced deformation.

A bottom-up engineering approach was used to define the formulation of the polymer: the ionic gel samples were manufactured as thin layers of different thickness (100, 150, and 350 μm), using a one-pot synthesis, by means of a free-radical UV photo-crosslinking reaction and a simple molding process (Figure S1, Supporting Information). The macromolecular PAA-co-PAN network (**Figure 1**a) is crosslinked using ethylene glycol dimethacrylate and it is able to absorb and retain a large amount of ionic liquid that operates as the transport medium for the migration of the active mobile ionic species through the polymer. We used 1-ethyl-3-methylimidazolium tetrafluoroborate ($EmimBF_4$) as a ionic liquid, which has already been widely used for the production of electroactive ionomeric actuators and quasi-solid-state electrolytes, due to its relatively low viscosity (about 151.7 cp at room temperature) and large electrochemical window (around 4.2 V).[28,29] The tetraethyl ammonium cation (TEA^+) was employed as the active charge carrier specie. This organic molecule has shown high electrochemical stability when used in large-displacement IPMC membranes.[30] The solvent uptake of the material, i.e., the molar ratio of the ionic liquid with respect to the acrylic acid monomer (AA) is $EmimBF_4$:AA = 37% mol:mol, while the TEA^+ cation concentration is 0.17×10^{-3} M. The PAA carboxyl groups, covalently bonded to the main backbone, offer fixed anionic sites for the TEA^+ cation coordination, while PAN was introduced to confer rubbery properties to the polymer matrix. The ratio between acrylic acid and acrylonitrile was set as 8:2 (mol:mol).

HNCs with high ionic exchange capability are embedded in the electrolyte to both increase its ionic conductivity and to operate as a reinforcement for the polymer.[31–33] These tubular nanostructures consist of a rolled up stacking of tetrahedral SiO_4 and octahedral AlO_6 sheets, with average hydrodynamic size of 150–200 nm, and present surface siloxanes groups exposed at the outer surface (negatively charged) and aluminum hydroxide pendants in the inner lumen (positively charged).[32] When dispersed in solution, the zeta potential of both inner and outer surfaces can be tuned by controlling a number of factors, including pH, ionic strength, and ionic medium type.[34] Due to their unique surface chemistry features, HNCs have been used for the controlled adsorption and intercalation of ionic liquids and various liquid phase electrolytes.[31–35] HNCs were included in the macromolecular network at a fixed ratio of 5% (w/w) with respect to acrylic acid. The mechanical properties of the materials in the standard formulation were evaluated using uniaxial tensile tests. The Young's modulus of the ionic gel was measured as 0.35 MPa, while its elongation at break was 255% (Figure S4, Supporting Information).

After molding of the ionic gel layers, IGMNs were fabricated by implanting supersonically accelerated gold nanoparticles into the polymers by means of SCBI. This metallization approach consists in directing a highly collimated beam of neutral metal clusters onto a polymeric target. By exploiting both the inertia of the nanoaggregates and their low kinetic energy (0.5 eV per atom), the clusters penetrate into the polymer, progressively creating a conductive layer up to the polymer surface, without any thermal damage or chemical modification of the organic substrate.[36,37]

A schematic representation of the SCBI fabrication process is reported in Figure 1b. The polymeric substrate (40 mm long, 15 mm wide) is fixed on a three-axis motorized sample holder allowing the rastering of the substrate along a direction perpendicular to the beam axis. This assures the homogeneous implantation of the nanoparticles over the entire surface of the ionic gel. Once the electrode with appropriate conductivity has been deposited (corresponding to a nanostructured layer thickness of 100 nm), the motorized holder is rotated by 180°, the opposite side of the polymer is processed (see the Supporting Information for more details).

As long as the gold cluster implantation proceeds, the electrode resistance decreases: in Figure 1c we report the electrode resistance evolution during implantation (a schematic of the setup used for in situ electrical characterization is shown in the

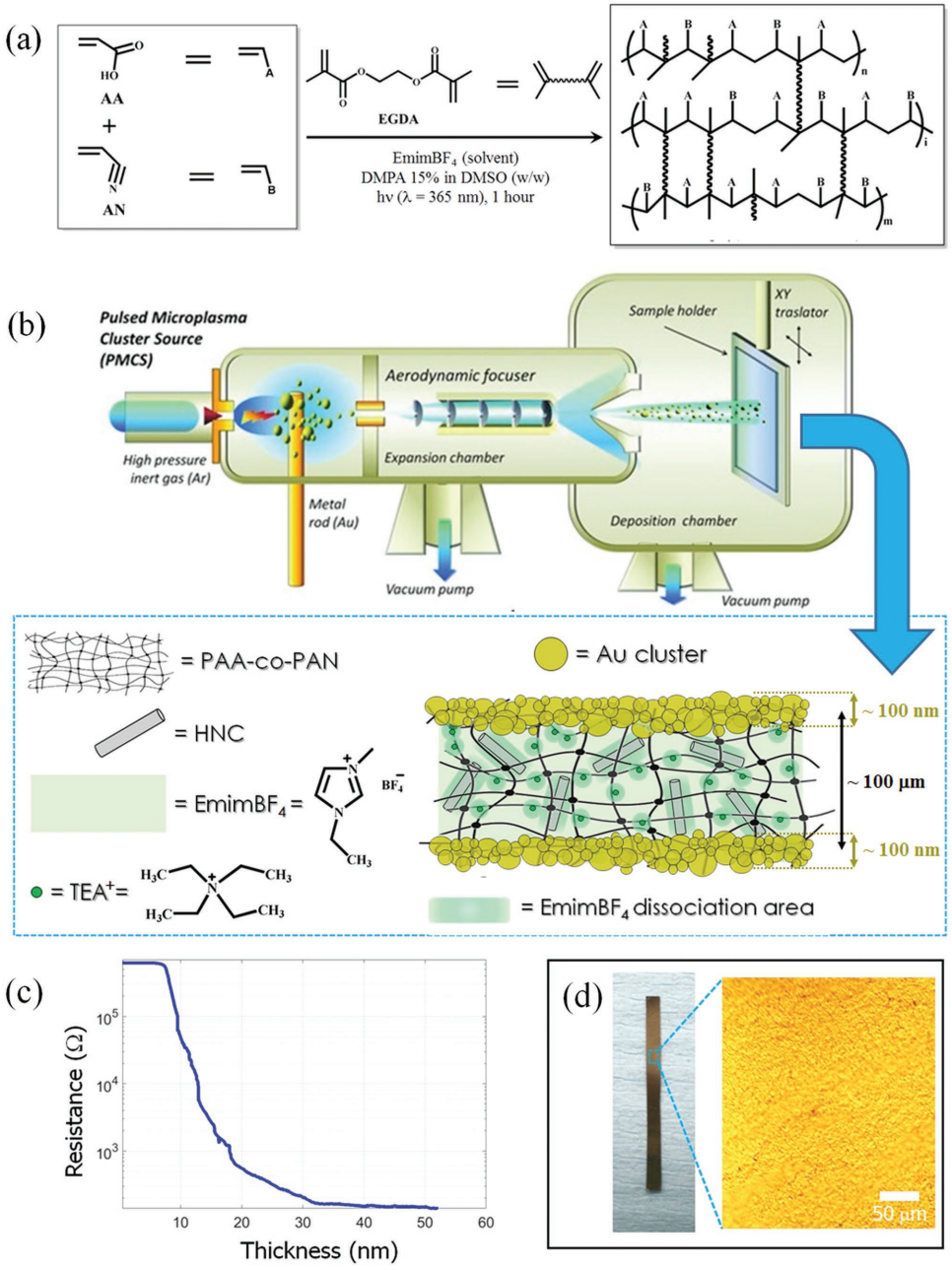

Figure 1. a) Schematic of the PAA-co-PAN network synthesis. b) Typical SCBI apparatus (adapted with permission[37]). The mix of gas and clusters produced in a cluster source attached to the expansion chamber is accelerated and collimated by the aerodynamic focuser. Nanoparticles then enter the deposition chamber and are implanted into the polymeric substrate that is fixed on a movable sample holder. The inset shows a cartoon of the produced IGMN structure. c) Resistance evolution of the IGMN during SCBI. d) Photograph of an IGMN-based actuator. The zoom shows an optical microscopy image of the metallized surface of the actuator.

Supporting Information). It can be observed that the pristine polymer has a resistance of about 10^6 Ω; a conduction onset is observed after the implantation of a 6 nm thick layer. The electrical percolation curve evolves upon implantation and the resistance decreases from 6×10^5 Ω to 10^2 Ω after the deposition of 27 nm thick film. After 30 nm thickness the ohmic regime is reached[37] and no significant changes in the resistance are recorded. The implantation process is stopped at a thickness of 100 nm where the electrodes surface specific resistance is 95 Ω cm^{-2}. A picture of an IGMN strip and an optical microscope image of the electrode surface are reported in Figure 1d.

On the basis of the material design, the actuation mechanism of the IGMNs is expected to have intermediate properties between that of IPMCs and bucky gels. In IPMCs, the ionic liquid absorbed by the polymer plays the role of the transport medium, while the counter-cations (such as alkali metals or organic compounds), coordinated to the fixed anionic

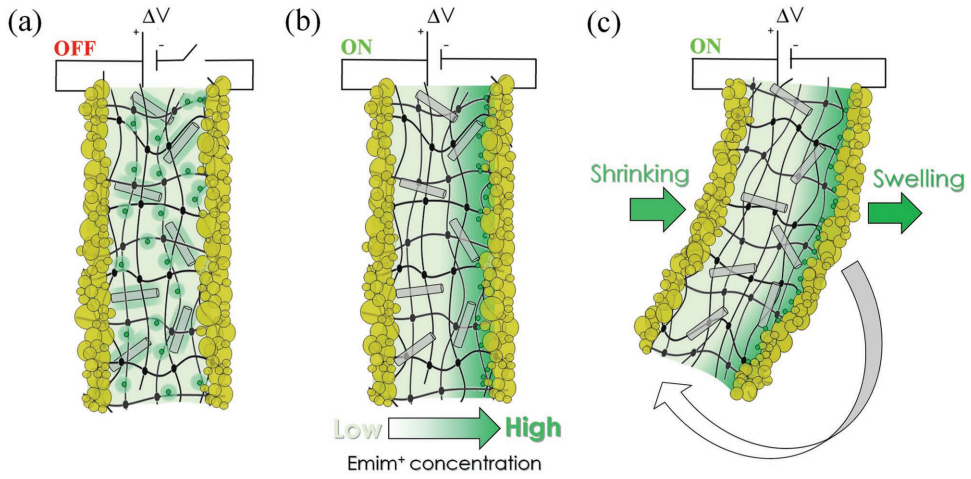

Figure 2. Actuation mechanism of the IGMN. a) IGMN-based actuator. b) When the electrical stimulus is applied, both the TEA^+ and $Emim^+$ cations migrate toward the cathode. c) The differential swelling at the anodic and cathodic side of the IGMN induces the bending of the actuator toward the anode.

sites, constitute the active mobile species that migrates across the polymer thickness when the electric field is applied.[13,38] In bucky gels, ionic liquid has a direct and active role in the actuation, since it is intercalated into the solid phase in a dissociated form, and therefore its anions and cations constitute themselves the mobile species drifting across the material and accumulating at the electrodes under the effect of the applied electric field.[13,20]

In the IGMN network (**Figure 2**a), both the mobile TEA^+ cations and the partially dissociated $EmimBF_4$ contribute to trigger the actuation of the system under electrical stimulation. $EmimBF_4$ can be absorbed by the composite through the interaction with the acidic PAA groups (in the same framework as it takes place in the carboxyl groups-rich phase of Flemion[38]) and orientate to form a hydration region around the mobile organic counter-ion. Furthermore, the imidazolium cation interacts with the surface siloxanes of the HNC. The nanostructures, which are homogeneously dispersed in the ionic gel matrix, induce a partial dissociation of the ionic liquid through an oxygen reduction reaction, which therefore promotes the $Emim^+$ cations migration toward the cathode when the electric field is applied (Figure 2b). In this sense, HNC has the same function of the carbonaceous nanostructures in bucky gel actuators, i.e., interacting with the imidazolium cations, but through a different molecular mechanism, and being present in the bulk of the electrolyte rather than in the electrode layers. Along with the $Emim^+$ accumulation at the cluster-assembled gold electrode, TEA^+ also migrates at the cathodic side of the actuator in the same framework as it takes place in IPMCs. The contribution of both the positive charged species that accumulate at the nanostructured electrode in a double-layer capacitance regime generates a differential swelling at the opposite sides of the actuator, which bends toward the anode (Figure 2c).

In order to obtain in-depth information on the role of the HNC in determining the nanocomposite responsive behavior, their interaction with the liquid phase of the electrolyte was analyzed using X-ray photoelectron spectroscopy (XPS) and X-ray diffraction (XRD). Furthermore, we used electrochemical impedance spectroscopy (EIS) to prove that the IGMN electrodes operate in a double-layer capacitance regime, as well as to get insights on the influence that both the fillers and the TEA^+ have on the electrochemical capacitance and ionic conductivity of the materials, which in turn dominate their actuation performance.

XPS was carried out on pure HNC powders and on HNC precipitates, recovered after being soaked under stirring overnight in pure $EmimBF_4$ and in a 0.17×10^{-3} M ionic liquid solution containing the quaternary ammonium cation (HNCs are 20% in weight with respect to the ionic liquid). In **Figure 3**a,b, the O1s and Si2p edges are shown, respectively. In both cases, the spectra were normalized. The O1s peak of the HNC was deconvolved in three features, related to different bonds of oxygen in the halloysite, namely, OH—, O—, and O_2. The areas of the fitted peaks are compliant with the content of the different oxygen chemical bonds. In both the samples treated with $EmimBF_4$ the O1s peak shows a shoulder at lower binding energies, indicating a reduction of the oxygen ascribable to an interaction with the ionic liquid. This shift is even more remarkable when TEA^+ is present, probably due to the polarization induced by the quaternary ammonium on the surrounding $EmimBF_4$, which in turn enables the $Emim^+$ cation to interact more effectively with the nanotubes. This behavior is mirrored by the silicon profiles, where a manifest shift toward a lower binding energy is well evident in the sample containing the TEA^+ and can be quantified in 0.7 eV, in agreement with what is reported in the literature.[39] This metallization of the silicon can be again imputable to the interaction between the ionic liquid and the outer surface of the HNC, which appears to be favorably promoted by the presence of TEA^+.

The interaction between HNC and ionic liquid was also confirmed by analyzing the same samples using XRD. The spectra profiles (Figure 3c) showed that $EmimBF_4$ could be partially intercalated in the nanotubes after the mixing process, as revealed by the presence of an absorption band at 10 Å. According to the literature, this change in the HNC spectrum can be related to the presence of nanoclay domains with larger

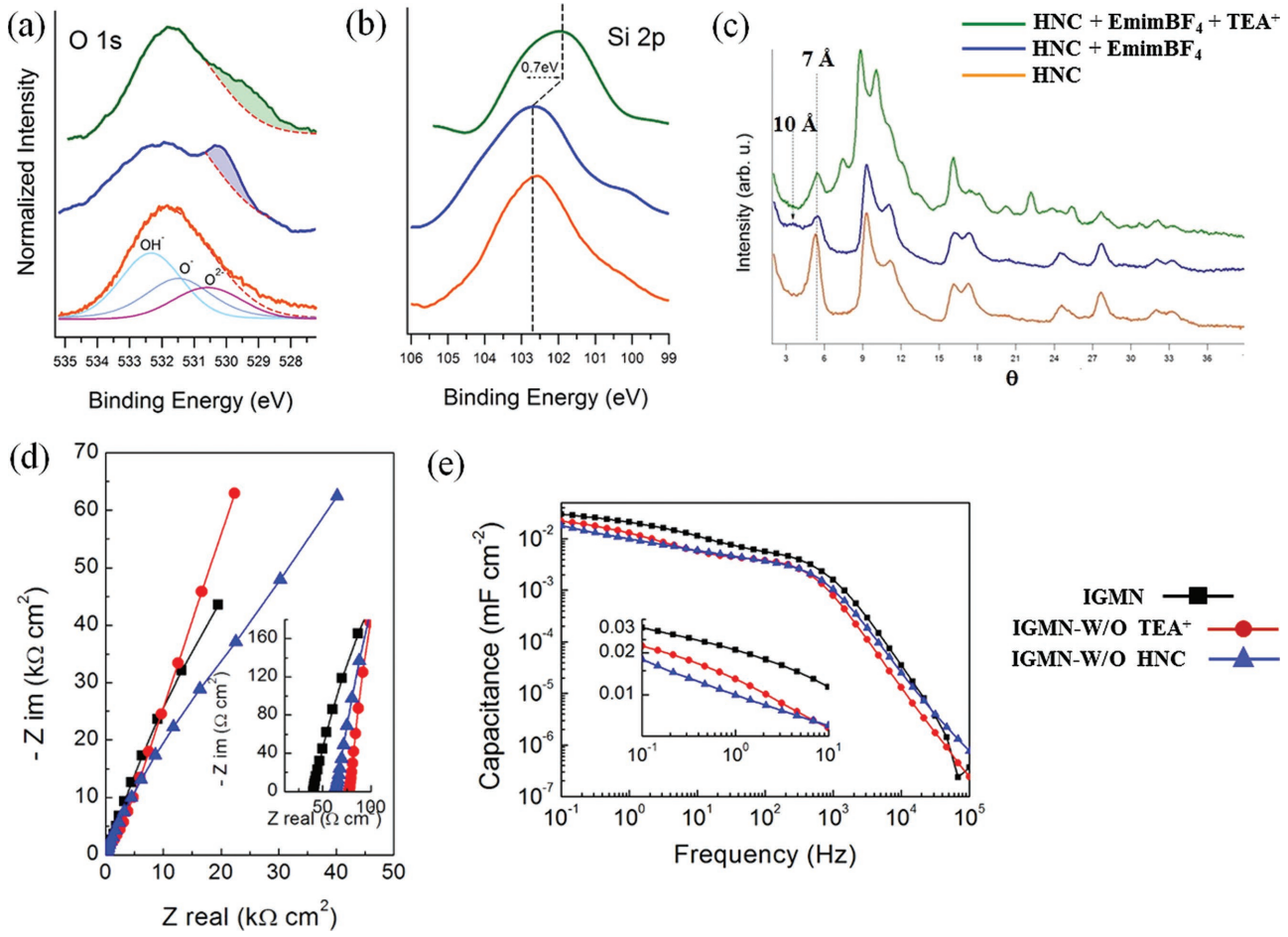

Figure 3. XPS spectra of HNC and HNC precipitate after immersion in $EmimBF_4$ and $EmimBF_4$ in the presence of TEA^+: a) O1s, b) Si 2p. c) XRD diffractogram. d) Impedance spectrum of the three types of nanocomposites. The inset shows a magnification of the high frequency intercept with the real impedance axis. e) Specific electrochemical capacitance of the samples produced. A magnification of the low-frequency region is reported in the inset.

lattice interspacing, caused by the ionic liquid intercalation in the nanostructures.[40]

To investigate the effects of the presence of HNC and TEA^+ cation on the electrochemical properties and actuation performance of the IGMNs, ionic gel samples without the embedded nanoclays (IGMN-W/O HNC) and without TEA^+ (IGMN-W/O TEA^+) were produced for a comparison with the standard formulation. These specimens were molded as 100 µm thick layers and subsequently metallized using SCBI.

The electrochemical characteristics of the produced nanocomposites were monitored using EIS. The Nyquist plot for the three formulations is reported in Figure 3d and shows that all samples have a capacitive behavior due to the formation of an electric double layer at the Au electrode interface.

The high-frequency intercept with the real impedance axis represents the equivalent series resistance (ESR) of the actuator (inset of Figure 3d). The ESR of the standard IGMN resulted to be ESR = 40 Ω cm^2. By considering the ESR to be dominated by the bulk ionic resistance of the IGMN,[41] the ionic conductivity of the actuator can be calculated as $\sigma = t/(A \times \mathrm{ESR})$, where t and A are the thickness and surface area of the IGMN, respectively. For the standard formulation used, σ = 0.35 mS cm^{-1}. This value is one order of magnitude higher with respect to the ionic conductivity of Nafion membranes swollen with imidazolium-based ionic liquids, having solvent uptake values comparable with the IGMN (around 40% mol:mol) and TEA^+ incorporated as the mobile cation,[41] as well as with respect to multiwalled carbon nanotube-based bucky gels.[42] Furthermore, the measured ionic conductivity is comparable with that of single-walled carbon nanotubes (SWCNTs)/PVDF-based bucky gels having higher solvent uptake values of a variety of ionic liquids with different viscosity and transport properties.[43] For the IGMN-W/O HNC and IGMN-W/O TEA^+ samples, the conductivity decreases to 0.18 mS cm^{-1} and 0.16 mS cm^{-1}, respectively, i.e., about 50% of the σ value measured for the standard IGMN formulation. These results suggest that both the presence of HNC and TEA+ have a significant influence on the electrolyte transport properties due to their interaction with $EmimBF_4$ and that the contributions of the nanofiller and mobile cation have an equivalent weight in determining these characteristics.

Electric double-layer capacitances of the IGMNs were calculated from the impedance spectra and are reported in Figure 3e. At 0.1 Hz, the specific capacitance of the standard IGMN was measured as C = 30 µF cm^{-2}. By taking into account the small

amount of gold employed for the fabrication of the electrodes (the overall thickness of the interpenetrating metal layer is around 100 nm, corresponding to an average amount of gold of about 1 mg), the measured C value can be considered significantly high and it proves the presence of a large electrode interface area for charge storage. In fact, for IPMC actuators swollen with ionic liquid, the specific electrochemical capacitance ranges from 0.1 mF cm^{-2} to 100 mF cm^{-2}.[44] When an organic counter-ion is included into the polymers as the active species, the capacitance range typically goes from 0.3 mF cm^{-2} to 10 mF cm^{-2}.[45] However, for these systems, the interpenetrating electrodes consist of a 10–20 µm deep platinum/polymer composite region, provided with an additional 1–5 µm thick surface layer of pure noble metal (usually platinum or gold) as the electrical signal collector.[44] Therefore, the double-layer capacitance in IPMCs is established in an effective layer that is two to four orders of magnitude thicker than the thin IGMN gold electrodes fabricated by means of SCBI. The specific electrochemical capacitance of the IGMN-W/O HNC and IGMN-W/O TEA^+ also dropped to lower values with respect to the one measured for the standard IGMN, being equal to 18 µF cm^{-2} and 23 µF cm^{-2}, respectively. This result confirms the active role of both the nanoclays and the quaternary ammonium cation in the charge accumulation process, which is of primary importance for the actuators strain generation. Cyclic voltammetry was also carried out on the standard IGMN formulation, showing that the electrochemical window of the composite was ±3 V (Figure S10, Supporting Information).

The electromechanical performance of the IGMN actuators was monitored using a custom-made setup where samples were fixed in a classical cantilever configuration and underwent electrical stimulation (Figure S11, Supporting Information). A square wave voltage of variable amplitude and frequency was applied to the actuators and their response was recorded by acquiring video sequences, from which captures could be collected and analyzed using an image processing software. For the standard material formulation (100 µm thick), the bending response to the electric field was observed to take place at 0.1 V and exhibited relatively low tip displacement values (around 0.06 mm) and reached values up to 0.25 mm at 1 V.

The net strain was calculated according to the geometry of the system as $\varepsilon = (2dt)/(L^2 + d^2)$, where d is the tip displacement, t is the actuator thickness, and L is the free length of the cantilever. Examples of the system bending actuation are reported in **Figure 4**b,e. The maximum net strain of 1.04% was achieved by the 350 µm thick sample under the application of 5 V for 30 s.

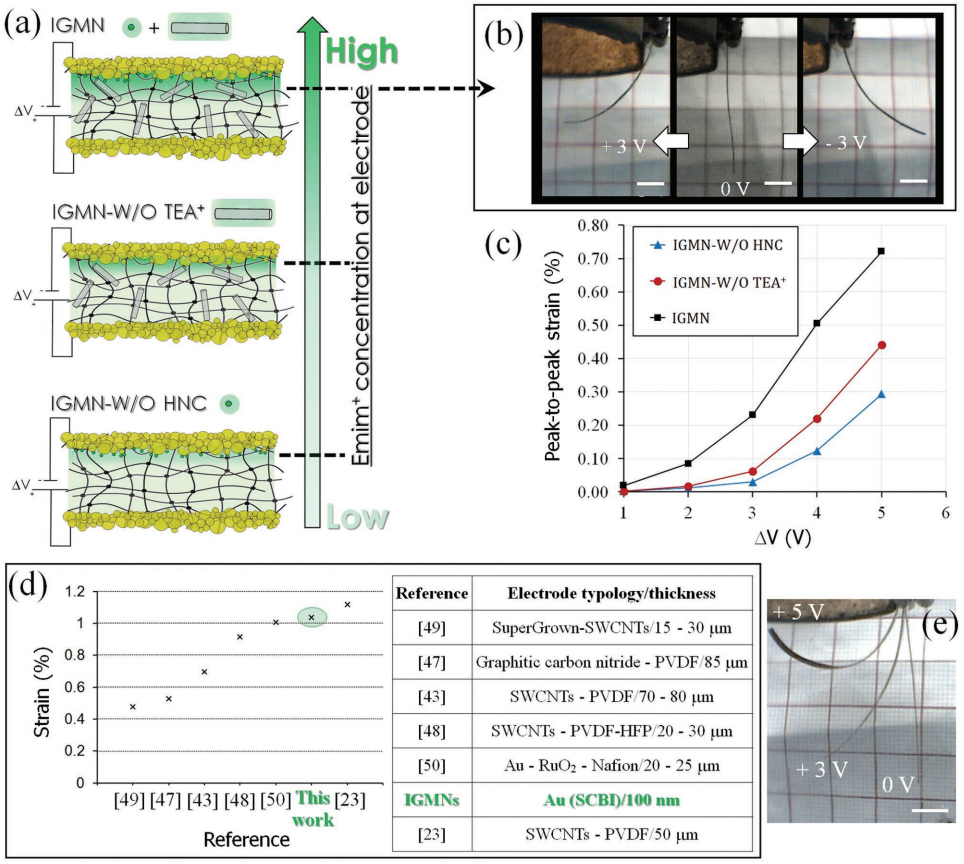

Figure 4. Actuation performance of the IGMNs. a) Schematic of the different samples produced, having increasing $Emim^+$ cation concentration at the cathodic side after the application of the electric field (scale bar is 5 mm). b) Example of bending for the IGMN standard formulation at 3 V and 0.02 Hz. c) Peak-to-peak strain profile as a function of the applied voltage for all the IGMN formulations. d) Visual chart comparing the results obtained in this manuscript with the results reported in the literature in terms of electromechanical performance of the actuators and related electrodes typology. e) Example of bending for the IGMN standard formulation at 3 and 5 V (scale bar is 5 mm).

The specimen demonstrated a stable frequency response for frequency values up to 10 Hz for all the thickness tested and the generated strain showed a decreasing profile when the frequency of the driving signal was increased (Figure S12, Supporting Information).

Cyclic measurements were also carried out at 2 V and 1 Hz for 76 000 cycles. No fatigue effects or decrease of performance was registered in more than 20 h of observation (Figure S16a, Supporting Information). To investigate the actuators durability for higher strains, we also performed durability tests at 2 V and lower frequencies (0.5 and 0.1 Hz). At 0.5 Hz, no significant changes in the actuation behavior were observed for over 15 000 cycles, while at 0.1 Hz a reduction in the tip displacement of about 20% with respect to the initial value was observed after 1000 cycles (Figure S16b,c, Supporting Information). A more pronounced decrease of performance was recorded for cyclic tests conducted on an IGMN bender actuated at 5 V and 0.1 Hz, which showed a tip displacement decrease down to 60% after 1000 cycles (Figure S16d, Supporting Information).

The electrodes morphology of the actuators tested in the high-strain cyclic measurements was then assessed using a scanning electron microscopy (SEM) and compared to that of a standard IGMN sample that did not undergo actuation. From the imaging of the samples cross-section and surface areas (Figure S18, Supporting Information), there was no evidence of the electrodes cracking or delamination, since the cluster assembled layer showed to preserve its homogeneity and morphology profile, as compared to the reference IGMN, in all of the cases monitored (Figure S17, Supporting Information). Therefore, the observed fatigue effects could have been induced by the bulk material mechanical hysteresis and by changes of its electrochemical properties along the actuation cycles. Furthermore, the clamping pressure applied to the materials by the electrical interconnections could have affected the actuators' performance to some extent, by inducing an overall stiffening of the material along the cantilever length and by causing disruptive effects at the IGMN/electrical contact interface, as also highlighted by the SEM analysis (Figure S18, Supporting Information).

The electromechanical performance of the IGMN-W/O HNC and IGMN-W/O TEA^+ samples was analyzed using the same setup and compared with the standard IGMN at 0.02 Hz in the voltage range going from 1 to 5 V (all samples were 100 μm thick). A decrease in the generated peak-to-peak strain (equal to 2ε) with respect to the standard IGMN actuator was observed for both samples, reflecting the decrease in the measured electrochemical capacitance for the two material formulations. This trend confirms the effect that both the nanofiller and the organic cation have on the dissociation of the ionic liquid and therefore on the electrochemical capacitance and electromechanical performance of the composites.

A schematic of the $Emim^+$ cation concentration distribution in the nanocomposites for the three material formulations after the application of the electric field is reported in Figure 4a, while a comparison between the peak-to-peak strain values for all the samples formulation is reported in Figure 4c. The actuation performance of the IGMNs can be considered highly relevant in the framework of electroactive ionic polymers, as reported by the most recent literature on in-air working IPMCs, bucky gels, and other electroactive ionic polymers and blends, such as engineered PSS block co-polymers provided with ionic nanochannels and poly(ethylene oxide)-based electrolytes with chemically modified graphite electrodes.[24,43,46–50] A visual chart comparing the results obtained in this manuscript with the results reported in the literature in terms of electromechanical performance of the actuators and related electrodes typology and thickness is shown in Figure 4d. Moreover, according to the cantilever beam model employed to describe the bending behavior of IPMC actuators,[51] the output force corresponding to the maximum net strain value of 1.04% can be estimated to be around 0.01 mN (calculation details are reported in the Supporting Information). This value is heavily underestimated, since it does not consider the stiffening effect of the system during deformation[50] and the relationship between the actuator electrochemical capacitance and the generated force, which is known to strongly influence the bending stroke and to depend on the actuator structure.[8] In this context, it is therefore more relevant to observe that the IGMN-based actuators have the ability to lift weights up to five times their own weight without significantly decreasing their bending performance, as experimentally evaluated on a qualitative level by employing U-shaped plastic components positioned on the benders tip. Taking also into account that the output force largely depends on the system geometry and material mechanical properties,[50] the results obtained suggest that the produced nanocomposites are suitable for applications in soft robotics, such as bioinspired soft robots manufacturing, as well as biohybrid systems and interfaces development for the manipulation and mechanical stimulation of biological tissues and entities.[52–55]

In order to investigate the effect of the electrode thickness on the IGMN actuators performance, we produced a nanocomposite with 30 nm thick gold electrodes. Although the electrochemical characteristics of the sample were measured to be largely similar to that of the standard IGMNs (Figure S11, Supporting Information), its actuation performance showed to be significantly hampered with respect to the nanocomposite with thicker electrodes. In fact, with respect to the reference standard IGMN, a reduction of the tip displacement up to about 35% and 55% at 3 and 5 V, respectively, was observed (Figure S15, Supporting Information). This behavior could be due to large values of the thinner electrode surface resistance (from 500 to 800 Ω, as measured with a multimeter after the specimen fabrication), which also showed to be poorly consistent along the actuator surface area, and that in turn affected the uniformity and quality of the transmission of the electrical stimulus across the polymeric layer. An intermediate value of the electrodes thickness, namely, between 30 and 100 nm, could reasonably represent a suitable tradeoff to simultaneously preserve functional electrical properties of the nanostructured gold and the overall nanocomposite stiffness.

In conclusion, we demonstrated the fabrication of an electroactive IGMN based on ionic conductive PAA-co-PAN network with embedded HNC and metallized by supersonic cluster beam implantation. The electroresponsive properties of the materials are intermediate between that of IPMCs and bucky gels. This feature is due to the synergistic effect of the quaternary ammonium TEA^+ counter-ion and HNC on the transport ability and electrochemical characteristics of the functional

nanocomposites. Both the organic cation and the inorganic nanostructures confer high ionic conductivity (0.35 mS cm^{-1}) and large double-layer capacitance (30 μF cm^{-2}) to the composites, by favoring the partial dissociation of the $EmimBF_4$ ionic liquid incorporated in the structure (solvent molar uptake is 37%). The production of cluster-assembled gold thin films, interpenetrating with the quasi-solid state electrolyte, enabled the manufacturing of elastic soft actuators with low surface electric resistance and large surface area for an effective charge storage. The actuators fabricated with IGMNs showed sensitivity to the applied electric field starting at 0.1 V and exhibited high-performance actuation in response to electrical stimuli at low voltages (up to 1.04% net strain at 5 V) and good durability in their frequency response (up to 76 000 cycles at 2 V and 1 Hz). The manufacturing process adopted for the actuators fabrication is cost effective and suitable for industrial production scale up. Actuators based on the novel IGMNs presented here are an interesting technological solution for the development of smart flexible components suitable for the manufacturing of biomimetic robots, soft sensors, and wearable biomedical devices.

Experimental Section

The experimental details can be found in the Supporting Information.

Supporting Information

Supporting Information is available from the Wiley Online Library or from the author.

Acknowledgements

Y.Y. and T.S. contributed equally to this work. Prof. Michele Perego, Dr. Tommaso Giammaria, and Dr. Fabio Zanenga from the MDM Laboratory, IMM-CNR (Via Olivetti 2, 20864, Agrate Brianza, Italy), are gratefully acknowledged for the SEM analysis.

Keywords

electroactive polymers, nanocomposites, smart materials, soft actuators, soft robotics

Received: November 11, 2016
Revised: February 21, 2017
Published online: April 18, 2017

[1] D. Rus, M. T. Tolley, *Nature* **2015**, *521*, 467.
[2] S. Bauer, S. Bauer-Gogonea, I. Graz, M. Kaltenbrunner, C. Keplinger, R. Schwödiauer, *Adv. Mater.* **2014**, *26*, 149.
[3] L. Kong, W. Chen, *Adv. Mater.* **2014**, *26*, 1025.
[4] V. K. Nguyen, Y. Yoo, *Sens. Actuators, B* **2007**, *123*, 183.
[5] N. Terasawa, K. Asaka, *Sens. Actuators, B* **2015**, *210*, 748.
[6] D. Niu, W. Jiang, H. Liu, T. Zhao, B. Lei, Y. Li, L. Yin, Y. Shi, B. Chen, B. Lu, *Sci. Rep.* **2016**, *6*, 27366.
[7] J.-W. Lee, Y.-T. Yoo, *Sens. Actuators, B* **2011**, *159*, 103.
[8] Y. Bahramzadeh, M. Shahinpoo, *Soft Robot.* **2013**, *1*, 38.
[9] J.-W. Lee, S. Yu, S. M. Hong, C. M. Koo, *J. Mater. Chem. C* **2013**, *1*, 3784.
[10] J. K. Kwang, S. Mohsen, *Smart Mater. Struct.* **2003**, *12*, 65.
[11] S. Nemat-Nasser, J. Y. Li, *J. Appl. Phys.* **2000**, *87*, 3321.
[12] S. Y. Kim, S. Kim, M. J. Park, *Nat. Commun.* **2010**, *1*, 88.
[13] R. Gao, D. Wang, J. R. Heflin, T. E. Long, *J. Mater. Chem.* **2012**, *22*, 13473.
[14] M. Shahinpoor, K. J. Kim, *Sens. Actuators, A* **2002**, *96*, 125.
[15] W. Shi, L. A. Baker, *RSC Adv.* **2015**, *5*, 99284.
[16] B. J. Akle, M. D. Bennett, D. J. Leo, K. B. Wiles, J. E. McGrath, *J. Mater. Sci.* **2007**, *42*, 7031.
[17] H. Okazaki, S. Sawada, M. Kimura, H. Tanaka, T. Matsumoto, T. Ohtake, S. Inoue, *IEEE Electron Device Lett.* **2012**, *33*, 1087.
[18] A. Kusoglu, Z. Weber, *J. Phys. Chem. Lett.* **2015**, *6*, 4547.
[19] L. Zu, Y. Li, H. Lian, Y. Hu, W. Chang, B. Liu, Y. Liu, X. Ao, Q. Li, X. Cui, *Macromol. Mater. Eng.* **2016**, *9*, 1144.
[20] J. H. Park, S. W. Lee, D. S. Song, J. Y. Jho, *ACS Appl. Mater. Interfaces* **2015**, *7*, 16659.
[21] Z. Zhou, Q. Li, L. Chen, C. Liu, S. Fan, *J. Mater. Chem. B* **2016**, *4*, 1228.
[22] M. Kotal, J. Kim, K. J. Kim, I.-K. Oh, *Adv. Mater.* **2016**, *28*, 1610.
[23] N. Terasawa, I. Takeuchi, *J. Mater. Chem. C* **2013**, *1*, 5272.
[24] T. Fukushima, K. Asaka, A. Kosaka, T. Aida, *Angew. Chem., Int. Ed.* **2005**, *44*, 2410.
[25] B. Bavani, N. Alek, S. Elisabeth, *Smart Mater. Struct.* **2015**, *24*, 045032.
[26] S. Mohsen, J. K. Kwang, *Smart Mater. Struct.* **2000**, *9*, 543.
[27] C. Ghisleri, F. Borghi, L. Ravagnan, A. Podestà, C. Melis, L. Colombo, P. Milani, *J. Phys. D: Appl. Phys.* **2014**, *47*, 015301.
[28] M. Hayyan, F. S. Mjalli, M. A. Hashim, I. M. AlNashef, T. X. Mei, *J. Ind. Eng. Chem.* **2013**, *19*, 106.
[29] X.-H. Fan, Y.-P. Chen, C.-S. Su, *J. Chem. Eng. Data* **2016**, *61*, 920.
[30] K. Takagi, N. Tomita, K. Asaka, *Adv. Robot.* **2014**, *28*, 513.
[31] Y. Lvov, E. Abdullayev, *Prog. Polym. Sci.* **2013**, *38*, 1690.
[32] Y. Lvov, W. Wang, L. Zhang, R. Fakhrullin, *Adv. Mater.* **2016**, *28*, 1227.
[33] K. Pravin, K. Ravindranath, *Int. J. Sci. Res.* **2013**, *4*, 1766.
[34] C. Bretti, S. Cataldo, A. Gianguzza, G. Lando, G. Lazzara, A. Pettignano, S. Sammartano, *J. Phys. Chem. C* **2016**, *120*, 7849.
[35] E. Abdullayev, Y. Lvov, *J. Mater. Chem. B* **2013**, *1*, 2894.
[36] G. Corbelli, C. Ghisleri, M. Marelli, P. Milani, L. Ravagnan, *Adv. Mater.* **2011**, *23*, 4504.
[37] F. Borghi, C. Melis, C. Ghisleri, A. Podestà, L. Ravagnan, L. Colombo, P. Milani, *Appl. Phys. Lett.* **2015**, *106*, 121902.
[38] D. J. Leo, K. Farinholt, T. Wallmersperger, *Proc. SPIE* **2005**, *5759*, 170.
[39] B. Guo, X. Liu, W. Y. Zhou, Y. Lei, D. Jia, *J. Macromol. Sci., Part B: Phys.* **2010**, *49*, 1029.
[40] E. Horváth, J. Kristóf, R. L. Frost, Á. Rédey, V. Vágvölgyi, T. Cseh, *J. Therm. Anal. Calorim.* **2003**, *71*, 707.
[41] M. D. Bennett, D. J. Leo, G. L. Wilkes, F. L. Beyer, T. W. Pechar, *Polymer* **2006**, *47*, 6782.
[42] Y. Chen, J. Tao, L. Deng, L. Li, J. Li, Y. Yang, N. M. Khashab, *ACS Appl. Mater. Interfaces* **2013**, *5*, 7478.
[43] N. Terasawa, K. Asaka, *Sens. Actuators, B* **2014**, *193*, 851.
[44] S. Nemat-Nasser, *J. Appl. Phys.* **2002**, *92*, 2899.
[45] S. Nemat-Nasser, Y. Wu, *J. Appl. Phys.* **2003**, *93*, 5255.
[46] G. Wu, Y. Hu, Y. Liu, J. Zhao, X. Chen, V. Whoehling, C. Plesse, G. T. Nguyen, F. Vidal, W. Chen, *Nat. Commun.* **2015**, *6*, 7258.
[47] G. Wu, G. H. Li, T. Lan, Y. Hu, Q. W. Li, T. Zhang, W. Chen, *J. Mater. Chem. A* **2014**, *2*, 16836.
[48] O. Kim, T. J. Shin, M. J. Park, *Nat. Commun.* **2013**, *4*, 2208.

[49] K. Mukai, K. Asaka, T. Sugino, K. Kiyohara, I. Takeuchi, N. Terasawa, D. N. Futaba, K. Hata, T. Fukushima, T. Aida, *Adv. Mater.* **2009**, *21*, 1582.
[50] B. J. Akle, M. D. Bennett, D. J. Leo, *Sens. Actuators, A* **2006**, *126*, 173.
[51] J. H. Park, S. W. Lee, D. S. Song, J. Y. Jho, *ACS Appl. Mater. Interfaces* **2015**, *7*, 16659.
[52] S. Kim, C. Laschi, B. Trimmer, *Trends Biotechnol.* **2013**, *31*, 287.
[53] R. Pfeifer, M. Lungarella, F. Iida, *Commun. ACM* **2012**, *55*, 76.
[54] C. A. Powell, B. L. Smiley, J. Mills, H. H. Vandenburgh, *Am. J. Physiol.: Cell Physiol.* **2002**, *283*, C1557.
[55] J. Rosster, H. Hauser, *IEEE Rob. Autom. Mag.* **2016**, *23*, 17.

Metal-polymer nanocomposites for optics and plasmonics

Marco A.C. Potenza, Chloé Minnai, Paolo Milani*
CIMAINA and Dipartimento di Fisica, Università di Milano, via Celoria 16, 20133 Milano, Italy

ABSTRACT

Stretchable and conformable optical devices open very exciting perspectives for the fabrication of systems incorporating diffracting and optical power in a single element and of tunable plasmonic filters and absorbers. The use of nanocomposites obtained by inserting metallic nanoparticles produced in the gas phase into polymeric matrices allows to effectively fabricate cheap and simple stretchable optical elements able to withstand thousands of deformations and stretching cycles without any degradation of their optical properties. The nanocomposite-based reflective optical devices show excellent performances and stability compared to similar devices fabricated with standard techniques. The nanocomposite-based devices can be therefore applied to arbitrary curved non-optical grade surfaces in order to achieve optical power and to minimize aberrations like astigmatism. Examples discussed here include stretchable reflecting gratings, plasmonic filters tunable by mechanical stretching and light absorbers.

Keywords: stretchable optics, metal-polymer nanocomposites, gratings, plasmonic filters

1. INTRODUCTION

Adaptive optics is a technology based on optical systems that can dynamically change their shape to compensate for optical artifacts (due to optical aberrations, for example) introduced by the medium between the object and the image [1]. In biological systems (like the human eye) this is obtained by the capability of mechanically changing conformation to “accommodate” for the changes of the optical conditions [2].

Deformable optical elements are the basis for adaptive optics. Applications using the capability of controlling wavefront phase modulations span from microscopy, spectroscopy [1,2], optical telecommunications [3], aerospace [4] and medical imaging [5,6]. The availability of components like lenses, mirrors and gratings could take huge advantage from the possibility to be deformed or conformed by simple adaptation over a preformed surface. This possibility opens the way to produce very cheap and almost disposable optical elements. Despite several attempts, the fabrication of reflective stretchable optical elements consisting of an elastomeric substrate covered by a reflecting metal film has been unsuccessful so far: the metallization of elastomeric substrates by classical thin film coating techniques (e.g. thermal metal evaporation, e-beam metal evaporation, electrodeposition…) results in a poorly adherent reflecting layer undergoing cracking and delamination even upon very small deformations [8-12]. The mismatch between the metal and the supporting elastomer mechanical properties causes, also in static conditions, the formation of buckling instabilities and wrinkles on the surface [13-15].

Recently it has been demonstrated the fabrication of stretchable reflective gratings based on metal-elastomer nanocomposites obtained by Supersonic Cluster Beam Implantation (SCBI) in Polydimethylsiloxane (PDMS). The implantation of electrically neutral metallic nanoparticles

accelerated in a supersonic expansion is a very effective method to metallize a polymer surface with stable and resilient layers [16]. Although the kinetic energy per atom in supersonically accelerated neutral clusters is four orders of magnitude lower than in the case of metal ion implantation in polymers, clusters (made of several thousands atoms) have sufficient inertia to penetrate inside the polymeric target and to form a nanocomposite layer while avoiding charging and carbonization of the polymeric substrate [17]. Metallic electrodes and micropatterns on stretchable substrates capable to sustain very large deformations with improving electrical conductance with cyclical deformation have been recently reported [16].

Stretchable diffraction gratings obtained by SCBI can easily withstand elongations up to 50% for thousands of cycles with no deterioration of their optical quality and dispersion performances. Moreover, their superior flexibility and resilience allow fitting the gratings upon surfaces of a given shape, thus making very simple and cheap imposing optical power in addition to dispersion properties, as it is currently needed in a number of optical devices [18, 19].

Elastomeric matrices represent simple, low-cost and effective media for the fabrication of mechanically tunable plasmonic nanocomposites by in situ doping with precursors from chemical reduction or physical vapor deposition [20-22]. An alternative approach is based on the mixing of preformed nanoparticles in a solvent subsequently used to prepare the polymer [23,24]. These methods present several weaknesses such as the poor control of spatial distribution and aggregation of the dispersed nanoparticles, no to mention the limited amount of nanoparticles that can be dispersed without negatively affecting the polymerization process of the matrix [21]. The functionalization of elastomeric surfaces with noble metal nanoparticles has been proposed as an alternative to obtain stretchable plasmonic nanocomposites: this approach allows a very precise control of nanoparticle size and reciprocal distance; however, surface-functionalized elastomers are quite fragile and their stability has not yet been characterized [25-27].

The possibility of tuning optical properties by changing several parameters of the nanocomposites opens a huge scenario of applications. Metal nanoparticles show localized surface plasmon resonances (LSPRs) consisting in a collective oscillation of conduction electrons excited by an electromagnetic field [28], the localization of the field in structures of nanometric dimensions has profound consequences on light amplification and manipulation due to the fact that changes in nanoparticle volume and/or shape can affect dramatically the optical properties [28, 29]. LSPRs in Au and Ag nanoparticles are of particular interest, in view of applications, since their frequency spans a wide spectral range from the visible to the near infrared [30,31].

Plasmonic nanocomposites consisting of Au or Ag nanoparticles embedded in a dielectric matrix are increasingly used for selective light absorption and/or transmission in optoelectronics, biosensing and solar energy harvesting [32-37]. The tuning of their optical properties can be obtained by selecting nanoparticle dimensions and geometries, particle density and hence inter-particle distance [30,31]. This passive tuning requires the preparation of the ingredients of the nanocomposite with predetermined characteristics prior to the fabrication. Active tuning has been recently demonstrated where the plasmonic properties of a nanocomposite are continuously modified by mechanic deformation of the nanoparticle-matrix system in order to change the inter-particle distance and hence select different spectral absorption regions [25-27]. Deformable nanocomposites have been reported to show plasmonic shifts up to around 70 nm for uniaxial deformations of about 20% [25].

2. NANOCOMPOSITE FABRICATION

SCBD/SCBI

In figure 1(a) a typical SCBI apparatus is reported. Neutral gold clusters are produced by a Pulsed Microplasma Cluster Source (PMCS) and accelerated for implantation in a supersonic expansion. A PMCS schematically consists of a ceramic body with a cavity where a target acting as a cathode, is sputtered by a localized electrical discharge ignited during the pulsed injection of an inert carrier gas at high pressure .The sputtered metal atoms from the target thermalize with the carrier gas and aggregate in the cavity forming metal clusters; the carrier gas-cluster mixture expands out of the PMCS through a nozzle into a low-pressure expansion chamber, thus producing a highly collimated supersonic beam with a divergence lower than 1°. The central part of the beam enters a second vacuum chamber (deposition chamber, at a pressure of about 10−5 mbar) through a skimmer and it impinges on a PDMS substrate supported by a motorized substrate holder.

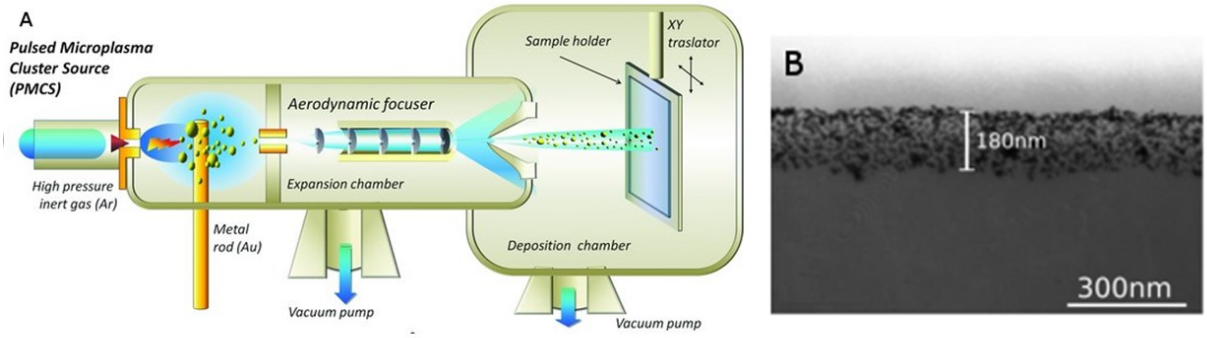

Figure 1: (a) Typical SCBI apparatus. The mix of gas and clusters produced in a cluster source attached to the expansion chamber is accelerated by a difference of pressure between the source and the expansion chamber and collimated by the aerodynamic focuser. Then the nanoparticles enter the deposition chamber and they are implanted in the polymeric substrate held on a movable sample holder allowing the deposition on large areas though a rastering technique. (b) TEM image of a thin section of PDMS implanted with an equivalent thickness of 30 nm. Nanoparticles penetration depth is approximately 180 nm. (Adapted from references [18][19])

Although the kinetic energy per atom in supersonically accelerated neutral clusters is about 0.5eV, clusters have sufficient inertia to penetrate inside the polymeric target without charging or carbonizing the polymeric substrate. This means that SCBI allows the direct fabrication of systems with a well-controlled cluster amount over a wide range of values which cannot be obtained with traditional approaches. Moreover, in figure 1(b) it can be observed that nanoparticles form a thin layer of about 200nm at the elastomeric surface and that the metallic film is not continuous but cluster maintains their individuality.

Co-depostion

Another approach to prepare metal–polymer nanocomposites is generally based on co- or tandem deposition of the metallic and polymeric components and formation of the metallic nanoparticles by self-organization. This leads to aggregation and formation of stable metal clusters which are embedded into in the polymer matrix upon growth of the nanocomposite film [38].

3. OPTICAL DEVICES

Gratings

Transparent gratings can be fabricated by making an elastomeric replica from a master consisting of a commercial glass diffraction grating. The transparent grating is then made reflective by implanting silver nanoparticles by means of a supersonic cluster beam implantation. Figure 2a reports the same single line scan taken on the PDMS grating metalized by SCBI: an excellent reproduction of the bare profile is observed.

Due to the possibility of varying nanocomposite filling factor in a wide range without damaging the substrate, it is possible to obtain highly reflective gratings (fig 2b, 2c), characterized by an excellent flexibility and resilience. These properties allow fitting the gratings upon surfaces of a given shape, thus making very simple and cheap imposing optical power in addition to dispersion properties.

A deformable grating fitted upon a cylindrical object, maintains its geometrical properties in terms of the distances of the grooves, irrespectively of their orientation. This is simply because the cylindrical surface is not endowed with any curvature (it is homologous to a plane surface) [18,19]. This is very important when exploiting the diffraction properties of a cylindrical grating, at variance with the case of a spherical or more complex curvature imposed to a grating, which introduces local changes in the groove spacing.

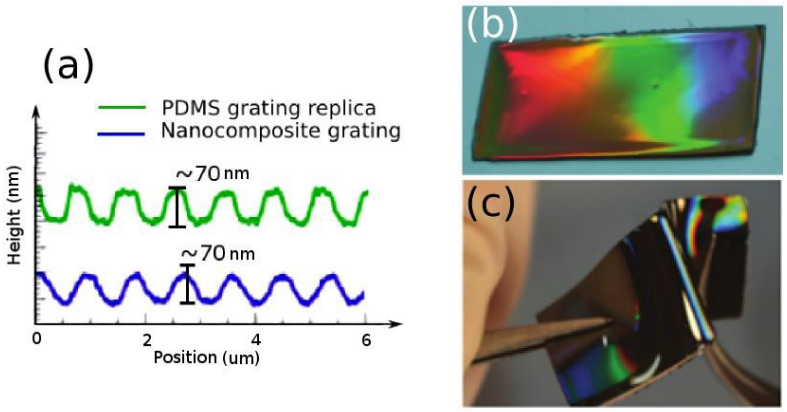

Figure 2: (a) AFM single profiles of the bare PDMS grating and the 60-nm Ag SCBI. (b) Picture of the stretchable and deformable reflective diffraction grating. (c) PDMS grating withstanding arbitrary deformations without deterioration (Adapted from reference [18]).

Spectrometers

Stretchable diffraction gratings obtained by SCBI can easily withstand elongations up to 50% for thousands of cycles with no deterioration of their optical quality and dispersion performances. Moreover grating response as a function of stretching is linear. These properties are currently needed in a large number of optical devices, for example such gratings are suitable for the fabrication of very simple and inexpensive scanning optical spectrometers. Indeed, the grating mounted on a uniaxial stretcher can be exploited to fabricate a very simple and cheap "linear" alternative to traditional rotating grating monochromators. It has been demonstrated [19] that such monochromators can be used to fabricate spectrometers able to span the entire visible range of wavelengths, which provide results in excellent agreement with traditional spectrometers (figure 3), and which maintain their optical performances for thousands of strain cycles.

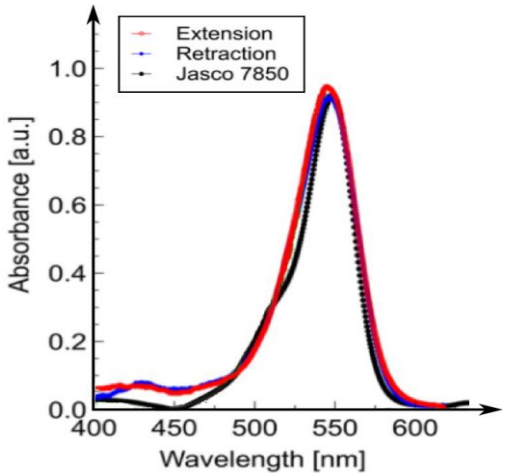

Figure 3: Absorption spectra for Rhodamine B dye in ethanol solution with a concentration of 3.2 x 10-4 M. Extension and retraction spectra acquired with the photodiode are perfectly coincident (solid red and blue lines) and comparable with the spectrum acquired with a commercial Jasco 7850 Uv-vis spectrophotometer (dashed-dotted black line) (Adapted from reference [19]).

Hyperspectral imaging

As recently demonstrated, the gratings can be fitted onto a prepared surface with a given shape/curvature allowing the realization of extremely cheap reflective optical elements endowed with optical power [39].

Although the spectral resolution of a high quality grating is still better, a number of applications requiring low resolution could be addressed by the use of these gratings. The field of hyperspectral imaging is rapidly growing since the combination of spectral and spatial information open the possibility to the monitoring rapidly chemical composition, product quality and conservation state, the stage of growth of plants, beyond the wide field of remote sensing, security and military applications.

Hyperspectral imaging is currently limited by the complexity of a typical camera, including the imaging and the spectroscopic devices. From one side, the technology drops the costs of cameras, electronics, computing, and also optics in some respects. But the complexity of coupling the two components in a hyperspectral camera remains.

The opportunity to operate with conformed gratings has already been considered. For example, relatively cheap spectrometers (low spectral resolution) mount the grating curved. Nevertheless the feasibility of a compact and cost-accessible hyperspectral camera are far to be obtained due to the influence of mechanical and optical components.

Curved diffraction gratings are typically fabricated by ruling engines, a delicate process exposed to failures. Holographic gratings could in principle do the job, but their production is still more delicate and restricted to very peculiar, demanding applications. Lithography, etching and ablation, although simpler, still need complicate hardware for fabrication. Nanocomposite based diffraction gratings could then be the breakthrough in this field, with the simultaneous advantage of mixing a relatively ease in fabrication, the extremely cheapness and the superior performances from the optical point of view.

Stretchable plasmonic filters

The high stretchability metal-polymer nanocomposites produced by SCBI can be exploited also for the realization of plasmonic filters [40]. The tuning of the plasmonic absorbtion properties is traditionally obtained by selecting nanoparticle dimensions and geometries, particle density, and hence inter-particle distance. This passive tuning requires the preparation of the ingredients of the nanocomposite with predetermined characteristics prior to the fabrication. Active tuning has been recently demonstrated where the plasmonic properties of a nanocomposite are continuously modified by mechanic deformation of the nanoparticle-matrix system in order to change the inter-particle distance and hence select different spectral absorption regions.

Nanocomposites made by implanting through SCBI gold clusters in an elastomeric matrix show a gradual redshift of the absorbance peak when stretched, as reported in fig. 4(a). Moreover, an increase in peak redshift, up to roughly 220 nm occurs for increasing values of the density of particle embedded in the polymer (fig. 4(b)); these values are significantly larger than those reported in the literature for stretchable nanocomposites.

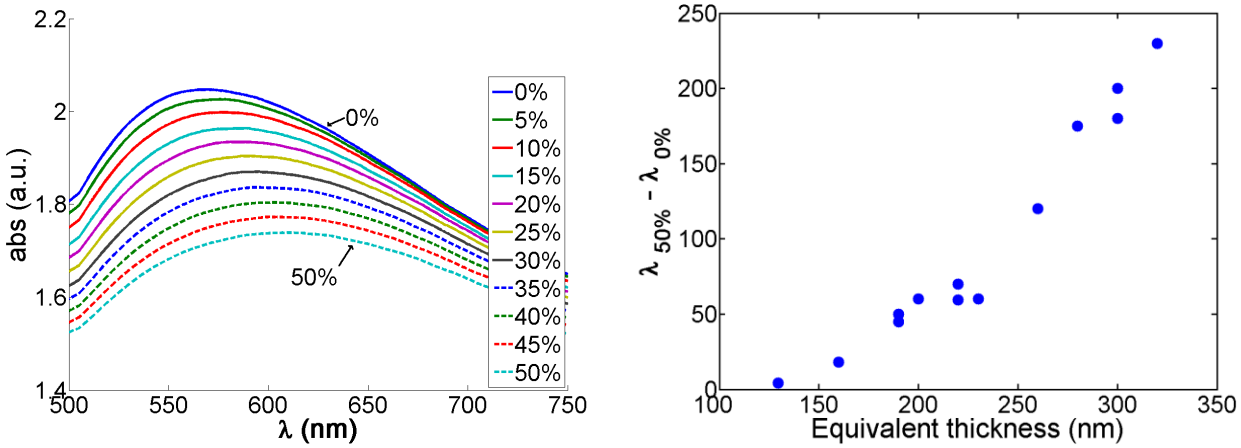

Figure 4: Left: Absorbance spectra acquired at different applied strains. Absorbances have been normalized as $-\log(I/I_{0\%})$, where I is the measured absorbance and $I_{0\%}$ is the absorbance of the peak recorded in the non-stretched sample. Right: Shifts of the surface plasmon resonance as a function of the nanocomposite equivalent thickness (defined as in ref [40]) for a uniaxial deformation of 50% of the original dimension. (Adapted from reference [40])

Cyclic stretching induces a rearrangement and reorganization of the embedded clusters affecting the plasmonic behavior.

A substantial plasmon shift remains and stabilizes after a suitable mechanical post deposition treatment, providing the evidence that nanocomposites produced by SCBI can be used as mechanically tunable optical filters or as components for stretchable optical devices.

4. ABSORBERS

Thanks to the localization of the surface plasmons, a nanocomposite can locally trap the incoming light and create high local electric fields. This behavior has been especially proved for the case of a metallic bead in vicinity of a metallic surface [41, 42]. This is the base for solutions for developing very strong absorbers. In all these cases the basic principle was the fabrication of a three layers structure, two metals separated by a dielectric material. Since structures were obtained by lithography, these solutions were intrinsically limited in view of a wide diffusion. More recent approaches suggested to exploit nanocomposites formed by metallic clusters embedded in dielectric matrix [43, 44]. Two main drawbacks have been evidenced: the need of high filling factors, close to the percolation threshold and the necessity of fabricate devices over extended areas. A possible solution has been identified as the vapor phase deposition [45]. Nanocomposites fabricated by SCBI can be an alternative capable of fulfilling the requirements of above.

The demand of perfect absorbers is mainly driven by the need of developing highly effective solar cells. By integrating these devices in deformable structures make it possible to fabricate wearable cells, which will follow the main trend of moving towards wearable devices.

5. CONCLUSIONS

Metal-polymer nanocomposites allow the fabrication of optical elements characterized by the stability of the optical performances upon substantial deformations. Stretchable and conformable optical gratings open novel and very exciting perspectives for the fabrication of optical devices incorporating diffracting and optical power in a single element. Starting from non-optical grade curved surfaces, one can fabricate optical elements by sticking stretchable gratings or mirrors fabricated by SCBI metallization of cheap replica molded and identical PDMS substrates.

Plasmonic nanocomposites can also be fabricated by implanting neutral gold clusters in a PDMS matrix by supersonic cluster beam implantation which can be used as tunable optical filters or as components for stretchable optical devices.

Faupel-absorbers

REFERENCES

[1] Williams, D. R. and Porter, J. in Adaptive Optics for Vision Science: Principles, Practices, Design and Applications, edited by J. Porter, H. Queener, J. Lin, K. Thorn, and A. A. S. Awwal, (John Wiley & Sons, Hoboken, NJ, USA 2006).

[2] Grewe, B. F., Voigt, F. F., M. van 't Hoff, and Helmchen F., "Fast two-layer two-photon imaging of neuronal cell populations using an electrically tunable lens", Biomed. Opt. Exp. 2, 2035 (2011).

[3] Albert, O., Sherman, L., Mourou, G., Norris, T. B., and Vdovin, G., "Smart microscope: an adaptive optics learning system for aberration correction in multiphoton confocal microscopy", Opt. Lett. 25, 52 (2000).

[4] Druon, F., Chériaux, G., Faure, J., Nees, J., Nantel, M., Maksimchuk, A., Mourou, G., Chanteloup, J. C., and Vdovin, G., "Wave-front correction of femtosecond terawatt lasers by deformable mirrors" Opt. Lett. 23,1043 (1998).

[5] Booth, M., Neil, M., and Wilson, T., "New modal wave-front sensor: application to adaptive confocal fluorescence microscopy and two-photon excitation fluorescence microscopy", J. Opt. Soc. Am. A 19, 2112 (2002).

[6] Iqbal A., and Amara, F. B., "Modeling of a magnetic-fluid deformable mirror for retinal imaging adaptive optics systems", Int. J. Optomechatron. 1, 180 (2007).

[7] Fernández, E. J., Iglesias I., and Artal P., "Closed-loop adaptive optics in the human eye" Opt. Lett. 26, 746 (2001).

[8] Wilbur J. L., Jackman R. J., Whitesides G. M., Cheung E. L., Lee L. K., and Prentiss M. G., "Elastomeric optics", Chem. Mater. 8, 1380 (1996).

[9] Graz, I. M., Cotton, D. P. J., and Lacour, S. P., "Extended cyclic uniaxial loading of stretchable gold thin-films on elastomeric substrates", Appl. Phys. Lett. 94, 071902 (2009).

[10] Graudejus, O., Morrison, B., Goletiani, C., Yu, Z., and Wagner, S., "Encapsulating elastically stretchable neural interfaces: yield, resolution, and recording/stimulation of neural activity", Adv. Funct. Mater. 22, 640 (2012).

[11] Douville, N. J., Li, Z., Takayama, S., and Thouless, M. D., "Fracture of metal coated elastomers", Soft Matter 7, 6493 (2011).

[12] Tuinea-Bobe, C. L., Lemoine, P., Manzoor, M. U., Tweedie, M., D'Sa, R. A., Gehin, C., and Wallace, E., "Photolithographic structuring of stretchable conductors and sub-kPa pressure sensors", J. Micromech. Microeng. 21, 115010 (2011).
[13] Bowden, N., Brittain, S., Evans, A. G., Hutchinson, J. W., and Whitesides, G. M., "Spontaneous formation of ordered structures in thin films of metals supported on an elastomeric polymer", Nature 393, 146 (1998).
[14] Rosset, S. and Shea, H. R., "Flexible and stretchable electrodes for dielectric elastomer actuators", Appl. Phys. A 110, 281 (2013).
[15] Chung, J. Y., Nolte, A. J., and Stafford, C. M., "Surface Wrinkling: A Versatile Platform for Measuring Thin-Film Properties", Adv. Mater. 23, 349 (2011).
[16] Ghisleri, C., Borghi, F., Ravagnan, L., Podestà, A., Melis, C., Colombo, L., and Milani, P., "Patterning of gold–polydimethylsiloxane (Au–PDMS) nanocomposites by supersonic cluster beam implantation", J. Phys. D: Appl. Phys. 47, 015301 (2014)
[17] Cardia, R., Melis, C., and Colombo, L., "Neutral-cluster implantation in polymers by computer experiments", J. Appl. Phys. 113, 224307 (2013)
[18] Ghisleri, C., Siano, M., Potenza, M. A. C., Ravagnan, L., and Milani, P., "Nanocomposite-based stretchable optics" Laser & Photonics Rev. 7, 1020 (2013)
[19] Ghisleri, C., Potenza, M. A. C., Ravagnan, L., Bellacicca, A. and Milani, P., "A simple scanning spectrometer based on a stretchable elastomeric reflective grating" Appl. Phys. Lett. 104, 061910 (2014)
[20] Caseri, W., "Nanocomposites of polymers and metals or semiconductors: historical background and optical properties", Macromol. Rapid Commun. 21, 705 (2000).
[21] Faupel, F., Zaporojtchenko, V., Greve, H., Schurmann, U., Chakravadhanula, V. S. K., Hanisch, C., Kulkarni, A., Gerber, A., Quandt, E., and Podschun, R., "Deposition of nanocomposites by plasmas", Contrib. Plasma Phys. 47, 537 (2007).
[22] Takele, H., Kulkarni, A., Jebril, S., Chakravadhanula, V. S. K., Hanisch, C., Strunskus, T., Zaporojtchenko, V., and Faupel, F., "Plasmonic properties of vapour-deposited polymer composites containing Ag nanoparticles and their changes upon annealing", J. Phys. D: Appl. Phys. 41, 125409 (2008).
[23] Vanherck, K., Verbiest, T., and Vankelecom, I., "Comparison of Two Synthesis Routes to Obtain Gold Nanoparticles in Polyimide", J. Phys. Chem. C 116, 115 (2012).
[24] Pastoriza-Santos, I., Pérez-Juste, J., Kickelbick, G., and Liz-Marzán, L., "Optically active poly (dimethylsiloxane) elastomer films through doping with gold nanoparticles", J. Nanosci. Nanotechnol. 6, 453 (2006).
[25] Cataldi, U., Caputo, R., Kurylyak, Y., Klein, G., Chekini, M., Umeton, C., and Bürgi, T., "Growing gold nanoparticles on a flexible substrate to enable simple mechanical control of their plasmonic coupling", J. Mater. Chem. C 2, 7927 (2014).
[26] Chiang, Y. F., Chen, C. W., Wang, C. H., Hsieh, C. Y., Chen, Y. T., Shih, H. Y., and Chen, Y. F., "Mechanically tunable surface plasmon resonance based on gold nanoparticles and elastic membrane polydimethylsiloxane composite", Appl. Phys. Lett. 96, 041904 (2010).
[27] Zhu, X., Shi, L., Liu, X., Zi, J., and Wang, Z., "A mechanically tunable plasmonic structure composed of a monolayer array of metal-capped colloidal spheres on an elastomeric substrate", Nano Res. 3, 807 (2010).
[28] Kreibig, U. and Vollmer, M., "Optical Properties of Metal Clusters" (Springer-Verlag, 1995).

[29] Grigorchuk, N. I., "Effect of surface plasmon linewidth oscillations on optical properties of metal nanoparticle embedded in a dielectric media", J. Phys. Chem. C 116, 23704 (2012).
[30] Kinnan, M. K. and Chumanov, G., "Plasmon coupling in two-dimensional arrays of silver nanoparticles: II. Effect of the particle size and interparticle distance", J. Phys. Chem. C 114, 7496 (2010).
[31] Ghosh, S. K. and Pal, T., "Interparticle coupling effect on the surface plasmon resonance of gold nanoparticles: from theory to applications", Chem. Rev. 107, 4797 (2007).
[32] Homola, J., "Present and future of surface plasmon resonance biosensors", Anal. Bioanal. Chem. 377, 528 (2003).
[33] Meen, T.-H., Tsai, J., Chao, S., Lin, Y., Wu, T., Chang, T., Ji, L., Water, W., Chen, W., Tang, I., and Huang, C., "Surface plasma resonant effect of gold nanoparticles on the photoelectrodes of dye-sensitized solar cells", Nanoscale Res. Lett. 8, 450 (2013).
[34] Pillai, S., Catchpole, K. R., Trupke, T., and Green, M. A., "Surface plasmon enhanced silicon solar cells", J. Appl. Phys. 101, 093105 (2007).
[35] Sorger, V. J., Oulton, R. F., Ma, R. M., and Zhang, X., "Toward integrated plasmonic circuits", MRS Bull. 37, 728 (2012).
[36] Millyard, M., Huang, F. M., White, R., Spigone, E., Kivioja, J., and Baumberg, J. J., "Stretch-induced plasmonic anisotropy of self-assembled gold nanoparticle mats", Appl. Phys. Lett. 100, 073101 (2012).
[37] Hedayati, M. K., Zillohu, A. U., Strunskus, T., Faupel, F., and Elbahri, M., "Plasmonic tunable metamaterial absorber as ultraviolet protection film", Appl. Phys. Lett. 104, 041103 (2014).
[38] Faupel, F., Zaporojtchenko, V., Strunskus, T., Elbahry, M., "Metal-Polymer Nanocomposites for Functional Applications", Adv. En. Mater. 12, 1177 (2010).
[39] Hyperspectral
[40] Minnai, C., Milani, P., "Metal-polymer nanocomposite with stable plasmonic tuning under cyclic strain conditions", Appl. Phys. Lett., 107, 073106, (2015).
[41] Lévêque, G., Martin, O.J. "Optical interactions in a plasmonic particle coupled to a metallic film", Opt. Express, 14, 9971 (2006).
[42] Lévêque, G., Martin, O.J., "Tunable composite nanoparticle for plasmonics", Opt. Lett, 31, 2750–2752 (2006)
[43] Faupel, F., Zaporojtchenko, V., Strunskus, T., Elbahri, M., "Metal-polymer nanocomposites for functional applications", Adv. Eng. Mater, 12, 1177 (2010).
[44] Hanemann, T., Szabó, D.V., "Polymer-nanoparticle composites: From synthesis to modern applications", Materials, 3, 3468 (2010).
[45] Beyene, H.T., Chakravadhanula, V.S.K., Hanisch, C., Strunskus, T., Zaporojtchenko, V., Elbahri, M., Faupel, F. "Vapor phase deposition, structure, and plasmonic properties of polymer-based composites containing Ag–Cu bimetallic nanoparticles", Plasmonics, 7, 107 (2012).